Spin dependent transport in antiferro and ferrimagnetic nanostructures

Pablo Merodio Camara

UNIVERSITÉ DE GRENOBLE

THÈSE

Pour obtenir le grade de

DOCTEUR DE L'UNIVERSITÉ DE GRENOBLE

Spécialité : **Physique**

Arrêté ministériel : 7 août 2006

Présentée par

Pablo MERODIO CÁMARA

Thèse dirigée par **Mairbek CHSHIEV**
et codirigée par **Vincent BALTZ et Hélène BÉA**

préparée au sein du Laboratoire **SPINTEC**
et de l'**École Doctorale de Physique de Grenoble**

Spin-dependent transport in antiferro and ferrimagnetic nanostructures

Thèse soutenue publiquement le **3 décembre 2014**,
devant le jury composé de :

M. Alain SCHUHL
Professeur, Université Joseph Fourier, Président
M. Robert STAMPS
Professeur, University of Glasgow, Rapporteur
M. André THIAVILLE
Directeur de recherche CNRS, Rapporteur
M. Vincent CROS
Directeur de recherche CNRS, Examinateur
M. Vitalii DUGAEV
Professeur, Rzeszów University of Technology, Examinateur
M. Mairbek CHSHIEV
Professeur, Université Joseph Fourier, Directeur de thèse
M. Vincent BALTZ
Chargé de recherche CNRS, Co-Directeur de thèse

A mis padres.
A Annika.

Acknowledgments

Estas líneas de agradecimiento cierran definitivamente este manuscrito, tres años de doctorado, muchos años de duro trabajo y una etapa importantísima de mi vida. He de confesar que me ha costado más escribirlas que cualquier capítulo de la tesis. Les debo tanto a tantas de las personas que vienen a continuación, que me parecía que unas simples palabras se quedarían más que cortas. Gracias a ellas he podido llegar hasta aquí.

En primer lugar me gustaría agradecer a Alan Schuhl, Vincent Cros, Vitalii Dugaev, Robert Stamps y André Thiaville que hayan aceptado participar como miembros del tribunal de mi tesis. Gracias también por los magníficos e indispensables informes de Robert, André, Vitalii y Alan sobre el manuscrito y la defensa. Gracias a André por haber corregido el manuscrito y a Robert por haber hecho que la sesión de preguntas haya sido tan agradable; a pesar de haber durado tanto y ser uno de los grandes temores de todo doctorando que se precie, casi puedo decir que la disfruté.

Siento la más profunda gratitud y aprecio hacia mis tres directores de tesis: Vincent, Hélène y Mair. Trabajar con ellos estos tres años ha sido un verdadero placer. Me han acompañado cuando lo he necesitado y me han dado toda la libertad del mundo en el momento adecuado. Puedo decir que la difícil, excitante e incierta tarea de investigación como estudiante de doctorado ha sido mucho más sencilla sabiendo que podía contar con ellos en todo momento, tanto científica como humanamente. Les agradezco enormemente todas las puertas que me han abierto, mucho de lo que he aprendido y todo el tiempo que tan generosamente me han dedicado.

Muchos estudiantes han tenido durante sus años de doctorado un "guía científico-espiritual". En mi caso ha sido Vincent, la primera persona que contacté para subirme a este tren. No sólo me ayudó enormemente a conseguir la beca de doctorado junto con Hélène y Mair, sino que también me ha apoyado, animado y motivado durante toda esta aventura, desde los momentos de desesperación por no conseguir ningún resultado hasta la difícil etapa de redacción y posterior defensa. Su carta de recomendación fue además definitiva para tener la increíble oportunidad de dar clases en la universidad durante los dos últimos años. No tengo palabras que puedan expresar mi agradecimiento por todo lo que ha hecho por mí.

Gracias a toda la gente de SPINTEC por haberme acogido en un laboratorio en el que el ambiente de trabajo ha sido inmejorable. Gracias a todos por su fantástico regalo de fin de tesis: tocar el piano cómodamente sentadito en mi nueva banqueta es una auténtica delicia.

Gracias a Bill, Ursula y Abhijit por haberme permitido trabajar el primer año en su proyecto de spin pumping y haberme explicado el funcionamiento de la FMR. Y a Nikolai por saber arreglar y conocer mucho mejor que yo el sistema segundos después de que yo mismo le haya explicado cómo

se utiliza. Mogollón de electrones han sido bombeados gracias a ellos (y a varias muestras depositadas por el amabilísimo Stéphane).

Grand merci a la legendaria Rachel, una de las personas más competentes que conozco. Su interés por las personas, su simpatía y su buen hacer me han salvado el trasero en más de una ocasión y facilitado enormemente las cosas en más de dos. Muchísimas gracias a Christophe (de verdad) por su paciencia, pedagogía y buen humor durante los primeros meses de formación en la PTA. No es fácil entrenar a Rompetechos en técnicas de nanofabricación, y si no fuera por él, la tensión máxima por no hacer explotar todas las máquinas extracaras de la sala limpia habría acabado conmigo (y con la sala limpia).

Contento estoy de haber compartido despacho con Alexandru, Abhijit, Bertrand, Antoine y Kamiltonian. Gracias a nuestras conversaciones absurdas y no tan absurdas tanto dentro como fuera del despacho, Kamiltitos y yo hemos logrado terminar este doctorado casi sin volvernos locos. Ahora ya somos aptos para dar el paso definitivo y tantas veces añorado de ser (felices y despreocupados) conductores de autobús.

Sufrir el desgraciado incidente de tener una tesis escrita en un documento Latex que no compila días antes de la entrega es un evento altamente desagradable. Si a alguien le ocurriere (Dios no lo quiera), le recomendaría encarecidamente tener a su lado a alguien como Eldar. La tarde que pasamos juntos solucionando los errores de compilación me salvaron del desastre global.

Les debo innumerables risas (sobre todo durante las comidas) a Marina, Murat, Eldar, Léa, Andrey y Hongxin. Una vía de escape inestimable, especialmente después de mi época de "Lobo Solitario".

Gracias a Emilie y a Nahuel por haberme dejado sus transparencias para preparar la audición de la Escuela Doctoral, una de las razones por las que pude conseguir la beca. Gracias también a Christophe y Emilie por el glorioso template de Latex en el que escribí todas estas cositas científicas sobre funciones de Green y tal y tal.

Merci beaucoup a Claudine Chaffy por haber sido mi tutora durante estos dos últimos años como profesor en la universidad. Por la tranquilidad que me dio desde el principio, por todo el material que puso a mi disposición, por sus inestimables consejos y por sus fantásticos informes sobre mi trabajo.

Grazie mille a Simone, mi director de stage de Master 2. Un tipo genial (y un músico apasionado) que me escribió una carta de recomendación para conseguir la beca de doctorado y trabajar en un proyecto de otro laboratorio. Sin comentarios. Creo que deberíamos haber compartido más cervezas, más conversaciones y más conciertos aquí en Grenoble.

Merci a Matthieu, mi codirector de proyecto de ingeniería, una gran persona que siempre se ha portado estupendamente conmigo.

Gracias a todos los amigos con los que he compartido estos años en Grenoble. Tengo muchísima suerte de poder disfrutar y haber conocido a gente genial como Pablete, Emilie, Lara, Alejandro, Martí, Cristina, Diego, Elisa, Wiebke, y a las recientes "incorporaciones": Laurent, Juan, Miguel, Rubén (mi canario favorito), Miguel V. y Maite. Les agradezco inmensamente su escandalosamente genial regalo de tesis. Me mataron de la risa con su sorpresa y me hicieron sentir muy feliz.

Si alguien puede conseguir cosas como hacer que tu tesis aparezca en un número inédito del "Nationel Geographik", esa es Karla Marina. A pesar de estar temblando el mundo, se preocupó de darme ánimos cada día durante la redacción, de sorprenderme con un inmejorable final de tesis y de afrontar la difícil tarea de hacer que confíe un poquito más en mí mismo. Dichoso soy por haberme transmitido su alegría de vivir y por poder descubrir, emocionarme y resonar con alguien tan especial.

Gracias a mis grandes amigos de toda la vida. Los que uno sabe que están ahí aunque no los vea a menudo. Cuando pienso en Carmen, Pablo, Gaspar, Gonzalo y David se me dibuja una sonrisa en la cara. Mi pierna derecha también tiene mucho que agradecerle a Carmen: si no hubiera sido por nuestra conversación semanal este verano, me habría pegado un tiro en la rodilla.

Gracias a mis abuelos. Porque no me olvido de todos los días que me han cuidado siendo un enano, de los maravillosos veranos en el pueblo, de las mañanas en "los pinos" y de las tostadas de mermelada de ciruela sentado en la encimera de la cocina de la Elipa.

Gracias a mi mejor amigo, Emilio. Porque me siento inmensamente afortunado y orgulloso de nuestra amistad. A mi lado ha estado en las etapas más importantes, en las más duras y en las más felices. Una parte esencial y fuente inagotable de disfrute, alegría y humor en mi vida.

A Anni. Por todo lo que hemos compartido juntos. Por sus tiernas palabras de aliento en momentos clave. Esta tesis se la dedico a ella, como muestra del lugar tan importante que siempre ocupará en mi corazón.

A mis padres, Chon y Antonio. Más que dedicársela a ellos, siento que esta tesis es también la suya. Insignificantes serían unas palabras de dedicatoria o agradecimiento para las personas que me lo han dado todo, siempre, en todo momento. Sólo espero que este logro y todo el esfuerzo, toda la satisfacción, toda la paz y toda la alegría por conseguirlo sirvan para expresar el cariño que siento hacia ellos.

Soy libre.

Contents

Chapter I

Introduction

I.1 Context

Information storage represents one of the main pillars of our modern technology-based society. Current technological needs for telecommunications, data processing, informatics or digital imaging require reliable memory devices with high access speed, low power consumption, non volatility and high memory storage density.

In conventional electronics, information is carried by electric charges, which are stored in capacitors and driven by the application of bias potentials. This technology relays on the electronic properties of semiconductor materials, where the spin of the electron basically plays no role. In contrast, magnetic recording utilizes the local orientation of spins in ferromagnets, -i.e., the local magnetization- for data storage and magnetic fields for information reading and writing.

The discovery of giant magnetoresistance in 1988 gave birth to "spintronics": an emerging technology based on the combination of both charge transport and magnetization. In turn, spintronics has given rise to a fast and not volatile memory concept: the Magnetic Random Access Memory (MRAM), and more recently to the spin transfer torque MRAM (STT-MRAM). This new class of magnetic memory presents very interesting features such as non-volatility, large read and write endurance and fast read and write operations. Although these characteristics point the MRAMs as potential candidates to replace a number of other memory technologies, the exclusive use of ferromagnetic (F) materials for their spin-dependent transport properties presents also some drawbacks. For instance, high storage density is limited by stray fields and high current densities are still required for writing operations due to high magnetic moments inherent to Fs. Since antiferromagnetic (AF) and ferrimagnetic (FI) materials exhibit vanishing or significantly reduced magnetic moments and stray fields with respect to Fs, this work aims to address a systematic study of spin-dependent transport properties of both materials for their potential application in non-volatile magnetic memories.

In this Chapter, I present a brief introduction to spintronics as the general framework in which the subject of this thesis is involved. Some of the main underlying spin-dependent transport phenomena of this flouring technology, namely giant magnetoresistance, tunneling magnetoresistance and spin transfer torque in currently used F nanostructures are shortly explained, since they will be investigated in the following chapters in the case of AF and FI nanomaterials. I included a concise description of the essential features characterising the three different magnetic orderings in the first section of this introduction. Next, I discuss the state-of-the-art in AF and FI-based spintronics. Finally, the general outline of the thesis is presented.

I.2 Magnetic ordering

The atomic magnetic moments in solid matter can be ordered in different ways (see Fig. I.1) depending on the interaction energy or exchange interaction between the spins $\mathbf{S}_i$ and $\mathbf{S}_j$ of neighbouring atoms i and j (Heisenberg Hamiltonian for N atoms, see IV.2.1 for more details):

$$e_{\text{ex}} = \sum_{i,j}^{N} -J_{i,j}\mathbf{S}_i \cdot \mathbf{S}_j$$

If the exchange integrals $J_{i,j}$ are positive, magnetic moments will align in the same direction and in the same sense, resulting in a net macroscopic magnetization: ferromagnetic order. If they are negative, magnetic moments will align in the same direction but in alternating senses, creating two different sublattices with opposite magnetic orientations, giving no net magnetization: antiferromagnetic order [1]; if in addition the opposing moments of each sublattice are unequal, then a spontaneous magnetization appears: ferrimagnetic order.

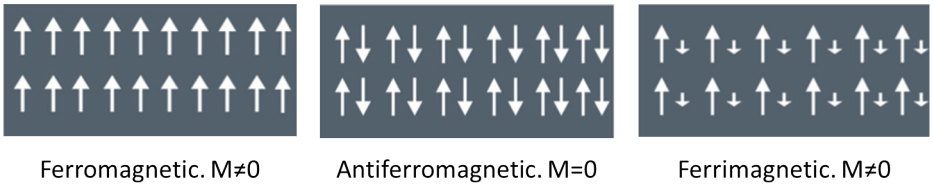

Figure I.1 – Three fundamental magnetic orderings of matter.

For these magnetic orderings to occur, the exchange interaction energy must overcome the thermal energy: ferromagnetism and ferrimagnetism orders appear below the Curie temperature T_C, and antiferromagnetism appears below the Néel temperature T_N.

1. More complicated antiferromagnetic configurations can also be found for spins arranged in a non-collinear way or in the case of frustrated systems where antiferromagnetic interactions can lead to multiple ground states with non-regular distributions of localized spins.

A very general magnetic ordering: ferrimagnetism

As explained above, a FI material hosts two populations of atoms with opposing and unequal magnetic moments formed from elements having an unfilled d or f electron shell, which results in a spontaneous magnetization. The two different populations consist of ions of different species or similar ions occupying crystallographically inequivalent sites. A subsystem formed by all the magnetic sites in the crystal with identical magnetic behaviour (pointing in a single direction) is called a sublattice. In the case of FIs, the magnetic moments of ions of different sublattices are aligned antiparallel due to a negative exchange interaction. The spontaneous magnetization is equal to the vector sum of the magnetizations of the sublattices.

Ferrimagnetism might be viewed as one of the most general cases of magnetic ordering. As such, ferromagnetism is a particular case of ferrimagnetism in which only one sublattice is present and antiferromagnetism is a limiting case in which the two sublattices consist of identical magnetic ions and the net magnetization is zero.

As in the case of antiferromagnetism, the FI ordering notion was introduced by L. Néel in 1948. The term "ferrimagnetism", is derived from the word ferrite, which is the name of a large class of oxides of the transition elements in which the phenomenon was first observed. Other examples of FI materials are: magnetic garnets, transition metals compounds such as MnGa, MnCoAl, CrMnSb, and the archetypal magnet, lodestone, which is a naturally magnetized piece of the mineral magnetite (Fe_3O_4), the oldest known magnetic material. The first magnetic compasses were made out of suspended pieces of lodestone, which in Middle English means 'course stone' or 'leading stone', indicating their importance to early navigation.

Note that the ideal picture of staggered AF and FI has to be nuanced in realistic systems where magnetic interaction frustrations occur due for instance to interfacial roughness, structural defects, peculiar 3-D AF and FI spin structures, interdiffusion of species and grain boundaries for polycrystals.

I.3 Conventional ferromagnetic-based spintronics

Conventional electronics has exploited until recently only the charge of the electron for technological applications. Spintronics (spin electronics) makes reference to a new technology emerged in the 1980s that takes also advantage of the electron spin to carry information. It paves the way for new revolutionary devices with spin-dependent effects arising from the interaction between itinerant spins and the magnetic properties of solid state materials. It has been used in a number of applications and has allowed for instance to strongly increase data storage capability. In comparison to conventional electronics, this new technology offers performance and additional functionalities for electronic devices.

The possibility to build magnetic multilayers with individual thicknesses comparable to the electron spin diffusion lengths and below, so that spin-dependent transport effects could be observed, lead in 1988 to the discovery of the Giant Magnetoresistance (GMR) effect, which is considered the beginning of the new spin-based electronics.

Giant magnetoresistance

Giant magnetoresistance (GMR) was first observed by the groups of Albert Fert and Peter Grünberg [Baibich et al., 1988], [Binasch et al., 1989], in thin-film structures composed of alternating F and non-magnetic (NM) conductive layers of several nanometers (thicknesses comparable to the electron mean free path). For current perpendicular to plane, the effect consists in a significant change in the resistance for an electric current flowing perpendicular to the plane of the layers when the relative magnetic configuration of the F layers switches from antiparallel to parallel (see Fig. I.2). The overall resistance is relatively low for parallel alignment and relatively high for antiparallel alignment. The ferromagnetic layers are spontaneously coupled antiferromagnetically through the NM metallic spacer (high resistance), but the magnetic configuration can be tuned via an external magnetic field.

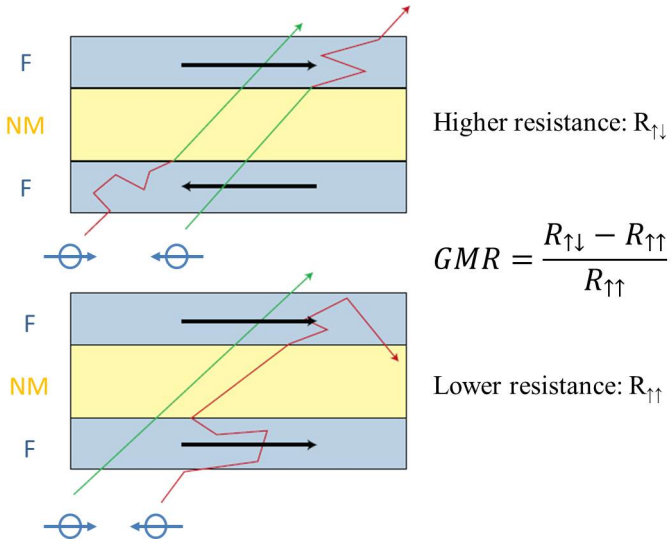

Figure I.2 – Schematic illustration of GMR adapted from Ref. [Chappert et al., 2007] and definiton of the GMR ratio.

As depicted in Fig. I.2, the GMR ratio is defined as the difference between the resistances in the antiparallel and the parallel states divided by the resistance of the parallel state (or divided by the resistance of the antiparallel state, depending on the convention). It strongly depends on temperature and thicknesses of the F and NM layers.

In addition to the spin-dependent reflections at the interfaces, the effect can be interpreted in terms of the spin-dependent density of states (DOS) of the F electrodes for the itinerant electrons at the Fermi energy. Electronic states are spin split in the Fs, which

leads to unequal DOS for up and down spins at the Fermi energy. In turn, the DOS at the Fermi level determines the conductance of each spin channel, i.e., up (down) spins will be scattered more likely in a F with majority down(up) electrons. For instance when no spin-flip scattering processes are considered, the bulk conductivity of spin-up and down carriers at the Fermi level is given by:

$$\sigma_{\uparrow(\downarrow)} = e^2 DOS_{\uparrow(\downarrow)}(E_F) D_{\uparrow(\downarrow)}$$

where $D_{\uparrow(\downarrow)}$ is the spin-dependent spin diffusion constant. When an electric field is applied to such a material, a flow of a spin-polarized current appears, with a polarization defined by the conductivities:

$$P = \frac{J_\uparrow - J_\downarrow}{J_\uparrow + J_\downarrow} = \frac{\sigma_\uparrow - \sigma_\downarrow}{\sigma_\uparrow + \sigma_\downarrow}$$

where the $J_{\uparrow(\downarrow)}$ denote the spin-resolved charge current densities.

Thus, when no spin-flip processes are considered, the overall resistance will depend on the magnetic orientation of the F leads.

Within three years after the discovery of GMR, the "spin valve" concept had been introduced. A spin valve is a GMR-based device with two ferromagnetic layers (alloys of nickel, iron, and cobalt) sandwiching a thin nonmagnetic metal spacer (usually copper). The resistance of the spin valve increases typically from 5 to 10 % when the relative orientation of the magnetizations of the two layers switches from parallel to antiparallel alignment [Wolf et al., 2001]. One of the two magnetic layers is called the "free layer", since its magnetization can be easily reoriented by relatively low magnetic fields. The other magnetic layer is called the "reference layer" or "pinned" layer, since its magnetization is relatively insensitive to moderate magnetic fields. Pinning is usually accomplished by using an antiferromagnetic layer in contact with the pinned F layer, which yields to a magnetic interfacial interaction called exchange bias [2].

Since the magnetization of the free layer can however be easily reoriented by relatively low magnetic fields, the spin-valve itself can probe the orientation of a small magnetic field and act as a magnetic sensor through the GMR effect. This sensor can be used in a magnetic-storage read head to detect the small magnetic field coming from an encoded bit on magnetic media (such as in a hard disk drive, HDD), as illustrated in Fig. I.3. The spin-valve sensor was introduced in 1997 by IBM to replace anisotropic magnetoresistance

2. Since the AF exhibits small or no net magnetization, the orientation of its spins is almost not affected by external magnetic fields, and it will pin the interfacial spins of the adjacent exchange-coupled F. The switching field of the F is significantly increased, and the hysteresis loop of the F film is shifted away from the H=0 axis by the exchange bias field H_B, which amounts to the exchange interaction energy of spins at the F/AF interface. The exchange bias field can be considered to be proportional to the scalar product of F and AF interfacial spins: $H_B \propto \mathbf{S}_F \cdot \mathbf{S}_{AF}$. A change in the direction of AF spins (due e.g. to the effects of STT) will therefore show as a hysteresis loop shift.

(AMR) sensors in commercial magnetoresistive HDD read heads.

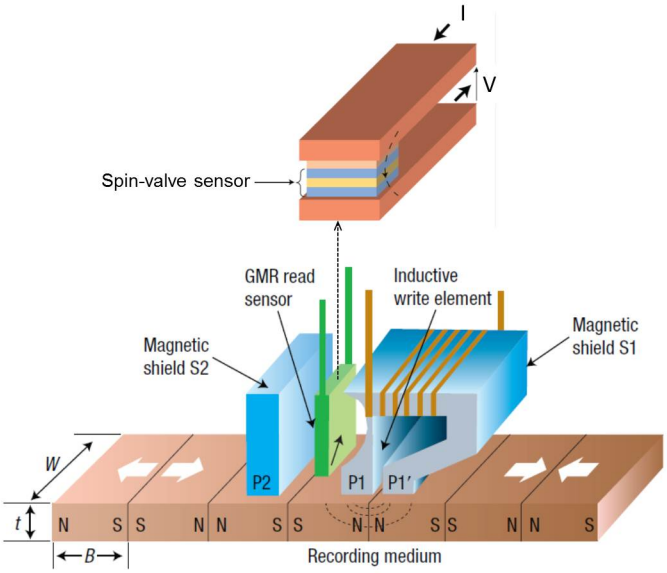

Figure I.3 – Spin valve magnetic sensor introduced by IBM as a magnetoresistive head for hard-disk recording, adapted from Ref [Chappert et al., 2007]. The inductive head creates a magnetic field for writing on the recording medium.

The HDD areal recording density rapidly increased by three orders of magnitude (from 0.1 to 100 Gbit/ in^2) between 1991 and 2003 [Chappert et al., 2007]. It gave birth to a large commercial sector within this field of spintronics, with sales exceeding $3 billion in 2005.

Shortly after the discovery of the GMR effect, when considerable progress had been made in deposition and nanopatterning techniques, it was found that replacing the non-magnetic metallic spacer with an insulating tunnel barrier of a few nanometers or less could result in large values of the magnetoresistance (MR) at room temperature. This effect is referred to as "tunneling MR" (TMR). The whole structure is called magnetic tunnel junction (MTJ).

Tunnelling magnetoresistance

TMR ratio is defined analogously to GMR, although the difference in the electric resistances for parallel and antiparallel states in MTJs is significantly enhanced. This makes MTJs particularly suitable for technological applications.

Some of the most important properties of a MTJ is that the tunnelling current depends on the applied voltage and the magnetic orientation of the two F leads, which can also be tuned by an external field. In contrast to spin valves, the barrier plays a fundamental role as a spin filter, and TMR ratios strongly depend on the quality of the barrier and the interfaces with the leads.

In the case of a MTJ, the tunnelling conductance depends not only on the DOS at the Fermi energy, but also on the tunnelling probability, which is different for various electronic states in the F. In other words, the tunnel barrier also has a filtering effect, i.e. electrons belonging to different energy bands are filtered differently by the barrier. However, nearly free dispersive s-bands which are hybridized with more localized d-bands in 3-d Fs can be assumed to provide all the tunnelling current [Tsymbal et al., 2003].

The probability for an electron to tunnel through the barrier depends on its Fermi wave vector but the dispersive bands that dominate tunnelling are similar to free electron bands, and therefore the DOS of these bands is in turn proportional to their Fermi wave vector. Electronic bands are spin-split in F metals, which implies different wave vectors for up and down spin electrons and consequently a tunnelling probability that depends on spin. Hence, as in the case of GMR, TMR might also be explained in terms of the F electrodes' DOS.

For the situation depicted in Fig. I.4, when the magnetizations of the two F leads are parallel, the DOS at the Fermi energy for majority(minority) electrons is high(low) in both leads. Majority electrons in the left lead are transmitted through the insulating barrier and occupy the majority band in the right lead.

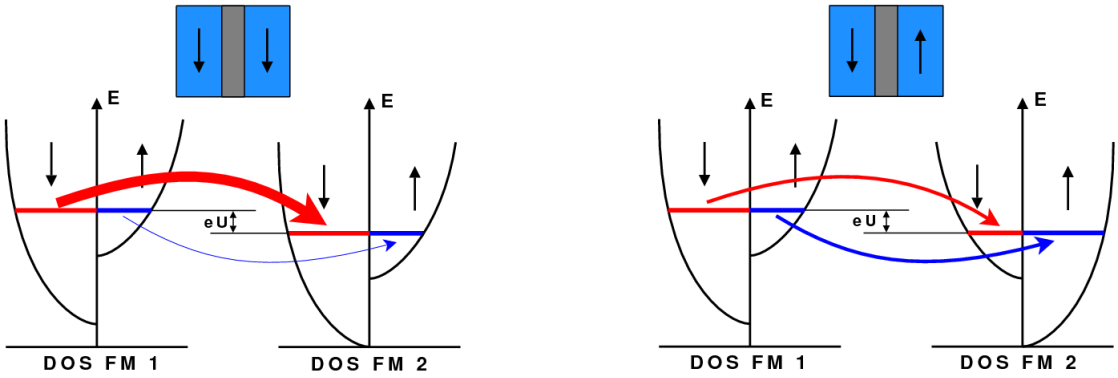

Figure I.4 – Schematic explanation of the TMR effect in terms of the spin-split DOS of two identical F leads for parallel (left) and antiparallel (right) states. The resistance in the parallel state is lower since the DOS at the Fermi level for majority down electrons at both leads is high. The Fermi levels at the left and right leads are shifted with respect to each other by an energy eU when a voltage U is applied across the structure.

Current is essentially carried by the majority channel and the electrical resistance is low. In the AP configuration, majority(minority) electrons in the left lead tunnel to the minority(majority) band in the right lead, where the DOS at the Fermi energy is low(high). Both spin channels contribute similarly to the current. The overall conductance is however lower than in the parallel state since the DOS for both spins is low either in the left or in the right lead.

Alternatively, spin valves and MTJ can be used as a magnetic bit, with the two-memory states corresponding to antiparallel and parallel configurations. Arrays of pat-

terned spin valves or MTJ can be used to store binary information with resistive read-out, creating a magnetic solid state memory. This is the basis for MRAMs.

The design principle of the first MRAM generation is illustrated in Fig. I.5. The magnetic elements to store binary information are integrated at the crossing points of two perpendicular arrays of conducting lines, working as a static semiconductor RAM chip but with the advantage of non-volatility with power off.

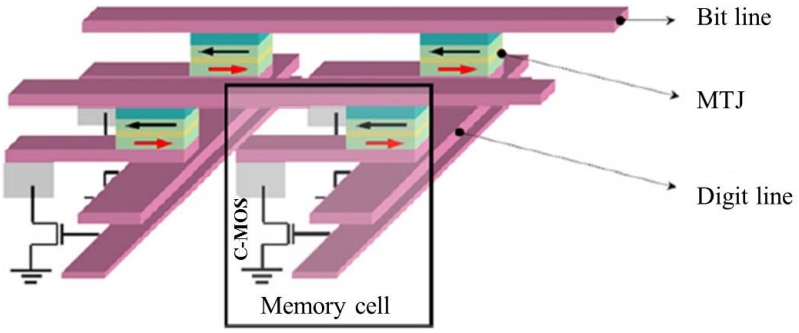

Figure I.5 – Basic cross point architecture of MRAM adapted from Ref. [Prejbeanu et al., 2013]. The working principle is explained in the text.

The free layer of the magnetic element to write can be reversed by the Oersted fields generated by current pulses sent through the two perpendicular lines having that magnetic element in common. There is the only point where the resulting field is high enough for the writing process. The magnetic state of an addressed cell can be read by measuring the resistance between the same two lines. The potential main advantages with respect to electric-based semiconductor memories are non-volatility, lower energy for writing and much faster write times. The main problem is the scalability due to the use of a magnetic field to write information. On the one hand, non-volatility and cell volume reduction impose high anisotropy constants (see IV.2.1), since the thermal excitations energy must be lower than the magnetic stability energy barrier given by KV, where K is the anisotropy constant and V is the volume of the magnetic element. In other words, the only way to increase the product KV while reducing the size of the magnet (V) is by increasing the anisotropy constant K. On the other hand the required writing field and consequently the required current increases proportionally with K. However, the reduced dimensions of the conducting lines restricts considerably the available current density due to electromigration [Chappert et al., 2007], that consists in the diffusion of metal atoms in the conductor due to momentum transfer from conducting electrons. In addition, smaller devices imply lower available power.

Last, but not least, the unavoidable spatial extension of the writing magnetic fields prevents the magnetic cells to be densely packed, since the writing process of one of them might also alter the magnetic state of its neighbouring magnetic elements, leading to undesired encoding errors.

The prediction in 1996 that a spin-polarized current directly traversing each magnetic cell could be used instead of external magnetic fields for switching the orientation of the free layer represented a promising improvement to solve the mentioned scalability problems. This effect was called spin transfer torque (STT).

Spin transfer torque

Spin transfer torque in tunnel junctions and spin valves with ferromagnetic leads is one of the essential underlying phenomena of modern spintronics by which the magnetic order of a ferromagnetic (F) thin film can be reoriented by the transfer of angular momentum from a spin-polarized current.

If the relative orientation of the magnetic layers in a spin valve or a magnetic tunnel junction has a strong impact on the current density showing as GMR or TMR effect, the spin transfer torque (STT) can be considered as the converse effect. In effect, a sufficiently large current density might change the relative orientation of the magnetic layers, or even reverse the magnetization direction of one of them, resulting in magnetization switching by a spin polarized current. That is, the magnetic order of a F thin film can be reoriented by the transfer of angular momentum from a spin-polarized current coming from a not collinear F layer. This effect was theoretically predicted by Slonczewski and Berger [Slonczewski, 1995],[Berger, 1996], and has been since then the object of extensive investigations due to its applications in spintronics devices [Wolf et al., 2001]. It was experimentally shown by the groups of M. Tsoi and Ralph-Buhrman, who observed variations in the resistance of different F multilayers when high current densities between 10^7 and 10^8 A/cm^2 were applied [Tsoi et al., 1998],[Myers et al., 1999]. The observation of STT in low-resistance MTJ was later observed using submicron-sized pillars [Huai et al., 2004] for a critical current of about 8×10^6 A/cm^2.

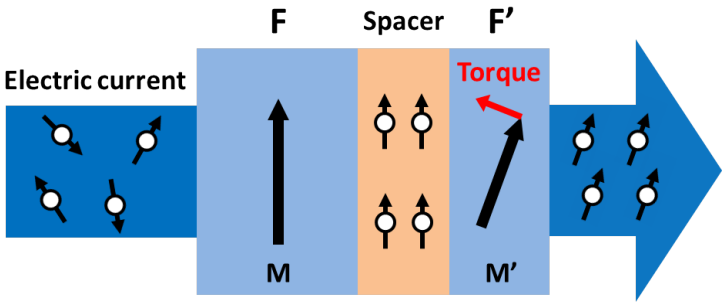

Figure I.6 – Conducting electrons flowing through the first thin F layer get spin polarized along the magnetization **M**. If magnetizations **M** and **M**' are not collinear, the spin orientation of the polarized electrons is modified again when traversing the second F' thin layer. This last change of spin angular momentum of conducting electrons implies a torque exerted on the magnetization **M** hence the term spin transfer torque.

The STT phenomenon in F materials is usually explained in terms of angular mo-

mentum conservation. Let's F and F' be two Fs with non collinear magnetizations **M** and **M**' separated by a nonmagnetic metallic spacer or a tunnel barrier (see Fig. I.6). When a current is applied, conducting s electrons flowing through F (considered as the reference layer) become spin polarized due to the the s–d exchange interaction along the direction of the magnetization **M**. In traversing the second F' (considered as a free layer), the injected electrons are then polarized in the direction **M**'. Hence, this magnetization **M**' exerts a torque on the spin angular momentum of the itinerant electrons and vice versa, spin angular momentum from the itinerant electrons is transferred to the localized electrons of F', responsible for the global magnetization **M**'. In other words, by conservation of angular momentum, the spin current exerts an equal and opposite torque on the magnetization **M**'. Therefore, there is a transfer of spin angular momentum from the itinerant electrons to the magnetization, and that is why it is called spin transfer.

For a sufficiently large current density, or critical current, the magnetization **M**' can completely reverse and switch from antiparallel to parallel state (and vice versa, changing the polarity of the current). Microwave precession of **M**' is also possible, when more complex dynamical modes are excited by current.

In such F materials, the loss of transverse spin momentum occurs over a very short distance (around 1 nm), so that STT is an interfacial effect, more efficient on a thin layer. The amplitude of the torque per unit area is proportional to the injected current density, so that the switching current decreases proportionally to the cross-sectional area of the structure. With today's advances in nanofabrication techniques, lateral sizes of around 100 nm can be easily achieved, this represents an important advantage of spin transfer over field-induced switching.

The spin transfer torque depends on the applied current density J and the relative orientation of the two magnetizations. It can be decomposed into one component in the plane of the layers, $\mathbf{T}_{\parallel}$, and another component out of the plane of the layers, $\mathbf{T}_{\perp}$. These two components read:

$$\mathbf{T}_{\parallel} = T_{\parallel}(J,\theta)\mathbf{M}' \times (\mathbf{M} \times \mathbf{M}') \qquad \mathbf{T}_{\perp} = T_{\perp}(J,\theta)\mathbf{M}' \times \mathbf{M} \tag{I.1}$$

The in-plane torque $\mathbf{T}_{\parallel}$ with amplitude $T_{\parallel}(J,\theta)$ is usually called "spin transfer torque", although this term will not be used here to denote only this component. The out-of-plane torque $\mathbf{T}_{\perp}$ with amplitude $T_{\perp}(J,\theta)$ is commonly called field-like torque, since it has the same form as the torque exerted on **M**' due to an external magnetic field "**M**". These two components are illustrated in Fig. II.1.

The unwanted influence of the writing process of a magnetic element on neighbouring cells is therefore significantly reduced if the STT effect is used instead of non-local external switching magnetic fields (field-induced writing). The writing current is directly sent into the magnetic element to write. Another important advantage is that the writing

process through the STT effect (current-induced writing) is scalable. It turns out that the amplitude of the torque per unit area is proportional to the injected current density; as the cross sectional area of the magnetic cell is reduced, the current required to switch decreases proportionally, since switching occurs at a certain threshold current density. This recent MRAM concept is called STT-MRAM.

Problematic

Despite the fact that today's nanofabrication techniques can achieve the production of magnetic nanopillars of diameter below 100 nm, the threshold current density for magnetization switching still remains very high, around $10^7 A/cm^2$ [Ikeda et al., 2007]. Although it has been significantly reduced since the development of MTJ based on MgO barriers, and perpendicular anisotropy structures, the high magnetization together with the interfacial character of STT inherent to F materials are serious limitations for the threshold current density reduction. Moreover, the large currents necessary for STT switching are detrimental to the barrier quality, which implies a loss of endurance with respect to magnetic field writing. In addition, the unavoidable presence of stray fields created by F thin layers represents an obstacle for high information storage density; similar to the field-induced writing scheme, large stray fields couple in densely packed arrays of magnetic cells, leading to likely encoding errors in integrated circuits.

As discussed below, the use of antiferro and ferrimagnetic materials appears naturally as a potential solution to these issues.

I.4 Antiferromagnetic spintronics: state-of-the-art

In the field of spintronics, the spin-dependent transport properties of Fs lie at the heart of devices working principles, hence the terminology F-spintronics. By way of contrast, AFs like IrMn, FeMn, NiMn, have been used so far mostly for their magnetic properties: as explained above, they pin the magnetization of an adjacent F via exchange bias in order to set the reference direction required for the spin of conduction electrons in spintronics devices [Nogués and Schuller, 1999], [Baltz et al., 2010]. However, AF-spintronics, i.e. spin dependent transport with AF, is now in its infancy [Basset et al., 2008], [MacDonald and Tsoi, 2011] and is identified as a significant exploratory topic in spintronics [Duine, 2011], [Sinova and Zutic, 2012], [Brataas et al., 2012]. In particular, AFs show no stray field which is beneficial for ultimate downsize scalability. Although synthetic antiferromagnets (SAF, i.e. two Fs coupled antiparallel usually by RKKY interactions) are used to overcome device malfunction at reduced lateral dimensions associated with F stray fields (e.g. crosstalk in MRAM: mutual influence of neighbouring cells supposed to be isolated one from another, defined above), SAFs never entirely compensate, and small,

but non-zero stray fields persist. With AFs, the net compensation is intrinsic except for a very small part at the interface (see Fig. I.7).

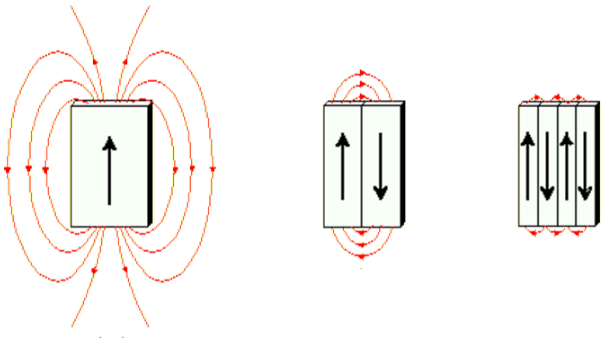

Figure I.7 – Reduction of the stray field for AF-like magnetic structures.

Over the last few years, a growing number of studies have considered both theoretical and device aspects of AF-spintronics [Duine, 2011], [Sinova and Zutic, 2012], [Brataas et al., 2012], [Saidaoui et al., 2014], including current-induced AF magnetic resonance for radio-frequency components [Gomonay et al., 2012], AF domain wall motion [Manchon et al., 2008b], [Logan et al., 2012], [Swaving and Duine, 2011], [Wieser et al., 2011], and tunnel anisotropic magnetoresistance with AFs for memories and logic devices [Park et al., 2011], [Petti et al., 2013].

In particular, a first theoretical toy model showed AF STT and GMR for metallic AF/PM/AF spin-valve-like multilayers [Núñez et al., 2006], where PM stands for a paramagnetic metallic spacer. The authors considered ideal crystalline uncompensated F monolayers with staggered AF order (i.e. two alternating F sublattices with opposite magnetizations). Owning to such alternating moment orientations, commensurate staggered torques occur generically. Furthermore, unlike the pioneering theoretical works on STT in F multilayers [Slonczewski, 1995], [Berger, 1996], which predict torques exerted by a spin polarized current close to the interface between a F and a nonmagnetic metal, STT is expected to act cooperatively through the entire volume of the AF electrodes. This feature together with the absence of shape anisotropy in AFs explain that smaller critical currents for local magnetization switching are also predicted for perfect epitaxial AFs compared to the typical values for Fs. The first theoretical model was soon followed by experimental evidence of AF-STT with currents injected in F/AF polycrystalline bilayers [Wei et al., 2007].

Ab-initio calculations based on nonequilibrium Green functions and spin-density functional theory further confirmed GMR and STT effects in AF elements for AF/NM/AF spin valve-like multilayers [Haney et al., 2007].

Later theoretical studies have focused on the effects of disorder on STT and GMR in AF spin valves, taking into account inelastic [Duine et al., 2007] and elastic electron scattering [Saidaoui et al., 2014]. While the latter shows without ambiguity that elastic

scattering is detrimental to STT in AFs, the former predicts that in contrast to F spin valves, inelastic scattering increases the STT efficiency. Authors of [Saidaoui et al., 2014] propose the use tunnelling junctions instead of spin valves to ensure momentum conservation and get rid of the undesirable effects of elastic scattering on STT.

The difficulty to pin the order parameter of an AF element along a reference direction together with the dwarfed magnetoresistance observed in AF/PM/AF multilayers [Wang et al., 2009] makes the experimental observation of STT in AF a technological challenge. Indirect mechanisms such as the study of exchange bias variations at F/AF interfaces due to the effect of a spin polarized current on the spin orientation of the AF interfacial layer [Wei et al., 2007], [Urazhdin and Anthony, 2007] have been used to study STT in AFs.

Tunnel anisotropic magnetoresistance has become also a promising effect to detect the orientation of the order parameter in AF elements since its observation in exchange-coupled F/AF bilayers [Martí et al., 2012] and IrMn-based tunnel junctions [Park et al., 2011]. Tunnel anisotropic magnetoresistance stands for a strong dependence of the resistance of a M/B/NM stack on the relative orientation of magnetic moments in the magnetic layer M and the crystalline anisotropy axes via spin-orbit interactions. The amount of current tunnelling perpendicularly across the junction is defined by the density of states (DOS) of M at the Fermi energy, which depends in turn on the order parameter orientation with respect to the crystalline anisotropy axes. In particular, the authors of [Park et al., 2011] observed more than 100% spin valve-like signal for a F/AF/B/NM stack with an AF at one side of the tunnel barrier and a non magnet at the other side. By using the exchange spring effect [Scholl et al., 2004], AF moments were rotated by the reversal of the F moments via external magnetic fields, which was detected by the measured tunnel anisotropic magnetoresistance.

Furthermore, the use of the auxiliary F layer was avoided by the authors of Ref [Petti et al., 2013], who detected distinct metastable resistance states by field cooling NM/B/AF tunnel junctions. The work of Marti et al. [Martí et al., 2014] provides in addition demonstration of electrically readable magnetic spintronics memory devices which contains no F elements and which stores the information in the AF at room temperature.

I.5 Ferrimagnetic spintronics: state-of-the-art

Ferrimagnetic materials are now used in most permanent magnets, recording media and microwave-oriented magnetic materials. Although they are not significantly exploited for their transport properties, they also present a good potential for spintronics devices such as MTJs due to their low magnetization and high polarization, as described below.

Micro-wave applications

The most known FI material for micro-wave applications is YIG (Ytrium iron garnet). It is a synthetic garnet FI insulator of chemical composition $Y_3Fe_2(FeO_4)_3$ that is used in microwave, optical and magneto-optical applications due to its low propagation loss properties [Boona and Heremans, 2014], [Odashima et al., 2013]. In particular, YIG is highly attractive for ferrimagnetic resonance and spin pumping investigations (see IV.2.3) due to its extremely low damping constant $\alpha \approx 4 \cdot 10^{-4}$ [Hahn et al., 2014], and insulating nature [Wang et al., 2014]. It has been recently used to show a large inverse spin Hall effect in the AF metal $Ir_{20}Mn_{80}$ [Mendes et al., 2014], which is investigated in Chapter IV.

Synthetic-ferrimagnets

The effects of STT in "synthetic-ferrimagnet" layers have been investigated in spin valves [Smith et al., 2008] and MTJ [Cornelissen et al., 2010], [You et al., 2011]. Synthetic-ferrimagnets are structures of the form F1/NM/F2, where F1 and F2 are two ferromagnetic films of different thicknesses separated by a nonmagnetic metallic spacer promoting strong antiparallel coupling between the two F layers. Synthetic-ferrimagnets are expected to provide a high volume to withstand thermal fluctuations while keeping the effective magnetic moment per area low [Ikeda et al., 2007],[Sousa et al., 2002], [Inomata et al., 2002], [Tezuka et al., 2003b], [Tezuka et al., 2003a].

Half-metallic ferrimagnets

The performance of spintronics devices is directly related to the spin polarization by the magnetic electrodes of spin valves and MTJ [Inomata et al., 2008]. A small magnetization combined with high spin polarization would considerably enhance the effects of STT for spintronics applications [Klaer et al., 2011]. This advantageous combination can be achieved by the concept of half-metallic ferrimagnetism. Half-metals have a metallic band structure for one spin channel (partially filled valence band) and an insulating band gap in the DOS at the Fermi level for the opposite spin, as shown in Fig. I.8.

They act as a conductor only to electrons of one spin orientation but as an insulator or semiconductor to those of the opposite orientation, thus providing a complete spin polarization of the current. The concept was introduced by van Leuken and de Groot[van Leuken and de Groot, 1995], who show that even AFs can show half metallic character due to a spin-polarized DOS at the Fermi level (see Fig. I.9 **(a)**).

Some kinds of half metals have been theoretically predicted, such as (La,Sr)MnO_3 perovskites, and Heusler alloys. The later represent a class of ternary intermetallic compounds with the general formula XYZ, where X and Y are transition metals and Z is

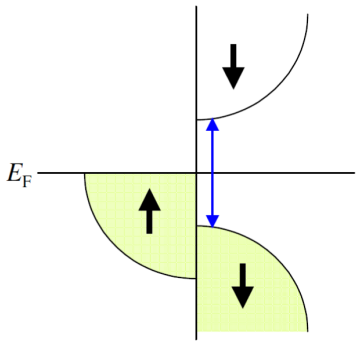

Figure I.8 – Schematic illustration of the spin-resolved DOS for a half-metal showing explicitly the gap at the Fermi level for the spin-down channel [Inomata et al., 2008].

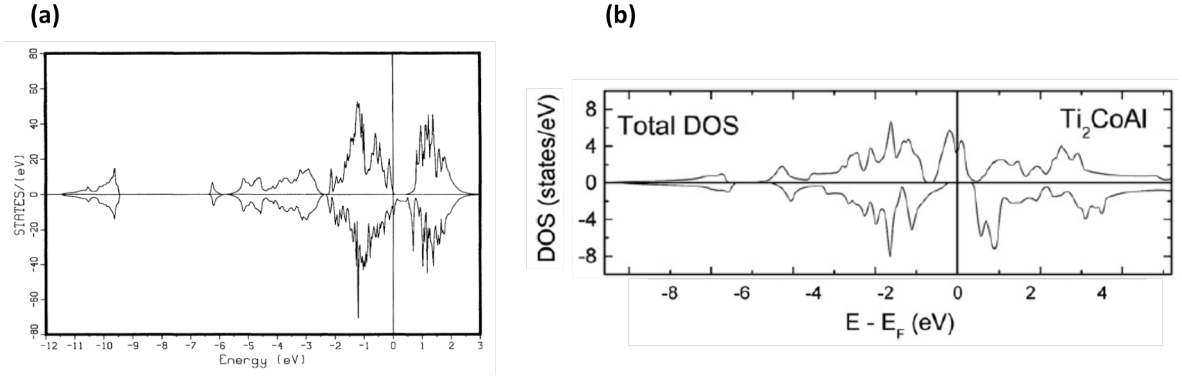

Figure I.9 – **(a)** Spin-polarized DOS for the half-metallic AF $V_7MnFe_8Sb_7In$ predicted in [van Leuken and de Groot, 1995] using the local density approximation. **(b)** Spin-resolved DOS for the half-metallic Ti_2CoAl ferrimagnet calculated in [Bayar et al., 2011] using density functional calculations.

a main group element [Bayar et al., 2011]. In particular, Co-based Heusler alloys are promising materials for spintronics applications and have been increasingly investigated [Inomata et al., 2008]. These Heusler alloys can show both F order, such as Co_2MnAl, Co_2MnSi, Co_2MnGe, Co_2MnSe, and FI order, such as $Mn_{3-x}Co_xGa$ or Ti_2CoAl (see Fig. I.9 **(b)**). The latter have been pointed out as promising materials for highly efficient STT devices in future spintronics applications [Klaer et al., 2011], [Bayar et al., 2011]. Interestingly, the nearly half-metallic FI Mn_3Ga, with a 88% spin polarization at the Fermi energy has also been explicitly identified as a suitable material for STT applications due to its high spin polarization, high Curie temperature and a low magnetic moment [Balke et al., 2007].

I.6 Outline of the thesis

The presence of undesirable stray fields and the need of very high current densities for current-induced magnetization switching being the main drawbacks of ferromagnets for spintronics applications, this work aims to address a comprehensive study of alternative materials with two different magnetic orders, namely antiferromagnets and ferrimagnets.

The vanishing magnetization of AFs implies the absence of surrounding stray fields, whereas the partially compensated magnetic structure of FIs makes these stray fields to be significantly reduced. In addition, lower demagnetizing fields imply lower critical currents for STT-related magnetization reversal.

Current-induced magnetization switching in thin F layers is favoured by spin transfer torques acting through all the F volume to reorient homogeneously the localized magnetic moments. However, very high current densities are required to produce STT over long characteristic lengths in Fs. In contrast, as explained above, STT is expected to act on a much longer length scale in AFs. Longer length scales are also likely to be observed in FIs due to the similarities between the magnetic structure of AFs and FIs. The spatial distribution of STT is therefore of fundamental interest, and is investigated thoroughly in this thesis.

Lower critical currents for STT switching together with the absence (or reduction) of stray fields in AF and FI would eventually lead to lower device power consumption and ultimate downsize scalability.

This work includes a theoretical investigation of STT and TMR in AF and FI-based magnetic tunnel junctions and an experimental study of STT characteristic lengths in AFs.

- In **Chapter** II the tight binding (TB) model and the nonequilibrium Keldysh formalism used here for the calculations on spin-dependent transport in magnetic tunnel junctions are described. The main outcome of this chapter is the derivation of an *analytical* expression for the retarded Green function for AF and FI leads, which is required for all the following calculations. Density of states (DOS) and local density of states (LDOS) for the AF and FI leads are calculated from the retarded Green function and next examined through their energy dependence. Their dispersion relations are also computed, which will be useful for the following chapter. A new method to extend the mentioned calculations to fully compensated AF is finally proposed.
- **Chapter** III reports the theoretical results obtained using the theory developed in Chapter II for 1-D and 3-D geometries. The first part is focused on the spatial distribution of STT in AF tunnel junctions (AF-MTJ). The important novelty with respect to previous works is the use of a tunnelling barrier instead of a metallic

spacer. STT is expected to be more robust face to disorder in MTJ, and TMR ratios are considerably higher than the equivalent GMR in spin valve structures. The dependence of STT and TMR on the applied voltage, magnetic and electronic characteristics of the AF leads and the barrier properties are discussed.

The second part presents the first theoretical work on STT in FIs. In particular, the influence of the magnetic and electronic properties of the FI on the spatial distribution of torques within the FI leads is determined quantitatively. As in the first part of the Chapter, the effects of the applied voltage on STT and TMR are also analysed. Due to the similar spatial behaviour of STT in FIs and fully compensated AFs, a preliminary study on the later is presented at the end of the Chapter.

- Since the effects of disorder were not taken into account in the theoretical calculations of Chapters II and III, an experimental investigation of STT charateristic lengths in actual AF thin layers is addressed in **Chapter** IV. A general introduction to ferromagnetic resonance (FMR) and spin pumping phenomena in which the experimental measurements are based is first presented in order to understand the experimental results. Next, STT characteristic lengths and spin current absorption mechanisms in two different AFs are analysed and compared. The directional character of the AF lattice with respect to the spin current polarization is discussed at the end of the Chapter.
- The conclusions of this work as well as the perspectives for further research are included in **Chapter** V.
- In addition to the definitions given along the text, a list of acronyms and abbreviations can be found in the glossary provided on page 137.
- **Appendix** A recalls the computation of the nonequilibrium Keldysh function, necessary to obtain the density operator or lesser Green's function.
- The calculation of the analytical expression for the retarded Green's function for AF and FI leads is described thoroughly in **Appendix** B, starting from the resolvent of a Bethe lattice.
- Finally, **Appendix** C reports a preliminary experimental investigation on the effect of a spin polarized current on AF nanostructures.

Chapter II

Quantum transport in magnetic tunnel junctions with tight binding models: nonequilibrium Keldysh formalism

In this chapter we will derive all the theoretical tools needed to investigate spin dependent transport properties of a magnetic tunnel junction with two different magnetic orders: AF and FI. We shall examine a steady state regime, but in a nonequilibrium state, since a bias voltage is considered to be applied across the junction, leading to different chemical potentials in each lead of the junction. Tight binding (TB) models and the nonequilibrium Keldysh formalism are particularly adapted in this case, and they will be used throughout this chapter to obtain the results presented in the next one. This latter formalism is an extension of the theory developed by Caroli et al. to calculate the tunneling current in a non magnetic tunnel junction [Caroli et al., 1971], and it is briefly described at the end of this Chapter. Even for the case of non-interacting electrons, it has proven to be more convenient to calculate physical quantities in conventional F-based tunnel junctions, compared to Landauer or Kubo-like approaches as demonstrated in previous works [Kalitsov et al., 2009],[Theodonis et al., 2006],[Kalitsov et al., 2006], [Edwards et al., 2005]. In addition, as discussed in the following sections, the spatial distributions of torques and spin densities are needed here, taking into account the specific local magnetic distribution of the leads, which cannot be treated by simple energy band approach to a tunneling contact.

I will thus present a method to study spin dependent transport properties in AF and FI tunnel junctions, whose magnetic order is much more complex than that of the extensively studied conventional F-based tunnel junctions.

II.1 Magnetic tunnel junction model

II.1.1 Coherent transport

A magnetic tunnel junction consists of a thin insulating layer of a few angstroms [Serrano-Guisan et al., 2011] separating two magnetic metal layers. The schematic geometry modelling the magnetic tunnel junctions analysed in this work is shown in Fig. II.1 for the most general case of FI-ordered leads. F and AF leads will be also studied, but they can be considered as limiting cases of the more complex FI order. The thickness of the insulating layer (taken here of a few atomic layers) allows the electrons to tunnel through the barrier when a voltage is applied between two metallic leads. The relative orientation of the order parameters of the two magnetic layers has a strong impact on the most important properties of the magnetic tunnel junction depending on spin dependent transport, namely the TMR and STT. In the case of F and FI leads this relative orientation can be changed via an applied magnetic field.

The current-carrying electrons responsible for the spin-dependent transport properties of the tunnel junction are assumed to be dispersive nearly free s-like electrons (characteristic of the $3d$ magnetic materials' electronic structures). Some properties of the tunnel junction such as the tunnelling conductance depend on the tunnelling probability of the different electronic states in the magnetic leads, however, as pointed out by Stearns [Stearns, 1977], most of the tunnelling current is carried by dispersive bands, since d electrons decay much faster than s electrons into the barrier region due to their large effective mass. Moreover, in the case of bulk Ni in [110] direction, the dispersive s band of majority spins is the only one that crosses the Fermi level. More realistic electronic structures of the insulator and the barrier interfaces are also disregarded here, thus, one of the essential assumptions here is that transport properties are mainly determined by dispersive s electrons. The spin of the electron is assumed to be conserved throughout the entire junction. Therefore transport occurs through two independent spin channels. It follows that electrons coming from one lead in a given spin state are accepted by the unfilled states of the same spin in the other lead. In addition, when a voltage is applied across the junction, nonequilibrium electrons from the occupied states below the Fermi level in the left lead tunnel to the empty states of energy higher than the Fermi level in the right lead (lowered by the bias-dependent chemical potential) [Tsymbal et al., 2003]. These electrons stay as hot electrons in the right lead, since energy losses (or quantum dephasing) due to inelastic scattering processes are neglected here (the emission of a magnon combines for instance spin flip and energy loss of the electron).

The cross section of typical tunnel junctions used in spintronics applications is large in comparison with the longitudinal dimensions (thickness) of the magnetic layer stack. Thus, boundary conditions on each cross section are expected to have little impact on the

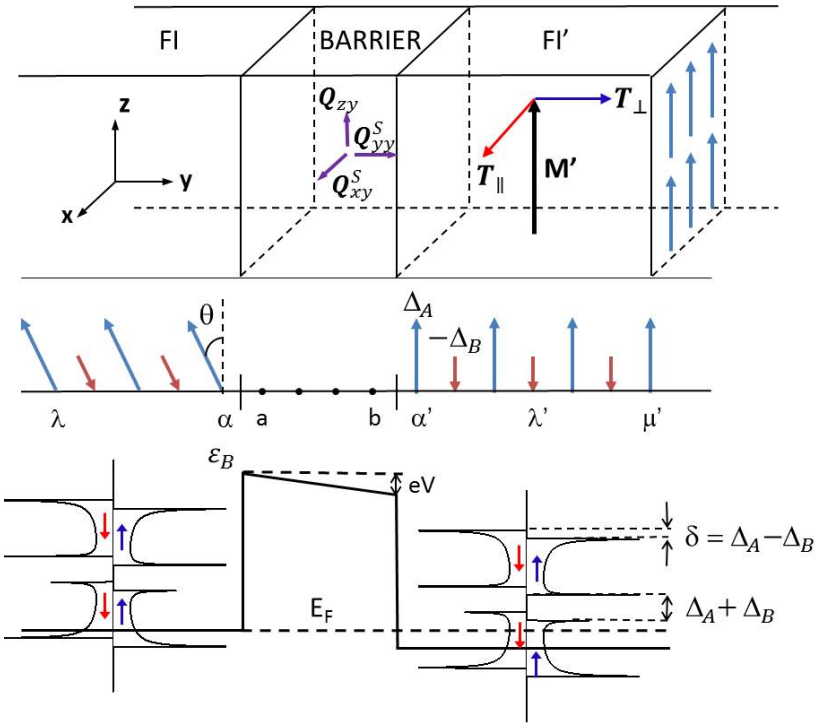

Figure II.1 – Schemes adapted from [Kalitsov et al., 2009] for the specific case of FI leads. (Top) Schematic picture of the FI-MTJ consisting of left and right semi-infinite FI leads separated by a nonmagnetic barrier of N_B atomic layers. The magnetization M' of the right lead points along the z direction. The non equilibrium on-site torques are represented by the in-plane $T_\parallel$ and out-of-plane $T_\perp$ components and the spin current densities are also indicated (Q_{ij}). (Middle) Schematic representation of sublattices A and B in the FI leads, with different spin splittings Δ_A and Δ_B corresponding to up and down localized spins respectively. The magnetization $\mathbf{M}$ of the left lead is parallel to the FI/B interface (i.e. in the xz plane) and is rotated by an angle θ around the y axis. The Greek primed and unprimed letters denote atomic sites in the right and left FI leads, respectively, and the Latin letters denote the sites in the barrier. (Bottom) Schematic illustration of the spin-resolved bands for itinerant electrons and the potential profile, where the 1-D densities of states for up and down itinerant spins are split by $\delta = \Delta_A - \Delta_B$ and the lower and upper bands for a given spin are separated by a gap of $\Delta_A + \Delta_B$. ϵ_B is the spin-independent on-site energy in the barrier and V is the potential applied through the junction. The lower dashed line indicates the Fermi level at equilibrium, set at 0 eV in all regions, when no voltage is applied.

tunnel junction properties. From a computational point of view, the calculation of these properties is greatly simplified if the quantum confinement on each section is completely ignored. Cross sections are thus commonly assumed to be effectively infinite, and periodic boundary conditions are applied in all the theoretical calculations.

Due to the fabrication process, actual tunnel junctions contain however a certain amount of structural disorder in both leads, in the barrier and at the barrier/leads interfaces, especially in amorphous barriers. This disorder might be present in the form of impurities, interstitial or vacancy defects, interdiffusion at the interfaces, interface

roughness, grain boundaries, stacking faults, etc. Collective excitations such as phonons (crystal lattice atoms) and magnons (lattice spin structure) contribute also to disorder in a "dynamic" way. This disorder is responsible for the elastic and inelastic scattering processes experienced by electrons in their motion through the tunnel junction. One of the main consequences of these scattering processes is the intermixing between transport modes with different transverse momenta $\mathbf{k}_{\parallel}$ in the plane perpendicular to transport and consequently the loss of coherence in the tunnelling process. However, since ballistic transport is considered here, all these scattering processes are neglected. Invoking the narrow layers' thickness of typical tunnel junction stacks, the electron mean free path (which is of the order of 50 monolayers in typical AF metals [Núñez et al., 2006]) is then assumed to be longer than the typical longitudinal dimensions of the junction. Calculations are carried out in the "clean limit" [Saidaoui et al., 2014], that is in the absence of electron momentum scattering by defects or other types of disorder. Thus, the structural quality of the junction could be decisive to observe the quantum effects reported in the next chapter, which are intended to be robust in epitaxially-grown tunnel junctions. Although the spin relaxation processes as well as momentum scattering with impurities are expected to weaken STT and TMR in AF-based tunnel junctions, the transport calculation model is expected to capture the essential features of spin dependent transport in AF-based tunnel junctions since this approach was successful to predict and explain STT and TMR properties in traditional F-MTJs (see for instance, [Theodonis et al., 2006] and [Kalitsov et al., 2009]). The precise effect of disorder is nevertheless out of the scope of this work, although it will be discussed as future research.

II.1.2 One-particle basis

The absence of defects together with the periodic boundary conditions lead to the translational invariance of the tunnel junction in the plane parallel to the barrier/leads interfaces. It is then useful to split the Hamiltonian of the system into a longitudinal part depending exclusively on the y direction of transport and a transversal part depending on x and z directions [Datta, 2000]:

$$\hat{H} = \hat{H}_{\mathrm{LNG}}(y) + \hat{H}_{\mathrm{TRV}}(x, z)$$

The above decomposition of the Hamiltonian suggests to use different quantum representations (one-particle Hilbert basis) in the longitudinal and transversal components, in order to separate the problem in simpler parts:

Transversal component of the Hamiltonian: Bloch states

The potential on an infinite plane perpendicular to transport is assumed to be periodic, and it is thus convenient to use a Bloch state basis. The Bloch states are basically plane

waves labelled by a transverse wave number $\mathbf{k}_\parallel$ (which is a 2-D vector), and they are eigenstates of the transversal part of the Hamiltonian:

$$\hat{H}_{\mathrm{TRV}} |\mathbf{k}\rangle = \epsilon_{\mathbf{k}_\parallel} |\mathbf{k}\rangle$$

Here $\epsilon_{\mathbf{k}_\parallel}$ is the energy of the plane wave or Bloch state, or in other words, the dispersion relation. The choice of the particular periodic distribution on each plane will determine the expression of $\epsilon_{\mathbf{k}_\parallel}$, and it will be treated in a subsequent section.

Longitudinal component of the Hamiltonian: discrete atomic-like basis

For the non-periodic longitudinal part of the Hamiltonian, a typical TB discrete basis of localized orbitals is used. These localized orbitals are assumed to be spatially confined, that is, only the overlap between nearest neighbours is not negligible.

With the above considerations, the Hilbert one-particle space consists of mix states $|p, \mathbf{k}_\parallel, \sigma\rangle$, where p denotes the site index or position in real space of the electronic orbital and σ stands for the spin state. This is a useful choice, since as pointed out by Datta [Datta, 2000], the matrix elements of the entire Hamiltonian in this basis are considerably simplified:

$$\begin{aligned}\langle p, \mathbf{k}_\parallel, \sigma| \hat{H} |q, \mathbf{k}'_\parallel, \sigma'\rangle &= \langle p, \mathbf{k}_\parallel, \sigma| \hat{H}_{\mathrm{LNG}} |q, \mathbf{k}'_\parallel, \sigma'\rangle + \langle p, \mathbf{k}_\parallel, \sigma| \hat{H}_{\mathrm{TRV}} |q, \mathbf{k}'_\parallel, \sigma'\rangle \\ &= (\langle p, \sigma| \hat{H}_{\mathrm{LNG}} |q, \sigma'\rangle + \epsilon_{\mathbf{k}_\parallel})\delta_{\sigma,\sigma'}\delta_{\mathbf{k}_\parallel,\mathbf{k}'_\parallel}\end{aligned}$$

As described above, two important assumptions are made here:

1) No spin flip processes connecting different spins σ and σ' are present (however $\hat{H}_L$ is spin-dependent).

2) Elastic and inelastic scattering processes connecting the two transverse modes (or reciprocal lattice vectosr) $\mathbf{k}_\parallel$ and $\mathbf{k}'_\parallel$ are neglected. Coherent transport is assumed.

As a consequence of assumption 2) each $\mathbf{k}_\parallel$ Bloch state can be treated as an independent transport channel; the individual $\mathbf{k}_\parallel$ contributions to the system transport properties are thus considered independently: each transverse mode $\mathbf{k}_\parallel$ has an extra energy of $\epsilon_{\mathbf{k}_\parallel}$ that is added up to the longitudinal energy whenever the total energy of the electron is used. Physical quantities will then depend on $E - \epsilon_{\mathbf{k}_\parallel}$, and the contributions of all the transport channels are considered through a $\mathbf{k}_\parallel$ integration of (sum over) all the $\mathbf{k}_\parallel$ states in the first Brillouin zone. The momentum conservation in the plane of layers thus requires that no scattering other than the specular scattering at perfect interfaces takes place. Transport across the whole junction is therefore coherent. From an experimental point of view, this ballistic approach is only applicable to perfectly flat interfaces, that is, to ideal epitaxially grown magnetic tunnel junctions. For rough electrode/barrier

interfaces or scattering by defects there is no reciprocal lattice vector conservation.

A 1-D and 3-D problem: real space and momentum representations

As stated above, the calculation of all physical quantities of interest for the 3-D xz-tranlationally invariant tunnel junction depicted on Fig. II.1 is reduced to a 1-D scattering problem plus a $\mathbf{k}_\parallel$ integration. The spatial dependence of the TB Hamiltonian for the whole junction is condensed in the quantum number specifying the layer in which an itinerant electron can be found. The strategy to study the properties of the 3-D junction is to solve firstly the 1-D scattering problem and then perform a $\mathbf{k}_\parallel$ integration after the consideration of a specific dispersion relation modelling the planes of the layer.

II.1.3 The magnetic tunnel junction Hamiltonian

Given the layer structure sketched in Fig. II.1, the FI-MTJ is described using a single orbital simple cubic tight binding (TB) Hamiltonian which sums the Hamiltonian terms accounting for the isolated left (L) and right (R) electrodes, the barrier (B), and the leads-barrier interactions:

$$\hat{H} = \hat{H}_R + \hat{H}_L + \hat{H}_B + \hat{H}_{int} \tag{II.1}$$

where

$$\hat{H}_L = \sum_{\lambda,\mathbf{k}_\parallel,\sigma} \left(\epsilon_{\mathbf{k}_\parallel} + \epsilon_\lambda^\sigma\right) \hat{c}^\dagger_{\lambda,\mathbf{k}_\parallel,\sigma}\hat{c}_{\lambda,\mathbf{k}_\parallel,\sigma} + \sum_{\lambda,\mu,\mathbf{k}_\parallel,\sigma} t_{\lambda,\mu}\hat{c}^\dagger_{\lambda,\mathbf{k}_\parallel,\sigma}\hat{c}_{\mu,\mathbf{k}_\parallel,\sigma} \tag{II.2}$$

$$\hat{H}_R = \sum_{\lambda',\mathbf{k}_\parallel,\sigma} \left(\epsilon_{\mathbf{k}_\parallel} + \epsilon_{\lambda'}^\sigma\right) \hat{c}^\dagger_{\lambda',\mathbf{k}_\parallel,\sigma}\hat{c}_{\lambda',\mathbf{k}_\parallel,\sigma} + \sum_{\lambda',\mu',\mathbf{k}_\parallel,\sigma} t_{\lambda',\mu'}\hat{c}^\dagger_{\lambda',\mathbf{k}_\parallel,\sigma}\hat{c}_{\mu',\mathbf{k}_\parallel,\sigma} \tag{II.3}$$

$$\hat{H}_B = \sum_{i,\mathbf{k}_\parallel,\sigma} \left(\epsilon_{\mathbf{k}_\parallel} + \epsilon_i\right) \hat{c}^\dagger_{i,\mathbf{k}_\parallel,\sigma}\hat{c}_{i,\mathbf{k}_\parallel,\sigma} + \sum_{i,j,\mathbf{k}_\parallel,\sigma} t_{i,j}\hat{c}^\dagger_{i,\mathbf{k}_\parallel,\sigma}\hat{c}_{j,\mathbf{k}_\parallel,\sigma} \tag{II.4}$$

$$\hat{H}_{int} = \sum_{\mathbf{k}_\parallel,\sigma} \left(t_{a,\alpha}\hat{c}^\dagger_{a,\mathbf{k}_\parallel,\sigma}\hat{c}_{\alpha,\mathbf{k}_\parallel,\sigma} + t_{b,\alpha'}\hat{c}^\dagger_{b,\mathbf{k}_\parallel,\sigma}\hat{c}_{\alpha',\mathbf{k}_\parallel,\sigma} + H.c.\right) \tag{II.5}$$

Here, $\hat{c}^\dagger_{p,\mathbf{k}_\parallel,\sigma}$ creates one s electron with spin σ on layer p in the Bloch state labelled by the transverse wave number $\mathbf{k}_\parallel$ (translational invariance in the xz plane is assumed through the entire junction). $\epsilon_{\mathbf{k}_\parallel}$ is the in-plane kinetic energy of the Bloch state and $t_{p,q}$ the spin-independent hopping matrix element between sites p and q. The coupling of the left (right) lead to the barrier is considered through the hopping parameter $t_{a,\alpha}(t_{b,\alpha'})$ between the first (last) layer of the barrier and last (first) layer of the left (right) lead. h.c. denotes the hermitian conjugate.

The spin-dependent on-site energies ϵ_p^σ within the leads are split into the s orbital energy (ϵ_0) and the magnetic $s-d$ exchange interaction between itinerant spins and localized magnetic moments (Δ_p^σ): $\epsilon_p^\sigma = \epsilon_0 + \Delta_p^\sigma$ We set ϵ_0= 1.5 eV in both leads and t= -1 eV in all regions so that all the FIs analysed here are fully characterised by their on-site dependent $s-d$ interaction Δ_p^σ. Unlike the case of ordinary F-MTJ with homogeneous exchange splitting value within the electrode, Δ_p^σ for FI-MTJ here not only alternates in orientation, but also varies in magnitude from one layer to the next one, which defines two different sublattices denoted here as A and B (see Fig. 1). Considering a right FI lead whose first layer next to the B/FI interface is formed by fully uncompensated up spins (sublattice A), the spin splitting in layer λ' writes :

$$\Delta_{\lambda'}^{\uparrow(\downarrow)} = \begin{cases} -(+)\Delta_A \text{ if } \lambda' \text{ is odd -sublattice A-} \\ +(-)\Delta_B \text{ if } \lambda' \text{ is even -sublattice B-} \end{cases}$$

As depicted in Fig. 1, majority and minority bands in the ferrimagnetic leads are split by $\delta = \Delta_A - \Delta_B$. When an external bias V is applied, the on-site energies inside the insulator are considered to drop linearly with the number of layers (here N_B =3) from ϵ_B = 5 eV at the FI/B interface. The parameters modelling the electronic properties of the FI leads constitute a reasonable choice used previously for ordinary F-MTJ based on magnetic transition metals and their alloys [Stamenova et al., 2005], [Zhang and Li, 2004].

II.2 Observables to calculate

The spin-dependent transport properties of the magnetic tunnel junction are analysed here through four essential physical quantities (observables): spin density, spin current density, charge current density and spin transfer torque. Thus, the corresponding quantum operators must be calculated. Their expectation values are then computed in order to obtain measurable quantities.

As it is known from statistical mechanics, the expectation value or thermal average at time t of any operator $\hat{O}(t)$ can be calculated using the density matrix $\hat{\rho}(t)$ [Bruus and Flensberg, 2002]:

$$\langle \hat{O}(t) \rangle = Tr[\hat{\rho}(t) \cdot \hat{O}] \tag{II.6}$$

where the symbol Tr denotes a trace over all many-body states (over all possible indices), i.e. a trace in the Fock space [Stefanucci and Leeuwen, 2013]. In a nonequilibrium state, the density matrix is expressed in terms of the lesser Green's function $\hat{G}^<$, defined by the ensemble average:

$$G^<_{\alpha,\beta}(t,t') = i\langle \hat{c}^\dagger_\beta(t')\hat{c}_\alpha(t) \rangle \tag{II.7}$$

where α, β represent any set of quantum numbers describing the one particle Hilbert state of the system. With this definition, the density matrix is the same as the equal-time lesser Green's function:

$$\rho_{\alpha,\beta}(t) = \langle \hat{c}^{\dagger}_{\beta}(t)\hat{c}_{\alpha}(t)\rangle = -iG^{<}_{\alpha,\beta}(t,t) \tag{II.8}$$

Thus, the lesser Green's function allows to calculate the time-dependent ensemble average of any one-body operator:

$$\langle \hat{O}(t)\rangle = -iTr[\hat{G}^{<}(t)\cdot\hat{O}] \tag{II.9}$$

The origin of the lesser Green's function in the framework of the nonequilibrium Keldysh formalism is described in II.8. The observables studied in this thesis are developed in terms of Green's functions in the following sections.

II.2.1 Spin density at site λ' in the right lead

The spin's mean value at time t in a plane λ' perpendicular to the direction of transport in the right lead reads:

$$\begin{aligned}\left\langle \hat{\mathbf{S}}_{\lambda'}(t)\right\rangle &= Tr[\hat{\rho}(t)\cdot\hat{\mathbf{S}}_{\lambda'}] = -iTr[\hat{G}^{<}(t,t)\cdot\hat{\mathbf{S}}_{\lambda'}] = -\frac{i}{2\pi}\int Tr[\hat{G}^{<}(\omega)\cdot\hat{\mathbf{S}}_{\lambda'}]d\omega \\ &= -\frac{i}{2\pi\hbar}\int Tr[\hat{G}^{<}(E/\hbar)\cdot\hat{\mathbf{S}}_{\lambda'}]dE = -\frac{i}{2\pi\hbar}\sum_{\mathbf{k}_{\parallel},\sigma,\sigma'}\int Tr[\hat{G}^{<}_{\lambda'\lambda'}(E/\hbar,\mathbf{k}_{\parallel})]\cdot\mathbf{S}dE\end{aligned}$$

Where $\hat{G}^{<}_{\lambda'\lambda'}$ is the lesser Green's function 2×2 matrix in spin space and $\hat{\mathbf{S}}_{\lambda'}$ is the local spin operator at site λ'. The explicit time-dependence disappears because only the stationary state is considered. The $\mathbf{k}_{\parallel}$ dependence of $\hat{G}^{<}_{\lambda'\lambda'}$ is only shown at the end of the equation. Taking the thermodynamic limit $V = Na^2 \longrightarrow \infty$, where N is the number of unit cells in the λ' plane and a is the lattice parameter, the summation in $\mathbf{k}_{\parallel}$ states can be replaced by an integral:

$$\sum_{\mathbf{k}_{\parallel}} \longrightarrow \frac{V}{(2\pi)^2}\int_{FBZ} d\mathbf{k}_{\parallel} = \frac{Na^2}{(2\pi)^2}\int_{FBZ} d\mathbf{k}_{\parallel} \tag{II.10}$$

Using this relation, the local spin reads:

$$\begin{aligned}\left\langle \hat{\mathbf{S}}_{\lambda'}\right\rangle = \mathbf{S}_{\lambda'} &= -\frac{i}{2\pi\hbar}\frac{Na^2}{(2\pi)^2}\int Tr[\hat{G}^{<}_{\lambda',\lambda'}(E/\hbar,\mathbf{k}_{\parallel})\cdot\mathbf{S}]d\mathbf{k}_{\parallel}dE \\ &= -\frac{i\hbar Na^2}{16\pi^3}\int Tr[\hat{G}^{<}_{\lambda',\lambda'}(E,\mathbf{k}_{\parallel})\cdot\boldsymbol{\sigma}]d\mathbf{k}_{\parallel}dE\end{aligned}$$

Where $\boldsymbol{\sigma}$ is the usual vector whose components are the spin operators (Pauli matrices). For the sake of simplicity, the lesser Green's function's dependence on E and $\mathbf{k}_\parallel$ will be omitted in the notation from now on. The spin density (spin by unit of surface) in the plane λ' is, finally:

$$\boxed{\mathbf{s}_{\lambda'} = -\frac{i\hbar}{16\pi^3}\int Tr[\hat{G}^<_{\lambda'\lambda'}\cdot\boldsymbol{\sigma}]dEd\mathbf{k}_\parallel \quad \text{(3-D)}} \tag{II.11}$$

In 1-D, the integration in $\mathbf{k}_\parallel$ is not necessary and the prefactor $1/(2\pi)^2$ of Eq. (II.10) disappears, so that Eq. (II.11) becomes:

$$\boxed{\mathbf{s}_{\lambda'} = -\frac{i\hbar}{4\pi}\int Tr[\hat{G}^<_{\lambda'\lambda'}\cdot\boldsymbol{\sigma}]dE \quad \text{(1-D)}} \tag{II.12}$$

The integration in the reciprocal space is restricted to the first Brillouin zone, FBZ.

By projecting the lesser Green's function into the three Pauli matrices components of $\boldsymbol{\sigma}$, the spin density in 3-D at site λ' in the x, y and z directions are given by:

$$s^x_{\lambda'} = -\frac{i\hbar}{16\pi^3}\int Tr_\sigma[\hat{G}^<_{\lambda'\lambda'}\cdot\hat{\sigma}_x]dEd\mathbf{k}_\parallel = -\frac{i\hbar}{16\pi^3}\int [G^<_{\lambda'\lambda'}(1,2)+G^<_{\lambda'\lambda'}(2,1)]dEd\mathbf{k}_\parallel$$

$$s^y_{\lambda'} = -\frac{i\hbar}{16\pi^3}\int Tr_\sigma[\hat{G}^<_{\lambda'\lambda'}\cdot\hat{\sigma}_y]dEd\mathbf{k}_\parallel = -\frac{i\hbar}{16\pi^3}\int [G^<_{\lambda'\lambda'}(1,2)-G^<_{\lambda'\lambda'}(2,1)]dEd\mathbf{k}_\parallel$$

$$s^z_{\lambda'} = -\frac{i\hbar}{16\pi^3}\int Tr_\sigma[\hat{G}^<_{\lambda'\lambda'}\cdot\hat{\sigma}_z]dEd\mathbf{k}_\parallel = -\frac{i\hbar}{16\pi^3}\int [G^<_{\lambda'\lambda'}(1,1)-G^<_{\lambda'\lambda'}(2,2)]dEd\mathbf{k}_\parallel$$

where the components of the lesser Green's function operator in spin space are defined as follows:

$$\hat{G}^<_{\lambda'\lambda'} = \begin{pmatrix} G^<_{\lambda'\lambda'}(1,1) & G^<_{\lambda'\lambda'}(1,2) \\ G^<_{\lambda'\lambda'}(2,1) & G^<_{\lambda'\lambda'}(2,2) \end{pmatrix} = \begin{pmatrix} G^{<\uparrow\uparrow}_{\lambda'\lambda'} & G^{<\uparrow\downarrow}_{\lambda'\lambda'} \\ G^{<\downarrow\uparrow}_{\lambda'\lambda'} & G^{<\downarrow\downarrow}_{\lambda'\lambda'} \end{pmatrix}$$

II.2.2 Spin current density at site λ' in the right lead

The spin current density is defined as the tensor product of the velocity operator and the spin density at site λ':

$$\hat{Q} = \hat{\mathbf{s}}_{\lambda'} \otimes \hat{\mathbf{v}} \tag{II.13}$$

In the case of the tunnel junction considered here, transport takes place only in the y direction, only the $\hat{Q}_{xy}, \hat{Q}_{yy}, \hat{Q}_{zy}$ components are nonzero, so that $\hat{Q}$ is not a tensor, but

a vector:

$$\hat{Q} = \hat{\mathbf{s}}_{\lambda'} \otimes (0, \hat{v}_y, 0) = (\hat{s}_x, \hat{s}_y, \hat{s}_z)^t \cdot (0, \hat{v}_y, 0) = \begin{pmatrix} 0 & \hat{s}_x\hat{v}_y & 0 \\ 0 & \hat{s}_y\hat{v}_y & 0 \\ 0 & \hat{s}_z\hat{v}_y & 0 \end{pmatrix}$$

$$\hat{\mathbf{Q}} = (\hat{Q}_{xy}, \hat{Q}_{yy}, \hat{Q}_{zy}) = (\hat{s}_x\hat{v}_y, \hat{s}_y\hat{v}_y, \hat{s}_z\hat{v}_y) \tag{II.14}$$

The left index is in spin space and the right index is in real space. For the sake of clarity, the y index in real space will be omitted in the notation, so that the three components in spin space of the spin current vector in the y direction are denoted by:

$$\hat{\mathbf{Q}} = (\hat{I}^x, \hat{I}^y, \hat{I}^z) \tag{II.15}$$

The velocity operator can be extracted from the Heisenberg equation:

$$\hat{\mathbf{v}}_y = \frac{d}{dt}\hat{y} = \frac{i}{\hbar}[\hat{H}, \hat{y}]$$

The diagonal parts of the TB Hamiltonian commute with the $\hat{y}$ operator. Let's calculate the the matrix elements of the velocity operator in the Hilbert space:

$$\begin{aligned} \langle p,\sigma|\,[\hat{H},\hat{y}]\,|q,\sigma\rangle &= \langle p,\sigma|\,\hat{H}\hat{y}\,|q,\sigma\rangle - \langle p,\sigma|\,\hat{y}\hat{H}\,|q,\sigma\rangle = q\,\langle p,\sigma|\,\hat{H}\,|q,\sigma\rangle - p\,\langle p,\sigma|\,\hat{H}\,|q,\sigma\rangle \\ &= (q-p)\,\langle p,\sigma|\,\hat{H}\,|q,\sigma\rangle = (q-p)t_{p,q} \end{aligned}$$

If only nearest neighbours are considered:

$$\hat{v}_y = \frac{i}{\hbar}t\sum_{p,\sigma}(\hat{c}^\dagger_{p,\sigma}\hat{c}_{p+1,\sigma} - \hat{c}^\dagger_{p+1,\sigma}\hat{c}_{p,\sigma}) \tag{II.16}$$

Combining Eqs. (II.11) and (II.16), the spin current density between layers λ' and $\lambda'+1$ for the 3-D case and the spin current between corresponding sites for the 1-D case can be obtained in terms of the lesser Green's function:

$$\boxed{\hat{\mathbf{I}}_{\lambda',\lambda'+1} = \frac{t}{16\pi^3}\int Tr_\sigma[(\hat{G}^{<\sigma,\sigma'}_{\lambda'+1,\lambda'} - \hat{G}^{<\sigma,\sigma'}_{\lambda',\lambda'+1})\cdot\hat{\sigma}]dEd\mathbf{k}_\parallel \quad \text{(3-D)}} \tag{II.17}$$

$$\boxed{\hat{\mathbf{I}}_{\lambda',\lambda'+1} = \frac{t}{4\pi}\int Tr_\sigma[(\hat{G}^{<\sigma,\sigma'}_{\lambda'+1,\lambda'} - \hat{G}^{<\sigma,\sigma'}_{\lambda',\lambda'+1})\cdot\hat{\sigma}]dE \quad \text{(1-D)}} \tag{II.18}$$

The x, y and z components of the spin current in spin space are thus:

$$\hat{I}^x_{\lambda',\lambda'+1} = \frac{t}{16\pi^3}\int Tr_\sigma[(\hat{G}^{<\sigma,\sigma'}_{\lambda'+1,\lambda'} - \hat{G}^{<\sigma,\sigma'}_{\lambda',\lambda'+1})\cdot\hat{\sigma}_x]dEd\mathbf{k}_\parallel \tag{II.19}$$

$$\hat{I}^{y}_{\lambda',\lambda'+1} = \frac{t}{16\pi^3}\int Tr_\sigma[(\hat{G}^{<\sigma,\sigma'}_{\lambda'+1,\lambda'} - \hat{G}^{<\sigma,\sigma'}_{\lambda',\lambda'+1})\cdot\hat{\sigma}_y]dEd\mathbf{k}_\parallel \tag{II.20}$$

$$\hat{I}^{z}_{\lambda',\lambda'+1} = \frac{t}{16\pi^3}\int Tr_\sigma[(\hat{G}^{<\sigma,\sigma'}_{\lambda'+1,\lambda'} - \hat{G}^{<\sigma,\sigma'}_{\lambda',\lambda'+1})\cdot\hat{\sigma}_z]dEd\mathbf{k}_\parallel \tag{II.21}$$

II.2.3 Charge current density

The charge current density can be extracted from Eq. (II.17) replacing $\frac{1}{2}\hat{\sigma}$ by a unit matrix multiplied by $\frac{e}{\hbar}$, where e is the electronic charge [Edwards et al., 2005]:

$$\boxed{\begin{aligned} I &= \frac{et}{8\pi^3\hbar}\int Tr_\sigma[\hat{G}^{<}_{\lambda'+1,\lambda'} - \hat{G}^{<}_{\lambda'\lambda'+1}]dEd\mathbf{k}_\parallel \\ &= \frac{et}{2\pi\hbar}\int[\hat{G}^{<}_{\lambda'+1,\lambda'}(1,1) + \hat{G}^{<}_{\lambda'+1,\lambda'}(2,2) - \hat{G}^{<}_{\lambda'\lambda'+1}(1,1) - \hat{G}^{<}_{\lambda'\lambda'+1}(2,2)]dEd\mathbf{k}_\parallel \end{aligned}} \tag{II.22}$$

Obviously, charge current density is conserved along the junction, and in particular at the right interface, where it writes:

$$I = \frac{et}{2\pi\hbar}\int Tr_\sigma[\hat{G}^{<}_{\alpha'b} - \hat{G}^{<}_{b\alpha'}]dEd\mathbf{k}_\parallel = \frac{et}{2\pi\hbar}\int[\hat{G}^{<}_{\alpha'b}(1,1) + \hat{G}^{<}_{\alpha'b}(2,2) - \hat{G}^{<}_{b\alpha'}(1,1) - \hat{G}^{<}_{b\alpha'}(2,2)]dEd\mathbf{k}_\parallel$$

II.2.4 Torque on site λ' in the right lead from the spin density current

In analogy to the continuity equation for the charge or the particle number, an equivalent continuity equation can be established for the spin density [Stiles and Zangwill, 2002]. The characteristic difference is that spin is not conserved due to the local exchange field inside the leads, giving rise to an external torque $\hat{\mathbf{T}}$ exerted by the lattice:

$$\frac{d\hat{\mathbf{s}}}{dt} = \frac{i}{\hbar}[\hat{H}, \hat{\mathbf{s}}] = -\nabla\cdot\hat{Q} + \hat{\mathbf{T}} \tag{II.23}$$

Since by definition it is the right index of the spin current tensor that is in real space, the divergence of this tensor at the right hand side of Eq. (II.23) is the divergence of each of its columns (the spatial derivative is taken with respect to the real space index). As mentioned above, only the $\hat{Q}_{xy}, \hat{Q}_{yy}, \hat{Q}_{zy}$ components are nonzero (all the spatial derivatives with respect to x and z variables are also zero due to the translational invariance in the xz plane of the tunnel junction):

$$\nabla \cdot \hat{Q} = \partial_k \hat{Q}_{ik} = \begin{pmatrix} \partial_x \hat{Q}_{xx} + \partial_y \hat{Q}_{xy} + \partial_z \hat{Q}_{xz} \\ \partial_x \hat{Q}_{yx} + \partial_y \hat{Q}_{yy} + \partial_z \hat{Q}_{yz} \\ \partial_x \hat{Q}_{zx} + \partial_y \hat{Q}_{zy} + \partial_z \hat{Q}_{zz} \end{pmatrix} = \begin{pmatrix} \partial_y \hat{Q}_{xy} \\ \partial_y \hat{Q}_{yy} \\ \partial_y \hat{Q}_{zy} \end{pmatrix} = \begin{pmatrix} \partial_y \hat{I}^x \\ \partial_y \hat{I}^y \\ \partial_y \hat{I}^z \end{pmatrix} = \partial_y \hat{\mathbf{I}}$$

The discrete TB basis imposes in turn the discrete form of the partial derivative of the spin current in the real y direction:

$$\nabla \cdot \hat{Q} = \partial_y \hat{\mathbf{I}} = \hat{\mathbf{I}}_{\lambda'-1,\lambda'} - \hat{\mathbf{I}}_{\lambda',\lambda'+1} = (\hat{I}^x_{\lambda'-1,\lambda'} - \hat{I}^x_{\lambda',\lambda'+1}, \hat{I}^y_{\lambda'-1,\lambda'} - \hat{I}^y_{\lambda',\lambda'+1}, \hat{I}^z_{\lambda'-1,\lambda'} - \hat{I}^z_{\lambda',\lambda'+1})$$

Here, the subscripts λ' and μ' of $\hat{\mathbf{I}}_{\lambda',\mu'}$ stand for the layers/sites λ' and μ' correlated by the Lesser Green's function in terms of which the spin current is written (see below).

$\hat{\mathbf{T}}$ accounts for all the external torques that act to change the direction of the spin density. Since only coherent transport is considered, no spin-flip scattering processes are taken into account, there is no transfer of angular momentum between the lattice and the spin current due to spin-flip; thus, no terms as $\frac{\hat{\mathbf{s}}}{\tau_{\uparrow\downarrow}}$ (where $\tau_{\uparrow\downarrow}$ is a spin flip relaxation time) [Stiles and Zangwill, 2002] appear in (II.23). The external torque is exerted by the exchange field and any external field that might be present. In the absence of external fields, the lattice is the only responsible for the torque exerted on transport electrons. In a steady state, the time derivative of the spin density is zero, and the current-induced torque exerted by transport electrons on the magnetization is in competition with the torque due to exchange, anisotropy fields and phenomenological damping (in the context of a Landau-Lifshitz Gilbert equation), and causes the spin in a given atomic plane to deviate from the anisotropy axis [Edwards et al., 2005]. In the stationary regime, Eq. (II.23) becomes:

$$\hat{\mathbf{T}} = \nabla \cdot \hat{Q} \tag{II.24}$$

The torque exerted on the total magnetization is then equal to the net flux of spin current in a magnetic volume V. The torque deposited on layer λ' then reads:

$$\hat{\mathbf{T}}_{\lambda'} = \hat{\mathbf{I}}_{\lambda'-1,\lambda'} - \hat{\mathbf{I}}_{\lambda',\lambda'+1} \tag{II.25}$$

By using Eqs. (II.17) and (II.18), $\mathbf{T}_{\lambda'}$ writes:

$$\mathbf{T}_{\lambda'} = \frac{t}{16\pi^3} \int Tr_\sigma[(\hat{G}^<_{\lambda',\lambda'-1} - \hat{G}^<_{\lambda'-1,\lambda'} - \hat{G}^<_{\lambda'+1,\lambda'} + \hat{G}^<_{\lambda',\lambda'+1}) \cdot \hat{\sigma}] dE d\mathbf{k}_\parallel \quad \text{(3-D)} \tag{II.26}$$

$$\mathbf{T}_{\lambda'} = \frac{t}{4\pi}\int Tr_\sigma[(\hat{G}^<_{\lambda',\lambda'-1} - \hat{G}^<_{\lambda'-1,\lambda'} - \hat{G}^<_{\lambda'+1,\lambda'} + \hat{G}^<_{\lambda',\lambda'+1})\cdot\hat{\sigma}]dE \quad \text{(1-D)} \tag{II.27}$$

The torque is then decomposed into parallel or in-plane (x direction, transversal to the order parameter) and perpendicular or out-of-plane (y direction) components.

In-plane torque $\hat{T}^{\parallel}_{\lambda'}$

The in-plane component reads:

$$\boxed{\hat{T}^{\parallel}_{\lambda'} = \frac{t}{16\pi^3}\int Tr_\sigma[(\hat{G}^<_{\lambda',\lambda'-1} - \hat{G}^<_{\lambda'-1,\lambda'} - \hat{G}^<_{\lambda'+1,\lambda'} + \hat{G}^<_{\lambda',\lambda'+1})\cdot\hat{\sigma}_x]dEd\mathbf{k}_\parallel \quad \text{(3-D)}} \tag{II.28}$$

$$\boxed{\hat{T}^{\parallel}_{\lambda'} = \frac{t}{4\pi}\int Tr_\sigma[(\hat{G}^<_{\lambda',\lambda'-1} - \hat{G}^<_{\lambda'-1,\lambda'} - \hat{G}^<_{\lambda'+1,\lambda'} + \hat{G}^<_{\lambda',\lambda'+1})\cdot\hat{\sigma}_x]dE \quad \text{(1-D)}} \tag{II.29}$$

Multiplying by $\hat{\sigma}_x = \begin{pmatrix} 0 & 1 \\ 1 & 0 \end{pmatrix}$ to the right and taking the trace amounts to sum all off-diagonal elements of these four matrices. The parallel torque then becomes:

$$\begin{aligned}\hat{T}^{\parallel}_{\lambda'} = \frac{t}{16\pi^3}\int [&\hat{G}^<_{\lambda',\lambda'-1}(1,2) + \hat{G}^<_{\lambda',\lambda'-1}(2,1) - \hat{G}^<_{\lambda'-1,\lambda'}(1,2) - \hat{G}^<_{\lambda'-1,\lambda'}(2,1)\\ &- \hat{G}^<_{\lambda'+1,\lambda'}(1,2) - \hat{G}^<_{\lambda'+1,\lambda'}(2,1) + \hat{G}^<_{\lambda',\lambda'+1}(1,2) + \hat{G}^<_{\lambda',\lambda'+1}(2,1)]dEd\mathbf{k}_\parallel\end{aligned}$$

The torque on the first site of the right lead in contact with the barrier's right interface takes a particular form that includes the correlation of the last site of the barrier and the first site of the right lead:

$$\begin{aligned}\hat{T}^{\parallel}_{\alpha'} = \frac{t}{16\pi^3}\int [&\hat{G}^<_{\alpha',b}(1,2) + \hat{G}^<_{\alpha',b}(2,1) - \hat{G}^<_{b,\alpha'}(1,2) - \hat{G}^<_{b,\alpha'}(2,1)\\ &- \hat{G}^<_{\alpha'+1,\alpha'}(1,2) - \hat{G}^<_{\alpha'+1,\alpha'}(2,1) + \hat{G}^<_{\alpha',\alpha'+1}(1,2) + \hat{G}^<_{\alpha',\alpha'+1}(2,1)]dEd\mathbf{k}_\parallel\end{aligned}$$

It will be shown that the correlation function at this interface is formally different from the correlation function inside the lead.

Out-of-plane torque $\hat{T}^{\perp}_{\lambda'}$

The out-of-plane torque writes:

$$\boxed{\hat{T}^{\perp}_{\lambda'} = \frac{t}{16\pi^3}\int Tr_{\sigma}[(\hat{G}^{<}_{\lambda',\lambda'-1} - \hat{G}^{<}_{\lambda'-1,\lambda'} - \hat{G}^{<}_{\lambda'+1,\lambda'} + \hat{G}^{<}_{\lambda',\lambda'+1})\cdot\hat{\sigma}_y]dEd\mathbf{k}_{\parallel} \quad \text{(3-D)}} \tag{II.30}$$

$$\boxed{\hat{T}^{\perp}_{\lambda'} = \frac{t}{4\pi}\int Tr_{\sigma}[(\hat{G}^{<}_{\lambda',\lambda'-1} - \hat{G}^{<}_{\lambda'-1,\lambda'} - \hat{G}^{<}_{\lambda'+1,\lambda'} + \hat{G}^{<}_{\lambda',\lambda'+1})\cdot\hat{\sigma}_y]dE \quad \text{(1-D)}} \tag{II.31}$$

Multiplying by $\hat{\sigma}_y = \begin{pmatrix} 0 & -i \\ i & 0 \end{pmatrix}$ to the right and taking the trace amounts to sum the (1,2) components, subtracting the (2,1) components and multiplying by i, which gives:

$$\begin{aligned}\hat{T}^{\perp}_{\lambda'} = \frac{t}{16\pi^3}\int i[&\hat{G}^{<}_{\lambda',\lambda'-1}(1,2) - \hat{G}^{<}_{\lambda',\lambda'-1}(2,1) - \hat{G}^{<}_{\lambda'-1,\lambda'}(1,2) + \hat{G}^{<}_{\lambda'-1,\lambda'}(2,1)\\ &- \hat{G}^{<}_{\lambda'+1,\lambda'}(1,2) + \hat{G}^{<}_{\lambda'+1,\lambda'}(2,1) + \hat{G}^{<}_{\lambda',\lambda'+1}(1,2) - \hat{G}^{<}_{\lambda',\lambda'+1}(2,1)]dEd\mathbf{k}_{\parallel}\end{aligned}$$

And again the torque on the first site of the right lead reads:

$$\begin{aligned}\hat{T}^{\perp}_{\alpha'} = \frac{t}{16\pi^3}\int i[&\hat{G}^{<}_{\alpha',b}(1,2) - \hat{G}^{<}_{\alpha',b}(2,1) - \hat{G}^{<}_{b,\alpha'}(1,2) + \hat{G}^{<}_{b,\alpha'}(2,1)\\ &- \hat{G}^{<}_{\alpha'+1,\alpha'}(1,2) + \hat{G}^{<}_{\alpha'+1,\alpha'}(2,1) + \hat{G}^{<}_{\alpha',\alpha'+1}(1,2) - \hat{G}^{<}_{\alpha',\alpha'+1}(2,1)]dEd\mathbf{k}_{\parallel}\end{aligned}$$

II.2.5 On-site torque from the exchange field

Alternatively, since ballistic transport is considered here, torques can also be extracted from the exchange field:

$$\hat{T} = \boldsymbol{\Delta}_{\lambda'}\hat{\mathbf{z}} \times \hat{s}_{\lambda'} \tag{II.32}$$

The exchange field $\boldsymbol{\Delta}_{\lambda'}$ is defined as an angular frequency so that the energy required to reverse one spin in layer λ' is $\hbar\boldsymbol{\Delta}_{\lambda'} = \epsilon^{\uparrow}_{\lambda'} - \epsilon^{\downarrow}_{\lambda'}$. Note the relation between the spin splitting $\Delta_{\lambda'}$ and the exchange field $\boldsymbol{\Delta}_{\lambda'}$ (bold sign): $\hbar\boldsymbol{\Delta}_{\lambda'} = 2\Delta_{\lambda'}$. $\boldsymbol{\Delta}_{\lambda'}$ is assumed to match the direction of local magnetization in the local spin density approximation (LSDA). The z component of torque is zero and the in-plane and out-of-plane components of the local torques defined in Fig. II.1 are given by the so called x and y components of spin accumulation, $\hat{s}^{x}_{\lambda'}$ and $\hat{s}^{y}_{\lambda'}$ respectively:

$$\hat{T} = \boldsymbol{\Delta}_{\lambda'}\hat{\mathbf{z}} \times \hat{\mathbf{s}}_{\lambda'} = \boldsymbol{\Delta}_{\lambda'}(0,0,1) \times (\hat{s}^{x}_{\lambda'}, \hat{s}^{y}_{\lambda'}, \hat{s}^{z}_{\lambda'}) = \boldsymbol{\Delta}_{\lambda'}(-\hat{s}^{y}_{\lambda'}, \hat{s}^{x}_{\lambda'}, 0)$$

According to the coordinates depicted in Fig. II.1, the out-of-plane spin accumulation (perpendicular to the B/FI interface) originates the in-plane torque $T^{\parallel}_{\lambda'}$, and the in-plane

spin accumulation (parallel to the B/FI interface) originates the out-of-plane torque $T_{\lambda'}^{\perp}$:

$$\boxed{T_{\lambda'}^{\parallel} = \mathbf{\Delta}_{\lambda'} \cdot s_{\lambda'}^{y} = \mathbf{\Delta}_{\lambda'} \cdot s_{\lambda'}^{\perp}} \tag{II.33}$$

$$\boxed{T_{\lambda'}^{\perp} = \mathbf{\Delta}_{\lambda'} \cdot s_{\lambda'}^{x} = \mathbf{\Delta}_{\lambda'} \cdot s_{\lambda'}^{\parallel}} \tag{II.34}$$

II.2.6 Total torque exerted in the right lead

The definition of the local torque as the (discrete) divergence of the spin current on each site is commonly used to calculate the total torque exerted on the right lead, which is the sum of local torques:

$$\mathbf{T}_{\lambda'} = -\nabla \cdot \mathbf{Q} = \mathbf{Q}_{\lambda'-1,\lambda'} - \mathbf{Q}_{\lambda',\lambda'+1} \tag{II.35}$$

$$\mathbf{T} = \sum_{\lambda'=1}^{\infty} (\mathbf{Q}_{\lambda'-1,\lambda'} - \mathbf{Q}_{\lambda',\lambda'+1}) \tag{II.36}$$

For the specific case of a F lead, $\mathbf{T} = \mathbf{Q}_{0,1} - \mathbf{Q}_{\infty,\infty} = \mathbf{Q}_{0,1}$, since the components of $\mathbf{Q}_{\lambda',\lambda'+1}$ transverse to $\mathbf{M}$' decay to zero as $\lambda' \to \infty$ [Kalitsov et al., 2009], [Kalitsov et al., 2006], [Brataas et al., 2006]. The total spin torque exerted on the right F lead is therefore simply the spin current at the B/F interface [Stiles and Zangwill, 2002].

However, it is likely that spin density current does not vanish far away from the barrier interface for the specific case of an AF lead, i.e. $\mathbf{Q}_{\infty,\infty} \neq 0$, as discussed in [Núñez et al., 2006]. The last simplification to compute the total torque can no longer be used to calculate the total torque on an AF. In addition, in the case of FI and AF leads, the spin density current terms in the sum $\sum_{\lambda'=1}^{\infty}(\mathbf{Q}_{\lambda'-1,\lambda'} - \mathbf{Q}_{\lambda',\lambda'+1})$ do not cancel since the orientation of localized spins must be taken into account through a switching sign in front of each term: a positive torque on one site tries to turn the localized spin in one sense, but a torque of the same sign acting on the next site tends to align the corresponding localized spin in the opposite sense. Heisenberg field is strong enough to make the lattice rigid, so that both effects are counterbalanced and the torque will not be effective. This is illustrated in Fig. II.2.

Thus, local torques must be summed up taking into account the orientation of localized spins on each site: local torques that tend to rotate the localized spin clockwise(counter clockwise), both in plane and out of plane, are considered positive(negative). With this convention:

$$T_{\text{effective}}^{\parallel} = \sum_{\lambda'=1}^{\infty} (-1)^{\lambda'} \cdot T_{\lambda'}^{\parallel} \tag{II.37}$$

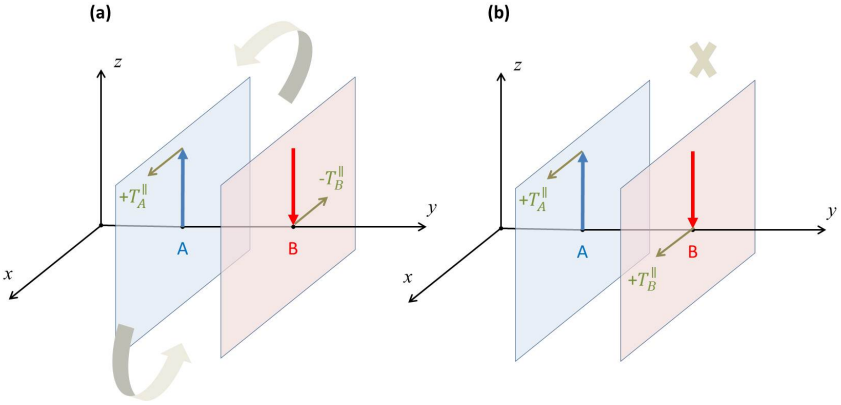

Figure II.2 – **(a)** Effective in-plane torque in an AF lead resulting from local torques of alternating sign from layer A (up spins) to the adjacent layer B (down spins). **(b)** Ineffective in-plane torque due to local torques of the same sign in adjacent layers; Heisenberg field maintains the lattice rigid and the order parameter does not change orientation.

$$T^{\perp}_{\text{effective}} = \sum_{\lambda'=1}^{\infty} (-1)^{\lambda'+1} \cdot T^{\perp}_{\lambda'} \tag{II.38}$$

That is the reason why for this thesis I studied the local distribution of torques $\mathbf{T}_{\lambda'}$ on each site/layer of the right lead instead of the single spin current density at the barrier interface, which is sufficient only for F leads.

II.3 Green's and Keldysh functions to calculate

As discussed in II.2, one needs to calculate the lesser Green's function to compute the required local observables. In addition, three more Green's functions need to be introduced: Keldysh, advanced and retarded Green's functions:

$$F_{\alpha,\beta}(t,t') = -i\langle[\hat{c}_\alpha(t), \hat{c}^\dagger_\beta(t')]_-\rangle \tag{II.39}$$

$$G^a_{\alpha,\beta}(t,t') = -i\theta(t-t')\langle[\hat{c}_\alpha(t), \hat{c}^\dagger_\beta(t')]_+\rangle \tag{II.40}$$

$$G^r_{\alpha,\beta}(t,t') = i\theta(t'-t)\langle[\hat{c}_\alpha(t), \hat{c}^\dagger_\beta(t')]_+\rangle \tag{II.41}$$

where $\theta(t)$ is the Heaviside step function, $[A,B]_- = AB - BA$ is the quantum commutator and $[A,B]_+ = AB + BA$ is the quantum anticommutator. A more detailed description of these functions and their physical significance is given in II.8.

When the stationary state is considered, the correlation functions only depend on the time difference $\tau = t - t'$. It is then advantageous to take the Fourier transform of these functions with respect to this time difference. In addition, since we consider spin

dependent transport, the lesser Green's function becomes a 2×2 matrix in spin space correlating sites/layers p and q within the tunnel junction. With these assumptions, its Fourier transform can be expressed in terms of nonequilibrium Keldysh, advanced and retarded Green's functions [Lifshitz and Pitaievskii, 1981]:

$$\hat{G}^{<}_{p,q} = \frac{1}{2}(\hat{F}_{p,q} + \hat{G}^{a}_{p,q} - \hat{G}^{r}_{p,q}) \tag{II.42}$$

The three correlation functions at the right hand side (r.h.s.) of Eq. (II.42) need to be calculated by solving a set of Dyson equations in order to obtain the lesser Green's function.

II.3.1 Retarded and advanced Green's functions

Let's start with the calculation of the retarded and advanced Green's functions. Given that $\hat{G}^{a}_{lm} = (\hat{G}^{r}_{ml})^{H}$, where H denotes hermitian conjugate, i.e. transposing the 2×2 matrix in spin space and taking the complex conjugate of its elements, it suffices to calculate the retarded Green's function, from which the advanced Green's function is straightforwardly obtained. In addition, since all the observables of interest are evaluated in this work in the right lead of the tunnel junction, only the retarded Green's function correlating sites at the right lead is considered here. In particular, three Green's functions are needed: $\hat{G}^{<}_{\alpha',b}$, $\hat{G}^{<}_{b,\alpha'}$ and $\hat{G}^{<}_{\lambda',\mu'}$. They correlate atomic sites across the right interface and inside the right lead, and are given by all the diagrams or possible paths connecting the two indices. Taking into account possible excursions of the electron across the interfaces, these three Green's functions can be expressed in terms of the two surface Green's functions of the barrier, $\hat{G}_{a,a}$ and $\hat{G}_{b,b}$ [Caroli et al., 1971]:

$$\hat{G}^{r}_{\alpha',b} = \hat{g}^{r}_{\alpha',\alpha'} T' \hat{G}^{r}_{b,b} \tag{II.43}$$

$$\hat{G}^{r}_{b,\alpha'} = \hat{G}^{r}_{b,b} T' \hat{g}^{r}_{\alpha,'\alpha'} \tag{II.44}$$

$$\hat{G}^{r}_{\lambda',\mu'} = \hat{g}^{r}_{\lambda',\mu'} + \hat{g}^{r}_{\lambda',\alpha'} T' \hat{G}^{r}_{b,b} T' \hat{g}^{r}_{\alpha',\mu'} \tag{II.45}$$

$\hat{g}_{\lambda',\mu'}$ are the retarded Green's functions for the right electrode alone, i.e., when it is not coupled with the rest of the junction through the right barrier interface. Thus, λ' and μ' are both contained in the right lead, otherwise $\hat{g}_{\lambda',\mu'} = 0$. T' is the hopping parameter (coupling) across the right barrier/right lead interface.

II.3.2 Nonequilibrium Keldysh functions

The nonequilibrium 2×2 Keldysh function matrix is calculated using the Dyson Quantum Kinetic equation. The detailed derivation of $\hat{F}_{\lambda'\mu'}$, $\hat{F}_{b'\alpha'}$ and $\hat{F}_{\alpha' b}$ is shown in Appendix A for the interested reader. Their final expressions read:

$$\hat{F}_{b\alpha'} = T^2 \hat{D}\hat{B}\hat{g}_{ba}(\hat{I} + \hat{\Sigma}_{aa}\hat{A}\hat{g}_{aa})\hat{f}_{\alpha\alpha}\hat{G}^a_{a\alpha'} + \hat{D}\hat{B}(\hat{g}_{ba}\hat{\Sigma}_{aa}\hat{A}\hat{g}_{ab} + \hat{g}_{bb})T'\hat{f}_{\alpha'\alpha'}(\hat{I} + T'\hat{G}^a_{b\alpha'}) \tag{II.46}$$

$$\hat{F}_{\alpha' b} = T\hat{L}\hat{N}\hat{\Sigma}_{bb}\hat{g}_{ba}\hat{M}\hat{f}_{\alpha\alpha}\hat{G}^a_{ab} + T\hat{L}\hat{N}\hat{f}_{\alpha'\alpha'}\hat{G}^a_{bb} \tag{II.47}$$

$$\begin{aligned}\hat{F}_{\lambda'\mu'} = {} & \hat{g}_{\lambda'\alpha'}T\hat{Den}^{-1}\hat{g}_{ba}T(\hat{I} + \hat{\Sigma}_{aa}\hat{A}\hat{g}_{aa})\hat{f}_{\alpha\alpha}T\hat{G}^a_{ab}T\hat{g}^a_{\alpha'\mu'}\hat{f}_{\lambda'\mu'} + \hat{f}_{\lambda'\alpha'}T\hat{G}^a_{bb}T\hat{g}^a_{\alpha'\mu'} \\ & + \hat{g}_{\lambda'\alpha'}T\hat{Den}^{-1}(\hat{g}_{bb} + \hat{g}_{ba}\hat{\Sigma}_{aa}\hat{A}\hat{g}_{ab})T(\hat{f}_{\alpha'\mu'} + \hat{f}_{\alpha'\alpha'}T\hat{G}^a_{bb}T\hat{g}^a_{\alpha'\mu'})\end{aligned} \tag{II.48}$$

The definitions of the matrices $\hat{\Sigma}_{aa}$, $\hat{\Sigma}_{bb}$, $\hat{A}$, $\hat{B}$, $\hat{D}$, $\hat{N}$, $\hat{M}$, $\hat{L}$ and $\hat{Den}^{-1}$ are given in the same Appendix.

II.3.3 Lesser Green's functions

The lesser Green's functions correlating atomic sites in the right lead can now be easily obtained using the results of the previous sections and Eq.(II.42):

$$\boxed{\begin{aligned}\hat{G}^<_{\alpha' b} &= \frac{1}{2}(\hat{F}_{\alpha' b} + \hat{G}^a_{\alpha' b} - \hat{G}^r_{\alpha' b}) = \frac{1}{2}[\hat{F}_{\alpha' b} + (\hat{G}^r_{b\alpha'})^H - \hat{G}^r_{\alpha' b}] \\ &= \frac{1}{2}[T\hat{L}\hat{N}\hat{\Sigma}_{bb}\hat{g}_{ba}\hat{M}\hat{f}_{\alpha\alpha}\hat{G}^a_{ab} + T\hat{L}\hat{N}\hat{f}_{\alpha'\alpha'}\hat{G}^a_{bb} + (\hat{G}^r_{bb}T\hat{g}^r_{\alpha'\alpha'})^H - \hat{g}^r_{\alpha'\alpha'}T\hat{G}^r_{bb}]\end{aligned}} \tag{II.49}$$

$$\boxed{\begin{aligned}\hat{G}^<_{b\alpha'} &= \frac{1}{2}(\hat{F}_{b\alpha'} + \hat{G}^a_{b\alpha'} - \hat{G}^r_{b\alpha'}) = \frac{1}{2}[\hat{F}_{b\alpha'} + (\hat{G}^r_{\alpha' b})^H - \hat{G}^r_{b\alpha'}] \\ &= \frac{1}{2}[T^2\hat{D}\hat{B}\hat{g}_{ba}(\hat{I} + \hat{\Sigma}_{aa}\hat{A}\hat{g}_{aa})\hat{f}_{\alpha\alpha}\hat{G}^a_{a\alpha'} + \hat{D}\hat{B}(\hat{g}_{bb} + \hat{g}_{ba}\hat{\Sigma}_{aa}\hat{A}\hat{g}_{ab})T\hat{f}_{\alpha'\alpha'}(\hat{I} + T\hat{G}^a_{b\alpha'}) \\ &+ (\hat{g}^r_{\alpha'\alpha'}T\hat{G}^r_{bb})^H - \hat{G}^r_{bb}T\hat{g}^r_{\alpha'\alpha'}]\end{aligned}} \tag{II.50}$$

$$\begin{aligned}\hat{G}^{<}_{\lambda'\mu'} &= \frac{1}{2}(\hat{F}_{\lambda'\mu'} + \hat{G}^{a}_{\lambda'\mu'} - \hat{G}^{r}_{\lambda'\mu'}) = \frac{1}{2}[\hat{F}_{\lambda'\mu'} + (\hat{G}^{r}_{\mu'\lambda'})^{H} - \hat{G}^{r}_{\lambda'\mu'}] \\ &= \frac{1}{2}[\hat{g}_{\lambda'\alpha'}T\hat{Den}^{-1}\hat{g}_{ba}T(\hat{I} + \hat{\Sigma}_{aa}\hat{A}\hat{g}_{aa})\hat{f}_{\alpha\alpha}T\hat{G}^{a}_{ab}T\hat{g}^{a}_{\alpha'\mu'} \\ &+ \hat{f}_{\lambda'\mu'} + \hat{f}_{\lambda'\alpha'}T\hat{G}^{a}_{bb}T\hat{g}^{a}_{\alpha'\mu'} + \hat{g}_{\lambda'\alpha'}T\hat{Den}^{-1}(\hat{g}_{bb} + \hat{g}_{ba}\hat{\Sigma}_{aa}\hat{A}\hat{g}_{ab})T(\hat{f}_{\alpha'\mu'} + \hat{f}_{\alpha'\alpha'}T\hat{G}^{a}_{bb}T\hat{g}^{a}_{\alpha'\mu'}) \\ &+ (\hat{g}^{r}_{\mu'\lambda'} + \hat{g}^{r}_{\mu'\alpha'}T\hat{G}^{r}_{bb}T\hat{g}^{r}_{\alpha'\lambda'})^{H} - \hat{g}^{r}_{\lambda'\mu'} - \hat{g}^{r}_{\lambda'\alpha'}T\hat{G}^{r}_{bb}T\hat{g}^{r}_{\alpha'\mu'}]\end{aligned} \tag{II.51}$$

where H denotes the hermitian conjugate. Note that the relation between retarded and advanced Green's function matrices is used: $\hat{G}^{a}_{pq} = (\hat{G}^{r}_{qp})^{H}$.

The essential building block in Eqs (II.49, II.50, II.51) is the retarded Green's function for the uncoupled right lead, $\hat{g}^{r}_{\lambda',\mu'}$. The analytical calculation of this Green's function for the most general case of a 1-D FI chain is one of the main calculations that I have developed in this work and is described in the next section and in Appendix B. AF and F orders are just limiting cases that can be easily derived from the FI case via the TB parameters choice.

II.4 Calculation of the Retarded Green's function for a one dimensional ferrimagnet

A 1-D FI chain of localized moments seen by one itinerant spin is characterized in a TB model by two on-site energies ϵ_1 and ϵ_2 (alternating from one site to the next one) and a hopping parameter t. This 1-D chain corresponds to a lattice without closed loops that can be mapped into a Bethe lattice or Cayley tree which is completely characterized by its number of nearest neighbours $Z = 2$ or its connectivity $K = Z - 1$ [Economou, 2006]. Splitting the 1-D TB Hamiltonian into an unperturbed site-diagonal part plus an off-diagonal perturbation and using renormalized perturbation expansion [Economou, 2006] allows to perform the calculation of the system's resolvent $\hat{g}_{\lambda',\mu'}(z)$, where z is a complex variable. This resolvent is a more general definition of the Green's function in the complex plane, from which the retarded Green's function can be defined as follows:

$$\hat{g}^{r}_{\lambda'.\mu'}(E) = \lim_{s\to 0^{+}} \hat{g}_{\lambda',\mu'}(z = E + is)$$

where E stands for the energy variable belonging to the real axis of the complex plane and s is the imaginary part of z.

The detailed derivation of the retarded Green's function from this resolvent is given in Appendix B. The retarded Green's function correlating sites l and m in the FI chain has a complex structure: it is a spin-dependent function of the energy E, and takes

different expressions depending on which interval of E it is evaluated on and what sites it correlates. In effect, the imaginary part of the retarded Green's function correlating a site l with itself is proportional to the LDOS at that site. This imaginary part does not vanish in two energy regions: the lower band and the upper band. Thus, there are three forbidden energy regions: the first one for energies lower than the lower band edge E_2, the gap separating the lower and the upper bands between ϵ_2 and ϵ_1 and the third one for energies higher than the upper band edge E_1 (see Fig. II.3).

$$g^r(l,m,E) = \begin{cases} g^r_{f1}(l,m,E) & \text{if } E < E_2 \\ g^r_{gap}(l,m,E) & \text{if } \epsilon_2 < E < \epsilon_1 \\ g^r_{f2}(l,m,E) & \text{if } E_1 < E \\ g^r_{lb}(l,m,E) & \text{if } E_2 < E < \epsilon_2 \\ g^r_{ub}(l,m,E) & \text{if } \epsilon_1 < E < E_1 \end{cases}$$

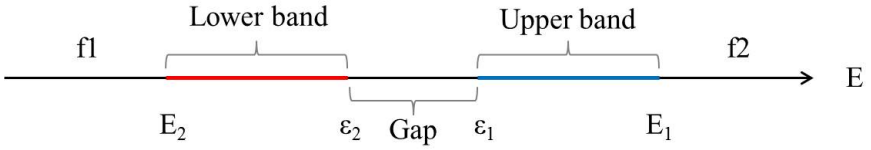

Figure II.3 – Schematic illustration of the different energy regions in which the retarded Green's function takes different expressions. The exact values of the band edges depending on the TB parameters of the FI are detailed in Appendix B.

The gap width is $\Delta_A + \Delta_B$ and both bands have the same bandwidths. The final energy dependence of the retarded Green's function is examined and plotted in the next section.

II.4.1 Energy dependence of the retarded Green's function for the infinite ferrimagnet chain

The energy dependence of the retarded Green's function for the infinite FI chain calculated above is plotted in Fig. II.4. The LDOS given by the imaginary part shows clearly the two sub-bands separated by the gap, while the real part does not vanish only in the forbidden energy regions. The imaginary part for a given spin in one sub-lattice and the imaginary part for the same spin in the other sub-lattice are symmetric with respect to an axis passing by the center of the gap: $E_c = \dfrac{\epsilon_1 + \epsilon_2}{2}$: $Im[g^{r\sigma}_{2,2}(E) = Im[g^{r\sigma}_{1,1}(-E + E_c)]$. The real part for a given spin in one sub-lattice and the real part for the same spin in the other sub-lattice are point-symmetric with respect to the center of the gap: $Re[g^{r\sigma}_{2,2}(E) = -Re[g^{r\sigma}_{1,1}(-E + E_c)]$.

The real and imaginary parts for a given spin in one sublattice are just shifted by $\delta =$

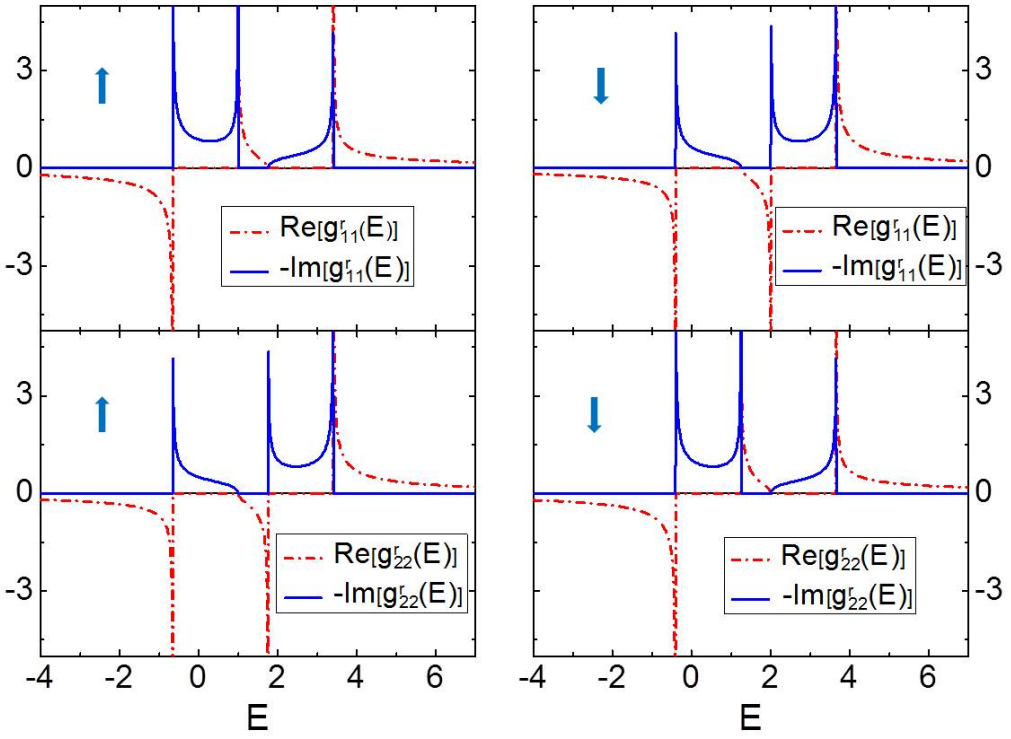

Figure II.4 – Real and imaginary parts of the (on-site) retarded Green's function's diagonal elements in real space for an infinite FI chain (Bethe lattice) with $\Delta_A = 0.5eV$, $\Delta_B = 0.25eV$ and $t = -1eV$. Left(right) panels: up(down) spins. Top(bottom) panels: on-site retarded Green's function on the A(B) sublattice (odd sites)(even sites). The vertical lines denote divergences.

$\Delta_A - \Delta_B$ with respect to the real and imaginary parts for the opposite spin in the other sublattice. The two sub-bands for up spins are thus left-shifted with respect to the sub-bands for down spins.Three of the band edges exhibit a square root singularity both for real and imaginary parts.
Note that $\int LDOS(p,E)dE = \int -\frac{1}{\pi} Im[g^r_{p,p}(E)]dE = 1$, i.e.: due to the simple one-band TB basis used, there is one state (orbital) per site for a given spin.

II.4.2 Energy dependence of the retarded Green's function for an infinite ferromagnetic chain

In the case of a F chain, the on-site energy for a given spin is constant regardless of the lattice site. Since all localized moments are equal and point in the same direction, there is only one type of site, so that the two sub-bands of the FI case arising from the two FI sublattices merge into a single band, as can be seen in Fig. II.5. The imaginary part (proportional to the LDOS) has square root singularities at the band edges that are characteristic of one dimensional systems [Economou, 2006].
Similar to the FI case, the imaginary part for a given spin is even-symmetric with respect to a vertical axis crossing the center of the band and the real part is odd-symmetric with

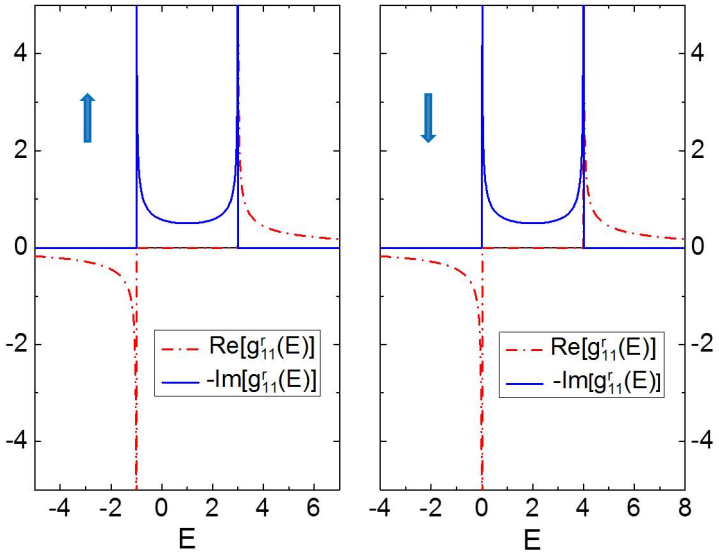

Figure II.5 – Real and imaginary parts of the (on-site) retarded Green's function's diagonal elements in real space for an infinite F chain with $\Delta = 0.5eV$ and $t = -1eV$. Left(right) panel: up(down) spins. Vertical lines denote divergences.

respect to the center of the band.

II.5 Calculation of the retarded Green's function for a semi infinite chain

Once the retarded Green's function for an infinite chain is calculated, it is necessary to calculate the retarded Green's function for a semi-infinite chain. Note that the uncoupled Green's functions at the r.h.s. of Eqs. (II.49), (II.50) and (II.51) refer to the right semi-infinite magnetic lead in contact with the non-magnetic barrier. To calculate the correlation functions of the right lead, we cut the infinite chain between sites 0 and 1 (sub-lattices B and A of the infinite chain), so that site 1 will be the first site of the right semi-infinite chain. The chain cut will be considered as a perturbation term added to the previous 1-D Hamiltonian, in order to use a Dyson equation to compute the Green's function for the semi-infinite chain:

$$\hat{H} = \hat{H}_0 + \hat{V}$$

where:

$\hat{H}$: Hamiltonian for the semi infinite chain
$\hat{H}_0$: Hamiltonian for the infinite chain
$\hat{V}$: Perturbation

For sites n and m on the same side of the cut: $n, m \geq 1$ or $n, m \leq 0$, we have

$$\langle n|\,\hat{H}_0\,|m\rangle = \langle n|\,\hat{H}\,|m\rangle \longrightarrow \langle n|\,\hat{V}\,|m\rangle = 0$$

However, two sites n and m on different sides of the chain can not be correlated:

$$\langle n|\,\hat{H}\,|m\rangle = 0 = \langle n|\,\hat{H}_0\,|m\rangle + \langle n|\,\hat{V}\,|m\rangle \longrightarrow \langle n|\,\hat{V}\,|m\rangle = -\langle n|\,\hat{H}_0\,|m\rangle$$

We shall study the matrix elements $\langle n|\,\hat{H}_0\,|m\rangle$ to compute the perturbation $\hat{V}$:
The Tight Binding Hamiltonian for one spin in an infinite chain reads:

$$\hat{H}_0 = \sum_l \epsilon_l\,|l\rangle\,\langle l| + t\,|l\rangle\,\langle l+1| + t\,|l+1\rangle\,\langle l| \tag{II.52}$$

Projecting Eq. (II.52) on sites n and m on different sides of the chain gives:

$$\begin{aligned}\langle n|\,\hat{H}_0\,|m\rangle &= \sum_l t(\langle n|l\rangle\langle l+1|m\rangle + \langle n|l+1\rangle\langle l|m\rangle)\\ &= \sum_l t(\delta_{n,l}\delta_{l+1,m} + \delta_{n,l+1}\delta_{l,m})\\ &= t(\delta_{n+1,m} + \delta_{n-1,m})\end{aligned}$$

For this expression to be different from 0, we must have $n+1=m$ or $n-1=m$ (n and m own to different sides of the cut).

Case 1) $n \leq 0$ on the left side of the chain and $m \geq 1$ on the right side of the chain. The only two sites giving a contribution to the perturbation are in this case: $n=0$, $m=1$:

$$\langle n|\,\hat{H}_0\,|m\rangle = t\delta_{n,0}\delta_{m,1}$$

Case 2) $n \geq 1$ on the right side of the chain and $m \leq 0$ on the left side of the chain. The only two sites giving a contribution to the perturbation are in this case: $n=1$, $m=0$:

$$\langle n|\,\hat{H}_0\,|m\rangle = t\delta_{n,1}\delta_{m,0}$$

Therefore:

$$\langle n|\,\hat{H}_0\,|m\rangle = t(\delta_{n+1,m} + \delta_{n-1,m}) = t(\delta_{n,0}\delta_{m,1} + \delta_{n,1}\delta_{m,0})$$

$$\hat{V} = \sum_{n,m}\langle n|\,\hat{V}\,|m\rangle\,|n\rangle\,\langle m| = -t\sum_{n,m}(\delta_{n,0}\delta_{m,1} + \delta_{n,1}\delta_{m,0})\,|n\rangle\,\langle m| = -t(|0\rangle\,\langle 1| + |1\rangle\,\langle 0|)$$

Once the perturbation operator is known, the Green's function of the semi-infinite chain (perturbed system) $\hat{g}^r$ can be calculated applying a Dyson equation to the Green's function of the infinite chain (unperturbed system) $\hat{g}_0^r$:

$$\hat{g}^r = \hat{g}_0^r + \hat{g}_0^r \hat{V} \hat{g}^r$$

$\hat{g}^r$ is the retarded Green's function corresponding to $\hat{H}$ (semi infinite chain) and $\hat{g}_0^r$ is the retarded Green's function corresponding to $\hat{H}_0$ (infinite chain, non perturbed Hamiltonian).

Projecting Dyson equation into sites n and m gives:

$$\begin{aligned} g^r(n,m,E) &= g_0^r(n,m,E) + \sum_{p,q} g_0^r(n,p,E) V(p,q) g^r(q,m,E) \\ &= g_0^r(n,m,E) - t \sum_{p,q} g_0^r(n,p,E)(\delta_{p,0}\delta_{q,1} + \delta_{p,1}\delta_{q,0}) g^r(q,m,E) \\ &= g_0^r(n,m,E) - t g_0^r(n,0,E) g^r(1,m,E) - t g_0^r(n,1,E) g^r(0,m,E) \end{aligned} \tag{II.53}$$

If we are interested only on the right hand side of the chain:

$$n, m \geq 1 \longrightarrow g^r(0,m,E) = 0$$

The amplitude of probability for going from one point at the right hand side of the cut to the last site on the left hand side (site 0) is zero. We have:

$$g^r(n,m,E) = g_0^r(n,m,E) - t g_0^r(n,0,E) g^r(1,m,E)$$

$$\begin{aligned} g^r(1,m,E) &= g_0^r(1,m,E) - t g_0^r(1,0,E) g^r(1,m,E) \\ &\longrightarrow [1 + t g_0^r(1,0,E)] g^r(1,m,E) = g_0^r(1,m,E) \\ &\longrightarrow g^r(1,m,E) = \frac{g_0^r(1,m,E)}{1 + t g_0^r(1,0,E)} \end{aligned}$$

$$\boxed{g^r(n,m,E) = g_0^r(n,m,E) - \frac{t g_0^r(n,0,E) g_0^r(1,m,E)}{1 + t g_0^r(1,0,E)}} \tag{II.54}$$

Or in matrix form in spin space:

$$\boxed{\hat{g}^r(n,m) = \hat{g}_0^r(n,m) - t \hat{g}_0^r(n,0)[\hat{I} + t g_0^r(1,0)]^{-1} \hat{g}_0^r(1,m)} \tag{II.55}$$

For this formula to be valid, n and m must be ≥ 1: the first site on the right hand side

of the chain is site number one.
If we are interested only on the left hand side of the chain:

$$n, m \leq 0 \longrightarrow g^r(1, m, E) = 0$$

$$g^r(n, m, E) = g_0^r(n, m, E) - t g_0^r(n, 1, E) g^r(0, m, E)$$

In all the calculations for the tunnel barrier, the only correlation function needed in the left lead is the surface Green's function on the last site: $g^r_{\alpha\alpha}$. If the convention of the cut between sites 0 and 1 is kept: $g^r_{\alpha\alpha} = g^r_{00}$.

$$g^r_{\alpha\alpha} = g^r(0, 0, E) = g_0^r(0, 0, E) - t g_0^r(0, 1, E) g^r(0, 0, E)$$

$$\boxed{g^r_{\alpha\alpha} = g^r(0, 0, E) = \frac{g_0^r(0, 0, E)}{1 + t g_0^r(0, 1, E)}} \tag{II.56}$$

Or in matrix form in spin space:

$$\boxed{\hat{g}^r_{\alpha\alpha} = [\hat{I} + t g_0^r(0, 1, E)]^{-1} \hat{g}_0^r(0, 0, E)} \tag{II.57}$$

II.5.1 Local density of states in a semi-infinite ferrimagnetic chain

Fig. II.6 shows the spin-resolved energy dependence of the right FI lead LDOS (proportional to the imaginary part of the retarded Green's function) for the five sites next to the right barrier interface. An AF lead exhibit the same LDOS, but majority and minority bands are not split. However, the different profiles of majority and minority LDOS at the B/AF interface might be the origin of spin polarization of AF leads; it will be discussed in the next chapter.

The imaginary part of the surface Green's function at the first site of the right lead is plotted on the top panel of Fig. II.6. The LDOS for up spins in a given site is symmetric to the LDOS for down spins when it is shifted to lower energies by $\delta = \Delta_A - \Delta_B$.

Note that the LDOS in Fig. II.6 approaches the bulk value (corresponding to the infinite chain) shown in Fig. II.4 as the site considered gets further away from the right barrier interface. The LDOS converges to the bulk value in an oscillatory way. This is more clearly illustrated in Fig. II.7, where the LDOS of the first site in an infinite chain (bulk) and sites 15 and 101 in a semi-infinite chain are plotted as a function of energy. The behaviour of these oscillations around the Fermi level is used as a first attempt to explain the theoretical results that will be presented in the next chapter.

By way of comparison, the LDOS for the limiting case of a F semi-infinite chain is shown in Fig. II.8.

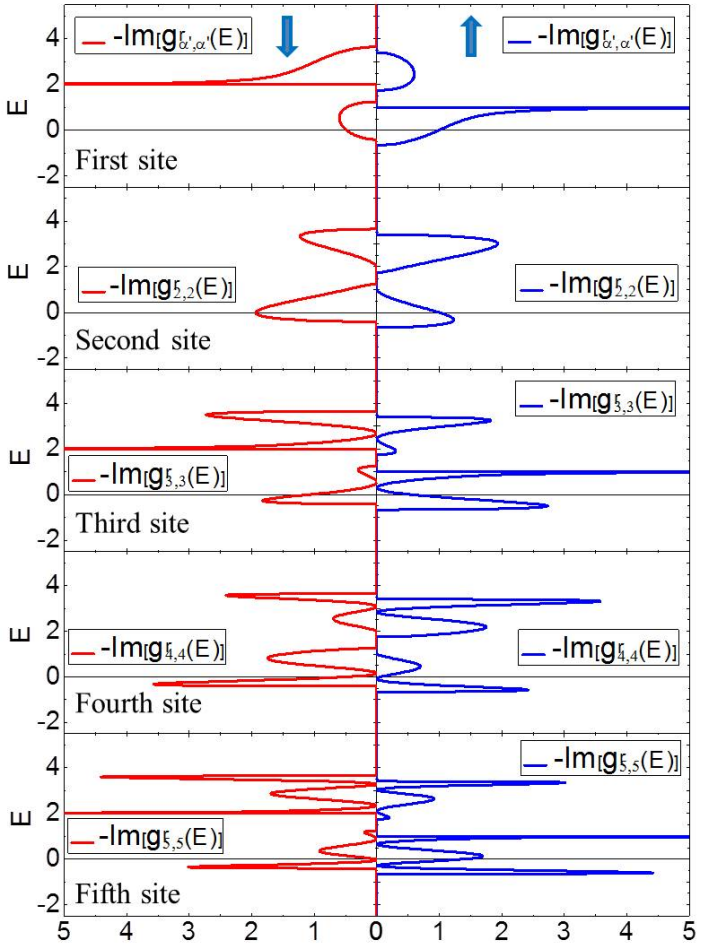

Figure II.6 – Imaginary part of the on-site retarded Green's function (LDOS) for a semi-infinite FI chain (Bethe lattice) with $\Delta_A = 0.5eV$, $\Delta_B = 0.25eV$ and $t = -1eV$. Blue(red) lines are for up(down) spins α' corresponds to the first site of the right lead in contact with the barrier. Odd (even) subscripts correspond to the sublattice A(B). The horizontal lines at 0 eV represent the Fermi level at equilibrium (when no voltage is applied).

As in the infinite case, the LDOS for up and down spins in a given site are just shifted, and they are symmetric with respect to the center of the single band. These LDOS approach the bulk value shown in Fig. II.5 in an oscillatory way as well.

Change of quantization axis

To take into account the angle θ between the magnetizations in the left and right leads, the surface Green's function $\hat{g}^r_{\alpha\alpha}$ must be rotated in spin space.
The matrix of a spin rotation around an axis given by the unitary vector $\mathbf{n}$ is:

$$\hat{U}_R(\mathbf{n}, \theta) = \hat{I}cos(\theta/2) - i(\mathbf{n} \cdot \hat{\sigma})sin(\theta/2)$$

In the case where $\mathbf{n} = \mathbf{j}$:

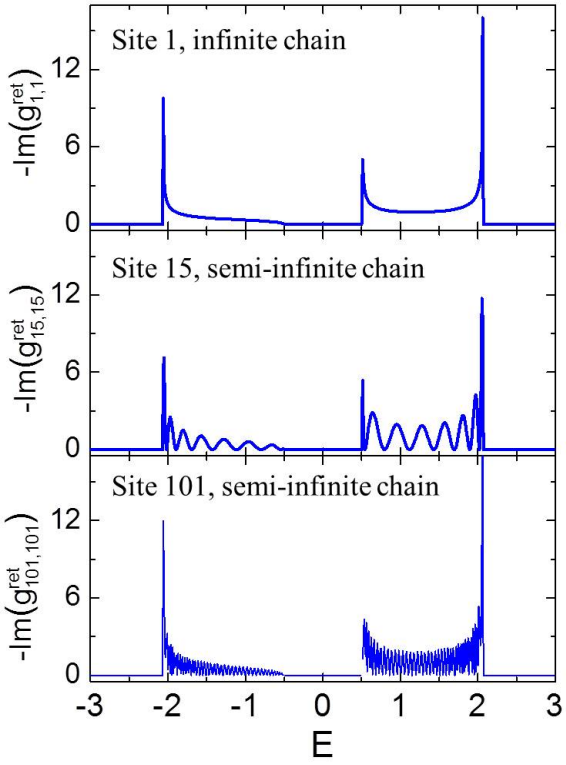

Figure II.7 – Imaginary part of the on-site retarded Green's function (LDOS) for down spin in an infinite FI chain at site 1 (top panel). Idem for a semi-infinite chain at sites 15 and 101 (middle and bottom panels).

$$\hat{U}_R(\theta) = \begin{pmatrix} cos(\theta/2) & -sin(\theta/2) \\ sin(\theta/2) & cos(\theta/2) \end{pmatrix}$$

The surface Green's function at the left lead then becomes:

$$\hat{g}'_{\alpha\alpha} = \hat{U}_R \cdot \hat{g}_{\alpha\alpha} \cdot \hat{U}_R^H = \begin{pmatrix} cos(\theta/2) & -sin(\theta/2) \\ sin(\theta/2) & cos(\theta/2) \end{pmatrix} \cdot \begin{pmatrix} g_{\alpha\alpha}^{\uparrow\uparrow} & 0 \\ 0 & g_{\alpha\alpha}^{\downarrow\downarrow} \end{pmatrix} \cdot \begin{pmatrix} cos(\theta/2) & sin(\theta/2) \\ -sin(\theta/2) & cos(\theta/2) \end{pmatrix}$$

$$\hat{g}'_{\alpha\alpha} = \begin{pmatrix} g_{\alpha\alpha}^{\uparrow\uparrow} cos^2(\theta/2) + g_{\alpha\alpha}^{\downarrow\downarrow} sin^2(\theta/2) & \frac{1}{2} sin(\theta)(g_{\alpha\alpha}^{\uparrow\uparrow} - g_{\alpha\alpha}^{\downarrow\downarrow}) \\ \frac{1}{2} sin(\theta)(g_{\alpha\alpha}^{\uparrow\uparrow} - g_{\alpha\alpha}^{\downarrow\downarrow}) & g_{\alpha\alpha}^{\uparrow\uparrow} sin^2(\theta/2) + g_{\alpha\alpha}^{\downarrow\downarrow} cos^2(\theta/2) \end{pmatrix}$$

Calculation of the retarded Green's function for a semi-infinite chain hosting one or two magnetic impurities

The Green's functions calculated above describe perfectly periodic magnetic chains. They can thus be used to model magnetic tunnel junctions with ideal epitaxially grown crystalline structures, in the absence of defects. The specific effect of the natural disorder usually encountered in actual polycrystalline junctions is therefore neglected. A first ap-

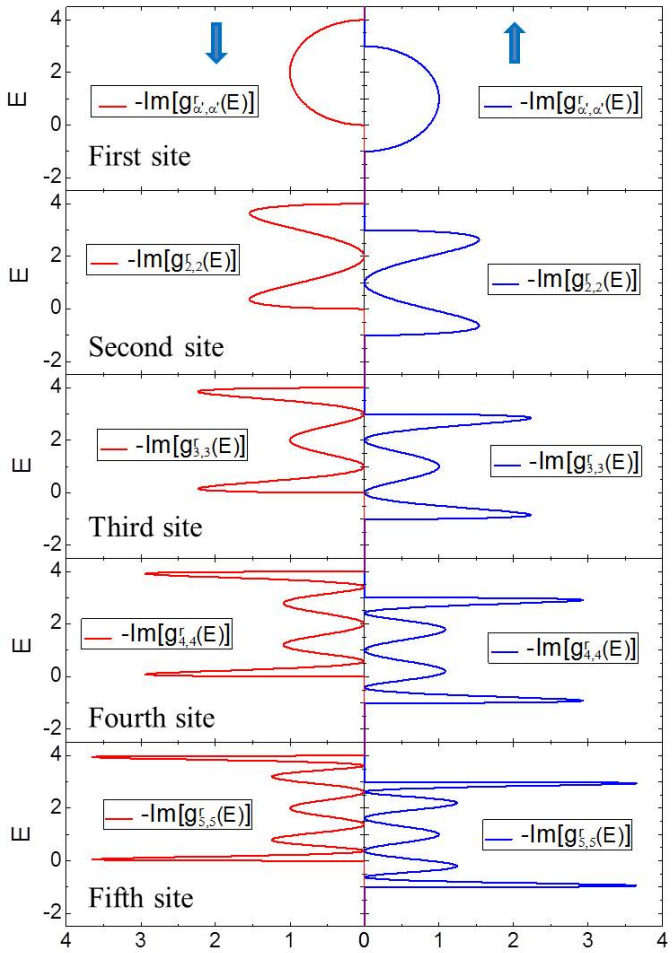

Figure II.8 – Imaginary part of the on-site retarded Green's function (LDOS) for a semi-infinite F chain with $\Delta = 0.5eV$ and $t = -1eV$. Blue(red) lines are for up(down) spins. α' corresponds to the first site of the right lead in contact with the barrier.

proach to analyse the effects of disorder is considering the presence of a given number of magnetic impurities with a specific spatial distribution, which break the former periodicity. These magnetic impurities might be present as a result of conventional sputtering deposition processes. Although this analysis was eventually not pursued, the results of the calculations for one and two magnetic impurities in the right lead are described below to be considered for future work.

Once the retarded Green's function of the semi-infinite right lead is calculated, it can be used to compute the retarded Green's function of a right lead hosting a substitutional magnetic impurity on a generic site l. For doing so, the Hamiltonian is split again into two parts:

$$\hat{H} = \hat{H}_0 + \hat{V}$$

where:

$\hat{H}$: Hamiltonian for a semi infinite chain with one magnetic impurity

$\hat{H}_0$: Hamiltonian for the pure semi infinite chain

$\hat{V}$: Perturbation due to a magnetic impurity on site l

In spin space:

$$\hat{V} = |l\rangle\, \hat{\epsilon}\, \langle l| = |l\rangle \begin{pmatrix} \epsilon_{\text{imp}}^{\uparrow} & 0 \\ 0 & \epsilon_{\text{imp}}^{\downarrow} \end{pmatrix} \langle l|$$

Here, $\epsilon_{\text{imp}}^{\uparrow}$ ($\epsilon_{\text{imp}}^{\downarrow}$) is the difference in energy of an itinerant spin up(down) at site l with and without the magnetic impurity. The Dyson equation for the perturbed Hamiltonian then reads: $\hat{g}^r = \hat{g}_0^r + \hat{g}_0^r \hat{V} \hat{g}^r$. $\hat{g}^r$ is the retarded Green's function corresponding to $\hat{H}$ (semi-infinite chain with a magnetic impurity on site l) and $\hat{g}_0^r$ is the retarded Green's function corresponding to $\hat{H}_0$ (semi-infinite chain without magnetic impurity).

Projecting the Dyson equation on sites n and m inside the right lead ($n, m \geq 1$) gives:

$$\hat{g}^r(n,m) = \hat{g}_0^r(n,m) + \sum_{i,j} \hat{g}_0^r(n,i) V(i,j) \hat{g}^r(j,m)$$

where the matrix elements of the perturbation in the TB basis are: $V(i,j) = \langle i|\, \hat{V}\, |j\rangle = \langle i|l\rangle \hat{\epsilon} \langle l|j\rangle = \delta_{i,l}\delta_{j,l}\hat{\epsilon}$. The Dyson equation then reads:

$$\begin{aligned} \hat{g}^r(n,m) &= \hat{g}_0^r(n,m) + \sum_{i,j} \hat{g}_0^r(n,i)\delta_{i,l}\delta_{j,l}\hat{\epsilon}\hat{g}^r(j,m) \\ &= \hat{g}_0^r(n,m) + \hat{g}_0^r(n,l)\hat{\epsilon}\hat{g}^r(l,m) \end{aligned}$$

$$\begin{aligned} \hat{g}^r(l,m) &= \hat{g}_0^r(l,m) + \hat{g}_0^r(l,l)\hat{\epsilon}\hat{g}^r(l,m) \\ &\longrightarrow [\hat{I} - \hat{g}_0^r(l,l)\hat{\epsilon}]\hat{g}^r(l,m) = \hat{g}_0^r(l,m) \\ &\longrightarrow \hat{g}^r(l,m) = [\hat{I} - \hat{g}_0^r(l,l)\hat{\epsilon}]^{-1}\hat{g}_0^r(l,m) \end{aligned}$$

$$\hat{g}^r(n,m) = \hat{g}_0^r(n,m) + \hat{g}_0^r(n,l)\hat{\epsilon}[\hat{I} - \hat{g}_0^r(l,l)\hat{\epsilon}]^{-1}\hat{g}_0^r(l,m) \tag{II.58}$$

The calculation of the retarded Green's function for a semi-infinite chain hosting two magnetic impurities is straight forward: considering the retarded Green's function $\hat{g}_0^r$ corresponding to one magnetic impurity at site l, a Dyson equation can be used to get the retarded Green's function corresponding to two magnetic impurities located at sites l and p, $\hat{g}^r$:

$$\hat{g}^r(n,m) = \hat{g}_0^r(n,m) + \hat{g}_0^r(n,p)\hat{\epsilon}'[\hat{I} - \hat{g}_0^r(p,p)\hat{\epsilon}']^{-1}\hat{g}_0^r(p,m) \tag{II.59}$$

where $\hat{\epsilon}'$ is the matrix of energy differences for an itinerant spin at site p with and without

the second impurity.

II.6 Dispersion relation for a one dimensional ferrimagnet

The electron motion inside the junction depicted in Fig. II.1 can be viewed as a scattering problem of electrons going out and coming into the left and right electrodes. As long as coherent transport is considered, the conservation of the transverse wave vector allows to ignore in a first step the dimensions perpendicular to the transport direction, reducing the calculations to a 1-D problem. In addition, the probability for an electron to travel through the barrier depends on its Fermi wave vector [Slonczewski, 1995], [Tsymbal et al., 2003]. This Fermi wave vector is different for up and down spins in F and FI materials, since majority and minority bands are spin split. As a consequence, their different tunnelling probabilities result in an imbalance of electric current carried by up and down spins, which is precisely at the origin of TMR. In particular, one of the assumptions made by Julliere [Julliere, 1975] was that the conductance of a spin channel was proportional to the product of the two DOS at the Fermi energy in the F electrodes. It is therefore important to study the scattering states characterized by the wave vector k_y parallel to the y direction through the dispersion relations and total DOS in the leads of the tunnel junction. Some important results of the next chapter are directly related to the features displayed by the dispersion relations of F, AF and FI chains. Let's start with the calculation of the dispersion relation for the general case of a FI chain.

As explained above, a FI can be considered as an alternating chain composed of two types of site per unit cell (on-site energies ϵ_A and ϵ_B) which are coupled by the hopping parameter t. Within the tight-binding approximation, the 1-D Hamiltonian for a given itinerant spin-reads:

$$\hat{H} = \sum_{n=-\infty}^{+\infty} (\epsilon_A |n, A\rangle \langle n, A| + \epsilon_B |n, B\rangle \langle n, B|) + \sum_{n=-\infty}^{+\infty} (t |n, A\rangle \langle n, B| + t |n, B\rangle \langle n+1, A| + H.c.)$$

or, in second quantized form:

$$\hat{H} = \sum_{n=-\infty}^{+\infty} (\epsilon_A \hat{a}_n^\dagger \hat{a}_n + \epsilon_B \hat{b}_n^\dagger \hat{b}_n) + \sum_{n=-\infty}^{+\infty} (t\hat{a}_n^\dagger \hat{b}_n + t\hat{a}_{n+1}^\dagger \hat{b}_n + H.c.)$$

where n is the cell index and $\hat{a}$ ($\hat{b}$) is the anihilation operator of one electron on a site A (B).
Since we are dealing with a periodic system, we can take the lattice Fourier transform of the Hamiltonian to pass from the site representation to the momentum representation,

using the usual convention: $\hat{a}_n = \sum_{k \in FBZ} e^{ikna}\hat{a}_k$ (a being the lattice constant):

$$\sum_n \hat{a}_n^\dagger \hat{a}_n = \sum_{n,k,k'} e^{-ikna}\hat{a}_k^\dagger e^{ik'na}\hat{a}_{k'} = \sum_{k,k'} \hat{a}_k^\dagger \hat{a}_{k'} \sum_n e^{i(k'-k)na} = \sum_{k,k'} \hat{a}_k^\dagger \hat{a}_{k'} N\delta_{k,k'} = N\sum_k \hat{a}_k^\dagger \hat{a}_k$$

$$\sum_n \hat{a}_n^\dagger \hat{b}_n = N\sum_k \hat{a}_k^\dagger \hat{b}_k$$

$$\sum_n \hat{a}_{n+1}^\dagger \hat{b}_n = \sum_{n,k,k'} e^{-ik(n+1)a}\hat{a}_k^\dagger e^{ik'na}\hat{b}_k = N\sum_k e^{-ika}\hat{a}_k^\dagger \hat{b}_k$$

The Hamiltonian then reads:

$$\hat{H} = \epsilon_A \sum_k \hat{a}_k^\dagger \hat{a}_k + \epsilon_B \sum_k \hat{b}_k^\dagger \hat{b}_k + t\sum_k [(1+e^{-iak})\hat{a}_k^\dagger \hat{b}_k + H.c.]$$

with $k \in [-\pi/a, \pi/a]$, a being the lattice constant.

This Hamiltonian is not diagonal yet, since it mixes $\hat{a}$ and $\hat{b}$ operators; we obtain a simpler 2×2 eigensystem projecting it on the basis $\{|k,A\rangle ; |k,B\rangle\}$:

$$\begin{pmatrix} \langle k,A|\hat{H}|k,A\rangle & \langle k,A|\hat{H}|k,B\rangle \\ \langle k,B|\hat{H}|k,A\rangle & \langle k,B|\hat{H}|k,B\rangle \end{pmatrix} \cdot \begin{pmatrix} |k,A\rangle \\ |k,B\rangle \end{pmatrix} = E(k) \begin{pmatrix} |k,A\rangle \\ |k,B\rangle \end{pmatrix}$$

The secular equation then reads:

$$\begin{vmatrix} \epsilon_A - E(k) & t(1+e^{ika}) \\ t(1+e^{-ika}) & \epsilon_B - E(k) \end{vmatrix} = 0$$

which gives the dispersion relation:

$$E(k) = \frac{\epsilon_A + \epsilon_B}{2} \pm \sqrt{\left(\frac{\epsilon_A - \epsilon_B}{2}\right)^2 + 4t^2 cos^2(ka/2)} \tag{II.60}$$

The sign - designs the lower band and the sign + the upper band. For a linear chain with A sites hosting localised up spins, the on-site spin-dependent energies can be split as:

$$\epsilon_{\lambda'}^{\uparrow(\downarrow)} = \begin{cases} \epsilon_A^{\uparrow(\downarrow)} = \epsilon_0 - (+)\Delta_A \\ \epsilon_B^{\uparrow(\downarrow)} = \epsilon_0 + (-)\Delta_B \end{cases}$$

Where ϵ_0 is the spin-independent s-orbital energy of the itinerant spins. With this convention, the spin-resolved dispersion relation is:

$$E^\uparrow(k) = \epsilon_0 - \frac{\delta}{2} \pm \sqrt{\left(\frac{\Delta_A + \Delta_B}{2}\right)^2 + 4t^2 cos^2(ka/2)} \tag{II.61}$$

$$E^{\downarrow}(k) = \epsilon_0 + \frac{\delta}{2} \pm \sqrt{\left(\frac{\Delta_A + \Delta_B}{2}\right)^2 + 4t^2 cos^2(ka/2)} \tag{II.62}$$

Majority and minority bands are thus split by δ and the band edges for up-spins are, in ascending order: $E_2^{\uparrow(\downarrow)}$, $\epsilon_A^{\uparrow}(\epsilon_B^{\downarrow})$, $\epsilon_B^{\uparrow}(\epsilon_B^{\downarrow})$, and $E_1^{\uparrow(\downarrow)}$, where

$$E_1^{\uparrow(\downarrow)} = \frac{\epsilon_A^{\uparrow(\downarrow)} + \epsilon_B^{\uparrow(\downarrow)}}{2} + \sqrt{\left(\frac{\epsilon_A^{\uparrow(\downarrow)} - \epsilon_B^{\uparrow(\downarrow)}}{2}\right)^2 + 4t^2}$$

$$E_2^{\uparrow(\downarrow)} = \frac{\epsilon_A^{\uparrow(\downarrow)} + \epsilon_B^{\uparrow(\downarrow)}}{2} - \sqrt{\left(\frac{\epsilon_A^{\uparrow(\downarrow)} - \epsilon_B^{\uparrow(\downarrow)}}{2}\right)^2 + 4t^2}$$

The bandgap is therefore: $B = \Delta_A + \Delta_B$, which is also consistent with the results of section II.4.

Fig. II.9 shows the dispersion relations (II.61) and (II.62), for up and down spins respectively split by the parameter δ. The Fermi wave vectors for up and down spins are thus different.

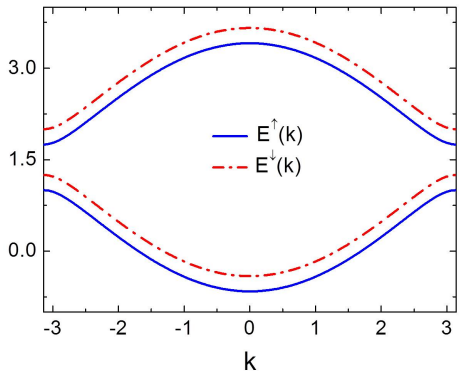

Figure II.9 – Spin-resolved dispersion relation within the FBZ for a 1-D FI with ϵ_0= 1.5 eV, Δ_A= 0.5 eV, Δ_B= 0.25 eV and t= -1 eV. The wave vector k is in 1/a units.

The density of k-states as a function of energy can be calculated directly from the dispersion relation:

$$DOS^{\uparrow(\downarrow)}(E) = \left.\frac{dk}{\pi dE}\right|_E =$$

$$\begin{cases} \dfrac{-(2E-\epsilon_A^{\uparrow(\downarrow)}-\epsilon_B^{\uparrow(\downarrow)})}{\pi a(E-\epsilon_A^{\uparrow(\downarrow)})(E-\epsilon_B^{\uparrow(\downarrow)})\sqrt{\dfrac{4t^2}{(E-\epsilon_A^{\uparrow(\downarrow)})(E-\epsilon_B^{\uparrow(\downarrow)})}-1}} & \text{if } E_2^{\uparrow(\downarrow)} < E < \epsilon_A^{\uparrow}(\epsilon_B^{\downarrow}) \text{ (lower band)} \\ \dfrac{2E-\epsilon_A^{\uparrow(\downarrow)}-\epsilon_B^{\uparrow(\downarrow)}}{\pi a(E-\epsilon_A^{\uparrow(\downarrow)})(E-\epsilon_B^{\uparrow(\downarrow)})\sqrt{\dfrac{4t^2}{(E-\epsilon_A^{\uparrow(\downarrow)})(E-\epsilon_B^{\uparrow(\downarrow)})}-1}} & \text{if } \epsilon_B^{\uparrow}(\epsilon_A^{\downarrow}) < E < E_1^{\uparrow(\downarrow)} \text{ (upper band)} \end{cases}$$

The factor $\frac{1}{\pi}$ comes from the normalization $\int dE DOS(E) = 1$.

As can be seen in Fig. II.10, the divergences of the 1-D FI DOS at the band edges are due to the vanishing derivative of the dispersion relation (II.60) at the center and at the edges of the FBZ. This DOS is the one shown at the bottom of Fig. II.1.

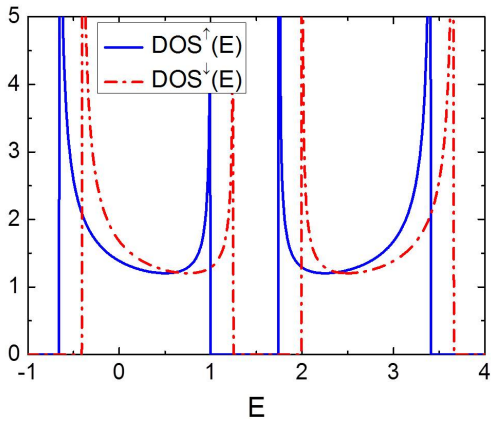

Figure II.10 – Spin-resolved DOS for a 1-D FI with ϵ_0= 1.5 eV, Δ_A= 0.5 eV, Δ_B= 0.25 eV and t= -1 eV.

In contrast to the LDOS, the total spin-resolved DOS for the scattering k states is symmetric with respect to the center of the gap.

II.6.1 Limiting case: antiferromagnetic chain

In the case of an AF chain, the opposite magnetic moments are equal, so that: $\Delta_A = \Delta_B = \Delta$ $\epsilon_A^{\uparrow} = \epsilon_B^{\downarrow}$, $\epsilon_A^{\downarrow} = \epsilon_B^{\uparrow}$, $B = 2 \cdot \Delta$ and $\delta = 0$ (majority and minority bands are no longer split because there is no macroscopic magnetization). The dispersion relation and DOS become:

$$E^{\uparrow}(k) = E^{\downarrow}(k) = \epsilon_0 \pm \sqrt{\Delta^2 + 4t^2 cos^2(ka/2)} \tag{II.63}$$

$$DOS^{\sigma}(E) = \begin{cases} \dfrac{-(2E-\epsilon_A^{\sigma}-\epsilon_B^{\sigma})}{\pi a(E-\epsilon_A^{\sigma})(E-\epsilon_B^{\sigma})\sqrt{\dfrac{4t^2}{(E-\epsilon_A^{\sigma})(E-\epsilon_B^{\sigma})}-1}} & \text{if } E_2^{\sigma} < E < \epsilon_A^{\uparrow}(\epsilon_B^{\downarrow}) \text{ (lower band)} \\ \dfrac{2E-\epsilon_A^{\sigma}-\epsilon_B^{\sigma}}{\pi a(E-\epsilon_A^{\sigma})(E-\epsilon_B^{\sigma})\sqrt{\dfrac{4t^2}{(E-\epsilon_A^{\sigma})(E-\epsilon_B^{\sigma})}-1}} & \text{if } \epsilon_B^{\uparrow}(\epsilon_A^{\downarrow}) < E < E_1^{\sigma} \text{ (upper band)} \end{cases}$$

Figs. II.11 and II.12 show that the dispersion relation and DOS for an AF chain are the same as those of a FI, however, majority and minority bands are no longer split since there is no macroscopic magnetization.

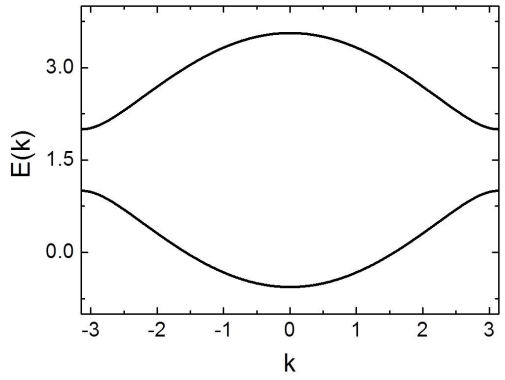

Figure II.11 – Dispersion relation within the FBZ for a 1-D AF with ϵ_0= 1.5 eV, Δ= 0.5 eV and t= -1 eV. The wave vector k is in 1/a units.

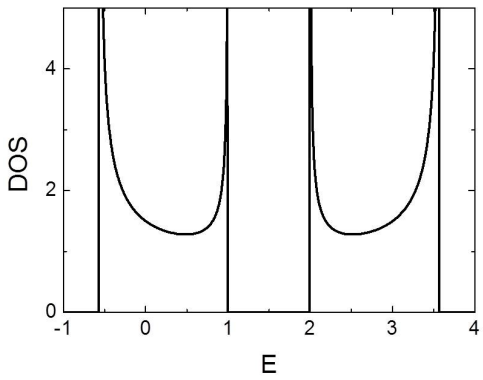

Figure II.12 – DOS for a 1-D AF with ϵ_0= 1.5 eV, Δ= 0.5 eV and t= -1 eV.

The Fermi wave vectors for up and down spins coincide in this case.

II.6.2 Limiting case: ferromagnetic chain

If all the localised moments are equal and point in the same direction, a ferromagnetic order is established. There is only one sublattice, and the energy for a given spin is constant and site-independent:

$$\epsilon^{\uparrow(\downarrow)} = \epsilon_0 - (+)\Delta$$

The dispersion relation and DOS become:

$$E^{\uparrow}(k) = \epsilon_0 - \Delta + 2tcos(ka) \tag{II.64}$$

$$E^{\downarrow}(k) = \epsilon_0 + \Delta + 2tcos(ka) \tag{II.65}$$

$$DOS^{\uparrow(\downarrow)}(E) = -\frac{1}{2\pi at}\frac{1}{\sqrt{1-\left(\frac{E-(\epsilon_0-(+)\Delta)}{2t}\right)^2}}$$

As shown in Figs. II.13 and II.14, lower and upper FI/AF sub-bands for a given spin merge into a symmetric single band. Majority and minority bands are also split.

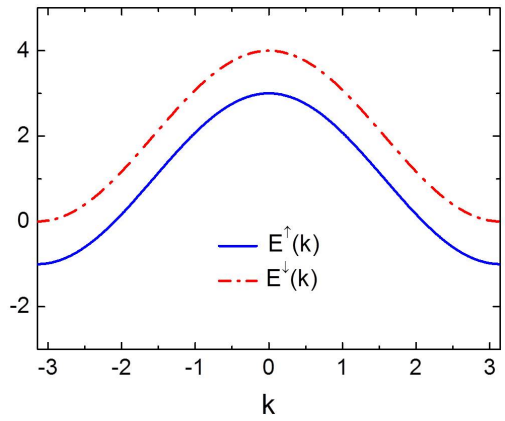

Figure II.13 – Spin-resolved dispersion relation within the FBZ for a 1-D F with ϵ_0= 1.5 eV, Δ= 0.5 eV and t= -1 eV. The wave vector k is in 1/a units.

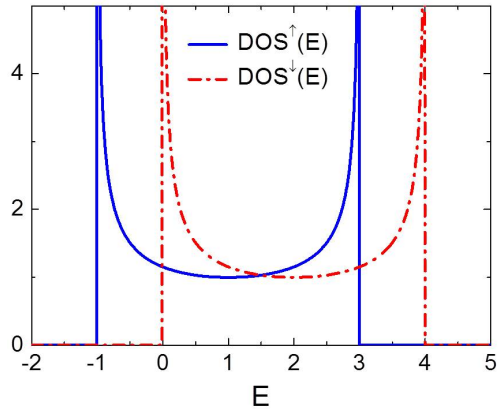

Figure II.14 – Spin-resolved DOS for a 1-D F with ϵ_0= 1.5 eV, Δ= 0.5 eV and t= -1 eV.

Similar to the FI case, the macroscopic magnetisation of the F chain differentiate the Fermi wave vectors for up and down spins, since they do not experience the same potential inside the magnetic leads.

II.7 Dispersion relations for 2-D square lattices of compensated spins

An AF material can be modelled as a chain of parallel 2-D planes of uncompensated spins pointing in the same direction in each of the planes, but alternating orientation from one plane to the next one. Alternatively, "pure compensated" AF materials can be modelled as a chain of compensated planes in which the net magnetization of each plane vanishes see Fig. II.15. In this section I propose a method to adapt the theory previously developed to this particular case. This method is based on the modification of the dispersion relation $\epsilon_{\mathbf{k}_\parallel}$ of the Bloch states according to the new in-plane magnetic configuration of localized moments. Preliminary theoretical results for this kind of systems are included in the next chapter.

Underlying the ballistic approach considered here, that is, momentum conservation in the plane of the layers ($\mathbf{k}_\parallel$), is the assumption that these planes are translational invariant.

The specific configuration of localized atoms distributed periodically on each of the planes determines the 2-D dispersion relation that must be used in coherent-based theoretical calculations, as explained in section II.1.1. A number of works on spin dependent transport in spin valves and magnetic tunnel junctions [Kalitsov et al., 2009],[Theodonis et al., 2006], [Kalitsov et al., 2006],[Núñez et al., 2006] are based in the simple in-plane spin configuration shown in Fig. II.15 a). This spin configuration constitutes a square Bravais lattice of uncompensated spins that gives rise to the commonly used TB 2-D dispersion relation depicted in Fig. II.16-a) [Economou, 2006]:

$$\epsilon_{\mathbf{k}_\parallel} = \epsilon_0 + 2t[cos(k_x a) + cos(k_z a)] \tag{II.66}$$

where ϵ_0 is the on-site energy on the plane. A successive parallel disposition of these planes constitutes the model for a ferromagnetically ordered lead (spins might be rotated by an angle θ, but the on-site energy ϵ_0 is the same in every plane for a given itinerant spin). In turn, the antiferromagnetic order can be modelled in different ways. One of them is considering an alternating disposition of uncompensated planes where each of them lies between two planes rotated 180°. The macroscopic magnetization is zero since the magnetization of a layer of uncompensated spins is compensated by the next one. An itinerant spin will successively encounter alternating uncompensated planes, so that its on-site energy will be layer-dependent. Another way to model AF order is considering a lead built up with parallel planes of compensated spins, as the one depicted in Fig. II.15 b). In this case, there exist two different on-site energies for a given spin on the same plane, ϵ_1 and ϵ_2, corresponding to the sites hosting up and down localized spins in the square Bravais lattice.

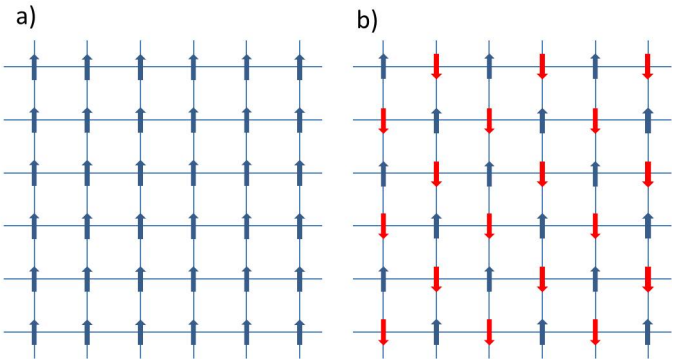

Figure II.15 – a) Bravais square lattice of uncompensated spins on a plane perpendicular to transport. b) Bravais lattice of compensated spins on a plane perpendicular to transport. The lattice parameter is a in both cases

This configuration would be closer to reality for instance in $IrMn_3$ FCC crystal lattice structures, which are deposited in the $(1,1,1)$ direction. In these structures, the close-packed plane is in turn the $(1,1,1)$ plane, which is formed of compensated spins [Srinivasan et al., 2008].

Consequently, the dispersion relation in Eq. (II.66) must be recalculated for these compensated planes, as described in the next section. In addition to the replacement of Eq. (II.66) by the new dispersion relation in all the calculations, the integration in $\mathbf{k}_{\parallel}$ space will now take place in a different Brillouin zone, according to the new reciprocal vectors of the direct lattice shown in Fig. II.15 b).

The two sub-lattices of up and down localized spins in Fig. II.15 b) are generated by the two families of direct lattice vectors $\{\mathbf{R}_1\}$ and $\{\mathbf{R}_2\}$. Any vector owning to one of these families can be expanded as a linear combination of the following primitive vectors:

$$\mathbf{a_1} = a(\mathbf{e}_1 + \mathbf{e}_3), \quad \mathbf{a_2} = a(\mathbf{e}_1 - \mathbf{e}_3)$$

They give rise to the following new reciprocal vectors:

$$\mathbf{b_1} = \frac{\pi}{a}(\mathbf{e}_1 + \mathbf{e}_3), \quad \mathbf{b_2} = \frac{\pi}{a}(\mathbf{e}_1 - \mathbf{e}_3)$$

Two linear combinations of atomic-like orbitals centred on each of the two sub-lattices $\Phi(\mathbf{r} - \mathbf{R_i})$ are used as basis of the in-plane Bloch states:

$$|\Psi^1_{\mathbf{k}}\rangle = \frac{1}{\sqrt{N}} \sum_{\mathbf{R_1}} e^{i\mathbf{k}\cdot\mathbf{R_1}} |\Phi(\mathbf{r} - \mathbf{R_1})\rangle$$

$$|\Psi^2_{\mathbf{k}}\rangle = \frac{1}{\sqrt{N}} \sum_{\mathbf{R_2}} e^{i\mathbf{k}\cdot\mathbf{R_2}} |\Phi(\mathbf{r} - \mathbf{R_2})\rangle$$

where, N is the number of unit cells of each of the sub-lattices.

Any Bloch state in the 2-D periodic lattice can be expressed as a linear combination of these basis Bloch functions:

$$|\Psi_{\mathbf{k}}\rangle = \alpha_{\mathbf{k}} |\Psi^1_{\mathbf{k}}\rangle + \beta_{\mathbf{k}} |\Psi^2_{\mathbf{k}}\rangle$$

By definition, the Bloch states are eigenstates of the periodic 2-D Hamiltonian:

$$\hat{H} |\Psi_{\mathbf{k}}\rangle = \epsilon_{\mathbf{k}_{\parallel}} |\Psi_{\mathbf{k}}\rangle$$

This equation can be arranged in a matrix form considering a 2-D space spanned by the two basis Bloch functions above:

$$\begin{pmatrix} H_{11} & H_{12} \\ H_{21} & H_{22} \end{pmatrix} \cdot \begin{pmatrix} \alpha_{\mathbf{k}} \\ \beta_{\mathbf{k}} \end{pmatrix} = \epsilon_{\mathbf{k}_{\parallel}} \cdot \begin{pmatrix} \alpha_{\mathbf{k}} \\ \beta_{\mathbf{k}} \end{pmatrix}$$

where the matrix elements are defined as the projections of the Hamiltonian into the Bloch basis: $H_{i,j} = \langle \Psi^i_{\mathbf{k}} | \hat{H} | \Psi^j_{\mathbf{k}} \rangle$. For this eigenvalue problem to have a solution the secular equation must be satisfied:

$$\begin{vmatrix} H_{11} - \epsilon_{\mathbf{k}_\parallel} & H_{12} \\ H_{21} & H_{22} - \epsilon_{\mathbf{k}_\parallel} \end{vmatrix} = 0$$

Considering an atomic function overlap with nearest neighbours only, the following relations hold:

$$\langle \Phi(\mathbf{R_1}) | \hat{H} | \Phi(\mathbf{R'_1}) \rangle = \epsilon_1 \delta_{\mathbf{R_1},\mathbf{R'_1}}$$

$$\langle \Phi(\mathbf{R_2}) | \hat{H} | \Phi(\mathbf{R'_2}) \rangle = \epsilon_1 \delta_{\mathbf{R_2},\mathbf{R'_2}}$$

$$\langle \Phi(\mathbf{R_1}) | \hat{H} | \Phi(\mathbf{R_2}) \rangle = t \neq 0 \text{ only if}$$

$$\mathbf{R_2} = \mathbf{R_1} + a\mathbf{e}_1; \;\; \mathbf{R_2} = \mathbf{R_1} - a\mathbf{e}_3; \;\; \mathbf{R_2} = \mathbf{R_1} - a\mathbf{e}_1; \;\; \mathbf{R_2} = \mathbf{R_1} + a\mathbf{e}_3$$

The matrix elements are thus greatly simplified:

$$H_{11} = \langle \Psi^1_{\mathbf{k}} | \hat{H} | \Psi^1_{\mathbf{k}} \rangle = \frac{1}{N} \sum_{\mathbf{R_1},\mathbf{R'_1}} e^{-i\mathbf{k}\cdot\mathbf{R_1}} e^{i\mathbf{k}\cdot\mathbf{R'_1}} \langle \Phi(\mathbf{R_1}) | \hat{H} | \Phi(\mathbf{R'_1}) \rangle = \frac{\epsilon_1}{N} \sum_{\mathbf{R_1},\mathbf{R'_1}} e^{-i\mathbf{k}\cdot(\mathbf{R_1}-\mathbf{R'_1})} \delta_{\mathbf{R_1},\mathbf{R'_1}} = \epsilon_1$$

$$H_{22} = \epsilon_2$$

$$H_{12} = \langle \Psi^1_{\mathbf{k}} | \hat{H} | \Psi^2_{\mathbf{k}} \rangle = \frac{1}{N} \sum_{\mathbf{R_1},\mathbf{R_2}} e^{-i\mathbf{k}\cdot\mathbf{R_1}} e^{i\mathbf{k}\cdot\mathbf{R_2}} \langle \Phi(\mathbf{R_1}) | \hat{H} | \Phi(\mathbf{R_2}) \rangle$$

$$\begin{aligned} \langle \Psi^1_{\mathbf{k}} | \hat{H} | \Psi^2_{\mathbf{k}} \rangle &= \frac{t}{N} \sum_{\mathbf{R_1}} e^{-i\mathbf{k}\cdot\mathbf{R_1}} [e^{i\mathbf{k}\cdot(\mathbf{R_1}+a\mathbf{e}_1)} + e^{i\mathbf{k}\cdot(\mathbf{R_1}-a\mathbf{e}_3)} + e^{i\mathbf{k}\cdot(\mathbf{R_1}-a\mathbf{e}_1)} + e^{i\mathbf{k}\cdot(\mathbf{R_1}+a\mathbf{e}_3)}] \\ &= \frac{t}{N} \sum_{\mathbf{R_1}} (e^{ik_x a} + e^{-ik_z a} + e^{-ik_x a} + e^{ik_z a}) \\ &= 2t[cos(k_x a) + cos(k_z a)] = \gamma(\mathbf{k}) = \gamma^*(\mathbf{k}) = \langle \Psi^2_{\mathbf{k}} | \hat{H} | \Psi^1_{\mathbf{k}} \rangle \end{aligned}$$

With these simplifications, the secular equation reads:

$$\begin{vmatrix} \epsilon_1 - \epsilon_{\mathbf{k}_\parallel} & \gamma(\mathbf{k}) \\ \gamma(\mathbf{k}) & \epsilon_2 - \epsilon(\mathbf{k}) \end{vmatrix} = 0 = [\epsilon_1 - \epsilon_{\mathbf{k}_\parallel}][\epsilon_2 - \epsilon_{\mathbf{k}_\parallel}] - \gamma^2(\mathbf{k}) = \epsilon^2_{\mathbf{k}_\parallel} - (\epsilon_1 + \epsilon_2)\epsilon_{\mathbf{k}_\parallel} + \epsilon_1\epsilon_2 - \gamma^2(\mathbf{k})$$

which gives the following dispersion relation for a square 2-D lattice of compensated spins:

$$\boxed{\begin{aligned}\epsilon_{\mathbf{k}_\parallel} &= \frac{\epsilon_1+\epsilon_2 \pm \sqrt{(\epsilon_1+\epsilon_2)^2 - 4[\epsilon_1\epsilon_2 - \gamma^2(\mathbf{k})]}}{2} \\ &= \frac{\epsilon_1+\epsilon_2 \pm \sqrt{(\epsilon_1-\epsilon_2)^2 + 16t^2[cos(k_x a)+cos(k_z a)]^2}}{2}\end{aligned}} \tag{II.67}$$

which is plotted in Fig. II.16 b).

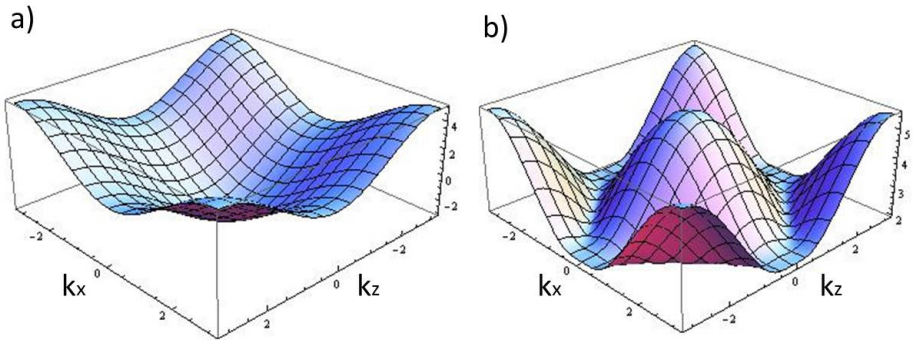

Figure II.16 – a) 2-D dispersion relation for an electron on the plane of uncompensated spins shown in Fig. II.15 a) corresponding to Eq. (II.66). $\epsilon_0 = 1$ eV and $t = -1$ eV. b) 2-D dispersion relation for an electron on the plane of compensated spins shown in Fig. II.15 b) corresponding to Eq. (II.67). $\epsilon_1 = 1$ eV, $\epsilon_2 = 2$ eV and $t = -1$ eV. The wave vectors k_x and k_z are in $\frac{1}{a}$ units.

II.8 Nonequilibrium Keldysh formalism

This section intends to give a very brief description of the Keldysh formalism and the origin of the Green's functions needed for physical systems out of equilibrium. It is freely taken mainly from [Caroli et al., 1971], [Roermund, 2010], [Rammer and Smith, 1986] and [Haug and Jauho, 2008].

The usual equilibrium diagram technique at zero temperature involves the calculation of the time-ordered (also called casual) zero-temperature single particle Green's function. This correlation function is mainly defined by a chronological product of the form:

$$\langle\Phi_0|\,\hat{T}\{\hat{A}(t)\hat{B}(t')\}\,|\Phi_0\rangle$$

where $\hat{T}$ is the usual chronological ordering operator which orders observables from $t = -\infty$ to $t = +\infty$, $\hat{A}(t)$ and $\hat{B}(t')$ are field or creation and annihilation operators in the Heisenberg picture acting at times t and t' and $|\Phi_0\rangle$ is the ground state of the system (space variables are omitted for the sake of clarity). When the system is affected by a perturbation -interactions between particles are turned on for instance- it is useful to employ the interaction representation, in order to get rid of the unknown exact eigenstate of the system, and express the correlation function in terms of the ground eigenstate $|\Phi_0\rangle$ of the unperturbed Hamiltonian instead, generally much easier to calculate. The connection between the exact and the non-perturbed ground state is accomplished by using the Gell-Mann and Low theorem, which yields to the interaction representation of the last expression:

$$\langle\Phi_0|\,\mathbf{S}(-\infty,+\infty)\hat{T}\{\tilde{A}(t)\tilde{B}(t')\mathbf{S}(+\infty,-\infty)\}\,|\Phi_0\rangle$$

where the evolution operator in the interaction representation or matrix $\mathbf{S}$ is defined as:

$$\mathbf{S}(t',t) = \hat{T}\{\exp[-\imath\int_t^{t'}\tilde{V}(t_1)dt_1]\}$$

Here, the total Hamiltonian has been split into an unperturbed part $\tilde{H}_0$ and a perturbation $\tilde{V}$. This perturbation is supposed to be adiabatically turned on from $t = -\infty$ and turned off at $t = +\infty$. The tilde symbol identifies operators in the interaction representation.

In the presence of irreversible effects, the evolution of the system from $t = -\infty$ to $t = +\infty$ amounts no longer to a simple phase shift of its state, since the system absorbs or emits energy during the evolution. As a consequence, the exact state of the system at $t = +\infty$ is in general not known (actually this is one of the things one wants to compute with the Green's functions); thus, all correlation functions must also refer only to the state $|\Phi_0\rangle$ at $t = -\infty$, when the perturbation is off and the Hamiltonian is easier to solve. The diagram technique is thus generalized by the following statement:

$$\langle\Phi_0|\,\mathbf{S}(-\infty,+\infty)\hat{T}\{\tilde{A}(t)\tilde{B}(t')\mathbf{S}(+\infty,-\infty)\}\,|\Phi_0\rangle = \langle\Phi_0|\,\hat{T}_C\{\mathbf{S}_C\tilde{A}(\tau)\tilde{B}(\tau')\}\,|\Phi_0\rangle \quad \text{(II.68)}$$

where $\hat{T}_C$ is an operator ordering times from right to left, not as usual from $t = -\infty$ to $t = +\infty$, but along a contour C made of a "positive" branch going from $\tau = -\infty$ to $\tau = +\infty$ and with a "negative" branch going from $\tau = +\infty$ to $\tau = -\infty$ (contour-ordering operator), as shown in Fig. II.17.

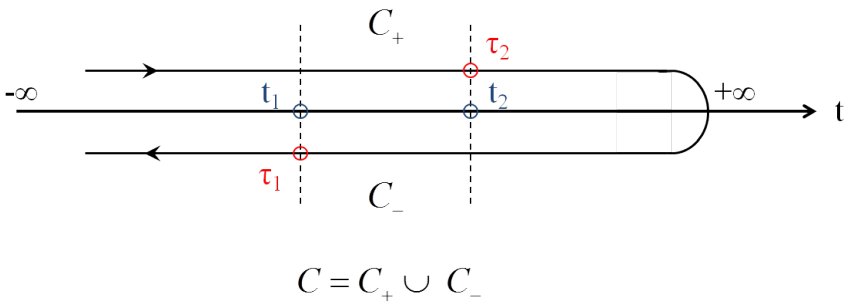

Figure II.17 – Representation of the Keldysh contour C, where $\hat{T}\{\tilde{A}(t_1)\tilde{B}(t_2)\} = \tilde{B}(t_2)\tilde{A}(t_1)$ but $\hat{T}_C\{\tilde{A}(\tau_1)\tilde{B}(\tau_2)\} = \tilde{A}(\tau_1)\tilde{B}(\tau_2)$. The time variable τ on the Keldysh contour must specify on which branch it is located.

In the preceding expression, the contour-evolution operator $\hat{S}_C$ corresponds to an evolution forward in time from $\tau = -\infty$ to $\tau = +\infty$ and then backward in time from $\tau = +\infty$ to $\tau = -\infty$:

$$\mathbf{S}_C = \mathbf{S}(-\infty,+\infty)\mathbf{S}(+\infty,-\infty) = \hat{T}_C\{\exp[\int_C \tilde{V}(\tau)d\tau]\}$$

where the times of $\mathbf{S}(+\infty,-\infty)$ are on the positive branch and the times of $\mathbf{S}(-\infty,+\infty)$ on the negative branch. It is clear that the presence of this term will introduce times on the negative branch of the contour in (II.68).

Times on the positive branch are ordered from $\tau = -\infty$ to $\tau = +\infty$ and times on the negative branch are ordered from $\tau = +\infty$ to $\tau = -\infty$. Any time of the negative branch is considered as posterior to any time of the positive branch. Now, each operator must specify both its time and on which side of the contour it lays, the positive or the negative branch. Hence, the Green's functions will take additional indices and the usual perturbation expansion of the Dyson equation takes a matrix form, as described below. It is now possible to calculate expression (II.68) with the usual Feynman-Dyson diagram technique; since the times belonging to the negative branch (noted with subscript -) are posterior to the times belonging to the negative branch (noted with subscript +), one needs to use the four Green's functions called casual, anti-casual, greater and lesser, whose expressions are respectively (see Fig. II.18):

$$
\begin{aligned}
G^{C}_{p,q}(t,t') &= -\imath \langle \Phi_0 | \hat{T}_C \{ \hat{c}_p(t_+) \hat{c}^{\dagger}_q(t'_+) \} | \Phi_0 \rangle = -\imath \langle \Phi_0 | \hat{T} \{ \hat{c}_p(t) \hat{c}^{\dagger}_q(t') \} | \Phi_0 \rangle \\
\tilde{G}^{C}_{p,q}(t,t') &= -\imath \langle \Phi_0 | \hat{T}_C \{ \hat{c}_p(t_-) \hat{c}^{\dagger}_q(t'_-) \} | \Phi_0 \rangle = -\imath \langle \Phi_0 | \tilde{T} \{ \hat{c}_p(t) \hat{c}^{\dagger}_q(t') \} | \Phi_0 \rangle \\
G^{>}_{p,q}(t,t') &= -\imath \langle \Phi_0 | \hat{T}_C \{ \hat{c}_p(t_-) \hat{c}^{\dagger}_q(t'_+) \} | \Phi_0 \rangle = -\imath \langle \Phi_0 | \, \hat{c}_p(t) \hat{c}^{\dagger}_q(t') \, | \Phi_0 \rangle \\
G^{<}_{p,q}(t,t') &= -\imath \langle \Phi_0 | \hat{T}_C \{ \hat{c}_p(t_+) \hat{c}^{\dagger}_q(t'_-) \} | \Phi_0 \rangle = -\imath \langle \Phi_0 | \, \hat{c}^{\dagger}_q(t') \hat{c}_p(t) \, | \Phi_0 \rangle
\end{aligned}
$$

Here, the operator $\tilde{T}$ orders times from $+\infty$ to $-\infty$ (anti-chronological order) and the subscripts of the creation and annihilation operators indicate site indices of a TB Hamiltonian.

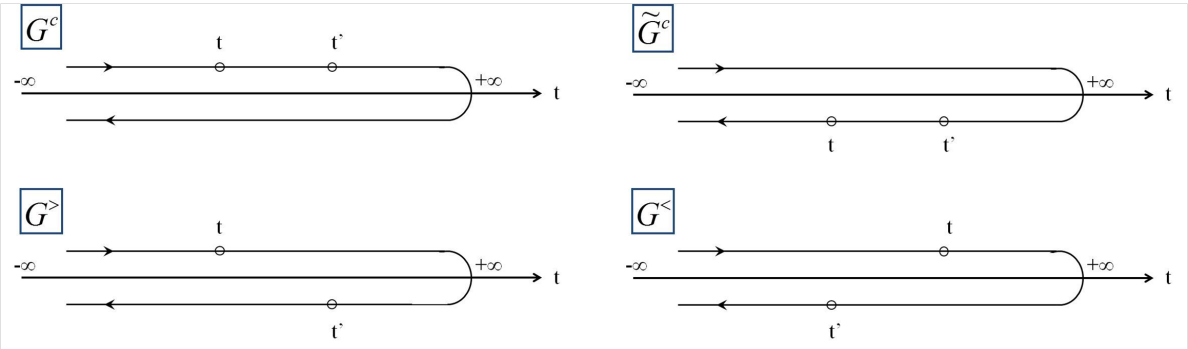

Figure II.18 – Illustration of the casual G^C, anti-casual $\tilde{G}^C$, greater $G^>$ and lesser $G^<$ Green's functions via their correlated times on the Keldysh contour.

In a diagram calculation, integrals are thus performed along the contour starting and ending at $\tau = -\infty$, and not from $t = -\infty$ to $t = +\infty$; this is equivalent to perform the integration from $-\infty$ to $+\infty$ and to sum over the subscripts $+$ and - corresponding to the branches of the contour. Because the negative branch of the contour goes from $\tau = +\infty$ to $\tau = -\infty$, any point of this branch corresponds to a (-) sign due to the differential in time, or equivalently any interaction on this branch corresponds to a (-) sign. Summing over subscripts $+$ and - is equivalent to using 2×2 matrices. Therefore the usual diagram technique still holds, if one defines a Green's function matrix:

$$
\mathbf{G} = \begin{pmatrix} G^{++} & G^{+-} \\ G^{-+} & G^{--} \end{pmatrix} = \begin{pmatrix} G^{C} & G^{<} \\ G^{>} & \tilde{G}^{C} \end{pmatrix}
$$

The Dyson equation then reads:

$$
\mathbf{G}_{p,q}(t,t') = \mathbf{G}^0_{p,q}(t,t') + \int \mathbf{G}^0_{p,k}(t,t_1) \mathbf{\Sigma}_{k,l}(t_1,t_2) \mathbf{G}_{l,q}(t_2,t') dt_1 dt_2 \tag{II.69}
$$

where

$$
\mathbf{\Sigma} = \begin{pmatrix} \Sigma^{C} & \Sigma^{<} \\ \Sigma^{>} & \tilde{\Sigma}^{C} \end{pmatrix}
$$

is the self-energy matrix and G^0 is the Green's function matrix in the absence of the perturbation. Obviously (II.69) represents 4 equations, but only 2 are independent. In our case we are concerned with a system in the steady state, i.e., all Green's functions depend only on the time difference $t-t'$, and it is useful to Fourier transform (II.69) with respect to time and work in the energy domain. Eq. (II.69) then writes:

$$\mathbf{G} = \mathbf{G}^0 + \mathbf{G}^0\mathbf{\Sigma}\mathbf{G} \tag{II.70}$$

where all quantities are 2×2 matrices with respect to the + and - indices. The fact that Eq. (II.69) represents only two independent equations becomes clearer if one makes the following canonical transformation (rotation): $\mathbf{G} \rightarrow \mathbf{G}' = \mathbf{R}^{-1}\mathbf{G}\mathbf{R}$, with $\mathbf{R} = (1 + \imath\sigma_y)/\sqrt{2}$, where σ_y is one of the Pauli matrices. Then, the transformed Green's function matrix becomes:

$$\mathbf{G}' = \begin{pmatrix} 0 & G^a \\ G^r & F \end{pmatrix}$$

where we finally get the retarded, advanced and Keldysh functions:

$$\begin{aligned} G^r &= G^C - G^< = -\tilde{G}^C + G^> \\ G^a &= G^C - G^> = -\tilde{G}^C + G^< \\ F &= G^C + \tilde{G}^C = G^> + G^< \end{aligned}$$

Retarded and advanced Green's functions describe the propagation of particles or excitations forward and backward in time respectively and contain all the spectral information on the local density of states. The Keldysh function satisfies a Quantum Kinetic equation (described below) which is analogous to the Boltzmann equation in the case of quantum systems where coherence of states is of fundamental importance. They are use to compute the lesser Green's function, which provides the average occupation number of each quantum state.

The same transformation for the self-energy yields:

$$\mathbf{\Sigma}' = \begin{pmatrix} \Omega & \Sigma^r \\ \Sigma^a & 0 \end{pmatrix}$$

with

$$\Sigma^r = \Sigma^C + \Sigma^< = -(\tilde{\Sigma}^C + \Sigma^>)$$
$$\Sigma^a = \Sigma^C + \Sigma^> = -(\tilde{\Sigma}^C + \Sigma^<)$$
$$\Omega = \Sigma^C + \tilde{\Sigma}^C = -(\Sigma^> + \Sigma^<)$$

Thus with the transformed (invariant) Dyson equation we obtain three equations and the Fourier transforms of the equations for G^a and G^r are obviously complex conjugates:

$$G^r = G_0^r + G_0^r \Sigma^r G^r$$
$$G^a = G_0^a + G_0^a \Sigma^a G^a$$
$$F = F_0 + G_0^r \Sigma^r F + F^0 \Sigma^a G^a + G_0^r \Omega G^a$$

The first two equations are the Dyson equations for the retarded and advanced Green's functions and the third one is the Quantum Kinetic equation.They provide a complete description of the system out of equilibrium.

In the case considered in this work, the perturbation consists in the connection of the leads with the isolating barrier through the couplings or hopping parameters at the interfaces. It is instantaneous and can be written as:

$$V(t) = \{t_{\alpha,a} \hat{c}_\alpha^\dagger(t) \hat{c}_a(t) + t_{\alpha',b} \hat{c}_{\alpha'}^\dagger(t) \hat{c}_b(t)\} + H.c.$$

where the time t is either on the positive or on the negative branch of the contour so that the interaction cannot connect the two branches. Consequently, $\mathbf{\Sigma}$ has the following form in the transformed Dyson equation:

$$\mathbf{\Sigma} = \begin{pmatrix} 0 & t_{\alpha,a} \\ t_{\alpha,a} & 0 \end{pmatrix} (\delta_{p,\alpha}\delta_{q,a} + \delta_{p,a}\delta_{q,\alpha}) + \begin{pmatrix} 0 & t_{\alpha',b} \\ t_{\alpha',b} & 0 \end{pmatrix} (\delta_{p,\alpha'}\delta_{q,b} + \delta_{p,b}\delta_{q,\alpha'})$$

The unperturbed system at $t = -\infty$ consists of the leads and barrier disconnected and maintained at different chemical potentials. Then the hopping at the interfaces is turned on adiabatically and non-equilibrium quantities are evaluated when the steady state is established.

Numerical implementation

The complexity and size of the systems considered in this work are unaffordable for analytical calculations to give quantitative theoretical predictions. Instead of using a simplified model analytically solvable, numerical simulations are performed here to take into account a more detailed description of the system. The numerical calculations are carried out by a quantum transport code built in Fortran 90. I coded the new spatially-resolved retarded, advanced, Keldysh and lesser Green's functions developed previously, together with all the observables described in II.2 for AF (uncompensated and compensated) and FI systems in 1-D and 3-D. A pre-existing code that was intended to calculate the interfacial spin current density in a AF/B/AF junction was used. The computation was performed in the CEA computer cluster "Summer", with a total of 288 Intel cores. The calculation of the local torque deposited in a single layer for 3-D systems took approximately one month. The bottleneck was the $\mathbf{k}_{\parallel}$ numerical integration in the FBZ, which was performed by the multidimensional adaptive integration algorithm Cuhre, included in the Fortran 90 interface. A number of convergence tests was performed all along this work to check the validity of the results presented in the next chapter.

Chapter III

Spin dependent transport in antiferro and ferrimagnetic tunnel junctions

This chapter is devoted to the investigation of the amplitude and characteristic lengths of STT and tunnelling magnetoresistance in epitaxial AF- and FI- based tunnel junctions using the theoretical tools developed in Chapter II.

First, a comprehensive analysis of the essential features characterising the spatial distribution of STT in AF materials is presented. This analysis is addressed from two different but physically equivalent points of view, namely the spatial variation of the transverse components of spin currents and spin accumulation, as described in II.2.5. The STT out-of-plane component exhibits a staggered spatial distribution similar to its in-plane component. This behaviour is specific to the use of a tunnel barrier and significantly differs from the out-of-plane torques reported in previous works using a metallic spacer, as outlined in Chapter I.

Next, the dependence of the charge current on the intrinsic magnetic properties of the leads as well as the magnetic state of the tunnel junction is analysed in order to examine the TMR ratio in purely AF tunnel junctions, which is of great technological interest. The TMR ratio is shown to be very sensitive to the specific magnetic properties of the AF leads, reaching values comparable to typical magnetoresistances found for usual spin valves.

FI materials merge characteristic features of both Fs and AFs, namely a spontaneous macroscopic magnetization together with a partially compensated magnetic structure. As a consequence, combined STT features of Fs and AFs may also occur in FIs, giving rise to high local STT values and long range STT spatial distributions. In fact, due to their complex magnetic structure, FI-based tunnel junctions exhibit a more interesting STT spatial behaviour, and are examined in a subsequent section. The spatial distribution of STT is shown to have non-trivial wave patterns which are strongly affected by the intrinsic magnetic and electronic properties of the FI material as well as by the applied bias across the junction. The strong sensitivity of TMR ratios to the electronic structure

and magnetic properties shown for AF leads is also observed in FI-based tunnel junctions.

III.1 Spin dependent transport in antiferromagnetic-based tunnel junctions

The STT picture proposed in [Núñez et al., 2006] for AFs arises from changes in the exchange field experienced by localized moments due to their magnetic interaction with nonequilibrium spin densities originated by conduction electrons. This is in contrast with the widely used theoretical framework for F systems, where the basic idea is that the precession of an electron about the magnetization of a F yields to a change in this magnetization by conservation of angular momentum, which is equal to the imbalance of inward and outward spin fluxes. Due to the vanishing magnetization in AF materials, this formalism can only be applied locally, unless the alternative mechanism for STT proposed in [Núñez et al., 2006] is used.

Together with the reflection-based polarizing mechanisms previously reported for AFs [Núñez et al., 2006], [Saidaoui et al., 2014], we emphasize that despite the fact that the overall DOS in AFs remains unpolarized at the Fermi level, the local interfacial DOS becomes spin polarized giving rise to TMR and STT. This is illustrated in Fig. II.6 for the FI case, the only difference compared to AFs being the absence of split of majority and minority bands. Thus STT and TMR behavior is strongly influenced by the two uncompensated layers next to the insulating barrier.

Apart from spin-valve structures using metallic spacers, usual F-based spintronics takes advantage since long of tunnel barriers (B) [Moodera et al., 1995]. Whereas GMR relies on spin dependent scattering at interfaces, tunnel magnetoresistance (TMR) rather relates to spin dependent densities of states. In addition, tunnel barriers filter the wave vectors' angles of incidence of incoming electrons, which lowers the effect of dephasing in three dimensional systems (3-D).

In effect, the tunnelling current distribution over the two-dimensional Brillouin zone (corresponding to the wave vector component parallel to the barrier interface) is strongly localized in certain regions. For instance, STT is mostly determined by electrons with perpendicular incidence and decreases quickly with $|\mathbf{k}_{\|}|$ in F tunnel junctions [Manchon et al., 2008a]. Similar behaviour is characteristic for spin dependent tunneling and TMR as demonstrated both using first principles calculations [Butler et al., 2001], tight-binding [Mathon and Umerski, 2001],[Kalitsov et al., 2009] and free electron approaches [Manchon et al., 2008a]. Such "a tunnelling cone" filtering mechanism which is absent in metallic structures weakens the effect of momentum dephasing processes [Ralph and Stiles, 2008]. Therefore, we investigate the specific behaviour of STT and TMR in AF-based tunnel junctions using tight binding calculations in the framework of

the Keldysh formalism both for 1-D and 3-D geometries. Due to the use of tunnel barriers, we anticipate unusual behaviours compared to AF-based spin-valves with metallic spacers, as will be detailed below.

I recall in Fig. III.1 the tunnel junction model thoroughly described in the previous chapter, for the particular case of AF leads. These semi-infinite leads are modelled as a chain of uncompensated localized spins with translational invariance in the plane perpendicular to the electron flow (y axis).

Following the method explained in Chapter II, a single band tight binding Hamiltonian for the itinerant electrons with a hopping parameter t= -1 eV in all regions is used. The insulating spacer here is a barrier of N_B sites (resp. layers) for 1-D (resp. 3-D) with a spin-independent on-site energy ϵ_B= 5 eV. The magnetic properties of each AF are embedded in the spin-splitting Δ, which accounts for the $s-d$ magnetic interaction between itinerant spins and localized moments.

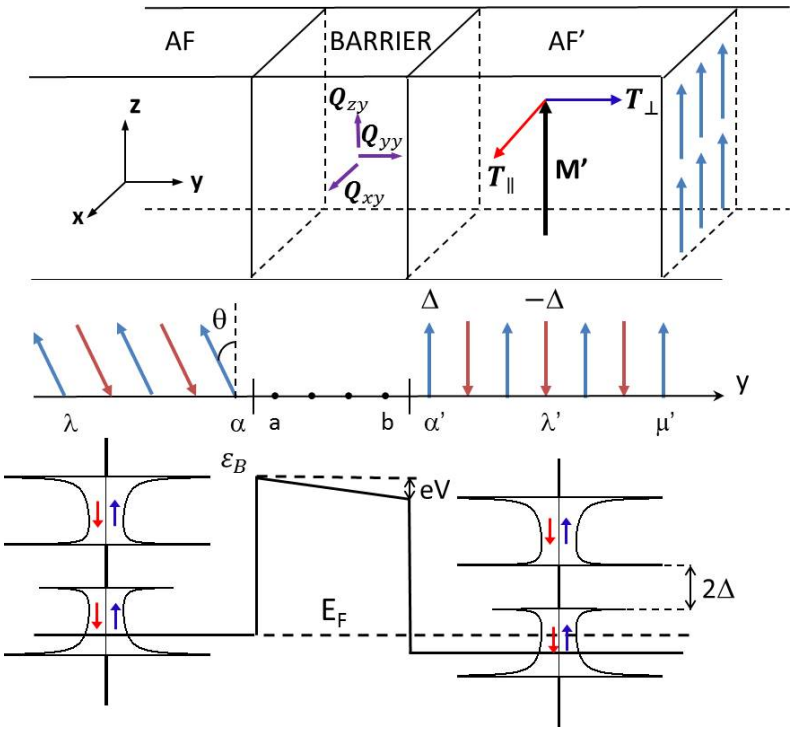

Figure III.1 – Layouts of the tunnel junction modified from [Kalitsov et al., 2009] for AF leads. (Middle) Schematic illustration of the two AF sublattices of up and down localized spins whose magnetic interaction with itinerant electrons is modeled by the staggered spin splitting Δ. The lower and upper bands for a given itinerant spin are separated by a gap of 2Δ.

The absolute value of the spin splitting Δ is constant, but alternates in sign for a given spin from one site(layer) to the next one due to the alternating orientation of the localized magnetic moments within the AF leads. In particular, localized up (resp. down) spins build up a magnetic sublattice in which the spin-dependent on-site energy is given by $\epsilon^{\uparrow(\downarrow)} = \epsilon_0 - (+)\Delta$. In addition, as shown in Fig. III.1, the existence of two sublattices

of localized up and down spins within the AF leads opens a gap in the density of states equal to 2Δ. However, since AFs do not exhibit any macroscopic magnetization, majority and minority bands are not split contrary to F and FI materials.

III.1.1 Spatial distributions of spin density and spin transfer torque in 1-D antiferromagnetic-based tunnel junctions: staggered torques

As discussed in III.1.2, all the following 1-D calculations concerning STT in AF-based tunnel junctions are performed for an angle $\theta = \pi/2$ (see Fig. III.1) between the orientations of the two interfacial spins, since it is expected to maximise the torque amplitude.

The voltage-induced part of in-plane (open circles) and out-of-plane (solid circles) spin torque spatial distributions within the right lead of a 1-D F/B/AF junction are plotted in Fig. III.2. These torques and spin densities were calculated using Eqs. II.29, II.31 II.12. The term "voltage-induced" is used here in order to distinguish the torques present even at equilibrium (zero voltage), from the torques originated by the electrons owning to the narrow transport energy window opened by bias voltages (these bias voltages separate the Fermi levels in both electrodes of the tunnel junction by varying the chemical potential at the right electrode). In addition, it is generally accepted that the term "voltage-induced" is more appropriate to describe tunneling transport while the term "current induced" is more suitable for metallic spin-valve systems [Slonczewski, 2005].

Let's first discuss the in-plane component of the torque. This component exhibits the perfectly staggered distribution that was previously observed by Núñez et al. [Núñez et al., 2006] for 3-D AF-based spin valves (see introduction chapter). The alternating sign of the torque (staggered character) is produced by the alternating localized magnetic moments of each sublattice in the AF lead. These alternating moments are responsible for the alternating exchange field seen by transport electrons. In turn, as described in Eq. (II.33), the constant out-of-plane spin density originated by these transport electrons couple to the alternating exchange field, which leads to the alternating sign of the torque from one site to the adjacent site.

Unlike the random distribution of the out-of-plane torque shown with such metallic spacer, in the case of an insulating spacer analysed here, the non-equilibrium, i.e. the voltage induced part of this torque component is also staggered. This is valid regardless of the left lead's magnetic order since we observed similar behaviour using AF and FI leads as polarisers (results with AF polarisers are shown in subsequent sections for 3-D junctions).

The red and blue thick lines in Fig. III.2 (top and bottom panels respectively) repre-

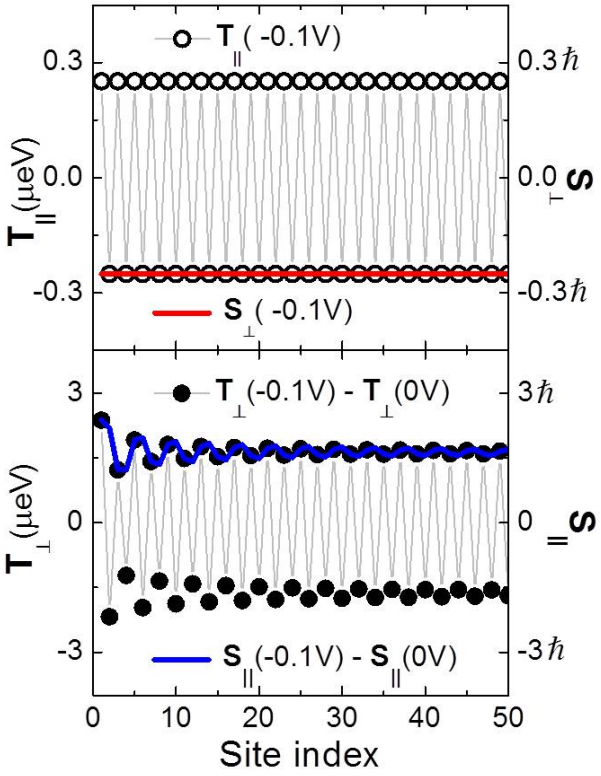

Figure III.2 – Computed spatial distribution of the in-plane and out-of-plane components of the voltage-induced torque ($T_{\parallel}$, top, and $T_{\perp}$, bottom) and spin density ($S_{\perp}$, top, and $S_{\parallel}$, bottom) for a 1-D F/B/AF junction with $\theta = \pi/2$, V= -0.1V and $\Delta = 0.5$ eV for both F and AF leads. The local out-of-plane torque $T_{\perp}(0\text{V})$ and in-plane spin density $S_{\parallel}(0\text{V})$ at zero bias were subtracted to obtain the out-of-plane torque and the in-plane spin accumulation respectively (see Fig. 3 for more details). Note that the equilibrium in-plane torque $T_{\parallel}$ (0V) and related out-of-plane spin density $S_{\perp}(0\text{V})$ are zero. The red and blue thick lines representing the out-of-plane (top) and in-plane (bottom) spin densities respectively refer to the right-hand ordinate.

sent the out-of-plane and in-plane spin accumulations in each site of the right lead. By taking into account the scale factors given by the on-site spin-splitting and the sign of the $s-d$ local magnetic interaction (due to the staggered orientation of each localized moment), the results represented in Fig. III.2 demonstrate that the torques are driven by spin accumulation, in agreement with Eqs. II.33 and II.34. A constant out-of-plane spin accumulation leads to a staggered in-plane torque. In turn, the in-plane spin accumulation oscillates slightly around a constant value, so that the out-of-plane torque exerted in each site of sublattice A oscillates converging to 1.62 μeV (the limiting torque in the bulk) and the torque deposited in sublattice B oscillates around the same value with opposite sign. Therefore, Fig. III.2 confirms that considering ballistic transport in structures comprising AF layers, voltage-induced torques can be computed from the exchange field as well as from the discrete divergence of the spin current. The perfectly staggered pattern is present even for thicker barrier thicknesses (low currents) and low interfacial coupling parameters (high metal-insulator interfacial roughness). It must be stressed that this in-

finite STT characteristic lengths are calculated for a perfectly crystalline structure. The influence of defects in real systems will be investigated experimentally in chapter 4.

In order to illustrate the effect of the equilibrium contribution to the out-of-plane torque, Fig. III.3 shows the spatial distribution of the out-of-plane torque at zero bias (bottom), and the total out-of-plane torque at 0.1V (top) in a 1-D F/B/AF junction. The total out-of-plane torque in each of the sublattices is split in two well defined branches converging to the bulk value far away from the barrier interface.

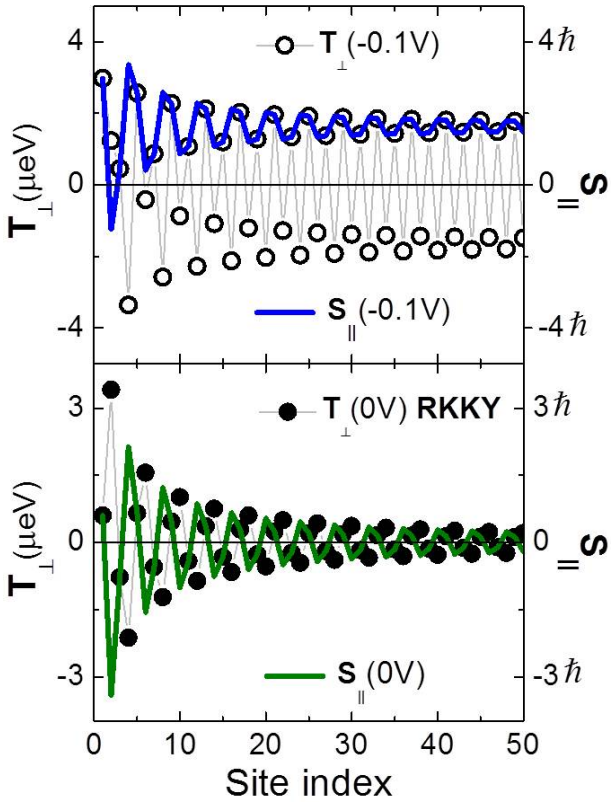

Figure III.3 – Computed spatial distribution of the total out-of-plane torque $T_\perp$ and the total in-plane spin density $S_\parallel$ for a 1-D F/B/AF junction with $\theta = \pi/2$ at -0.1V and 0V (RKKY interaction) with $\Delta = 0.5$ eV for both F and AF leads. The blue and green thick lines representing respectively the in-plane spin densities at -0.1V (top) and 0V (bottom) refer to the right-hand ordinate.

The subtraction of the equilibrium torque to the total torque of Fig. III.3 gave the non-equilibrium torque represented in Fig. III.2. The former accounts for the Ruderman-Kittel-Kasuya-Yosida (RKKY) interaction and is not associated with charge transport. This RKKY conduction-electron-mediated interaction, often referred to as interlayer exchange coupling (IEC) between localized spins in the left and right leads [Ruderman and Kittel, 1954], [Kasuya, 1956], [Yosida, 1957] is comparable in magnitude to the transport-induced out-of-plane torque near the B/AF interface (even higher at certain points). It decays so gradually that the total out-of-plane torque is strongly affected fairly deep into the electrode: subtracting the IEC to the total out-of-plane torque

smoothes out the oscillations (which are highlighted by the blue curve representing the in-plane spin accumulation in the upper plot of Fig. III.3), leading to the flatter staggered torque shown in the lower plot of Fig. III.2. The result is that the two branches in each sublattice converge much faster to the bulk value. Unlike the nonequilibrium out-of-plane torque, the torque exerted at zero bias in each individual sublattice of the right AF lead as well as the in-plane spin accumulation are staggered. Consequently, the global out-of-plane torque spatial distribution at zero bias is not, since the sign of the local torque and spin density alternates every two sites (owning to each of the sublattices).

The spatial distribution of the staggered in-plane torque is much simple, and can be characterized by the amplitude A, defined as the difference between the torques delivered in two sites owning to each of the sublattices, as shown in Fig. III.4 **(a)**. This figure illustrates the spatial distribution of the in-plane torque in a symmetric AF/B/AF junction, which demonstrates that similar STT spatial distributions were found using AFs instead of Fs as polarisers.

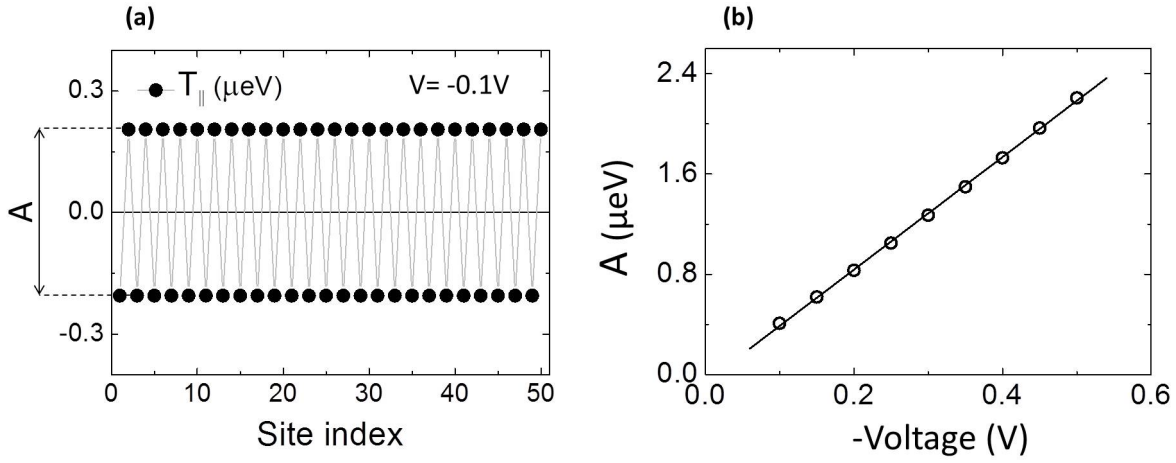

Figure III.4 – **(a)** Definition of the amplitude A (in μeV) of the in-plane torque in a 1-D AF/B/AF junction with $\theta = \pi/2$, V= -0.1V, ϵ_0= 1.5 eV and Δ= 0.5eV. **(b)** Voltage dependence of A in the same system. The line is a linear fit to the data.

The amplitude A is an important and useful parameter, since the total effective in-plane torque delivered in N sites of the right lead can be straightforwardly calculated from A: $T_{\parallel}^{\text{eff}} = \frac{N}{2}A$. It depends on the intrinsic magnetic properties of the AF lead via the spin splitting Δ, and can be also tuned externally via the voltage applied to the junction. Intuitively, the more current crosses the junction, the more torque is delivered to the right lead; the exact relation between the amplitude and the applied voltage is shown in Fig. III.4 **(b)**. The linear fit demonstrates that in the case of a 1-D AF-based tunnel junction, the amplitude A is proportional to the bias. It presents a constant slope of 4.5 μe, where e is the charge of the electron in coulombs. Obviously, it gives zero amplitude for zero bias, in contrast to the out-of-plane component.

III.1.2 Spin density and spin transfer torque in 3-D antiferromagnetic-based tunnel junctions with uncompensated layers

This section extends the previous calculations to 3-D AF-based tunnel junctions. The spatial distribution of the STT as well as the study of the current density are addressed firstly for AF leads consisting of alternating uncompensated layers (see Fig. II.15 **a)**). The investigation of the STT spatial distribution in the case of compensated AF layers (see Fig. II.15 **b)**) is reported in III.2.6 at the end of the section devoted to FI, since both systems show striking similarities concerning the local distribution of torques.
All the following discussions concern symmetric AF/B/AF junctions.

Before starting the calculation of the spatial distribution of torques in symmetric 3-D AF/B/AF junctions, I first checked the angle θ between the spins orientations at the AF/B and B/AF interfaces that maximises the spin current density at the B/AF interface. As explained in II.2.6, the spin current density at the B/AF interfaces is equivalent to the total torque deposited in a F lead. Although this is in general not true for AFs, it is expected to give in a first approximation the angle θ that maximises the amplitude of the torques in the AF case, saving a lot of computation time. The typical angular dependence of the in-plane and out-of-plane components of this spin current density is shown in Fig. III.5.

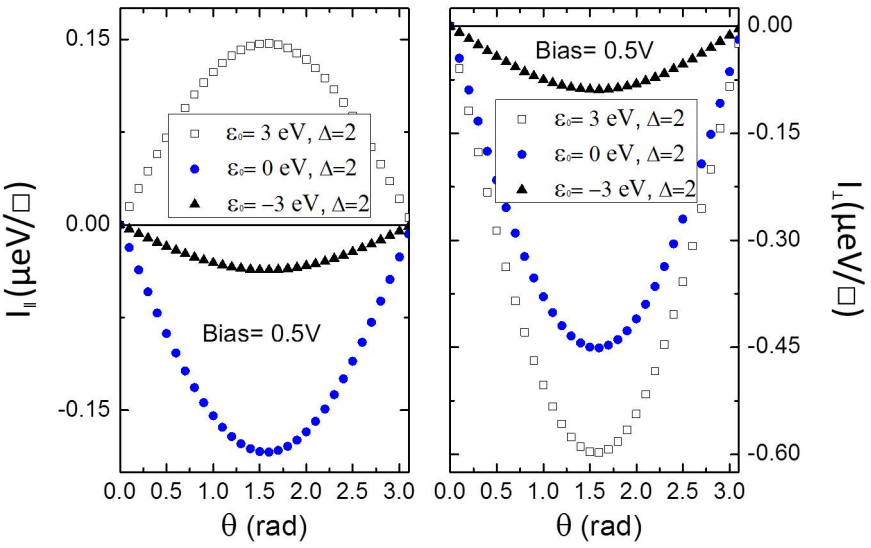

Figure III.5 – (Left) Angular dependence of the in-plane spin current density component for three different 3-D AF/B/AF MTJ with a bias of 0.5V and a barrier height U_B of 9 eV. (Right) Idem for the out-of-plane component.

The results shown in Fig. III.5 for three different AF/B/AF systems (modelled by the parameters shown in the insets) were computed for an insulating barrier with an enhanced height of 9 eV. The positive applied voltage of 0.5 V corresponds to a current

of left-going electrons. It clearly shows a $I \sim sin(\theta)$ dependence in all cases. Slight deviations from this dependence were observed for torques in AF spin valves, and were ascribed to the multiple spin-dependent reflections in the metallic spacer (similar to F spin valves) [Núñez et al., 2006], [Saidaoui et al., 2014], which are expected to be reduced here in the case of an insulating spacer. Consequently, the value $\theta = \pi/2$ expected to maximise in a first approximation the torque amplitude was used in all the numerical simulation performed in this work concerning STT in AFs.

Spatial distribution of torques and spin densities

The local distribution of the the two torque components is illustrated in Fig. III.6. It is clear that the staggered spatial distribution of the in-plane torque as well as the out-of-plane torque in the bulk survives the $\mathbf{k}_{\parallel}$ integration for 3-D geometries. The spatial behaviour of the in-plane component is similar in 1-D and 3-D systems.

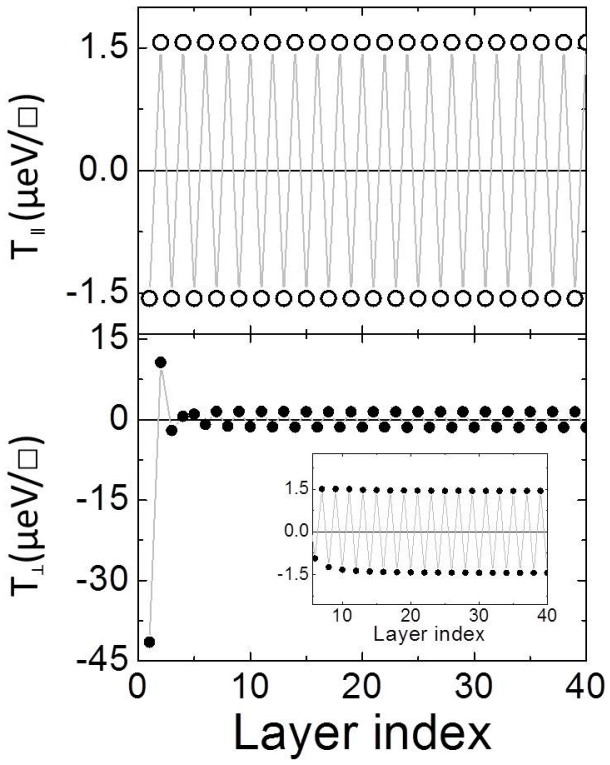

Figure III.6 – Computed spatial distributions of the total in-plane ($T_{\parallel}$) and out-of-plane ($T_{\perp}$) components of the torque in μeV per unit of surface □ for a 3-D AF/B/AF junction with $\theta = \pi/2$, V= -0.1V, ϵ_0= 1.5eV and Δ= 0.5 eV in both AF leads. The inset is a zoom of the out-of-plane component from the sixth layer to stress its staggered character.

In contrast, the total out-of-plane spatial distribution in 3-D AF-based tunnel junction is not significantly affected by the IEC beyond the first layers next to the B/AF interface. Indeed, IEC is shown in Fig. III.7, and it decays after a few layers (note that IEC decreases quickly as $1/N^2$ with increasing metallic spacer thicknesses N in conventional F spin valves [Edwards et al., 2005]). Although the profile of the total out-of-plane torque is

abruptly distorted near this interface due to a very high value of the IEC (shown in Fig. III.7), this equilibrium contribution is radically damped, and no significant deviations from the almost flat behaviour appear in the bulk. Interestingly, a similar STT behaviour was found again regardless of the magnetic nature of the polariser. A strong dephasing mechanism due to all the contributions of $\mathbf{k}_{\|}$ states is thought to be at the origin of this radically damped behaviour of the IEC in 3-D systems at zero bias.

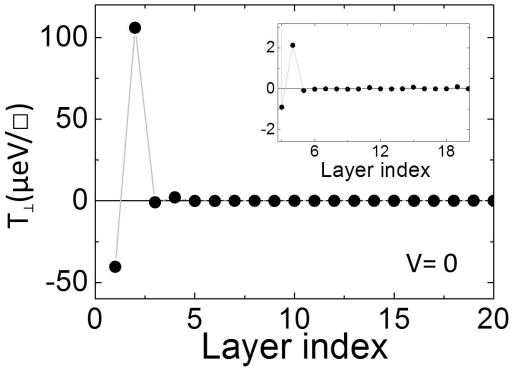

Figure III.7 – Spatial distribution of the out-of-plane torque in μeV per unit of surface □ at zero bias (RKKY interaction) for a 3-D AF/B/AF junction with $\theta = \pi/2$, V= -0.1V, ϵ_0= 1.5eV and Δ= 0.5 eV in both AF leads. The inset is a zoom of the torque from the third layer.

Comparison of antiferromagnetic tunnel junctions and spin valves

An important point to discuss is the difference between the random spatial distribution of the out-of-plane torque reported in ref. [Núñez et al., 2006] for AF-based spin valves and the staggered and ordered character of this torque component shown here for tunnel junctions. This might be ascribed to the multiple spin-dependent reflections that take place in the metallic spacer but not in the insulating barrier. In effect, in the case of tunnel junctions, the evanescent waves decaying exponentially do not stay in the barrier, which reduces considerably the quantum interference between spin-dependent leftward and rightward electrons' wave functions. In addition, the spatial profile of a given spin density component generated by itinerant electrons reflected off an AF displays a complex spatial pattern [Saidaoui et al., 2014]. Thus, in the particular case of the in plane spin component, quantum interference in a metallic spacer may lead to a non-coherent spatial distribution of the in-plane spin density (and consequently out-of-plane torque) both in the spacer and in the right lead. In contrast, as analogous staggered spatial distributions of the in-plane torque are present in both systems, the $\mathbf{k}_{\|}$-filtering effect of tunnel junctions is unlikely to be at the origin of the different out-of-plane torque behaviour, since the spin precession dephasing of the different $\mathbf{k}_{\|}$ states would affect similarly both torque components.

Relation between local spin densities and torques

The local out-of-plane and in-plane spin densities responsible for the local STT are depicted in Fig. III.8. A constant out-of-plane spin density originates a perfectly staggered in-plane torque in the whole right lead. A constant in-plane spin density originates a staggered out-of-plane torque in the bulk.

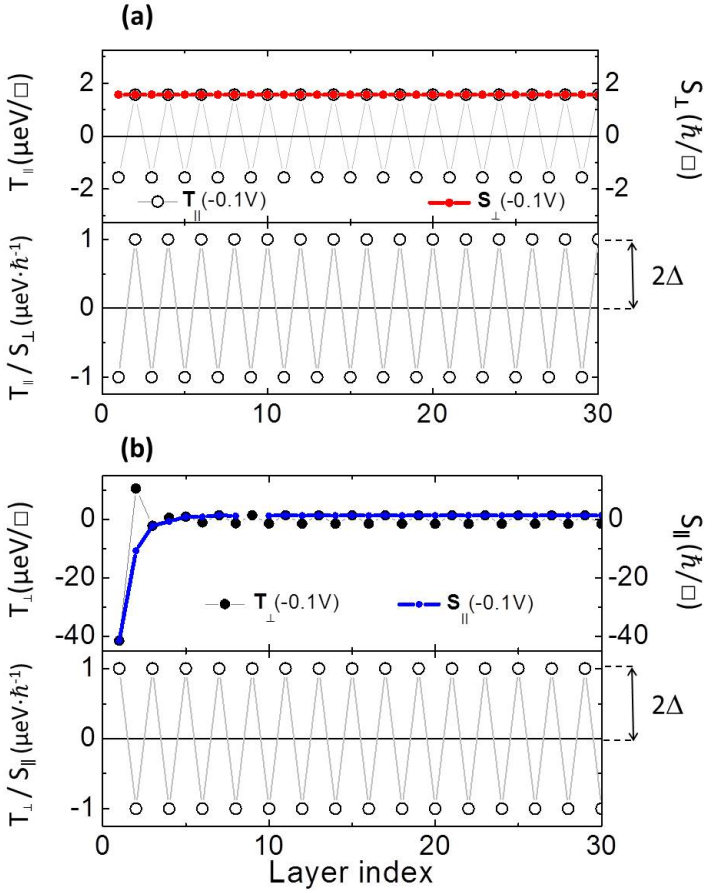

Figure III.8 – **(a)** (Top) Computed spatial distribution of the in-plane torque ($T_\parallel$) and out-of-plane spin density ($S_\perp$) for a 3-D AF/B/AF junction with $\theta = \pi/2$, V= -0.1V ϵ_0= 1.5 eV and $\Delta = 0.5$ eV in both AF leads. (Bottom) Local ratio $T_\parallel/S_\perp$ showing explicitly the exchange field $\mathbf{\Delta} = 2\Delta$ **(b)** (Top) Computed spatial distribution of the out-of-plane torque ($T_\perp$) and in-plane spin density $S_\parallel$) for the same system. (Bottom) Local ratio $T_\perp/S_\parallel$ showing explicitly the exchange field $\mathbf{\Delta} = 2\Delta$. The red and blue thick lines representing the out-of-plane and in-plane spin densities in **(a)** and **(b)** respectively refer to the right-hand ordinate.

The effect of the dramatic decrease of this last spin component in the first layers of the right lead is directly observed on the out-of-plane torque behaviour near the barrier interface. The relation between torques and spin densities is clearly illustrated in Fig. III.8, where the ratios $T_\parallel/S_\perp$ and $T_\perp/S_\parallel$ are plotted in the bottom panels; as can be seen in Eqs. (II.33) and (II.34), these ratios correspond to the local exchange field, which is staggered and equals $\mathbf{\Delta} = \pm 2\Delta = \pm 1$ in the particular case considered in the Fig. III.8.

Behaviour of the in-plane torque amplitude A

Similarly to the 1-D case, the amplitude A of the in-plane torque is strongly affected by the applied bias. As shown in Fig. III.9 **(a)**, the amplitude increases with voltage, but the linear dependence is lost.

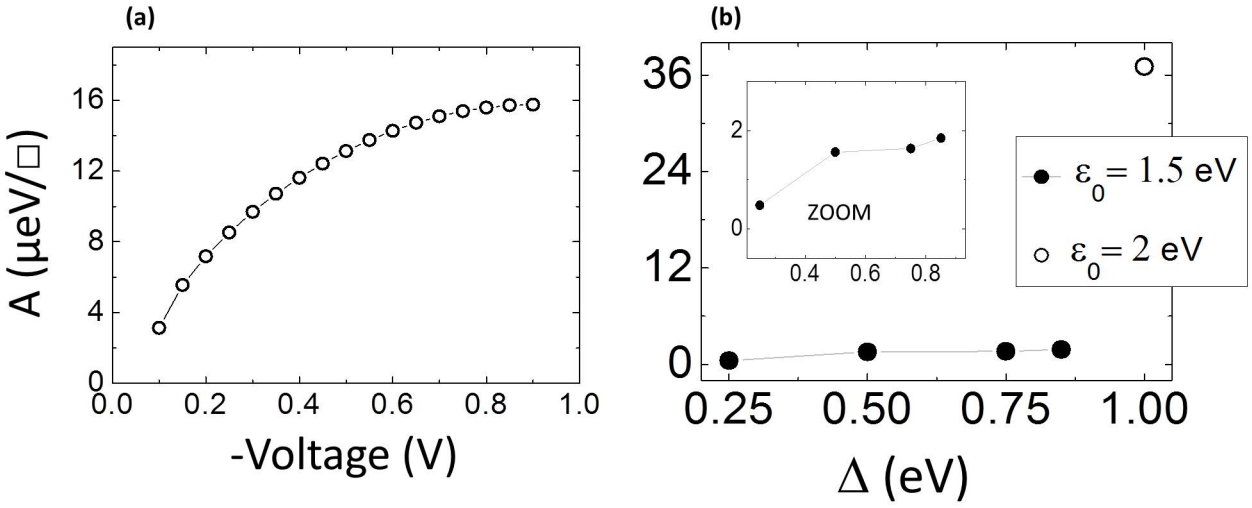

Figure III.9 – **(a)** Dependence of the in-plane torque amplitude A in μeV per unit of surface □ on the applied voltage for a 3-D AF/B/AF junction with $\theta = \pi/2$ and Δ= 0.5 eV. **(b)** Dependence of the in-plane torque amplitude A on the spin splitting Δ for the same junction at V= -0.1V. The inset is a zoom for the low values of the amplitude.

A quadratic-like dependence appears, reaching saturation for high voltages. This voltage dependence is shared in turn with the current density (see below), which is consistent, since it is the only responsible for the in-plane torque (the zero voltage part vanishes). The amplitude A vs the exchange splitting Δ of the AF is plotted in Fig. III.9 **(b)**. As can be seen in the inset, the amplitude increases slightly with the spin splitting Δ for a constant value of ϵ_0. However, the orbital energy ϵ_0 has a stronger impact. The open symbol at $\Delta = 1$ eV represents an AF with an orbital energy ϵ_0= 2 eV, to be compared to ϵ_0= 1.5 eV for the rest of the solid points. This increase of 0.5 eV in the orbital energy leads to a dramatic increase in the torque amplitude. An increase of the orbital energy keeping the exchange splitting constant amounts to a shift of the DOS to higher energies, maintaining the gap constant as well. This approaches the singularity of the DOS' lower edge to the Fermi energy, providing more states available for the charge current, and producing more torque. This demonstrates the importance of the electronic structure and consequently the position of the Fermi energy for the STT in AF-based tunnel junctions.

Effects of roughness at the barrier interfaces

As is already known, the tunnelling current is very much influenced by the electronic structure, interdiffusion and roughness at the barrier interfaces [Tsymbal et al., 2003].

The interface sensitivity is often explored experimentally by the insertion of ultrathin layers called dusting layers at the barrier-electrode interface. In particular, interface roughness leads to fluctuations in the barrier thickness and its coupling to the leads, strongly affecting tunnelling conductance.

In an attempt to examine the effects of the barrier interfaces, the STT behaviour is next analysed as a function of the hopping parameters $t_{\alpha,a}$ and $t_{b,\alpha'}$, which quantify the coupling at the barrier interfaces in the tunnel junction model used here (see II.1.3). The spatial distribution of the two torque components for two different values of the mentioned hopping parameters at the interfaces is plotted in Fig. III.10 **(a)** and **(b)**, corresponding to $t_{b,\alpha'}$= 0.4 eV and 0.7 eV respectively. The results reported previously for $t_{b,\alpha'}$= 1 eV are plotted in Fig. III.10 **(c)** by way of comparison. The hopping parameter inside the leads is kept at 1 eV.

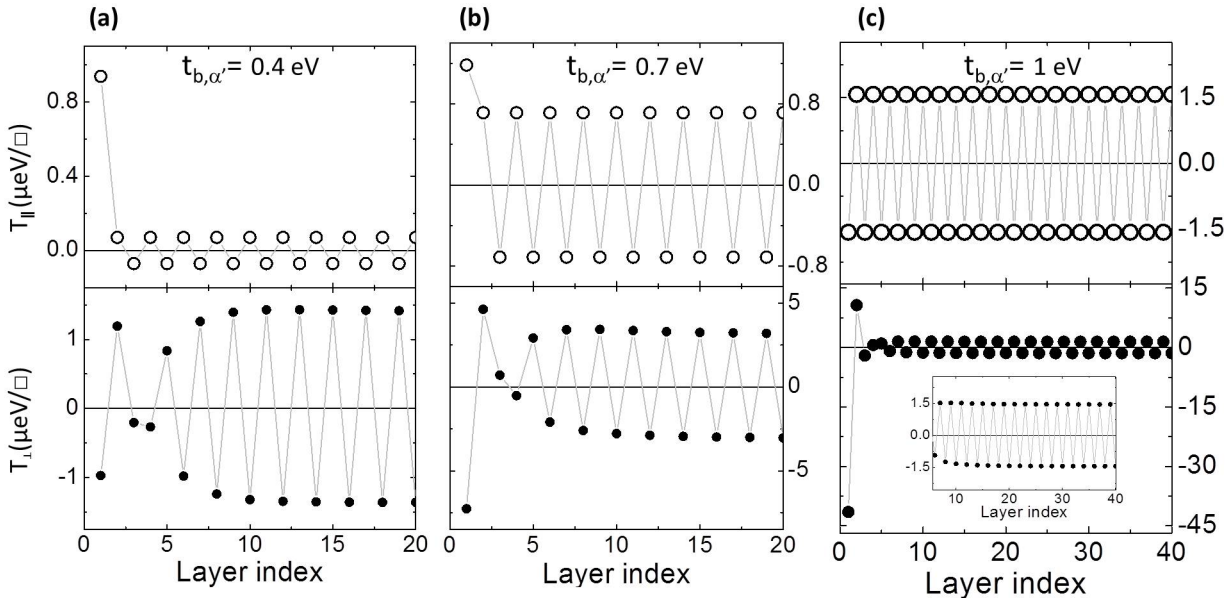

Figure III.10 – Computed spatial distributions of the in-plane ($T_\parallel$) and out-of-plane ($T_\perp$) components of the torque in μeV per unit of surface □ for a 3-D AF/B/AF junction with $\theta = \pi/2$, V= -0.1V, ϵ_0= 1.5eV and Δ= 0.5 eV in both AF leads. The hopping parameter at the barrier interfaces (coupling) is $t_{b,\alpha'} = t_{a,\alpha}$= **(a)** 0.4 eV. **(b)** 0.7 eV. **(c)** 1 eV. As in Fig. III.6, the inset is a zoom of the out-of-plane component from the sixth layer.

Both values of the coupling at the interfaces are lower than the typical value of 1 eV used in the rest of this work. Two important effects are observed in the Figure. The first is a significant decrease of the in-plane torque amplitude with the coupling; the second is a strong distortion of the in-plane component near the interface for lower coupling, i.e., the torque at the first layer of the lead becomes radically higher than the value that would correspond to the sublattice it owns to. Although this effect is harmful for the effective torque since the in-plane torque delivered at the first layer is subtracted to the torques deposited in the next layers (it tends to rotate the order parameter in the opposite sense of the torque deposited in the rest of the layers), the staggered character of both torques

is preserved in the bulk of the lead. In contrast, the distortions of the out-of-plane torque near the interface are more important for high coupling. As mentioned above, these interfacial effects are crucial to be minimised in order to have high values of the effective torque; they are analysed experimentally in Chapter IV for spin valve-like systems, and will be the object of theoretical future work, together with the effect of impurities using the method proposed in II.5 and most sophisticated techniques to treat the disorder such as coherent potential approximation (CPA). In any case, the staggered pattern of the STT spatial distribution seems to be robust against low currents/low coupling at the interface.

III.1.3 Charge current density and antiferromagnetic tunneling magnetoresistance

Given the importance of the TMR for non-volatile memory applications, we next examine the voltage dependence of the charge current density (responsible for the voltage-induced part of the torque) for different angles θ of the left lead order parameter (see Fig. III.1 for the definition of θ) in a symmetric 3-D AF-based tunnel junction.

The origin of the voltage dependence of TMR has an important contribution related to the electronic structure of the AF leads. When a voltage is applied across the junction, nonequilibrium electrons from the occupied states below the Fermi level in the left lead are able to tunnel to new empty states of energy higher than the Fermi level in the right lead (lowered by the bias-dependent chemical potential). Since the DOS of the AF lead is energy-dependent, the spin polarization and the conductance are also a function of energy, resulting in the variation of TMR with the applied voltage. In addition, the altered potential profile within the barrier contributes to the variation of the transmission coefficients with applied bias.

Fig. III.11-**(b)** shows the charge current density as a function of applied bias for antiparallel, perpendicular and parallel magnetic states of left and right AF leads (the magnetic states are defined here as the relative orientation of the two layers of uncompensated spins at the AF/B and B/AF interfaces, see Fig. III.1).

By way of comparison, the same features are shown in Fig. III.11-**(a)** for a conventional F-based tunnel junction. In the low bias region, where the charge density current can be considered as proportional to the applied bias in linear response theory [Bruus and Flensberg, 2002], differences between the three magnetic states are sensible only in the F case. In contrast, for the AF case, the three configurations can only be distinguished for voltages higher than a threshold of around 0.4 V. Higher voltages produce charge current saturation and decrease at very different rates for the three magnetic configurations. This is clearly illustrated by the TMR voltage dependence depicted in Fig. III.11-**(d)**. The position of the threshold might be ascribed to the curvature change of the AF DOS at the Fermi level (see Fig. III.1 and II.12) when a voltage is applied,

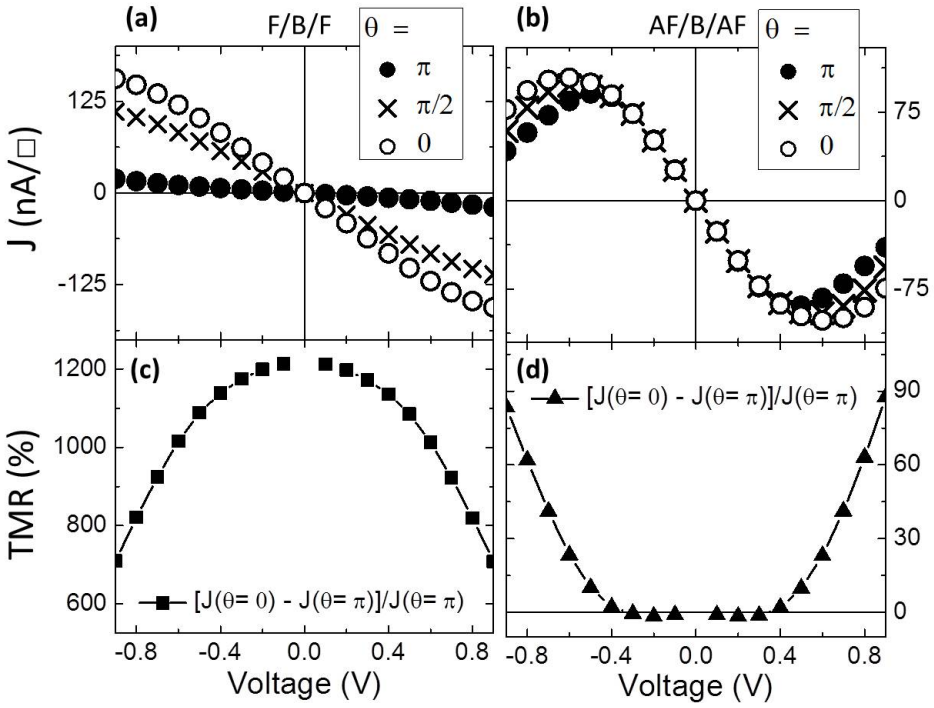

Figure III.11 – Calculated voltage dependence of the charge current density J in nA per unit of surface □ for three different angles θ (top) and TMR (bottom) in **(a)-(c)** a 3-D F/B/F tunnel junction with $\Delta = 0.75$ eV in both F leads and in **(b)-(d)** a 3-D AF/B/AF tunnel junction with $\Delta = 1$ eV and $\epsilon_0 = 2$ eV in both AF leads.

which amounts to a steep change in the number of states available in the right lead. Further investigations are however necessary in order to clarify this point. For bias below 0.4 V, the TMR is around -1% (negative TMR is also found for instance in the case of FI leads due to negative spin polarization [Kaiser and Parkin, 2006]), but interestingly it presents a dramatic increase with voltage from the threshold, reaching values as high as 90% for a bias of 0.9 V, to compare with the GMR ratio of around 10% shown in [Núñez et al., 2006]. This bias dependence of the TMR in this AF-based tunnel junction is opposite to the usual case of ordinary F-based tunnel junctions, where TMR reaches very high values (a TMR ratio in excess of 1000% for an epitaxial Fe/MgO/Fe junction has already been reported using tight-binding bands fitted to an ab initio band structure of iron and MgO [Mathon and Umerski, 2001]), but decreases significantly with applied voltage, as shown in Fig. III.11-**(c)**. From the experimental point of view, TMR ratios of 604% at room temperature and 1144% at 5 K approaching the theoretically predicted value [Mathon and Umerski, 2001] were found in sputtered CoFeB/MgO/ CoFeB F-based tunnel junctions [Ikeda et al., 2008], while only a MR ratio of 0.5% was observed in the AF spin valve structure IrMn/Cu/IrMn [Wang et al., 2009]. This low MR ratio indicates the high sensitivity of AF STT and MR to momentum scattering due to disorder, and points out AF-based tunnel junctions as an attractive system for spintronics applications due to its momentum conservation properties [Saidaoui et al., 2014].

Different trends were found however for different AF. For instance, as shown in Fig. III.12 a decreasing TMR with voltage was observed for an AF with ϵ_0= 1.5 eV and Δ= 0.5 eV. The effect of this change in the electronic and magnetic parameters on the lower band of the AF lead (the only one considered here) amounts to a slight down shift of the lower band edge. Currents in this system are significantly lower than in the previous case, which demonstrates the extreme sensitivity of the current properties in AF-based tunnel junctions to the AF electronic band structure characteristics and the specific position of the Fermi level.

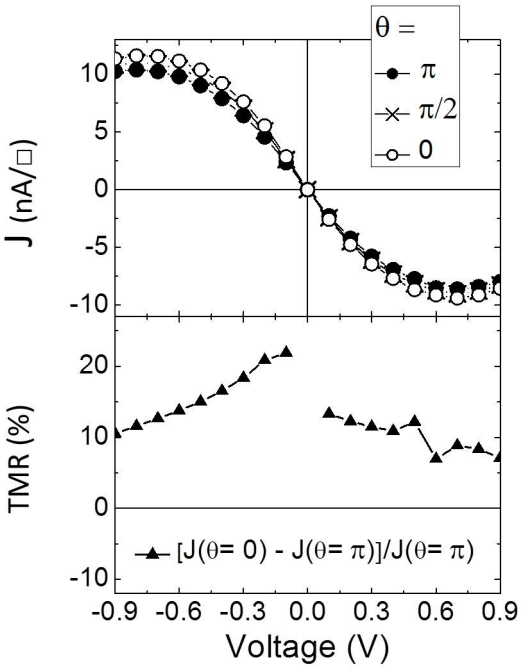

Figure III.12 – Calculated voltage dependence of the charge current density J in nA by unit of surface □ for three different angles θ (top) and TMR (bottom) in a 3-D AF/B/AF tunnel junction with $\Delta = 0.5$ eV and ϵ_0= 1.5 eV in both AF leads.

Due to numerical instability, the J-V curves are not symmetric in this particular case for positive and negative voltages (as it should be due to the symmetry of the junction), which is amplified in the calculation of the TMR ratio (see Fig. III.12 (bottom)). The bumped behaviour for positive voltages suggests that the negative voltage (corresponding to right-going electrons) is the more reliable branch. TMR ratios over 10% are found in all this voltage range. In conclusion, the particular choice of the AF strongly affects not only the value of the TMR but also its voltage dependence.

III.1.4 Summary

In summary, the spatial distribution of the STT in epitaxial AF-based tunnel junctions was computed and analysed in terms of local spin accumulation and the discrete divergence of the spin current transverse component. The resulting voltage-induced part of the out-of

plane torque (as well as the total out-of plane torque in the bulk) deposited in an AF lead is found to be perfectly staggered, in contrast with the random behaviour previously reported for a metallic spacer.

The STT spatial pattern is independent of the magnetic nature of the left lead, i.e. F, AF or FI, which points out that the main role of polariser is played by the closest spins next to the barrier's left interface.

In addition, it is demonstrated that unlike conventional F-based tunnel junctions, AF-based tunnel junctions can show monotonically increasing TMR with voltage, reaching values as high as 90% for a bias of 0.9 V. However, the particular voltage dependence of the TMR is shown to be strongly affected by the electronic structure of the AF leads [Merodio et al., 2014b].

In the following section, the analysis carried out for AF-based tunnel junctions will be extended to the case of FIs, for which AFs constitute simpler limiting cases. As will be seen, the additional magnetic complexity inherent to FI materials yields to a richer physics concerning the STT spatial behaviour in FI-based tunnel junctions.

III.2 Spin dependent transport in ferrimagnetic-based tunnel junctions

In this section, we present a theoretical study of STT in ferrimagnet based tunnel junctions. We show that electronic structure parameters such as band widths and exchange splittings of the FI leads strongly influence STT. In particular, the STT spatial distribution within the leads shows a striking spin-modulated wave-like behaviour resulting from the interplay between the exchange splittings of the two FI sublattices. This wave-like behaviour can also be tuned via the applied voltage across the junction. Additionally, the fundamental parameter for quantifying STT characteristic lengths in FI metals is identified here, which shall also be accessible to experiments for instance by ferromagnetic resonance and spin pumping measurements. As will be discussed in the next chapter, I used these methods to measure experimentally characteristic penetration depths of a spin current into an AF (limiting case of a FI).

All the calculations here concerning STT in FIs are performed at $\theta = \pi/2$, since this angle is expected to maximise STT, as in the case of conventional F-MTJ [Manchon et al., 2008a].

III.2.1 Characteristic lengths of spin density and spin transfer torque in 1-D ferrimagnetic-based tunnel junctions: spin-modulated torque waves

In order to illustrate the essential features of the STT spatial distribution in the right FI lead, a 1-D FI-MTJ for which the calculation of local torques does not require the $\mathbf{k}_{\parallel}$ integration is first examined. Fig. III.13 shows the corresponding voltage-induced part of local on-site torques and spin accumulations. The equilibrium zero voltage torques were subtracted.

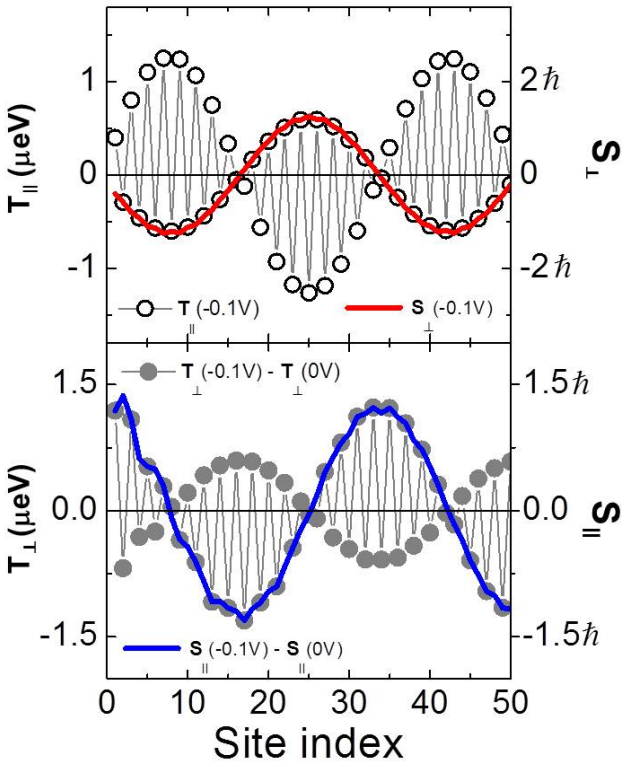

Figure III.13 – Spatial distribution of the in-plane ($T_{\parallel}$) and out-of-plane ($T_{\perp}$) nonequilibrium torque components and local spin density components ($S_{\perp}$ and $S_{\parallel}$) for a 1-D system; $\theta = \pi/2$, $\Delta_A = 0.5$ eV, $\Delta_B = 0.25$ eV and V= -0.1V. The equilibrium torques and local spin densities were subtracted: $T_{\parallel}(0\text{V})$ and $S_{\perp}(0\text{V})$ equal zero in contrast to $T_{\perp}(0\text{V})$ and $S_{\parallel}(0\text{V})$ that result from interlayer equilibrium RKKY interactions. The thick red and blue curves(symbols) refer to the right-(left-)hand ordinate.

While the in-plane torque is zero at equilibrium (V= 0V), the out-of-plane torque is not since it accounts for the Ruderman-Kittel-Kasuya-Yosida (RKKY) interaction, as mentioned in the previous section. Interestingly, both in-plane and out-of-plane torques are staggered and commensurate with the lattice moment orientations, similar to the case of AF leads (see Fig. III.2). Here, in addition, and due to the specific FI order of the lead, the torques exhibit a striking wave-like behaviour: the FI sublattices A and B host two "torque waves" dephased by half of a period one with respect to the other. Note also that the higher the exchange field, the higher the amplitude of the corresponding torque wave.

Fig. III.13 demonstrates that the spin transfer torques calculated using Eqs. II.29 and II.31 are perfectly modulated by spin accumulation, similar to the AF case. In particular, the torque deposited in each sublattice scales with the spin density according to the spin splitting/exchange field of that sublattice. This is shown for sublattice B in Fig. III.13 (top), (lower spin splitting/lower torques) and for sublattice A in Fig. III.13 (bottom), (higher spin splitting/higher torque).

Indeed, as explained in II.2.1, spin accumulation is calculated independently from Eq. II.12, its spatial distribution oscillates exactly at the same period as that of the STT and the ratios $T_{\parallel}/S_y$ and $T_{\perp}/S_x$ are constant. Using spin accumulation thus provides an alternative method for calculating torques, not only in ordinary F-MTJ but also more generally in FI- and AF-MTJs.

The variables controlling the modulation of the STT are next examined.

III.2.2 Period and amplitude of the spin-modulated torque waves

The STT waves presented here can be characterized by their amplitude A (similar to the AF case) and their period P. Both parameters are depicted in Fig. III.14 for clarity. In the same Figure, A and P are plotted as a function of voltage in the right panel. In contrast to the AF case (see Fig. III.4), the amplitude A does not increase monotonically with voltage, but reaches a maximum for a bias of 0.35 V. This might be related with the saturation of the current at the same voltage, which is examined in the next section for 3-D junctions.

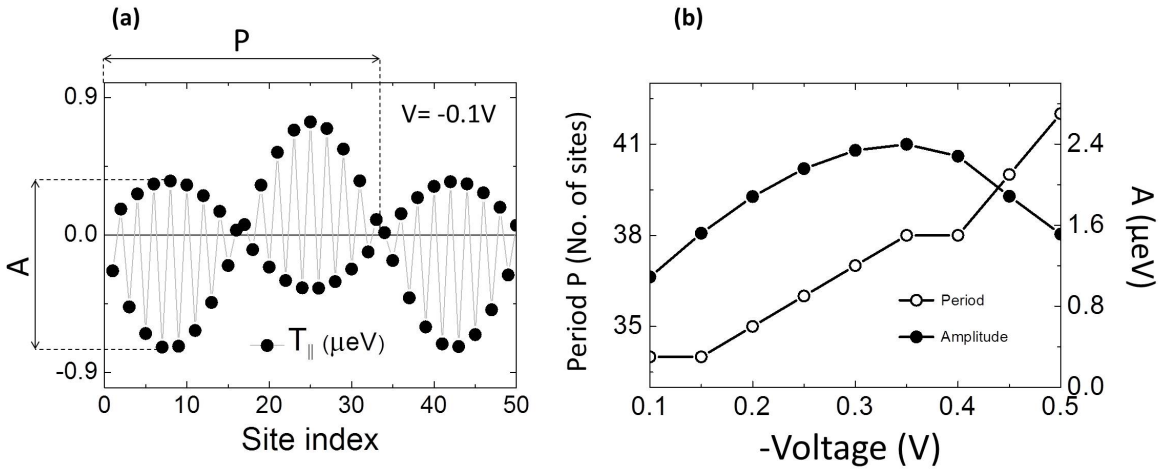

Figure III.14 – **(a)** Definition of the amplitude A (in μeV) and the period P (in number of layers) of the in-plane torque in a 1-D FI/B/FI junction with $\theta = \pi/2$, V= -0.1V, ϵ_0= 1.5 eV, Δ_A= 0.5 eV and Δ_B= 0.25 eV. **(b)** Voltage dependence of P (open circles referred to the left hand ordinate) and A (solid circles referred to the right hand ordinate) in the same system.

In turn, the period P of the waves increases monotonically with the applied bias,

despite the two plateaus at 0.15 and 0.4 V caused by the discrete character of the period and the discrete voltages considered in the calculations, so likely not ascribed to physical reasons. It is worth noting that while the first half period of the torque wave tries to turn the magnetization in one direction, the next half period tries to do the opposite, since the wave changes sign for each sublattice, and the exchange energy is high enough to maintain the lattice rigid. In order to have a high effective torque, it is therefore important to apply a high voltage, but not far from the bias at which saturation of the torque waves amplitude is reached.

Influence of spin splittings on the torque modulation

The intrinsic magnetic properties of the FI leads have also a very strong influence in the torque wave shape, and are next examined. Fig. III.15 represents the local distribution of the in-plane and out-of plane torque components for two different FI leads, characterized by the spin splittings in each of the sublattices.

It is apparent that the spatial profile of the in-plane component is much smoother than that of the out-of plane component. This is due to the strong influence of the slow-decaying RKKY interaction in 1-D geometries, whose behaviour is similar to the AF case. The subtraction of this zero voltage interaction gives the uniform profile shown in Fig. III.13.

Apart from the higher amplitude of the in-plane torque for the FI shown in Fig. III.15 **(b)** with respect to the FI plotted in Fig. III.15 **(a)**, the most striking difference is the dramatic change of the period. This period depends on the interplay between the spin splittings Δ_A and Δ_B of each sublattice; in particular, the period P depends on the difference $\delta = \Delta_A - \Delta_B$. A high δ leads to a short spatial period P and vice versa, a low δ leads to a longer P, as illustrated in Fig. III.16.

The linear fit in Fig. III.16 shows that for a given voltage, the torque wave's period (P) is inversely proportional to the difference (δ) of magnetic $s-d$ exchange interactions between itinerant spins and localized magnetic moments in each of the two FI sublattices:

$$\boxed{P \propto \frac{1}{\delta}} \tag{III.1}$$

Given the above relation, the limiting case characterized by $\delta = 0$, i.e. when the FI becomes a fully compensated AF, results in a diverging period. This agrees with the perfectly staggered and non oscillating $T_{\parallel}$ spatial distributions described in III.1.1 and reported previously in AF-based spin valves [Núñez et al., 2006]. Interestingly, a Taylor expansion at the Fermi energy of the dispersion relation for a 1-D FI up to second order in the wave vector recasts relation (III.1) in terms of the Fermi wave vectors for up and down spins for the case of low band filling:

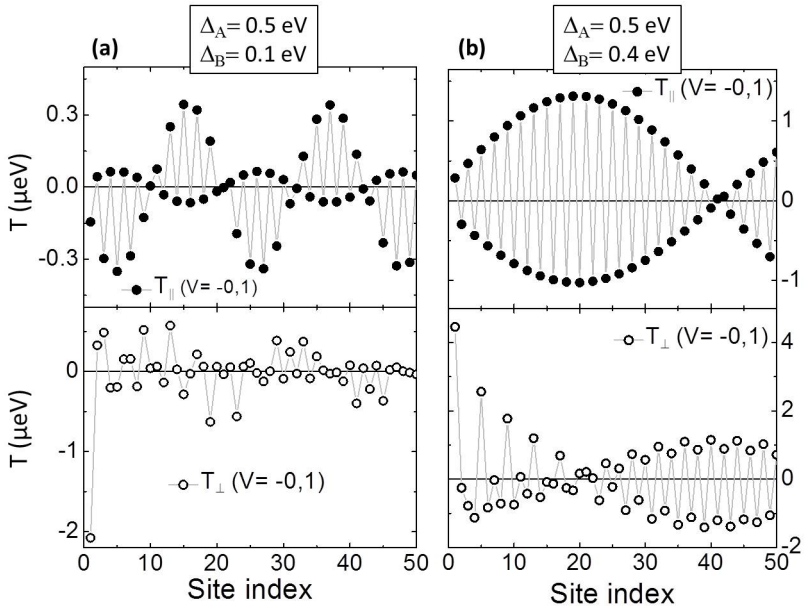

Figure III.15 – Computed spatial distributions of the in-plane ($T_\parallel$) and out-of-plane ($T_\perp$) components of the torque in μeV for a 1-D FI/B/FI junction with $\theta = \pi/2$, V= -0.1V, ϵ_0= 1.5eV and **(a)** Δ_A= 0.5 eV; Δ_B= 0.1 eV (δ= 0.4 eV). **(b)** Δ_A= 0.5 eV; Δ_B= 0.4 eV (δ= 0.1 eV).

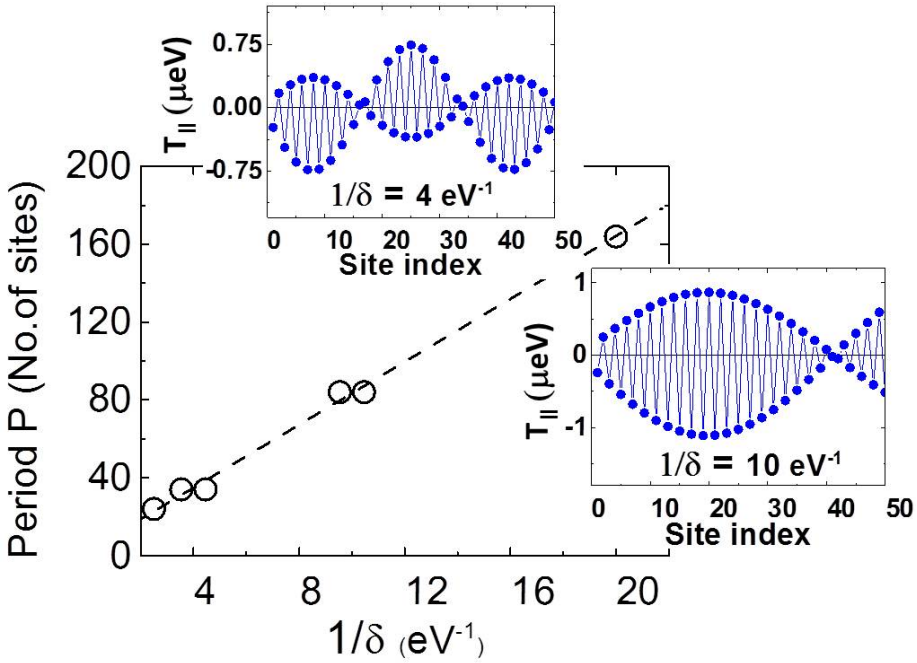

Figure III.16 – For six different 1-D FI/B/FI MTJ, $1/\delta$ dependence of the in-plane torque component period (P) for $\theta = \pi/2$ and V= -0.1V. The double symbols at 4 and 10 eV^{-1} represent FI electrodes with unequal spin splittings Δ_A, Δ_B but the same $\delta = \Delta_A - \Delta_B$. These symbols are horizontally shifted to show the presence of two points/FIs. Upper(Lower) inset: spatial distribution of the parallel torque wave for $1/\delta = 4$ eV^{-1} ($1/\delta = 10$ eV^{-1}). Dashed line is a linear fit to the data.

$$P \propto \frac{1}{\delta} \propto \frac{1}{(k_f^{\uparrow})^2 - (k_f^{\downarrow})^2} = \frac{1}{(k_f^{\uparrow} + k_f^{\downarrow})(k_f^{\uparrow} - k_f^{\downarrow})} \tag{III.2}$$

This expression is related to the length scales at which torque oscillations decay in conventional F-MTJ from the B/F interface. The two factors $1/(k_f^{\uparrow} - k_f^{\downarrow})$ and $1/(k_f^{\uparrow} + k_f^{\downarrow})$ are respectively proportional to the voltage-induced and RKKY torque oscillations period in F-based tunnel junctions [Manchon et al., 2008b]. Moreover, as pointed out by Berger, the following relation between the exchange field $\mathbf{\Delta}$ and the spin dependent Fermi wave vectors applies in Fs [Berger, 1996]:

$$(\hbar^2/2m)((k_f^{\uparrow})^2 - (k_f^{\downarrow})^2) = -2\mu_B \mathbf{\Delta}$$

where $\mathbf{\Delta}$ is defined here as an actual magnetic field. Consequently, the δ parameter plays the role of a global "effective" exchange field in FIs, similar to the F case. This is consistent, since the net magnetization of the FI is higher for higher values of δ. In addition, for the range of energies considered here, the parameter δ and $k_f^{\uparrow} - k_f^{\downarrow}$ are proportional to each other with great accuracy; the period P can thus be viewed as inversely proportional to the spatial frequency $\Delta k = k_f^{\uparrow} - k_f^{\downarrow}$. Similar to the spatial precession of up and down spin components of the scattering state in Fs, the period of the STT waves in FIs results in a first approximation from the precession around the net magnetization.

Influence of the bandwidth on the torque modulation

Here it is also shown that the bandwidth of the electronic band structure strongly influences both the torque waves' period and the amplitude of the oscillations. As a result of the TB model used, both upper and lower bandwidths can be parametrized by the hopping parameter t, which determines electron mobility inside the whole structure. Although the effect of the variation of t on STT will be examined, its particular value is the same in all regions of the FI-MTJ, i.e. only homogeneous variations are considered. The effect of local changes of the hopping/coupling at the B/FI interface are analysed in III.2.4. Fig. III.17-(a) shows the wave period dependence on t for different FI parameters. The two FI represented by crosses and open circles display the same period regardless of t since they share the same value of δ despite unequal spin splittings. The period is however proportional to t in every case and results from the electron mobility increase for higher values of the hopping.

The amplitude of the oscillations A scales with t^5, as can be seen in Fig. III.17-(b); the power factor accounts for the lesser Green's function dependence on the hopping parameter in three regions of the FI-MTJ and the hoppings/couplings at to interfaces. It is noteworthy that the hopping parameter does not influence the commensurability between the torques and the lattice moment staggered character.

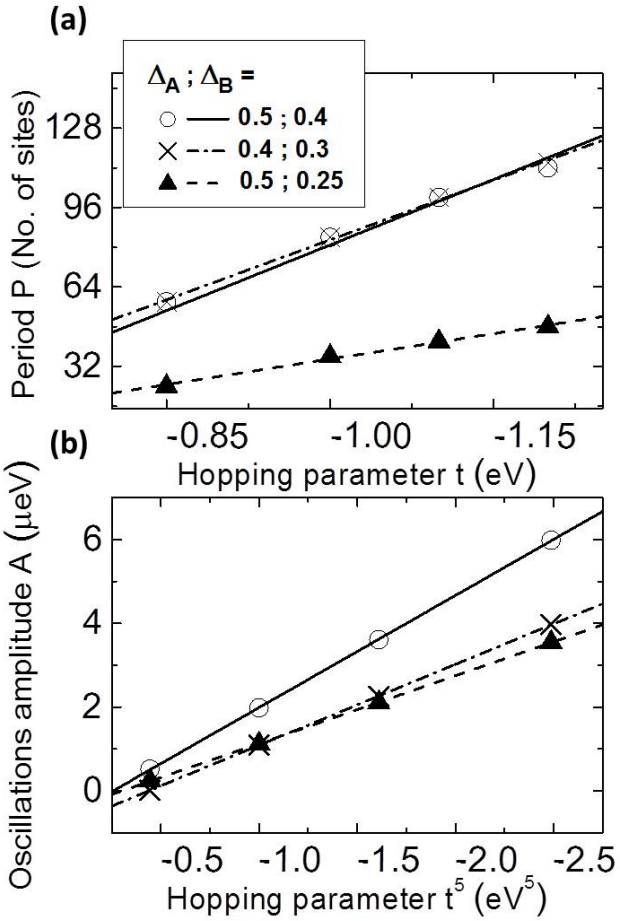

Figure III.17 – **(a)** Dependence on the hopping parameter t of the in-plane torque component waves period P for $\theta = \pi/2$ and V= -0.1V. **(b)** Corresponding dependence with t^5 of the torque waves amplitude. The three FI leads of **(a)** and **(b)** have Δ_A and Δ_B given in eV in the caption of **(a)**. The lines are linear fit to the data.

Influence of voltage on the torque modulation period

Regarding the dependence of the period on the applied bias examined in Fig. III.14, it must be stressed that relation (III.1) is valid for any given voltage. Fig. III.18 shows the $1/\delta$ dependence of the torque wave period P for three different applied bias. Data corresponding to V= -0.1 (plotted in Fig. III.16) is also shown by way of comparison.

As can be seen, the period slightly increases with bias for $1/\delta \geq 4$, but for a fixed value of this applied bias, the period is inversely proportional to δ. Moreover, the slope of the three linear fits corresponding to different applied bias is very similar, with a value of around 8 sites $\cdot$ eV. Therefore, an increase of the bias roughly amounts to a vertical shift of the period linear fit. The voltage dependence of this vertical shift is illustrated in Fig. III.14 for a 1-D FI/B/FI junction with ϵ_0= 1.5 eV, Δ_A= 0.5 eV and Δ_B= 0.25 eV.

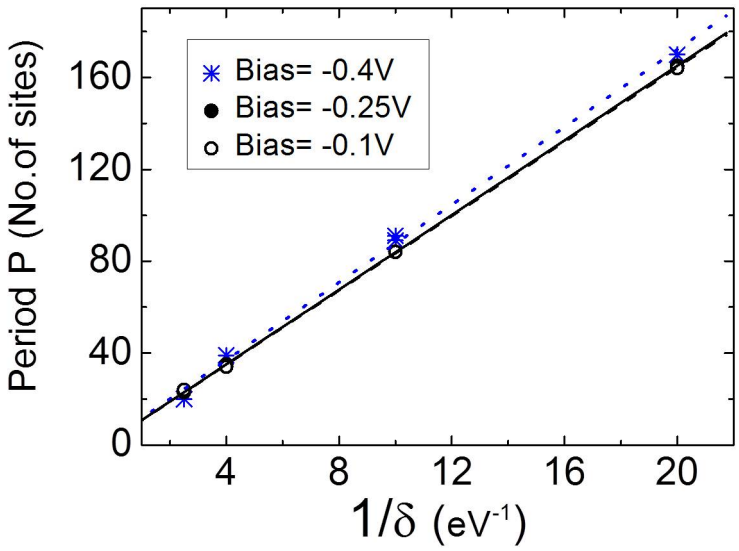

Figure III.18 – For different 1-D FI/B/FI MTJ, $1/\delta$ dependence of the in-plane torque component period P for $\theta = \pi/2$ and three different applied bias. The dash black, solid black and dot blue lines are linear fits to the data corresponding to -0.1V, -0.25V and -0.4V respectively.

Barrier effects on the torque wave's period and amplitude

In order to test the robustness of the wavy STT profiles shown above, the influence of the barrier properties was next investigated through the variation of barrier height U_B, the number of sites N_B and the hopping elements $t_{\alpha,a} = t_{b,\alpha'}$ at the interfaces.

For all the set of barrier parameters considered here, the staggered and wavy spatial distribution of torques is always present (not shown). While these three parameters affect the amplitude of the torques (see Fig. III.19), only a slight variation of the oscillations period was detected for different hoppings at the interfaces (a variation of 4 sites for a period of 34 sites (roughly 10%) was observed when the hopping at the interfaces $t_{\alpha,a} = t_{b,\alpha'}$ was multiplied by 4). Fig. III.19 represents the amplitude variations with the barrier height, the number of sites and the hopping parameter at the interfaces.

As can be seen in Fig. III.19 **(c)**, a good contact at the barrier interfaces, i.e. high hopping parameter $t_{b,\alpha'}$ is crucial to have high torque amplitudes. The dependence on the barrier height and the number of layers from Fig. III.19 **(a)** and **(b)** is quite intuitive: the amplitude decreases with the barrier height and exponentially decays with the number of sites, due to the specific dependence of the conductance on the transmission coefficients of the junction.

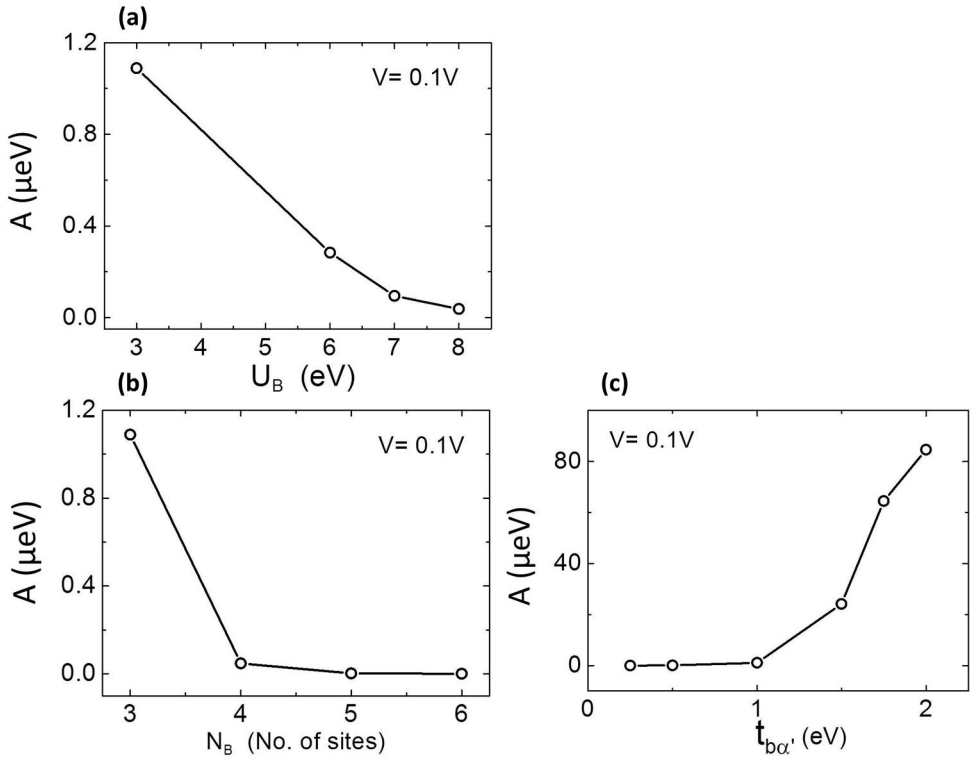

Figure III.19 – Dependence of the torque wave's amplitude on **(a)** the barrier height U_B. **(b)** the barrier's number of sites N_B. **(c)** the hopping parameter $t_{b,\alpha'}$ at the interfaces.

III.2.3 Spatial distributions of spin density and spin transfer torque in 3-D ferrimagnetic-based tunnel junctions: spin-modulated torque waves with damping

The STT local distribution is next analysed in more realistic 3-D FI-MTJ. In this case, the full integration in energy and $\mathbf{k}_{\|}$ states is needed, which could potentially extinct the STT wave-like behaviour.

The spatial distribution of the two torque components for two different FIs in a 3-D geometry is shown in Fig. III.20. Despite the weak damping that spoils the oscillations' periodic character similar to the case of F-MTJ ([Manchon et al., 2008a], [Wang et al., 2008]), the torque waves are found to be still present. The damping is introduced by the dephased torque contributions due to $\mathbf{k}_{\|}$ integration.

The out-of-plane component of the torque seems to be as smooth as the in-plane component, except at the first layers next to the interface, where strong distortions appear. This is explained by the short range action of the RKKY interaction in 3-D geometries. Similarly to the AF case, the zero voltage contribution of the STT decays very fast from the interface, not affecting the STT in the bulk, as can be appreciated in Fig. III.21.

As shown in Fig. III.22, the parameter δ strongly affects the spatial extension of the STT wave beatings in the 3-D case, similar to the 1-D geometries reported in III.2.2. As illustrated in Fig. III.20, almost three STT wave beatings appear in the first 50 layers for

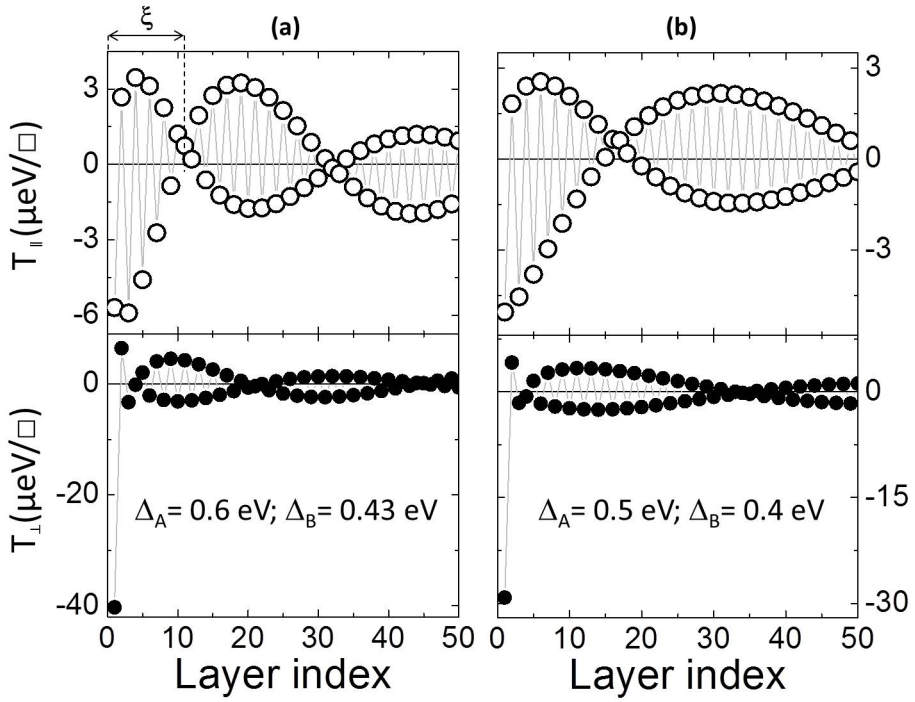

Figure III.20 – Computed spatial distributions of the in-plane ($T_{\parallel}$) and out-of-plane ($T_{\perp}$) components of the torque in μeV per unit of surface $\square$ for a 3-D FI/B/FI junction with $\theta = \pi/2$, V= -0.1V, ϵ_0= 1.5eV and **(a)** Δ_A= 0.6 eV; Δ_B= 0.43 eV (δ= 0.17 eV). **(b)** Δ_A= 0.5 eV; Δ_B= 0.4 eV (δ= 0.1 eV).

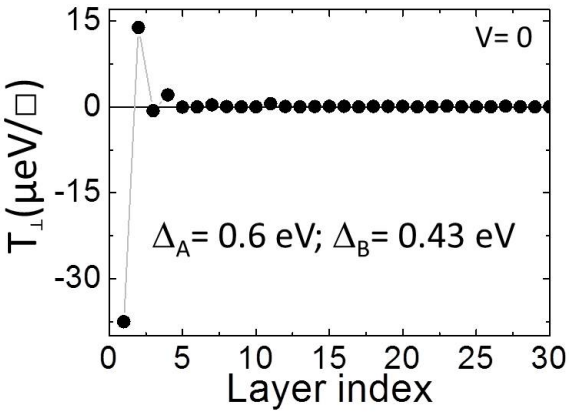

Figure III.21 – Spatial distribution of the out-of-plane torque in μeV per unit of surface $\square$ at zero bias (RKKY interaction) for a 3-D FI/B/FI junction with $\theta = \pi/2$, V= -0.1V, ϵ_0= 1.5eV, Δ_A= 0.6 eV and Δ_B= 0.43 eV (δ= 0.17 eV).

the FI with δ= 0.17 eV, but only two appear for the FI characterised by δ= 0.10 eV.

Since damping spoils the periodic character of these oscillations, the concept of period P previously discussed no longer stands. Of note, these damped oscillations cannot be defined as pseudo-oscillations, and a new parameter ξ is therefore introduced to keep track of the wavy length scale. We define ξ as the number of layers between the B/FI interface and the first layer at which the torque wave gets zero, as illustrated in Fig. III.20. It would correspond to half a period in the 1-D case.

III.2.4 Pseudoperiod of the spin-modulated torque waves

The two insets in Fig. III.22 illustrate the in-plane torque deposited in each layer of the right lead in two 3-D FI-MTJ with different δ. ξ is plotted in Fig. III.22 as a function of $\frac{1}{\delta}$ which governs the oscillations period in 1-D FI-MTJ.

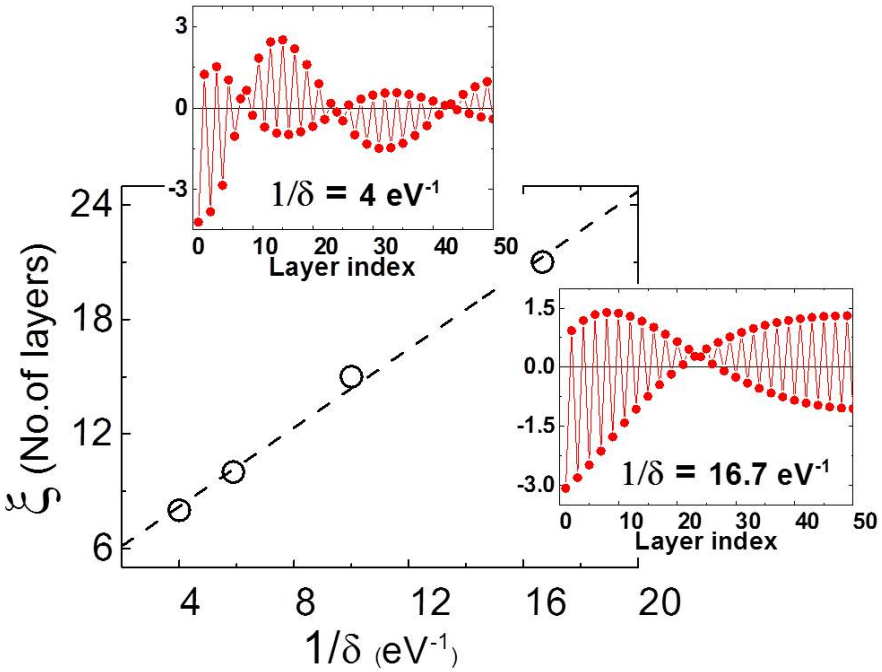

Figure III.22 – For four 3-D FI leads, $1/\delta$ dependence of the torque characteristic length (ξ) for $\theta = \pi/2$ and V= -0.1V. Upper(Lower) inset: spatial distribution (in μeV per unit area) of the in-plane torque wave for $1/\delta = 4$ eV^{-1} ($1/\delta = 16.7$ eV^{-1}). The dashed line is a linear fit to the data.

The linear fit provides clear evidence that relation (III.1) holds for ξ even in 3-D FI-MTJ, thus confirming that the parameter δ is a key indicator for quantifying STT characteristic lengths in FI metals.

$$\boxed{\xi \propto \frac{1}{\delta}} \tag{III.3}$$

It must be emphasized here the importance of the staggered character of the in-plane torque over the penetration depth given by ξ. In effect, similar to the AF case examined in III.1.1, the torque deposited in sublattice A adds up to the torque delivered in sublattice B, since localized spins owning to different sublattices are aligned in opposite directions (see Fig. II.2). This is in contrast to the case of ordinary F-MTJ, where positive and negative local torques are counterbalanced to give the total torque delivered, which is found to be comparable in amplitude to the torques discussed in this letter. Therefore, in-plane torques in FI leads with low values of δ are expected to be very efficient thus driving current induced order parameter dynamics.

STT from the exchange field

The local out-of-plane and in-plane spin densities shown to be responsible for the local STT in AF-based tunnel junctions are depicted in Fig. III.23 for the FI case. A damped out-of-plane spin density wave on sublattice A yields a damped in-plane torque wave in the same sublattice. The lower torque exerted on sublattice B is due to the lower amplitude of the out-of-plane spin density wave in this sublattice (see Fig. III.23).

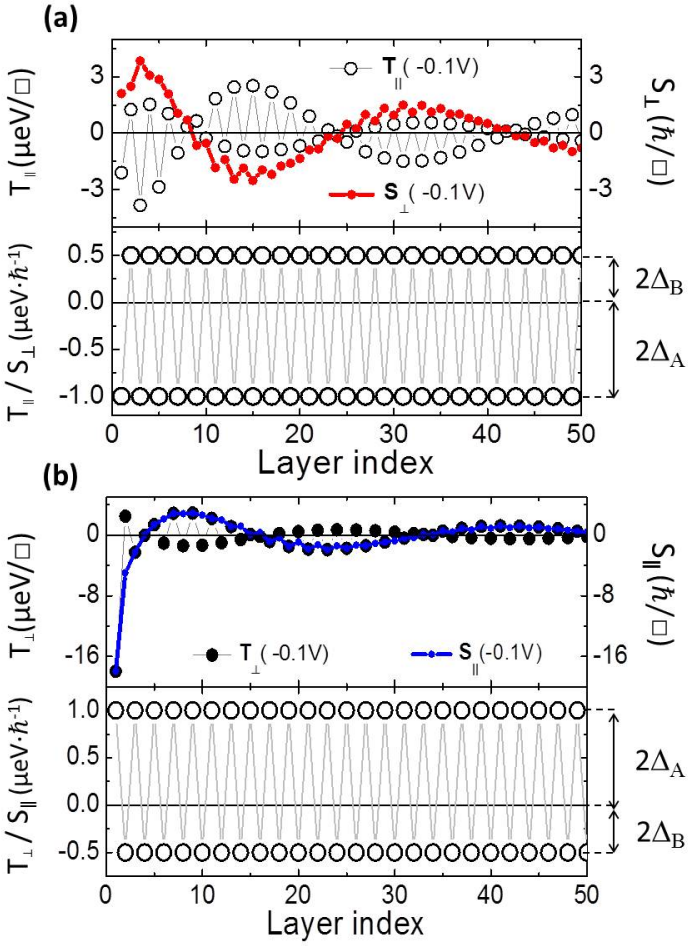

Figure III.23 – **(a)** (Top) Computed spatial distribution of the in-plane torque ($T_\parallel$) and out-of-plane spin density ($S_\perp$) for a 3-D FI/B/FI junction with $\theta = \pi/2$, V= -0.1V ϵ_0= 1.5 eV, Δ_A= 0.5 eV and Δ_B= 0.25 eV in both FI leads. (Bottom) Local ratio $T_\parallel/S_\perp$ showing explicitly the exchange field $\mathbf{\Delta}_A = 2\Delta_A$; $\mathbf{\Delta}_B = 2\Delta_B$ **(b)** (Top) Computed spatial distribution of the out-of-plane torque ($T_\perp$) and in-plane spin density $S_\parallel$) for the same system. (Bottom) Local ratio $T_\perp/S_\parallel$ showing explicitly the exchange field $\mathbf{\Delta}_A = 2\Delta_A$; $\mathbf{\Delta}_B = 2\Delta_B$. The red and blue thick lines representing the out-of-plane and in-plane spin densities in **(a)** and **(b)** respectively refer to the right-hand ordinate.

The relation between torques and spin densities, accounted for by the ratios $T_\parallel/S_\perp$ and $T_\perp/S_\parallel$ are plotted in the bottom panels of Fig. III.23 **(a)** and **(b)**; in contrast to the AF case (see Fig. III.8), the spin splittings on each sublattice are not the same, and the exchange field $\mathbf{\Delta}$ oscillates with a staggered character between the values ± 0.5 and ± 1

eV in the case of the FI with Δ_A= 0.5 eV and Δ_B= 0.25 eV examined in the Figure.

Effects of roughness at the barrier interfaces

The robustness of the STT wave patterns face to barrier effects is next tested by reducing the hopping parameters $t_{\alpha,a}$ and $t_{b,\alpha'}$ at the interfaces, similarly to what we did for the 3-D AF case in section III.1.2, and in 1-D FI systems in section III.2.2. Fig. III.24 **(a)** and **(b)**, show the STT spatial distribution corresponding to $t_{b,\alpha'}$= 0.4 eV and 0.7 eV respectively. The hopping parameter inside the leads is kept at 1 eV.
As can be seen both components are reduced when the coupling becomes weaker, but the staggered and wavy profile do not disappear.

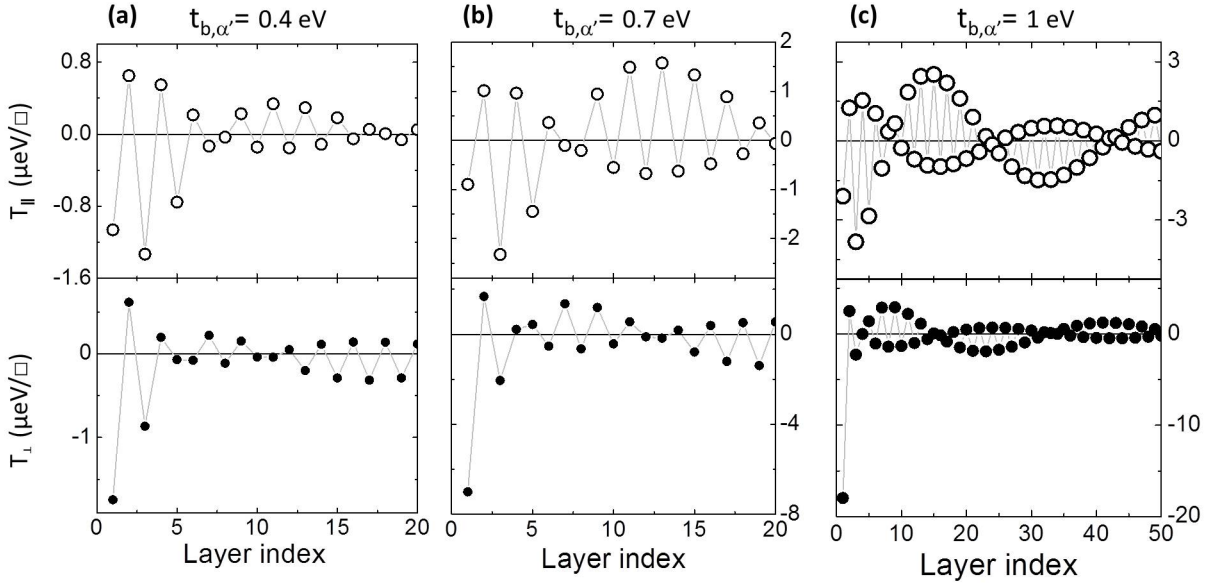

Figure III.24 – Computed spatial distributions of the in-plane ($T_\parallel$) and out-of-plane ($T_\perp$) components of the torque in μeV per unit of surface □ for a 3-D FI/B/FI junction with $\theta = \pi/2$, V= -0.1V, ϵ_0= 1.5eV, Δ_A= 0.5 eV and Δ_B= 0.25 eV in both FI leads. The hopping parameter at the barrier interfaces (coupling) is $t_{b,\alpha'} = t_{a,\alpha}$= **(a)** 0.4 eV. **(b)** 0.7 eV. **(c)** 1 eV.

III.2.5 Charge current density and ferrimagnetic tunneling magnetoresistance

The voltage dependence of the charge current density is shown in Fig. III.25 as a function of applied bias for antiparallel, perpendicular and parallel magnetic states of left and right FI leads. The behaviour is analogous to that of the AF-based tunnel junctions, that is, linear increase for low bias and saturation at a voltage which is specific for each magnetic configuration (see Figs. III.11 **(b)** and III.12).

TMR ratios are shown to be strongly sensitive to the magnetic properties of the FI. This is similar to the AF case, where TMR is shown to be strongly influeced the

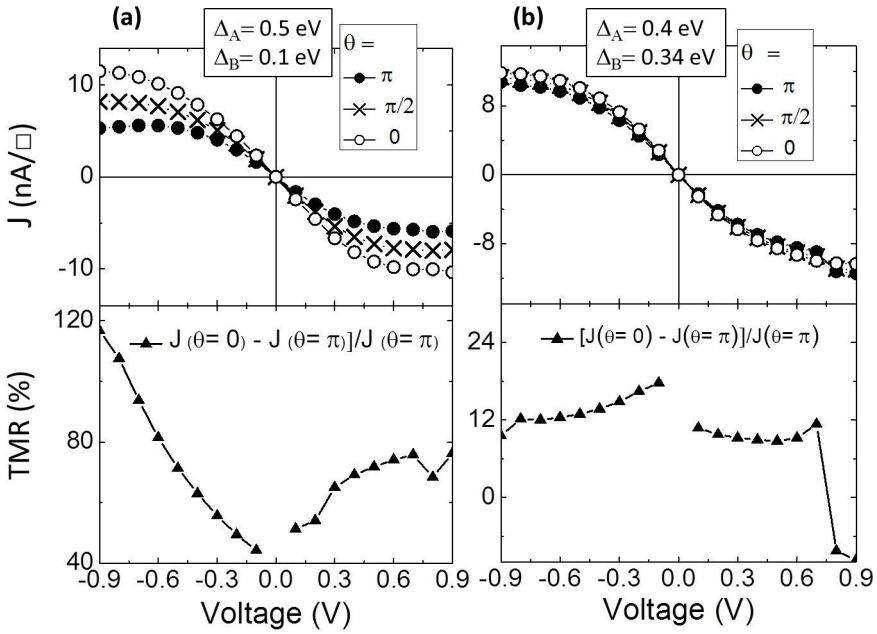

Figure III.25 – Calculated voltage dependence of the charge current density I in nA by unit of surface □ for three different angles θ (top) and TMR (bottom) in a 3-D FI/B/FI tunnel junction with **(a)** Δ_A= 0.5 eV; Δ_B= 0.25 eV. **(b)** Δ_A= 0.4 eV; Δ_B= 0.34 eV.

electronic structure properties. The two TMR curves represented in Fig III.25 **(a)** and **(b)** corresponding to two different spin splittings sets exhibit opposite trends with increasing bias. The maximum values reached at -0.9 and -0.1 eV respectively differ by one order of magnitude.

The same numerical instability problem encountered for AF leads is found here, i.e. the J-V curves are not symmetric for positive and negative voltages. A more detailed study of this issue should be carried out in future works since it must be taken into account to chose the better FI material for technological applications.

III.2.6 Spatial distributions of spin density and spin transfer torque in 3-D antiferromagnetic-based tunnel junctions with compensated layers: out-of-plane torque modulations

Although this section is devoted to AF-based tunnel junctions, it has been included here since the spatial behaviour of the out-of-plane torque component exhibit striking similarities with that of FI. As explained in chapter 2, AF order can be modelled by alternating layers of *compensated* spins (called G-type AF in ref [Saidaoui et al., 2014]). Actual crystal lattices such as $IrMn_3$ are deposited in the (1,1,1) direction, perpendicular to a family of compensated planes. It is therefore interesting to investigate whether the STT is still present in these configurations, where there is no net magnetization in the xz plane of the system, perpendicular to transport. The spatial distribution of STT for a

3-D symmetric AF/B/AF tunnel junction constituted of two leads of compensated layers is depicted in Fig. III.26.

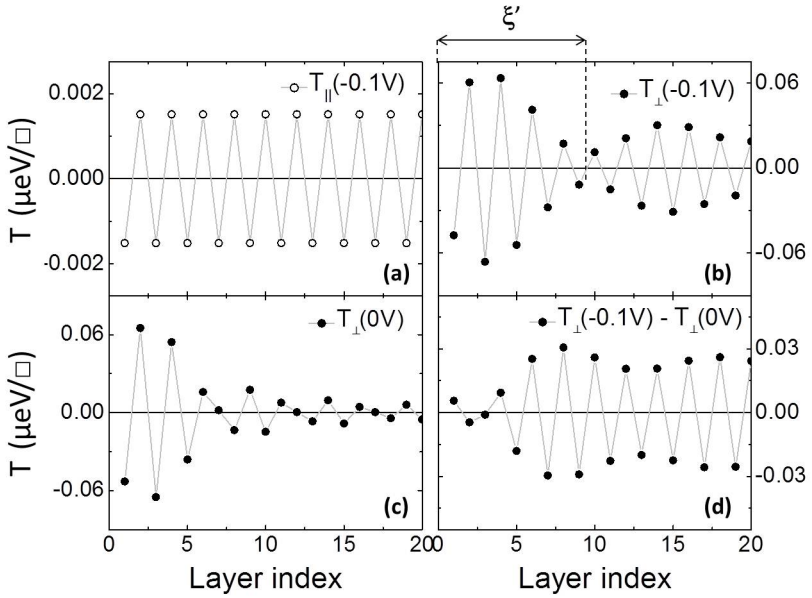

Figure III.26 – Computed spatial distributions of the STT components for a 3-D symmetric AF/B/AF junction of compensated layers with $\theta = \pi/2$, ϵ_0= 1.5eV and Δ= 0.45 eV in both AF leads. **(a)** In-plane torque ($T_{\parallel}$) at V= -0.1 V. **(b)** Out-of-plane torque ($T_{\perp}$) at V= -0.1 V. **(c)** Out-of-plane torque at V= 0V (RKKY interaction). **(d)** Voltage-induced-out-of-plane torque (the out-of-plane torque at zero bias was subtracted to the out-of-plane torque at -0.1V).

The in-plane and out-of-plane torques components are still present but they are reduced by 3 and 2 orders of magnitude respectively with respect to the uncompensated case. In addition, it is impossible to know whether these torques are efficient, since their local distribution on each atomic site of the fully compensated planes cannot be calculated with the formalism used here. In other words, if the torque deposited in each compensated layer has the same sign in every atomic site, then it will not be efficient, since opposite magnetic moments on the compensated plane are intended to rotate in opposite senses. However, first principles calculations applied to AF spin valves show that this spatial distribution within each compensated plane of a FeMn AF can be polarised differently in inequivalent sublattices, being thus efficient [Xu et al., 2008].

Here, the same staggered behaviour reported for uncompensated AFs is found for the in-plane component, but the out-of-plane component appears to be modulated analogously to the FI case. The oscillations are damped too (which is not the case for uncompensated AF), and the sign of the torque deposited in each sublattice is conserved, which is advantageous for the effective torque. Again, these modulations can be characterized by their amplitude and a parameter ξ' analogous to ξ for FI, defining the length of the first modulation beating (depicted in Fig. III.26 **(b)**). The dependence of both parameters on the spin splitting Δ is plotted in Fig. III.27.

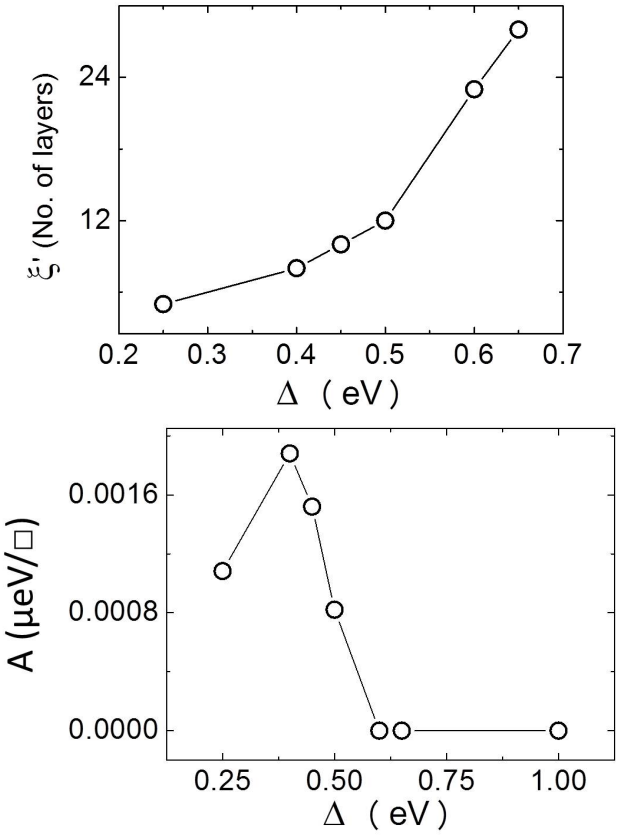

Figure III.27 – Variation of the wave length scale ξ' and the amplitude A with the spin splitting Δ in a 3-D AF/B/AF junction of compensated layers with $\theta = \pi/2$, ϵ_0= 1.5eV and V= -0.1 V.

As can be seen in the top panel of the Figure, the dependence of ξ' on the spin splitting Δ in fully compensated AFs is analogous to that of ξ on $1/\delta$. The pseudoperiod ξ' does not follow a well-defined law, but it increases monotonically with the spin splitting. Higher values of Δ would be favourable for the effective torque, since the amplitude of the modulation is higher for the first beating, however the left panel of Fig. III.27 demonstrates that this amplitude decreases dramatically with the spin splitting from conventional values above 0.35 eV. Despite the interesting spatial behaviour of the out-of-plane component, the magnitude of STT is vanishing small in fully compensated AF-based tunnel junctions, what makes the uncompensated configuration a better candidate for technological applications.

III.2.7 Investigation on the origin of the spatial distribution of spin transfer torque in ferrimagnetic- and antiferromagnetic-based tunnel junctions: local density of states.

As a first attempt to explain the interesting distribution of torques and consequently spin densities inside the magnetic leads in tunnel junctions, the site-resolved LDOS for a

given spin at the Fermi level was investigated in a 1-D chain with F, AF and FI order, in order to seek for a correlation between spin accumulation and the number of states available in a given layer. The results for one F, one AF and two FI chains are shown in Fig. III.28 **(a)**, **(b)**, **(c)** and **(d)** respectively.

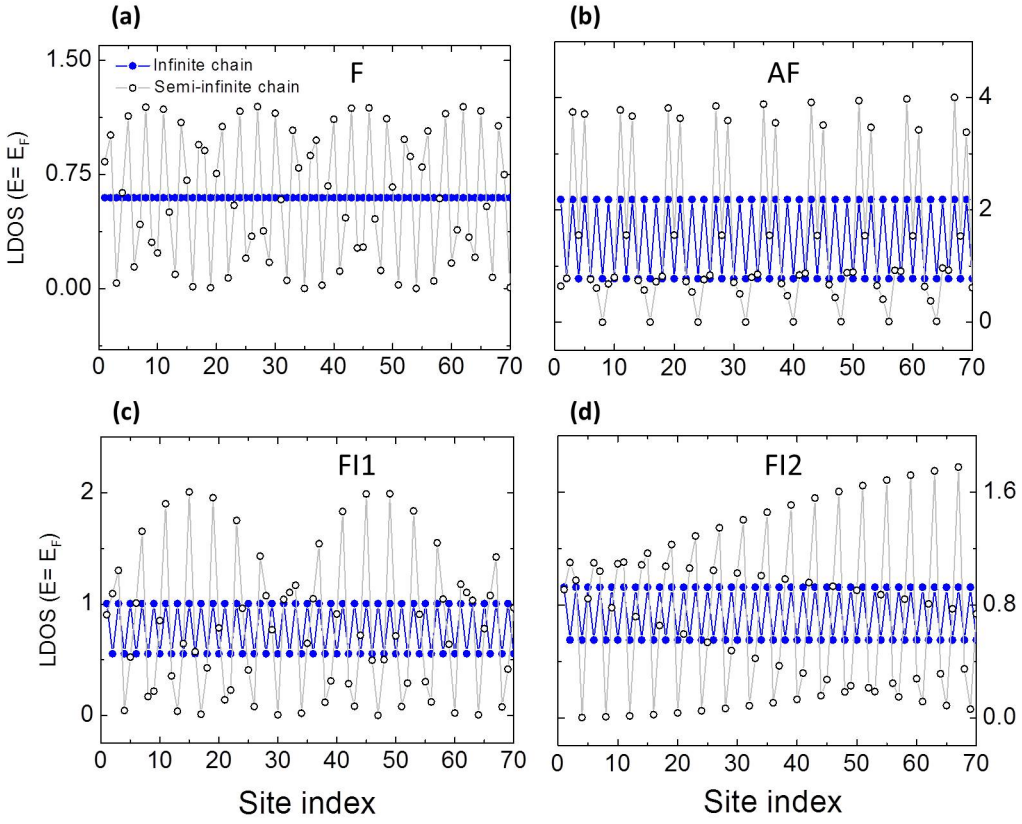

Figure III.28 – Spatial variation of the local density of states (LDOS) at the Fermi level for an itinerant spin in a 1-D infinite chain (blue solid circles) and a 1-D semi-infinite chain (open circles) with: **(a)** Ferromagnetic order characterized by ϵ_0= 1.5 eV and Δ= 0.5 eV. **(b)** Antiferromagnetic order, ϵ_0= 2 eV and Δ= 1 eV. **(c)** Ferrimagnetic order, ϵ_0= 1.5 eV, Δ_A= 0.5 eV and Δ_B= 0.4 eV (δ= 0.1 eV). **(d)** Ferrimagnetic order, ϵ_0= 1.5 eV, Δ_A= 0.5 eV and Δ_B= 0.25 eV (δ= 0.25 eV).

The blue solid circles represent the LDOS of an infinite chain. When the chain is cut at the site index 0 to reproduce a semi-infinite lead, the LDOS is represented by the open symbols. The translational symmetry of infinite chains imposes that the site-resolved energy profile of the LDOS for a given spin possesses only one profile in the F case (all sites are equivalent) and two profiles in the AF and FI cases (each site correspond to one of the two sublattices of up and down localized spins) (see Fig. II.4).

The energy dependence of the LDOS is depicted in Figs. II.4 and II.5 for a FI and a F chain respectively. Thus, the LDOS at the Fermi level takes only one value in a F chain and two values in a FI or AF chain, for a given spin. This is clearly illustrated in Fig. III.28. However, when the chain is cut, the translational symmetry is broken and not all sites are equivalent any more, as can be observed in Figs. II.6 and II.8. For a F lead,

the LDOS corresponding to the semi-infinite chain exhibits a double wavy pattern that oscillates around the constant value for the infinite chain. One wave is located in even sites and the other in odd sites, they have the same amplitude, but are spatially shifted.

For the FI case, there exist multiple waves oscillating around the two constant values for the infinite chain. The amplitude of the waves hosted in sublattice A (where the spin splitting is higher) are also higher. This could explain the oscillatory behaviour of the spin density, but the dependence of the period on the parameter δ is opposite. Note that the spatial period of the LDOS waves in Fig. III.28 **(d)** is much longer than that of **(c)**, although they correspond to FIs with δ= 0.25 eV, and δ= 0.1 eV respectively. In other words, similar oscillatory behaviour is observed in STT and LDOS, however, their variations with δ are opposite in certain cases, and they cannot be directly linked.

In turn, the LDOS pattern encountered for AF leads is far more complex than the simple flat distribution of spin accumulation shown in Fig. III.8. Further investigations are thus required to explain the fundamental origin of the rich spatial distributions of torques and spin densities.

III.2.8 Summary

In conclusion, a detailed analysis of the STT spatial distribution in FI-based tunnel junctions has been carried out using a TB Hamiltonian that captures its essential electric and magnetic qualitative characteristics, in the framework of the nonequilibrium Keldysh formalism. The in-plane and out-of-plane torques are found to be spatially staggered, and they exhibit a striking wave-like behaviour perfectly modulated by spin accumulation. Thus, this work has addressed the equivalence of torques computed from the exchange field along the z direction in FI-MTJ and through the divergence of the spin current.

The characteristic lengths of the torque oscillations are shown to be strongly dependent on the electronic and magnetic features of the FI, namely the spin splittings of the two FI sublattices and the bandwidth parametrized here by the hopping matrix element of the TB Hamiltonian. Furthermore, the fundamental parameter that governs the torque waves period in 1-D FI-MTJ and the spatial extension of the damped torque oscillations in 3-D FI-MTJ is identified. This fundamental parameter can be considered as an effective exchange field in FIs, similar to the homogeneous exchange field in the F case. The mentioned characteristic lengths can also be tuned via the applied bias across the junction [Merodio et al., 2014c].

These theoretical results may be of importance to choose the best suited FI material for STT-based spintronics devices and will serve as a guideline for experiments on spin penetration length in these materials using, for example, ferromagnetic resonance and spin pumping effect [Ghosh et al., 2012], [Merodio et al., 2014a]. In addition, experiments such as spin-transfer driven ferromagnetic resonance and spin-torque diode effect

[Tulapurkar et al., 2005], [Sankey et al., 2006], [Sankey et al., 2008], [Kubota et al., 2008], where the magnitude and direction of the STT are extracted in magnetic tunnel junctions, could also demonstrate the theoretical results predicted in this work.

Chapter IV

Experimental determination of STT characteristic lengths in antiferromagnets

IV.1 Introduction

The property that STT acts throughout the entire volume of an AF rely on phase-coherent interferences and will surely apply strictly only in idealized AFs with perfect epitaxially grown crystal lattices. However, as explained in II.1.1, realistic polycrystalline AFs contain spin disorder that will produce noncoherent spin scattering both in the AF bulk and at interfaces: impurities, interstitial or vacancy defects, interdiffusion at the interfaces, interface roughness, grain boundaries,stacking faults, complex spin structures, e.g. 3Q for IrMn and FeMn, etc. Therefore, we decided to experimentally investigate the effect of disorder on the STT characteristic lengths in two different AFs: IrMn and FeMn. However, as explained in IV.3.1 the required lateral size of the samples used here to study spin-dependent characteristic lengths in AFs is too large to deposit a thin and continuous insulating layer of good quality. Therefore, spin-valve-like structures were used here instead of AF tunnel junctions, replacing the insulating layer with a thicker metallic spacer. The averaging over the incidence angles of the incoming electrons wave vectors will thus come into play. This wave vectors averaging might affect the STT efficiency through the AF thickness, in contrast to the 3-D theoretical predictions performed in III for tunnel barriers, which filter the wave vectors incidence angles.

Some of the critical parameters for spin dependent transport in general are: 1) the spin penetration depth originating different mechanisms like spin flip related to the terminology: spin diffusion length and spin precession dephasing with the associated spin dephasing length terminology, and 2) the spin mixing conductances, since they both control current perpendicular to plane GMR [Bass and Jr, 2007]. Magnetoresistive and dynamic

experiments are the most common tools to study spin length scales and mixing conductances in thin films [Bass and Jr, 2007]. However, these two types of studies are not ideal for AF materials since the former shows very low magnetoresistive signals and the latter requires very high (THz) frequencies for dynamics excitation. Earlier attempts to characterize characteristic lengths in IrMn and FeMn using NiFe/Cu/AF/Cu/NiFe spin valves and cryogenic-temperature are reported in in Refs. [Park et al., 2000],[Acharyya et al., 2010], [Acharyya et al., 2011]. Although the authors could not extract definite values they concluded on significant spin flipping at (IrMn,FeMn)/Cu interfaces and pointed towards nanometric spin penetration depths in IrMn and FeMn. An alternative way to determine spin absorption and spin mixing conductances in thin films was recently implemented. It is based on the spin pumping phenomenon, the STT reciprocal effect and is best suited for AFs [Berger, 1996]-[Ghosh et al., 2012]. The method indirectly monitors spin absorption in materials surrounding a F_{res} layer excited at resonance by ferromagnetic resonance (FMR). The oscillating F_{res} magnetization transfers spin angular momentum to conduction electrons of the adjacent layers. Loss of spin angular momentum by the conduction electrons results in F_{res} resonance linewidth broadening. This latter is related to the attenuation (i.e. to the Gilbert damping α) of the F_{res} excitations. One can distinguish between local, i.e. intrinsic losses, that is inside the precessing F_{res} (α^0), and non-local, i.e. extrinsic damping where spins are lost outside the F_{res} (α^{pump}), i.e. absorbed by the surrounding materials/interfaces under study. For various materials/interfaces, this method compares the spin absorption efficiency (related to spin mixing conductances) since depending on the materials/interfaces properties the spins can be entirely absorbed or backscattered into the F_{res}. Additionally, this technique determines spin absorption length scales by investigating the F_{res} damping variations with the thickness of the neighbouring spin sink (i.e. absorbing material under investigation)[Mizukami et al., 2001].

In this chapter, spin dependent transport in two typical AF polycrystalline thin films, IrMn and FeMn is studied using the spin pumping technique, in order to measure the characteristic length scales and thereby to determine spin absorption mechanisms in these two materials. The first part is devoted to a more detailed description of the underlying FMR and spin pumping working principles necessary to understand how characteristic lengths in the two AFs are measured. The sample preparation process, measurement setup and experimental results are addressed in the second part.

IV.2 Ferromagnetic resonance and spin pumping

The spin pumping effect and the FMR technique are directly related to the magnetization behaviour of a F element when a time-varying magnetic field is applied. The time evolution of the magnetization is captured by the Landau-Lifshitz-Gilbert equation, which describes the influence of external magnetic fields and the presence of adjacent materials

next to the F on its magnetization dynamics. A brief discussion of this equation is thus essential to understand FMR and spin pumping effect underlying features.

IV.2.1 Magnetization dynamics: Landau-Lifshitz-Gilbert equation

In the absence of STT, the time dependence of the total or spontaneous magnetization $\mathbf{M}$ for a magnetic system obeys the following dynamical equation known as Landau-Lifschitz-Gilbert (LLG) equation [Lakshmanan, 2011]:

$$\frac{d\mathbf{M}}{dt} = -\gamma \mathbf{M} \times \mathbf{H}_{\text{eff}} + \frac{\alpha}{|\mathbf{M}|}(\mathbf{M} \times \frac{d\mathbf{M}}{dt}) \tag{IV.1}$$

where the modulus $|\mathbf{M}|$ is assumed to remain constant, so that the magnetization vector can be written as $\mathbf{M} = |\mathbf{M}| \cdot \mathbf{m}$, with $\mathbf{m}$ being a unit vector pointing in the magnetization direction. The two terms at the right hand side of the LLG equation are described in detail below.

First term of the Landau-Lifschitz-Gilbert equation: magnetization precession

The first term at the right-hand side of equation (IV.1) corresponds to the magnetization precession around an effective field $\mathbf{H}_{\text{eff}}$ whose origin is described bellow. $\gamma = -g\frac{e}{2m_e}$ is the gyromagnetic ratio (g is the Landé factor, e and m_e are the charge and the electron mass respectively) and μ_0 is the magnetic permeability in vacuum.

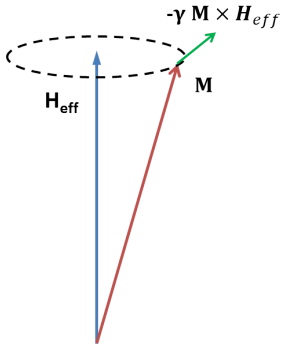

Figure IV.1 – Precession movement of the magnetization $\mathbf{M}(t)$ around the effective field $\mathbf{H}_{eff}$ described by the first term at the right-hand side of Eq. (IV.1).

The effective field is the local field felt by the magnetization (to which spins respond) and corresponds to the variational derivative of the magnetic energy density with respect to the orientation of the magnetization:

$$\mathbf{H}_{\text{eff}} = -\frac{1}{\mu_0 |\mathbf{M}|}\frac{\delta e_{\text{tot}}}{\delta \mathbf{m}} \tag{IV.2}$$

The total magnetic energy density is the sum of four energy contributions: exchange, anisotropy, Zeeman and demagnetizing energies:

$$e_{\mathrm{tot}} = e_{\mathrm{ex}} + e_{\mathrm{a}} + e_{\mathrm{Zeem}} + e_{\mathrm{dem}}$$

Exchange energy

Exchange interaction occurs between the spins of neighbouring atoms. This short range interaction tends to align nearby spins in the same direction and has a purely quantum mechanical origin. A change in the direction of the spins leads to a change in the electrostatic repulsion between neighbouring electrons, since the spatial overlap of the electronic wave functions permitted by the exclusion principle is different for different spin configurations. The exchange energy for a system of N atoms with spins $\mathbf{S}_i$ reads (Heisenberg Hamiltonian):

$$e_{\mathrm{ex}} = \sum_{i,j}^{N} -J_{i,j}\mathbf{S}_i \cdot \mathbf{S}_j$$

where $J_{i,j}$ are the exchange integrals related to the spatial overlap of neighbouring electronic orbitals. A positive(negative) value of these exchange integrals leads to a ferromagnetic(antiferromagnetic) order. Thus, the exchange interaction is responsible for the spontaneous ordering of atomic magnetic moments occurring in magnetic solids.

In a classical approach, a suitable expression of the exchange energy must be available at a continuous scale, by averaging the atomic description. For instance, the exchange energy for a simple cubic lattice of lattice parameter a reads:

$$e_{\mathrm{ex}} = \frac{JS^2}{a} \int dV((\nabla m_x)^2 + (\nabla m_y)^2 + (\nabla m_z)^2)$$

where $S = |\mathbf{S}_i|$. The exchange coupling constant J depends on temperature because of the temperature variation of the interatomic distances.

Magnetocrystalline anisotropy energy

In a classical picture, exchange interactions makes all spins to be parallel, but the energy remains invariant whatever the direction the spins are aligned with. Exchange interaction determines only the orientation of the sublattice magnetizations relative to each other. However, the total magnetic energy of a ferromagnet does depend on the particular orientation of the spontaneous magnetization with respect to the crystal lattice or crystallographic axes. The main energy contribution which depends on the direction of the magnetization is called magnetocrystalline anisotropy energy e_a and is several orders of magnitude weaker than the exchange interaction. It is minimum when the magnetization is aligned along certain equivalent directions related with the symmetry

operations living invariant the environment of each magnetic atom. These energetically favourable directions are called "easy axis".

The origin of the magnetocrystalline anisotropy is the spin-orbit interaction $\hat{H} = \lambda \hat{\mathbf{L}} \cdot \hat{\mathbf{S}}$, which couples spin angular moments with orbital angular moments (in contrast with exchange interaction which couples only spin angular moment). Thus, the orientation of the spins is indirectly related with the direction of the orbital moment. This orbital moment created by the orbital motion of electrons couples in turn with the crystal field created by neighbouring charges. Consequently, the energy of these orbitals depends on their orientation with respect to the surrounding crystal field. The spin orientation will then align with the preferential direction that minimises the spin-orbit interaction. For cubic crystals, the anisotropy energy up to sixth order in the magnetization components reads:

$$e_a(\mathbf{m}) = K_1(m_x^2 m_y^2 + m_y^2 m_z^2 + m_z^2 m_x^2) + K_2 m_x^2 m_y^2 m_z^2$$

where the anisotropy constants K_1 and K_2 depend on the material both in magnitude and sign, and strongly vary with temperature.

In small samples and ultrathin magnetic films other anisotropy contributions such as surface, interface, and exchange anisotropies might come into play. This effect is attributed to the reduced symmetry of the atoms close to a surface with respect to those in the bulk. Hence the form of the magnetocrystalline anisotropy is different at the surface.

Zeeman energy

The Zeeman energy is simply the energy of the interaction between the magnetization and an external magnetic field:

$$e_{\text{Zeem}} = -\mu_0 \mathbf{M} \cdot \mathbf{H}_{ext}$$

Obviously, the magnetization tends to align with the external field in order to minimise this energy term.

Magnetostatic (stray field) energy

The magnetostatic energy arises from the coupling of the magnetization with the field created by matter, i.e. the field created by the magnetization itself, called "stray field" or "demagnetizing field":

$$e_{\text{dem}} = -\frac{1}{2}\mu_0 \mathbf{M} \cdot \mathbf{H}_d$$

The internal demagnetizing field $\mathbf{H}_d$ is opposite to the magnetization, and reduces the external applied field. The magnetostatic energy is also small in comparison with the

exchange energy contribution, but is a long range contribution responsible for the domain formation in ferromagnetic materials, which reduces the magnetic energy stored in the field. The stray field or "demagnetizing field" is proportional to the magnetization; the proportionality is given by the demagnetizing factors $N_{i,j}$ of the demagnetizing tensor $\overline{\overline{N}}$: $\mathbf{H}_d = -\overline{\overline{N}} \cdot \mathbf{M}$. $\overline{\overline{N}}$ depends on the shape of the sample. Indeed, the demagnetizing field is high when the magnetization is in a direction of small dimension. It will induce the magnetization to orient towards the largest dimensions of the sample, for instance, in the plane of a thin film or along the axis of a nanowire.

Second term of the Landau-Lifschitz-Gilbert equation: intrinsic damping of the magnetization precession

The second term at the right-hand side of Eq. IV.1 is a phenomenological term which accounts for damping processes (similar to a viscous force in an harmonic oscillator). The phenomenological damping factor α is a positive number in the range of 0.01-0.04 for longitudinal magnetic recording media [Inaba et al., 1997], usually found from comparison with experiments. It represents all relaxation mechanisms arising from the coupling of the magnetization with the environment, namely crystal lattice vibrations, magnons, conduction electrons and other external sources. Thus, the magnetization relaxes in a timescale of the order of nanoseconds.

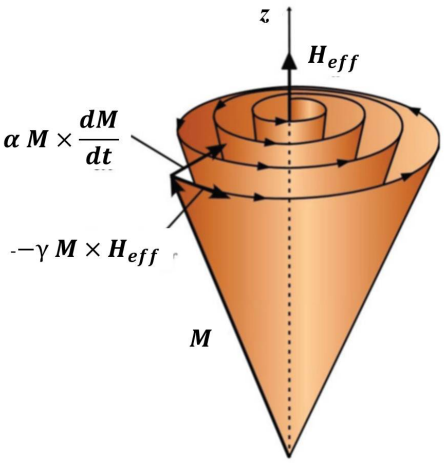

Figure IV.2 – Illustration of the precession movement of the magnetization $\mathbf{M}$ around the effective field $\mathbf{H}_{eff}$ described by both terms at the right-hand side of Eq. IV.1, adapted from Ref [Rezende et al., 2013].

This dissipative term is the responsible for the magnetization to be eventually aligned with the effective field, otherwise the precession movement would continue forever and the equilibrium would never be reached. The smaller the value of α the longer the magnetization precesses before equilibrium is achieved. It acts perpendicular both to the magnetization $\mathbf{M}$ and the direction of motion $\frac{d\mathbf{M}}{dt}$, and just like the precession term con-

serves the magnitude of the magnetization. As will be described bellow, it explains the linewidth of the absorption signal in resonance experiments.

IV.2.2 Ferromagnetic resonance

Detecting the precessional motion of the magnetization in a ferromagnetic sample is the underlying principle of ferromagnetic resonance (FMR) to measure its magnetic properties. This method utilizes an applied static magnetic field H_{DC} that exerts a torque on the sample magnetization and makes the magnetic moments to precess around the total effective field H_{eff}; in order to counterbalance the damping term in Eq. (IV.1), a transverse RF field H_{RF} (microwaves ranging typically 1-35 GHz) is applied perpendicular to the static field H_{DC}. As explained below, when the RF field frequency ω matches the resonance frequency extracted from Eq. (IV.1) and determined by the applied H_{DC} field, the microwave power is absorbed by the sample. The most important magnetic properties of the sample are extracted from the power absorption Lorentz-like resonance signal.

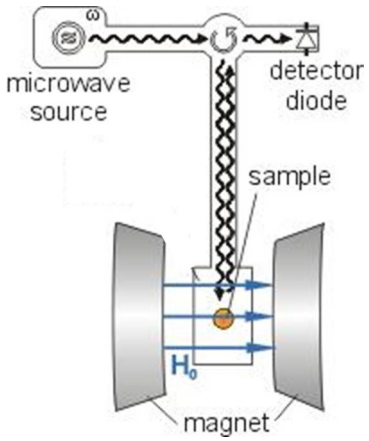

Figure IV.3 – Scheme of the FMR measurement setup

As described below, this power absorption resonance signal is related to the susceptibility of the sample, which is calculated solving the LLG Eq. (IV.1) for the experimental configuration shown in Fig. IV.4 making the following assumptions:

1. The sample is measured in a region where the applied static field H_{DC} aligned along the **x** direction is homogeneous.
2. The macrospin approximation is made, i.e., the magnetization of the sample is spatially uniform. The spins in the small volume of the sample remain parallel by virtue of the exchange interaction.
3. The magnetization lies in-plane and the surface dimensions are much larger than the thickness. The demagnetizing factors therefore reduce to: $N_x = N_y = 0$ and $N_z = 1$.

4. The two surfaces originate a uniaxial perpendicular anisotropy which is small compared to the demagnetizing field. This surface anisotropy (not negligible only in ultrathin magnetic layers) is ascribed to the reduced symmetry of atoms near the interface, and can be described as a surface field contribution to the total effective field: $H^S = \frac{2K_a^S}{\mu_0 M_s t}$, where t is the thickness of the F layer and K_a^S is a perpendicular anisotropy constant in units of J/m^2.

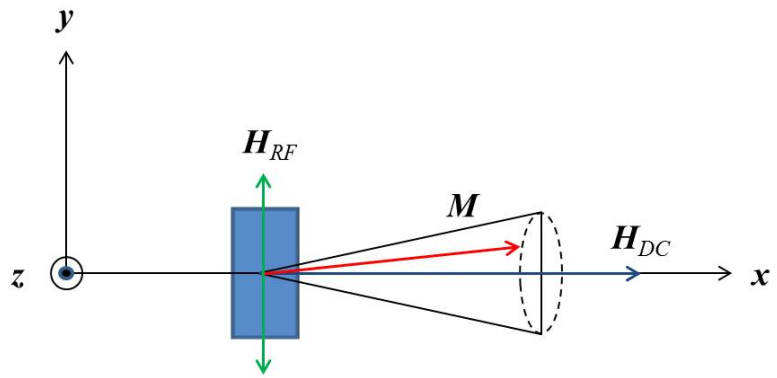

Figure IV.4 – Schematic illustration of the FMR measurement configuration: the static DC field is applied in the plane of the sample along the **x** direction; the RF field is applied in the plane of the sample perpendicular to the DC field.

As sketched in Fig. IV.4, the magnetization is aligned along the **x** direction. The RF field is applied along the **y** direction, perpendicular to the static DC field.

For the configuration shown in Fig. IV.4, $\mathbf{M} = M_s\mathbf{x} + m_y\mathbf{y} + m_z\mathbf{z}$, where m_y and m_z are considered as small deviations ($m_y, m_z << M_s$) from the equilibrium magnetization in the direction of $\mathbf{H}_{\text{DC}}$ when the RF field is applied. The effective field can be written as:

$$\mathbf{H}_{\text{eff}} = (H_{\text{DC}} + H_{\text{uni}})\mathbf{x} + H_{\text{RF}}\mathbf{y} - \frac{M_{\text{eff}}}{M_s} m_z \mathbf{z}$$

where the uniaxial anisotropy field and the effective magnetization are defined by $H_{\text{uni}} = \frac{2K_a^u}{\mu_0 M_s}$ and $M_{\text{eff}} = (M_s - \frac{2K_a^S}{\mu_0 M_s t})$ respectively. With these definitions, the resonance frequency as well as the linewidth of the power absorption resonance signal can be calculated from the susceptibility tensor component χ_{yy}, which relates the y magnetization component m_y with the applied RF field H_{RF} in the y direction: $m_y = \chi_{yy} H_{\text{RF}}$. The susceptibility tensor is obtained solving Eq. (IV.1) in the linear approximation considering small transverse components m_y and m_z with harmonic time dependence of the form $exp(i\omega t)$. Introducing these components into Eq. (IV.1) results in a system of coupled equations of motion for m_y and m_z from which the diagonal susceptibility can be obtained neglecting non linear terms in H_{RF}, m_y and m_z [Ghosh, 2013]:

$$\chi_{yy} = \chi'_{yy} + i\chi''_{yy} = M_s \frac{(A + i\alpha\frac{\omega}{\gamma})[AB - \left(\frac{\omega}{\gamma}\right)^2(\alpha^2+1) - i\alpha\frac{\omega}{\gamma}(A+B)]}{[AB - \left(\frac{\omega}{\gamma}\right)^2(\alpha^2+1)]^2 + [\alpha\frac{\omega}{\gamma}(A+B)]^2} \tag{IV.3}$$

where $A = M_{\text{eff}} + H_{\text{DC}} + H_{\text{uni}}$ and $B = H_{\text{DC}} + H_{\text{uni}}$.

Extraction of the resonance frequency from Kittel law

The maximum magnetization in the y direction (response) for a given H_{RF} field (excitation) is reached when the denominator of Eq. (IV.3) is minimum. Thus the resonance condition can be expressed as:

$$AB - \left(\frac{\omega_{\text{res}}}{\gamma}\right)^2(\alpha^2+1) = 0$$

Here $\alpha^2 + 1 \approx 1$, since $\alpha << 1$, and the resonance condition reduces to $\left(\frac{\omega_{\text{res}}}{\gamma}\right)^2 = AB$. This condition gives the Kittel resonance formula, which gives the sought resonance frequency:

$$\left(\frac{\omega_{\text{res}}}{\gamma}\right)^2 = (M_{\text{eff}} + H_{\text{DC}} + H_{\text{uni}})(H_{\text{DC}} + H_{\text{uni}}) \tag{IV.4}$$

Extraction of the damping parameter α from the linewidth of the power absorption resonance signal

The time dependence of the power absorbed by the sample from the total field applied is given by the time derivative of the Zeeman energy:

$$P(t) = \frac{d\epsilon_{Zeem}}{dt} = \frac{d}{dt}[-\mu_0 \mathbf{M} \cdot (\mathbf{H}_{\text{DC}} + \mathbf{H}_{\text{RF}})] = -2\mu_0 m_y \frac{dH_{\text{RF}}}{dt} = -2\mu_0 Re(\chi_{yy} H_{\text{RF}}) \frac{dH_{\text{RF}}}{dt}$$

Using the mean value theorem, the average absorbed power absorbed during one cycle of duration $T = \frac{2\pi}{\omega}$ can be calculated straightforwardly:

$$\langle P \rangle = \frac{\omega}{2\pi} \int_0^{2\pi/\omega} P(t)dt = \mu_0 \omega \chi''_{yy} (H_{\text{RF}})^2 \tag{IV.5}$$

The absorbed power depends only on the imaginary part of the susceptibility function, which is associated with irreversible processes that lead to energy dissipation in the magnetic system. FMR measures the power absorption characteristics, which can be used to extract information about the relaxation processes using Eq. (IV.5). For the FMR mea-

surements performed in this work, it is difficult to vary the microwave frequency over large ranges; instead, the static magnetic field H_{DC} is varied to reach the resonance conditions, since there is a correspondence between ω_{res} and $\mathbf{H}_{\mathrm{DC}}$ given in Eq. IV.4. The imaginary part of the susceptibility function in Eq (IV.5) is a Lorentzian function of the applied H_{DC} field centred at the resonance field H_{res}. The linewidth of this Lorentzian is given by its full width half maxima $\Delta H_{1/2}$. However, experimentally it is easier to measure the differential absorption $\dfrac{\partial \chi''}{\partial H}$ (see Fig. IV.5).

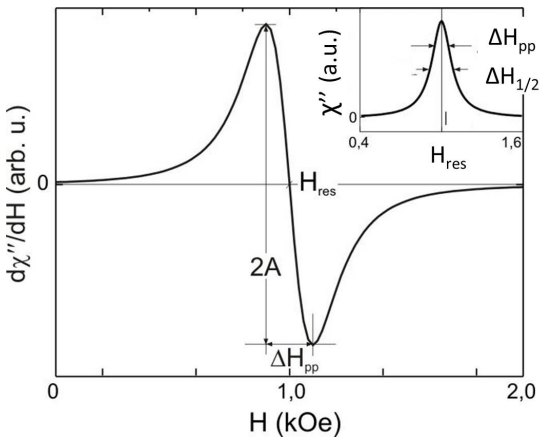

Figure IV.5 – Differential absorption $\dfrac{\partial \chi''}{\partial H}$ as a function of the applied static field. The inset corresponds to the Lorentzian susceptibility χ''.

The full width half maxima of the conventional Lorentzian is related to the peak-to-peak spacing ΔH_{pp} of this differential absorption through $\Delta H_{pp} = \dfrac{1}{\sqrt{3}}\Delta H_{1/2}$. ΔH_{pp} is experimentally measured in order to extract the relaxation damping parameter through the relation:

$$\Delta H_{pp}(\omega) = \Delta H_0 + \frac{2}{\sqrt{3}|\gamma|}\alpha\omega_{\mathrm{res}} \tag{IV.6}$$

Where γ the gyromagnetic ratio and ΔH_0 the inhomogeneous broadening associated with spatial variations in the magnitude of the out-of-plane magnetic anisotropy. The linewidth is therefore a linear function of the frequency, with a constant term ΔH_0 that takes the sample inhomogeneity into account. If several ΔH_{pp} measurements are performed at different microwave frequencies ω, then the damping factor ω can be easily obtained from the slope given in Eq. (IV.6).

IV.2.3 Spin pumping

As discussed in the previous chapters, a spin-polarized current can exert a torque on the order parameter of a magnetic element, leading to current-induced magnetic dynamics. The reciprocal of this phenomenon is the interfacial 'pumping' of spins by a precessing

magnetization of a ferromagnet F_{res} into adjacent nonmagnetic layers. In other words, the precessing magnetization vector of a ferromagnet emits a pure spin current when in contact with a normal (paramagnetic) metal (see Fig. IV.6).

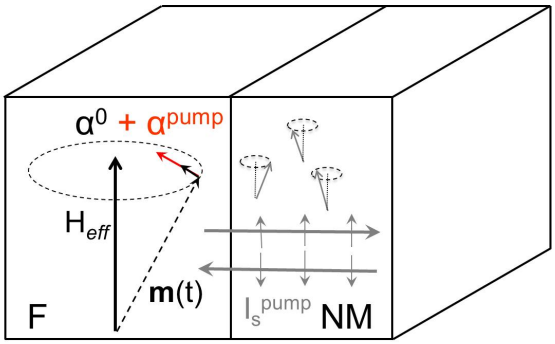

Figure IV.6 – Spin pumping effect in a F/NM structure. The precessing magnetization of the F pumps a pure spin current into the adjacent NM material, where it is absorbed.

Unlike a spin-polarized current, there is no net charge transport: the number of spins polarized along a given quantization axis going out of the precessing ferromagnet equals the number of spin polarized in the opposite direction entering the ferromagnet, thus, only angular momentum is transferred. This transfer of angular momentum affects in turn the magnetization dynamics of the ferromagnet, which can be described in terms of the Landau-Lifshitz-Gilbert equation as an enhanced Gilbert damping $\Delta\alpha$. The enhanced Gilbert damping can be viewed as an additional torque acting on the magnetization vector. It can be monitored using the FMR methods described previously, through the resonance signal linewidth broadening.

Using a scattering matrix approach it was demonstrated that the spin current pumped out of the ferromagnet into the NM layer is given by:

$$\mathbf{I}_{\text{s}}^{\text{pump}} = \frac{\hbar}{4\pi}(g_r^{\uparrow\downarrow}(\mathbf{m} \times \frac{d\mathbf{m}}{dt}) + g_i^{\uparrow\downarrow}\frac{d\mathbf{m}}{dt}) \tag{IV.7}$$

$\mathbf{m}$ is the magnetization and $g_r^{\uparrow\downarrow}$ and $g_i^{\uparrow\downarrow}$ are the real and imaginary part of the transverse spin mixing conductance, which describes spin transport at the interface between two metals. It determines how much spin current crosses the interface. The pumped spin current, flows perpendicular to the F/NM interface, and delivers some of its angular momentum to the NM lattice, for instance by spin-flip relaxation processes or spin dephasing mechanism. The delivered angular momentum at the NM causes a loss of angular momentum to the ferromagnet F, which manifests itself as an additional damping (torque) term. This additional term α^{pump}, or extrinsic damping has a non-local nature in the sense that angular momentum is lost outside the precessing F, that is, absorbed by the surrounding materials/interfaces under study. It must be distinguished from the usual local intrinsic damping α_0 discussed above. The extrinsic damping term must be included in the LLG equation taking into account the expression of the pumped spin current given

in Eq. (IV.7):

$$\frac{d\mathbf{m}}{dt} = -\gamma\mathbf{m}\times\mathbf{H}_{\text{eff}} + \alpha_0\mathbf{m}\times\frac{d\mathbf{m}}{dt} + \frac{\gamma\hbar}{4\pi M_s V}(g_r^{\uparrow\downarrow}(\mathbf{m}\times\frac{d\mathbf{m}}{dt}) + g_i^{\uparrow\downarrow}\frac{d\mathbf{m}}{dt}) \tag{IV.8}$$

where $V$is the volume of the F. The imaginary component $g_i^{\uparrow\downarrow}$ in Eq. (IV.8) is negligible with respect to the real component $g_r^{\uparrow\downarrow}$, so that the additional extrinsic damping term in Eq. (IV.8) reads: $\frac{\gamma\hbar}{4\pi M_s V}g_r^{\uparrow\downarrow}\mathbf{m}\times\frac{d\mathbf{m}}{dt}$. It has a form similar to that of the intrinsic Gilbert damping $(\mathbf{m}\times\frac{d\mathbf{m}}{dt})$, so that both terms can be merged in the same damping term. The most general additional damping coefficient due to non-local losses arising from the spin pumping effect is:

$$\Delta\alpha = \alpha_{\text{pump=}}\frac{|\gamma|\hbar}{4\pi M_s V}g_{\text{eff}}^{\uparrow\downarrow} = \frac{|\gamma|\hbar}{4\pi M_s}(\frac{g_{\text{eff}}^{\uparrow\downarrow}}{S})\frac{1}{t_{\text{F}}} \tag{IV.9}$$

where the effective spin mixing conductance $g_{\text{eff}}^{\uparrow\downarrow}$ takes into account all additional layers and interfaces encountered by the spin current (other than the simple F/NM structure, such as the one depicted in Fig. IV.10), and is a function of the layer configuration. Note that the additional damping term depends on the inverse of the ferromagnetic layer thickness t_F, which points out an interface effect.

The spins transmitted through the F/NM interface can continue to precess in the effective field while they diffuse away from the surface. However, since these spins take a random walk through the conductor, at any distance larger than the electron mean free path away from the interface the transverse components of the spin accumulation average out (spin dephasing), and only the component along the static magnetization remains. Besides, for a metal with a fast spin-flip relaxation time, the spin injection can be balanced by spin-flip relaxation, i.e., spin currents are absorbed quickly in the metal and exert a torque. This kind of metal is denoted a good spin sink.

To summarize, spin-pumping can be thought of as the transfer of angular momentum out of a ferromagnet with precessing magnetization into the adjacent layers due to a pure spin current. This is the source of enhancement of resonance linewidths experimentally observed in FMR measurements, which accurately probe the total (intrinsic + non-local) Gilbert damping factor. Transport-related interface effects described by the spin mixing conductances can be analysed using FMR for various materials and interfaces. In addition, this technique investigates the spin absorption length scales in F/NM/M (where M represents a material with any magnetic order) nanostructures examining the total damping variations with the thickness of the material M under investigation. In particular, it will be used in the present thesis to determine spin characteristic length scales and spin absorption mechanisms in two typical AF polycrystalline thin films, IrMn and FeMn. The cases where M=F and PM were thoroughly studied [Ghosh et al., 2012].

IV.3 Experimental determination of characteristic lengths for spin dependent transport in NiFe/Cu/AF trilayers

In order to study spin absorption in AF layers with the FMR technique, F/NM/AF heterostructures were used. The F material was chosen to be NiFe since it gave the better signal-to-noise ratio in comparison with Co, the second F tested. The thickness of 8 nm was chosen to have a high α^{pump} value (α^{pump} is inversely proportional to the thickness of the F layer [Ghosh, 2013]) and a good layer quality (continuous layer). Cu(3 nm) was used to decouple the F from the AF. The two AF analysed here are IrMn and FeMn; their thicknesses were varied to study the evolution of α^{pump}.

IV.3.1 Samples preparation

Sample deposition

Samples were deposited using a classical Plassys dc-magnetron sputtering equipment. Magnetron sputtering is a thin film deposition process in which atoms from a solid "target" fabricated from materials that one wants to deposit are ejected due to bombardment by energetic particles onto a substrate (here Si/SiO_2(500nm)). These energetic particles are the positive ions of the inert gas Argon introduced in the vacuum chamber (Ar^+), which are part of a plasma constituted of Argon atoms, Argon ions and electrons. The plasma is created by means of electric discharges applied to the target that ionise the Ar atoms through collisions with electrons. Ar ions are accelerated by an additional DC electric field and strike the target (bombardment) with sufficient force to eject atoms from it. A magnetron placed beneath the target creates a closed magnetic field that traps the plasma near the surface of the target, enhancing the efficiency of the initial ionization process. The atoms ejected from the target (source) reach the substrate placed in its vicinity and condense on the surface producing the desired thin film. A shutter installed between the substrate and the target controls the deposition time. Here, the base pressure was 10^{-3} mbar and typical sputtering rates range between 0.5 and 1 Angstrom/s.

Calibration of the deposited layer thickness

We checked the accuracy of the deposited thicknesses by calibration of the Plassys equipment using x-ray reflectivity measurements on a control sample. The reflectivity measurements consist in the analysis of the X-ray interference pattern between the X-rays reflected at the surface of the sample and those reflected at the interface between the deposited layer and the substrate. The reflectivity profile shows oscillations caused by this X-ray interference, which are called Kiessing fringes. The oscillation depends on the

film thickness, and the thicker the film, the shorter the period of the oscillations. This method has a precision of about 0.5nm. The sample to sample reproducibility was also tested using the same technique, as shown in Fig. IV.7.

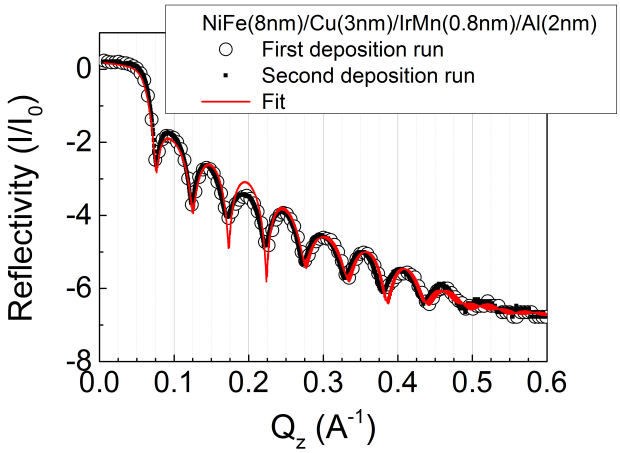

Figure IV.7 – X-ray reflectivity measurements of two NiFe(8nm)/Cu(3 nm)/IrMn(0.8nm)/Al(2nm) stacks deposited in different runs (but using the same target). The red line is the fit from which layer thicknesses are extracted.

The reflectivity patterns of the two deposited stacks almost superpose, indicating a good reproducibility. The red line corresponding to the fit obtained with adjustable thicknesses gave in addition less than 5 % of error with respect to the nominal values.

Sample cut

The optimal sample size for the FMR measurements was determined to be 3×2 mm^2 [Ghosh, 2013]. This size gives a good FMR absorption signal but is small enough to cover an approximately homogeneous DC field region. In addition, the macrospin approximation is expected to be applicable for this geometry. At a first stage, the thin layers were deposited on typical thermally oxidised silicon substrates of 3×26 mm^2. I hand-cut them in samples of approximately 3×2 mm^2. However, high dispersion in the damping measurements was found and ascribed to the geometrical variations from sample to sample due to the imprecision of the cut. A high-precision disc saw machine was then used to eliminate uncertainty due to the sample geometry, but it was detected that the liquid used to cool down the sample during the cutting process removed partially the materials deposited. The most adequate preparation method was found to be saw cut of the substrates and then deposition of the thin layers. This sequence eliminates uncertainty in the sample sizes and problems of material removal during the cut. It gave the most reproducible results.

Deposited samples: summary

NiFe(8)/Cu(3)/AF(t_{AF})/Al(2) (nm) heterostructures have been deposited at room temperature by dc-magnetron sputtering onto thermally oxidised $3 \times 2\ mm^2$ silicon substrates [Baltz et al., 2010] , [Ghosh et al., 2012], in order to study spin dependent transport in two usual AF materials. The AFs with varying thicknesses t_{AF} are made from $Ir_{20}Mn_{80}$ and $Fe_{50}Mn_{50}$, respectively. The F_{res} NiFe(8) layer is deposited from a $Ni_{20}Fe_{80}$ target. The Al(2) cap oxidises in air and consequently forms an AlO_x protecting film with a low spin current absorption [Ghosh et al., 2012] . The Cu(3) breaks the F/AF direct magnetic exchange interactions, evidenced through negligible hysteresis loop shifts measured by vibrating sample magnetometry (VSM) at 300 and 4 K after field cooling procedure. Fig. (IV.8) shows the hysteresis loops for two Si/SiO_2/NiFe(8)/Cu(3)/IrMn(t_{IrMn}) /Al(2) stacks with 0 and 8 nm of IrMn. They exhibit the same negligible shift of around 2.5 Oe, which is therefore likely ascribed to vortex trapped in the superconducting coil of the VSM set up. This was further confirmed by rotating the sample 180°, which kept the field shift invariant.

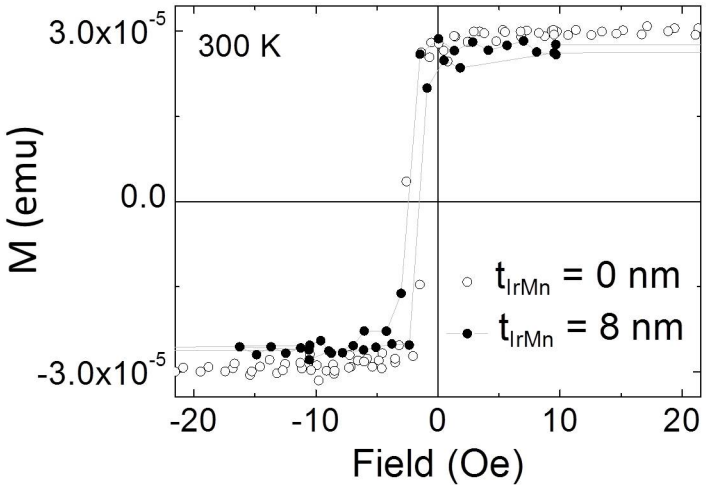

Figure IV.8 – Hysteresis loops at 300K for two Si/SiO_2/NiFe(8)/Cu(3)/IrMn(t_{IrMn})/Al(2) stacks with t_{IrMn}= 0 (open circles) and 8 nm (solid circles).

In addition, given that Cu(3) is a light element and since its spin diffusion length is much longer than its 3 nm thickness [Bass and Jr, 2007], it does not alter spin propagation between the F and the AF.

IV.3.2 Experimental setup

A scheme of the FMR measurement set-up used is represented in Fig. IV.9. This measurement facility was developed by Abhijit Ghosh and William Bailey during Abhijit's thesis work [Ghosh, 2013]. The microwave signal is provided by a vector network analyser that generates the range of frequencies 2-20 GHz with an input power of 15 dBm to

remain in the linear regime. The microwave signal is transmitted through a double ground coplanar wave guide CPW situated between the magnetic poles (separated 20 mm). The sample is placed up-side down on this CPW, so that the DC (homogeneous at the sample emplacement) and RF fields are applied in-plane, one perpendicular to the other, as shown in Fig. IV.9. A phase sensitive lock-in detection was used in order to improve the signal to noise ratio. The signal processed by the lock-in amplifier is a derivative of the absorbed power (which is assumed to be Lorentzian) vs applied field. The peak-to peak linewidth ΔH_{pp} is then extracted from this derivative, as described above.

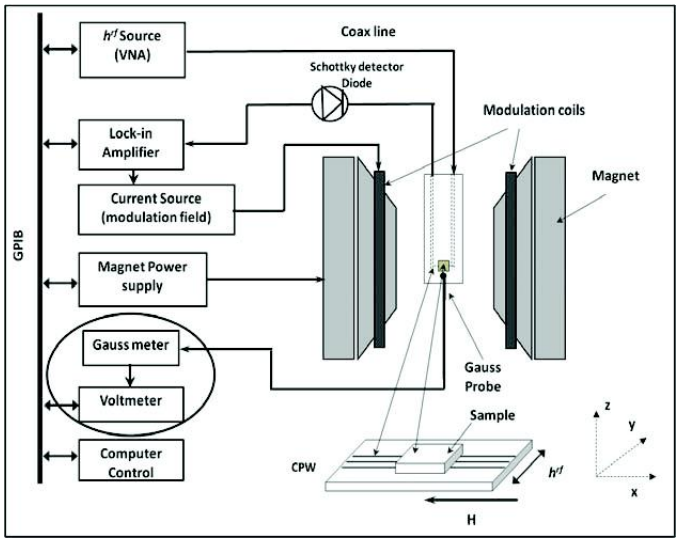

Figure IV.9 – FMR measurement setup scheme

The different linewidths are extracted at frequencies ranging from 2 to 20 GHz in steps of 2 GHz (10 frequencies in total, see Fig. IV.11). Relation (IV.6) gives the damping parameter α and separate the sample inhomogeneity component ΔH_0 (unlike FMR cavity resonators which perform only a one-frequency measurement).

IV.3.3 Characteristic lengths measurement principle for NiFe/Cu/AF trilayers

This section summarizes how I used FMR and spin pumping effect to determine spin dependent characteristic lengths in AFs using NiFe/Cu/AF trilayers.

Fig. IV.10 illustrates the FMR measurement configuration and principle. The local magnetization ($\mathbf{m}(t)$) of the NiFe is excited to resonance by a small RF pumping magnetic field (H_{RF}). As a consequence, the NiFe generates a pure spin current (I_s^{pump}) when oscillating around the local effective field (H_{eff}) due to the spin pumping effect. This spin current diffuses through the NiFe/Cu/AF trilayers and concurrently transfers spin angular momentum to the conduction electrons. It is so to say absorbed or reflected at interfaces and within layers due to spin dependent scattering and in return it affects the

NiFe Gilbert damping: $\alpha = \alpha^0 + \alpha^{\text{pump}}$, where α^0 is the local intrinsic F damping and α^{pump} is the extra non-local damping.

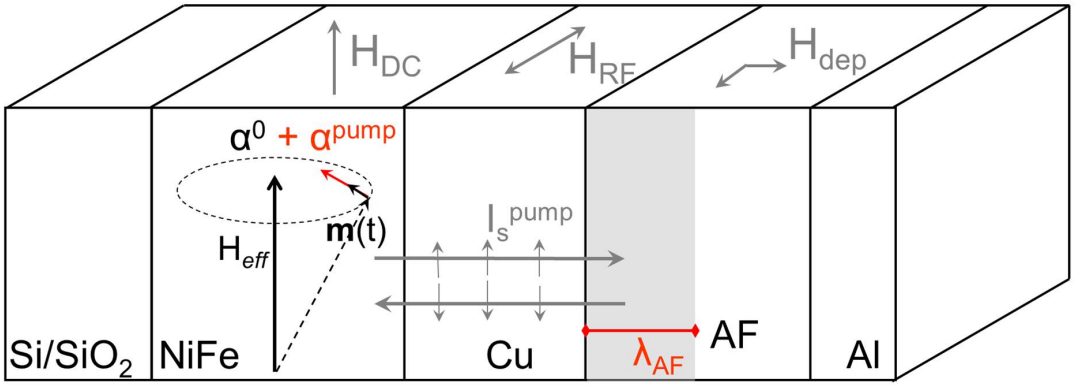

Figure IV.10 – Scheme illustrating the phenomenon for our Si/SiO_2//NiFe/Cu/AF/Al stacks with AF = IrMn or FeMn and deposited either without or with a magnetic field (H_{dep}) applied along different directions. A precession of the NiFe magnetization around the effective magnetic field (H_{eff}) is initiated by application of an external RF field (H_{RF}) under a given static DC field (H_{DC}). Relaxation of the NiFe magnetization along H_{eff} originates from two main sources: the intrinsic damping inherent to the NiFe layer (α^0) and the damping due to the spin current generated by the F excitations then diffused through the multilayer and finally pumped/reflected by the AF (α^{pump}). Beyond a critical length (λ_{AF}) characteristic of the spin dependent transport in the AF, the coherence of the spin current in the AF is lost and the damping saturates.

In the figure, λ_{AF} denotes the critical absorption depth over which the coherence of the spin current within the AF is lost. Consequently the extra F damping due to the AF levels out above λ_{AF} [Ghosh et al., 2012]. The NiFe total Gilbert damping (α) is extracted from series of F resonance spectra obtained with a broadband coplanar waveguide. In-plane DC bias magnetic field (H_{DC}) is employed. A small 2 to 20 Oe modulation field of 201 Hz is applied along the DC field for lock-in detection of the transmitted signal to improve sensitivity and excitation frequencies ($\omega/2\pi$) ranging between 2 and 20 GHz are used. For each frequency the resonance linewidth is determined by fitting the resonance spectra (differential power absorption vs H_{DC}) to a Lorentzian derivative. The total Gilbert damping α is extracted from Eq. IV.6. A linewidth versus $\omega/2\pi$ plots and a representative spectrum are shown in Fig. IV.11. The inhomogeneity component ΔH_0 was always controlled in order to have acceptable values ensuring a correct homogeneity of the sample. Typical values of ΔH_0 were of the order of 0.6 Oe.

For the various NiFe(8)/Cu(3)/AF(t_{AF})/Al(2) (nm) heterostructures, the non-local damping α^{pump} ascribed to the absorption of spin angular momentum by the AF only is straightforwardly obtained by subtracting the Gilbert damping obtained for $t_{AF} = 0$ from the total Gilbert damping.

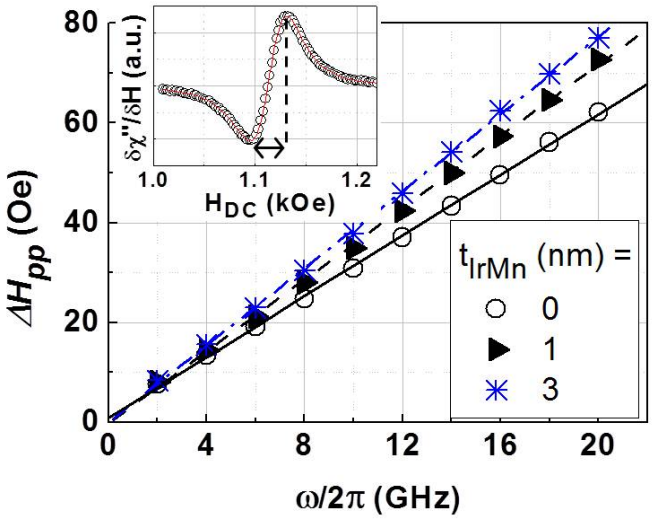

Figure IV.11 – Dependence of the resonance linewidth (ΔH_{pp}) with the excitation frequencies ($\omega/2\pi$) for Si/SiO_2//NiFe(8)/Cu(3)/IrMn(t_{IrMn})/Al(2) (nm) stacks with t_{IrMn} = 0; 1 and 3 nm. The lines are linear fit to the data. Inset: typical resonance spectrum, i.e. differential power absorption $\frac{\partial \chi''}{\partial H}$ VS DC bias field (H_{DC}) for t_{IrMn} = 1 nm and ($\omega/2\pi$) = 10 GHz; the peak-to-peak linewidth gives ΔH_{pp} and is indicated by the arrow.

IV.3.4 STT characteristic lengths in IrMn and FeMn

Fig. IV.12 shows α^{pump} vs t_{AF} for IrMn and FeMn. For some t_{AF}, either the same sample is measured twice or two samples of the same composition are deposited and measured. The maximum difference is observed for t_{FeMn} = 15 nm and defines the error bars of $\sim 1.4 \times 10^{-4}$.

Two different behaviours are observed depending on the AF type. In the case of IrMn, it is observed that α^{pump} increases linearly with t_{IrMn} and cuts off to a maximum at an empirical critical thickness $\lambda_{\mathrm{IrMn}}/2$ of around 1.4 nm. Like in Ref.[Foros et al., 2005], it was considered that the spins relax on the way forward in the IrMn depth, reflect and return backward through the IrMn to the NiFe layer, thus traversing and relaxing linearly twice in the IrMn depth. The linear behaviour is similar to F spin sinks [Ghosh et al., 2012], indicating that the nature of the absorption for IrMn mainly relates to dephasing of the spin current transverse component as well: the spins undergo Larmor precession as they go into the material because the majority and minority Fermi wave vectors are different. Spins with different initial conditions precess at different rates leading to classical dephasing.

Given that, λ_{IrMn} is mostly related to spin dephasing proportional to the integration over the Fermi wave vectors of $\pi/(k_F^{\uparrow} - k_F^{\downarrow})$ where $k_F^{\uparrow(\downarrow)}$ are the majority (minority) Fermi wave vectors, or equivalently $hv_g/(2\Delta_{ex})$, with v_g the spin-averaged group velocity and Δ_{ex} the exchange splitting. Δ_{ex} is smaller for IrMn compared with the usual F due to a

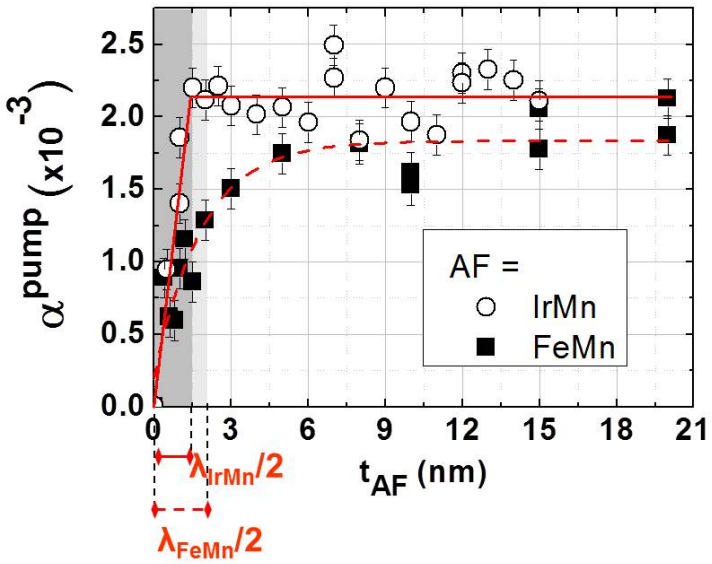

Figure IV.12 – Dependence with t_{AF} of the AF contribution, via spin pumping, to the NiFe magnetization damping (α^{pump}) for Si/SiO_2//NiFe(8)/Cu(3)/AF(t_{AF})/Al(2) (nm) stacks with various AF thicknesses (t_{AF}) and AF = IrMn and FeMn. For IrMn, the straight line is a linear fit proportional to: $2t_{\text{IrMn}}/\lambda_{\text{IrMn}}$ for $t_{\text{IrMn}} < 1.4$ nm and a guide to the eye above. For FeMn, the dashed line is an exponential fit of the form: $A \cdot [1 - exp(-2t_{\text{FeMn}}/\lambda_{\text{FeMn}})]$. The spin dependent transport characteristic length in the AF is λ_{AF}.

low critical order temperature T_N of around $350-400°$ C [Lombard et al., 2010] . Because of that, λ_{IrMn} was expected to be even larger than the critical lengths of usual F: CoFeB, Co or NiFe for which $\lambda_F/2 \sim 1.2$ nm [Ghosh et al., 2012] , [Bailey et al., 2012] . Although the linear behaviour of α^{pump} vs t_{IrMn} clearly points out spin dephasing mechanism as the main source of absorption, the fact that Ir is a heavy element and carries d electrons in the conduction band, probably introduces to a lesser extent some additional spin flip mechanisms balancing the effect of lower Δ_{ex} and contributing to slightly reducing the characteristic penetration length to a value similar to that of usual F.

From Fig. IV.12, it can be observed that the α^{pump} vs t_{FeMn} follows a totally different trend with an exponential $[1 - exp(-2t_{\text{FeMn}}/\lambda_{\text{FeMn}})]$ thickness dependence. Such a trend is typical of a paramagnetic spin sink for which the absorption of the spin current is mainly due to spin flipping [Foros et al., 2005] , [Mizukami et al., 2001] . For consistency, the empirical factor 2 was also considered here [Foros et al., 2005], taking into account the forward and backward path of spins within the FeMn layer. Fits of the raw data with the above exponential law give a $\lambda_{\text{FeMn}}/2$ of around 1.9 nm. In this case, λ_{FeMn} relates to spin diffusion in contrast to λ_{IrMn} originating from spin dephasing, although practically both give values proportional to critical spin penetration depths. Given that,

λ_{IrMn} concerns the spin transverse component absorption when λ_{FeMn} is associated to both longitudinal and transverse components absorptions. Such paramagnetic α^{pump} vs t_{FeMn} variations at room-T are the consequence of the low exchange splitting Δ_{ex} of FeMn [Nogués and Schuller, 1999] , [Bailey et al., 2012] . It is not unlikely that, at room-T FeMn films thinner than λ_{FeMn} are paramagnetic rather than antiferromagnetic given the reduced bulk T_N of FeMn compared to IrMn [Nogués and Schuller, 1999] to which adds finite size effects additionally reducing T_N [Lombard et al., 2010], [Zhang and Willis, 2001] . Accurately measuring and estimating finite size effects on T_N is not simple and very few corresponding literature is available for AF materials. A toy model in Ref. [Zhang and Willis, 2001] reproduces finite size effects on F layers critical temperature. The model is transferable to AFs [Ambrose and Chien, 1996] and gives the following general power law: $T_N(n) = T_N(\mathrm{bulk}) \cdot [1 - \frac{N_0 + 1}{2n} k]$, where n is the number of AF monolayers (ML), N_0 the AF exchange length and k an integer. For 3D Ising models, k is close to 1.6. Conversely, accurate values of N_0 are not straightforwardly accessible to experiments and models. Alternatively, T_N is accessible to experiments via ultrafast measurements of F/AF exchange bias bilayers. The blocking temperature (T_B) is the temperature above which the F is no longer pinned in a fixed direction by the AF. It depends on various parameters among which the F/AF interfacial coupling, the AF bulk properties (AF-AF exchange stiffness and grain volume) and time. In particular, T_B increases with the F magnetization sweep-rate and reaches the AF intrinsic critical Néel-T (T_N) in the nanosecond regime [Lombard et al., 2010] . Ref. [Lombard et al., 2010] is to our knowledge the only paper dealing with that: for 30 ns pulses, the critical T for IrMn reduces from $350-400$°C (i.e. bulk value) for 6.5 nm to 200°C for 4.5 nm. In the case of FeMn, the same authors measure a reduction from 200°C (i.e. bulk value) for 7 nm to 100°C for 5 nm. Such measurements are compatible with T_N lower than room-temperature for few nm thick FeMn.

Fig. IV.12 also shows that for both IrMn and FeMn layers, α^{pump} levels out for thick AF. The α^{pump} saturation value ($\alpha^{\mathrm{pump}}_{\mathrm{sat}}$), i.e. after maximum spin absorption, seems to be slightly larger for IrMn. Given the above mentioned distinct behaviours for IrMn and FeMn, $\alpha^{\mathrm{pump}}_{\mathrm{sat}}$ originates from the corresponding distinct mechanisms. For the paramagnetic-like FeMn, $\alpha^{\mathrm{pump}}_{\mathrm{sat}}$ is mostly related to spin flipping that is bulk-like. In contrast, for the F-like IrMn, $\alpha^{\mathrm{pump}}_{\mathrm{sat}}$ mostly relates to the effective spin mixing conductance ($g^{\uparrow}_{\mathrm{eff}} \downarrow$) that mostly depends on the Cu/IrMn interface ($g^{\uparrow}_{\mathrm{Cu/IrMn}} \downarrow$) since the values of α^{pump} reported in this study result from the difference between the damping for NiFe(8)/Cu(3)/AF(t_{AF})/Al(2) and NiFe(8)/Cu(3)/Al(2) (nm). As described in Ref. [Ghosh et al., 2012] , the measured values of effective spin mixing conductance from the addition of the AF layer do not depend on the spin mixing conductance of NiFe/Cu ($g^{\uparrow}_{\mathrm{NiFe/Cu}} \downarrow / S \sim 14.4 \pm 1.4 nm^{-2}$, which cancels due to the Cu Sharvin conductance correction of the same order of magnitude. In addition, to a first approximation, given

that the AF randomizes spins over short distances, the Cu/AF interface mainly drives spin mixing. If the uncompensated spins at the AF interface were fully oriented toward the same direction, Cu/IrMn spin pumping conductivity ($g^{\uparrow}_{\mathrm{Cu/IrMn}} \downarrow /S$) would be expected to be similar to Cu/F, typically around 14 to 16 nm^{-2}. However AF interfaces are known to be highly frustrated [Takano et al., 1997] , [Akmaldinov et al., 2013] and the resulting overall picture gives few uncompensated spins (e.g. tiny F regions) at the AF interface, also responsible for exchange bias. While an AF spin surface in contact with a F is tuned by the interfacial F spin configuration that orients the AF uncompensated spins in a preferential direction after field cooling, in the present case of Cu/AF the AF interfacial uncompensated spins are rather randomly oriented positively and negatively. Therefore, the influence of the uncompensated AF interfacial spins on the Cu/AF spin mixing conductance is hard to anticipate here. Finally, note that the Cu/IrMn interface is surely more complex due to the formation of CuMn spin-glasses [Akmaldinov et al., 2013] , [Chouhan and Mookerjee, 2011].

IV.3.5 Isotropic character of the spin current absorption: effects of magnetic field during sample deposition

For the F-like spin absorbing IrMn, it might be inferred that spin pumping, i.e. the reciprocal effect to STT should also show a directional character. An advantage of F_{res}/N/AF trilayers with respect to F_{res}/N/F for investigating this issue is that a F spin sink is oriented by the high resonance DC bias magnetic fields necessary for the experiment at high H_{RF} frequencies. In contrast, once oriented, the AF is not affected by such DC magnetic fields and stays still during the experiment. As will be discussed below, this attempt to evidence the anisotropy character of spin pumping either failed within the noise level or unexpectedly do show no directional character.

For the F-like spin absorbing IrMn, Fig. IV.13 shows α^{pump} vs t_{IrMn} for samples fabricated with three different magnetic field configurations during the deposition process: no field (same data as in Fig. IV.12 reproduced here as a reference and meaning a random orientation of the IrMn interfacial uncompensated spins) and static magnetic fields (H_{dep}) along the transversal and longitudinal in-plane directions in order to orient the first few IrMn layers when still paramagnetic at the first stage of the growth. We performed atomic force microscopy measurements in order to detect surface inhomogeneities due to preferential growing of the sample during the deposition process under applied field. No significant anisotropies were found in the surface profile.

What matters in the following is the orientation of the IrMn interface relatively to the DC magnetic field that governs the F_{res} precession axis, which is along the transversal direction of the sample.

Despite the fact that the noise level precludes drawing fine conclusion on the damping

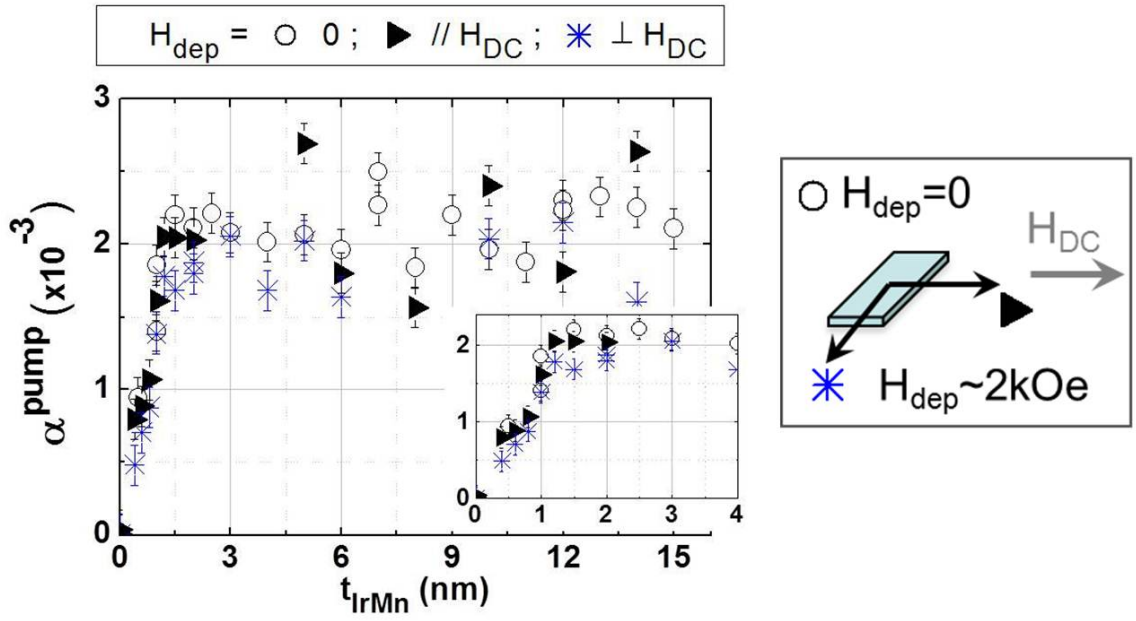

Figure IV.13 – Dependence with t_{IrMn} of the IrMn contribution, via spin pumping, to the NiFe magnetization damping (α^{pump}) for Si/SiO_2//NiFe(8)/Cu(3)/IrMn(t_{IrMn})/Al(2) (nm) stacks with various IrMn thicknesses (t_{IrMn}) and for various directions of magnetic field applied during deposition (H_{dep}). The inset is a zoom of the low thicknesses region.

level, all three α^{pump} vs t_{IrMn} curves superimpose: same linear increase before levelling out, same saturation damping and same saturation threshold λ (better visible from the zoom shown as inset in Fig. IV.13). This finding does not support the initial assumption that the absorption of the transverse component of the spin current pumped by the F depends on the orientation of the localized spins in the first IrMn layers. It could be argued that the reason why this absorption is apparently isotropic is that localized spins in the IrMn are not necessarily oriented by the external field applied during deposition due to other magnetic energies that might come into play. Thus, the isotropic character of the absorption via measurements of α for NiFe(8)/Cu(3)/NiFe(3)/IrMn(7)/Al(2) (nm) stacks with a NiFe(3) spin sink pinned by usual exchange bias field cooling along the transversal (parallel and antiparallel to H_{DC}) and longitudinal directions was further tested (see Fig. IV.14).

Fig. IV.15 shows the hysteresis loops for these stacks performed at 300 K to measure the pinned layer reversal field. They confirm the longitudinal and transversal orientations of the pinned ferromagnet.

Excitation frequencies only ranging between 2 and 4 GHz are used so that the DC bias field does not exceed the pinned layer reversal field of around 600 Oe. The differences in the damping parameter for the three orientations of the second ferromagnet NiFe(3) are within the experimental error. These results are however not conclusive, since the effect on linewidth is so small at these low frequencies that it would be probably not within the

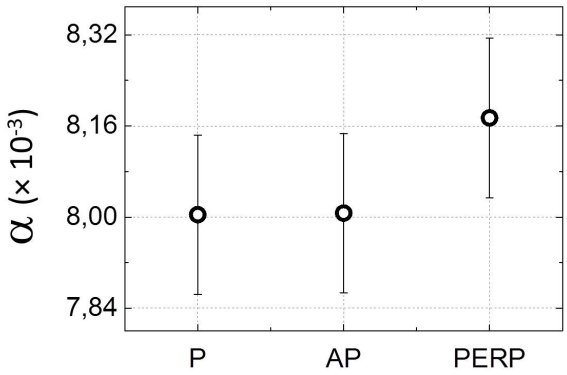

Figure IV.14 – Total damping parameter α for three Si/SiO_2//NiFe(8)/Cu(3)/NiFe(3)/IrMn(7)/Al(2) (nm) stacks annealed 1 hour at 300^o C under applied magnetic field along three directions: transversal to the sample and parallel to the DC field, (P), transversal to the sample and antiparallel to the DC field, (AP), and longitudinal to the sample and perpendicular to the DC field $\mathbf{H}_{\mathrm{DC}}$, (PERP).

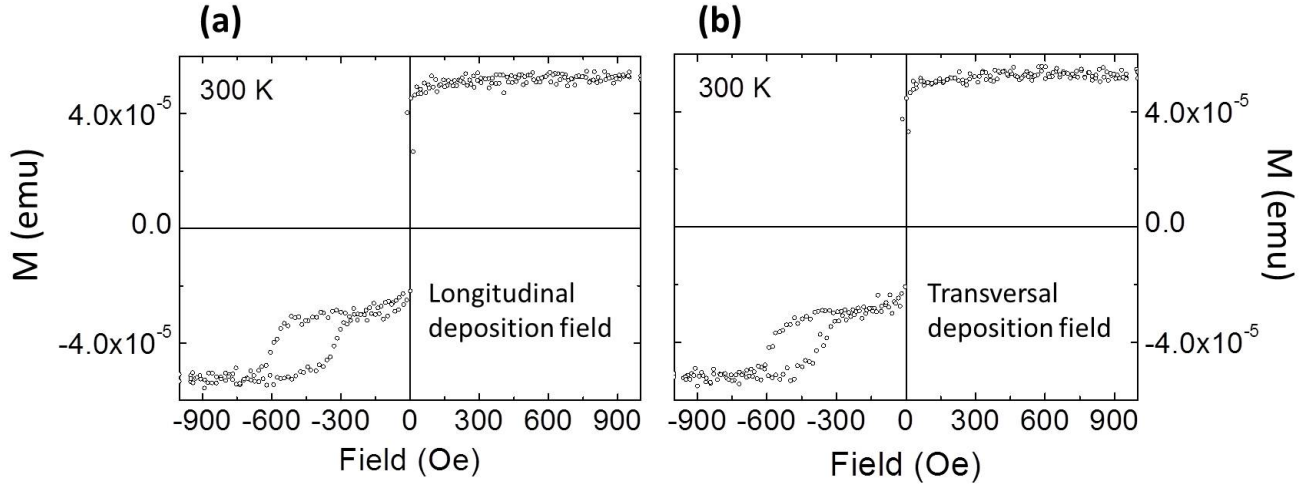

Figure IV.15 – **(a)** Hysteresis loop measured along the longitudinal direction at 300 K for a Si/SiO_2/NiFe(8)/Cu(3)/NiFe(3)/IrMn(7)/Al(2) stack annealed 1 hour under longitudinal field at 300°C. **(b)** Hysteresis loop measured along the transverse direction at 300 K for a similar stack annealed 1 hour under transverse field at 300°C.

experimental resolution and indistinguishable from inhomogeneous broadening.

IV.4 Summary

To conclude, in the context of AF-spintronics the main contribution of the present study is the determination of room temperature critical penetration depths and absorption mechanisms of spin currents in $Ir_{20}Mn_{80}$ and $Fe_{50}Mn_{50}$ spin sinks by means of F-resonance and spin pumping. Different room temperature absorption mechanisms of spins were evidenced: dephasing for IrMn and spin flipping for FeMn probably due to the room temperature paramagnetic character of FeMn for thicknesses lower than the penetration

depth [Merodio et al., 2014a]. Although not entirely understood, results on the directional character of spin current absorption were discussed as a basis for comparisons with potential future works.

Further research could involve: 1) Other AFs (e.g. with a variable content of heavy spin scatterers). 2) Various degrees of crystallinity up to single-crystal AF. 3) Various interfacial qualities determined by roughness, stacking faults, species intermixing, etc.; 4) Variable temperature for studies of the para- to antiferro-magnetic transition temperature that is difficult to determine by many other techniques. 5) Nanostructured elements since AFs can be influenced by size effects. 6) FI materials. 7) The use of an insulating barrier instead of a metallic spacer.

Note that we also tried to experimentally investigate the effect of a spin-polarized current on an AF in F/NM/F/AF structures with controlled geometries in order to complement the work of [Wei et al., 2007]. Although we obtained very disperse results, this thorough attempt is described in Appendix C, along with suggestions for future studies.

Chapter V

Summary and perspectives

In the theoretical part of this thesis, the spin-dependent transport properties of epitaxial magnetic tunnel junctions with AF and FI leads have been investigated using a tight-binding Hamiltonian modelling their essential electric an magnetic properties, in the framework of the nonequilibrium Keldysh formalism. Special attention has been paid to the spatial distribution of STT within the metallic leads, in order to elucidate the associated characteristic lengths. Indeed, longer STT characteristic lengths are of fundamental importance for lower magnetization switching current densities in STT-MRAM applications. The STT spatial distributions has been analysed in terms of spin accumulation and divergences of the spin current transverse components. Both schemes are found to be equivalent.

Concerning the AF leads, both in-plane and out-of-plane torque components are shown to be staggered. This is a new result to be compared with the random behaviour previously reported for the out-of-plane component using a metallic spacer instead of an insulating barrier. Due to this staggered character and the non-decaying torque amplitudes in the bulk, torques in AFs are found to be very efficient and even overcome those observed in conventional F, where STT represents an interfacial phenomenon. The amplitude of the torques increases linearly with the applied bias for 1-D geometries. Increasing amplitudes are also observed for 3-D systems, but reaching saturation at voltages around 0.9 V.

We demonstrate that unlike conventional F-based tunnel junctions, AF-based tunnel junctions can show monotonically increasing TMR with voltage, reaching values as high as 90% for a bias of 0.9 V. The particular voltage dependence of the TMR is however shown to be strongly affected by the electronic structure of the AF leads.

The magnetic complexity inherent to FI structures is expected to combine STT characteristics of F and AF materials. Compared to AF, similar staggered character of both torque components was observed. Torques and localized moments in the FI structure are also commensurate, which implies again high efficiency for current-induced magnetization switching. In addition, and more interesting, both torque components exhibit a striking wave-like behaviour perfectly modulated by spin accumulation. In 3-D FI-MTJ, these

modulated torques are damped over longer length scales in comparison with F-MTJ. We demonstrate that the electronic and magnetic characteristics of the FI are responsible for the specific features of the torque waves, and consequently for the STT characteristic lengths in FIs. In particular, we identify a fundamental parameter predicted to be inversely proportional to the torque waves spatial period in 1-D FI-MTJ and the spatial extension of the damped torque oscillations in 3-D FI-MTJ. This parameter corresponds to the difference between the spin splittings of the two FI sublattices and can be considered as an effective exchange field in FIs, similar to the homogeneous exchange field characterising Fs. In addition, the bandwidth parametrized here by the hopping matrix element of the TB Hamiltonian is found to be proportional to the mentioned spatial periods. Regarding extrinsic variables, the STT characteristic lengths can also be tuned via the applied bias across the junction; in particular, the spatial period increases monotonically with the applied voltage. Interestingly, its aforementioned dependence on the FI effective exchange field holds for each given voltage. Hence, STT in FI is predicted to be highly efficient due to its long decaying characteristic lengths and its staggered character commensurate with the magnetic lattice.

Since ideal coherent transport is considered throughout this theoretical part, the effects of disorder represent the obvious object of investigation for future work. Although elastic and inelastic scattering have been predicted by previous authors to have a strong impact on STT and GMR in AF-based spin valves, the use of a tunnelling barrier instead of a metallic spacer is expected to be a suitable mean to ensure momentum conservation and thus overcome at least partially the negative effects of disorder; in effect, tunnelling process is likely less sensitive to elastic scattering. In particular, the characteristic lengths over which the STT does not vanish are expected to be still longer than in conventional F-MTJs. We believe that disorder does not represent an insurmountable constraint for STT and TMR in AF-MTJs. The similarities between Fs and FIs in terms of magnetization and band splitting (which is absent for AFs) suggest that STT in FI leads might be as robust face to disorder as it is for conventional Fs.

The effects of disorder in the STT characteristic lengths in actual AF thin layers are addressed in the experimental part of this thesis. In particular, critical penetration depths and absorption mechanisms of spin currents in $Ir_{20}Mn_{80}$ and $Fe_{50}Mn_{50}$ spin sinks at room temperature by means of F-resonance and spin pumping were determined. Different room temperature absorption mechanisms of spins were evidenced: dephasing for IrMn and spin flipping for FeMn.

Further research using similar AF thin layers could involve a comprehensive study of the directional character of spin current absorption, other AFs (e.g. with a variable content of heavy spin scatterers) and different degrees of crystallinity and interfacial qualities. Ideally, similar investigations could be carried out for AF and FI nanostructured elements, using in particular tunnel junctions to compare with the theoretical results of this work.

Glossary

1-D: One Dimension

3-D: Three Dimensions

AF: Antiferromagnet

B: Barrier

CPA: Coherent Potential Approximation

CPW: Coplanar Wave Guide

DC: Direct Current

DOS: Density of States

HDD: Hard Disk Drive

IEC: Interlayer Exchange Coupling

F: Ferromagnet

FBZ: First Brillouin Zone

FCC: Face Centered Cubic

FI: Ferrimagnet

FMR: Ferro Magnetic Resonance

GMR: Giant Magneto Resistance

L: Left

LDOS: Local Density of States

LLG: Landau-Lifschitz-Gilbert

MR: Magneto Resistance

MRAM: Magnetic Random Access Memory

MTJ: Magnetic Tunnel Junction

NM: Non Magnetic

No: Number

PM: Para Magnetic

RF: Radio Frequency

RKKY: Ruderman-Kittel-Kasuya-Yosida

r.h.s.: Right Hand Side

R: Right

STT: Spin Transfer Torque

TB: Tight Binding

TMR: Tunnelling Magneto Resistance

Bibliography

[Acharyya et al., 2010] Acharyya, R., Nguyen, H. Y. T., Pratt, W., and Bass, J. (2010). Spin-flipping associated with the antiferromagnet IrMn. *Magnetics, IEEE Transactions on*, 46(6):1454–1456.

[Acharyya et al., 2011] Acharyya, R., Nguyen, H. Y. T., Pratt, W. P., and Bass, J. (2011). A study of spin-flipping in sputtered IrMn using Py-based exchange-biased spin-valves. *Journal of Applied Physics*, 109(7):07C503.

[Akmaldinov et al., 2013] Akmaldinov, K., Auffret, S., Joumard, I., Dieny, B., and Baltz, V. (2013). Benefit of inserting a (Cu/Pt) intermixing dual barrier for the blocking temperature distribution of exchange biased Co/(Cu/Pt)/IrMn stacks. *Applied Physics Letters*, 103(4):042415.

[Ambrose and Chien, 1996] Ambrose, T. and Chien, C. L. (1996). Finite-size effects and uncompensated magnetization in thin antiferromagnetic CoO layers. *Phys. Rev. Lett.*, 76:1743–1746.

[Baibich et al., 1988] Baibich, M. N., Broto, J. M., Fert, A., Van Dau, F. N., Petroff, F., Etienne, P., Creuzet, G., Friederich, A., and Chazelas, J. (1988). Giant magnetoresistance of (001)Fe/(001)Cr magnetic superlattices. *Phys. Rev. Lett.*, 61:2472–2475.

[Bailey et al., 2012] Bailey, W. E., Ghosh, A., Auffret, S., Gautier, E., Ebels, U., Wilhelm, F., and Rogalev, A. (2012). Pd magnetism induced by indirect interlayer exchange coupling. *Phys. Rev. B*, 86:144403.

[Balke et al., 2007] Balke, B., Fecher, G. H., Winterlik, J., and Felser, C. (2007). Mn_3Ga, a compensated ferrimagnet with high curie temperature and low magnetic moment for spin torque transfer applications. *Applied Physics Letters*, 90(15):152504.

[Baltz et al., 2010] Baltz, V., Rodmacq, B., Zarefy, A., Lechevallier, L., and Dieny, B. (2010). Bimodal distribution of blocking temperature in exchange-biased ferromagnetic/antiferromagnetic bilayers. *Phys. Rev. B*, 81:052404.

[Bass and Jr, 2007] Bass, J. and Jr, W. P. P. (2007). Spin-diffusion lengths in metals and alloys, and spin-flipping at metal/metal interfaces: an experimentalist's critical review. *Journal of Physics: Condensed Matter*, 19(18):183201.

[Basset et al., 2008] Basset, J., Sharma, A., Wei, Z., Bass, J., and Tsoi, M. (2008). Towards antiferromagnetic metal spintronics. *Proceedings of SPIE*, 7036(05).

[Bayar et al., 2011] Bayar, E., Kervan, N., and Kervan, S. (2011). Half-metallic ferrimagnetism in the Ti_2CoAl heusler compound. *Journal of Magnetism and Magnetic Materials*, 323(23):2945–2948.

[Berger, 1996] Berger, L. (1996). Emission of spin waves by a magnetic multilayer traversed by a current. *Phys. Rev. B*, 54:9353–9358.

[Binasch et al., 1989] Binasch, G., Grünberg, P., Saurenbach, F., and Zinn, W. (1989). Enhanced magnetoresistance in layered magnetic structures with antiferromagnetic interlayer exchange. *Phys. Rev. B*, 39:4828–4830.

[Boona and Heremans, 2014] Boona, S. R. and Heremans, J. P. (2014). Magnon thermal mean free path in yttrium iron garnet. *Phys. Rev. B*, 90:064421.

[Brataas et al., 2006] Brataas, A., Bauer, G., and Kelly, P. (2006). Non-collinear magnetoelectronics. *Physics Reports*, 427(4):157–255.

[Brataas et al., 2012] Brataas, A. D., Kent, A. D., and Ohno, H. (2012). Current-induced torques in magnetic materials. *Nat. Mat.*, 11:372–381.

[Bruus and Flensberg, 2002] Bruus, H. and Flensberg, K. (2002). *Introduction to Many-body quantum theory in condensed matter physics.* Oxford University Press, Oxford, second edition.

[Butler et al., 2001] Butler, W. H., Zhang, X.-G., Schulthess, T. C., and MacLaren, J. M. (2001). Spin-dependent tunneling conductance of Fe|MgO|Fe sandwiches. *Phys. Rev. B*, 63:054416.

[Caroli et al., 1971] Caroli, C., Combescot, R., Nozières, P., and Saint-James, D. (1971). Direct calculation of the tunneling current. *Journal of Physics C: Solid State Physics*, 4(8):916.

[Chappert et al., 2007] Chappert, C., Fert, A., and Nguyen van Dau, F. (2007). The emergence of spin electronics in data storage. *Nat. Mat.*, 6:813–823.

[Chouhan and Mookerjee, 2011] Chouhan, R. K. and Mookerjee, A. (2011). Magnetic phase diagram for cumn. *Journal of Magnetism and Magnetic Materials*, 323(6):868–873.

[Cornelissen et al., 2010] Cornelissen, S., Bianchini, L., Devolder, T., Kim, J.-V., Van Roy, W., Lagae, L., and Chappert, C. (2010). Free layer versus synthetic ferrimagnet layer auto-oscillations in nanopillars processed from MgO-based magnetic tunnel junctions. *Phys. Rev. B*, 81:144408.

[Datta, 2000] Datta, S. (2000). Nanoscale device modeling: the Green's function method. *Superlattices and Microstructures*, 28.

[Duine, 2011] Duine, R. (2011). Spintronics: An alternating alternative. *Nat. Mat.*, 10:344–345.

[Duine et al., 2007] Duine, R. A., Haney, P. M., Núñez, A. S., and MacDonald, A. H. (2007). Inelastic scattering in ferromagnetic and antiferromagnetic spin valves. *Phys. Rev. B*, 75:014433.

[Economou, 2006] Economou, E. N. (2006). *Green's Functions in Quantum Physics*. Springer Series in Solid-State Sciences, Springer, Heidelberg, third edition.

[Edwards et al., 2005] Edwards, D. M., Federici, F., Mathon, J., and Umerski, A. (2005). Self-consistent theory of current-induced switching of magnetization. *Phys. Rev. B*, 71:054407.

[Foros et al., 2005] Foros, J., Woltersdorf, G., Heinrich, B., and Brataas, A. (2005). Scattering of spin current injected in Pd(001). *Journal of Applied Physics*, 97(10):10A714.

[Ghosh, 2013] Ghosh, A. (2013). *Spin pumping and spin absorption in magnetic heterostructures*. PhD thesis, Université de Grenoble.

[Ghosh et al., 2012] Ghosh, A., Auffret, S., Ebels, U., and Bailey, W. E. (2012). Penetration depth of transverse spin current in ultrathin ferromagnets. *Phys. Rev. Lett.*, 109:127202.

[Gomonay et al., 2012] Gomonay, H. V., Kunitsyn, R. V., and Loktev, V. M. (2012). Symmetry and the macroscopic dynamics of antiferromagnetic materials in the presence of spin-polarized current. *Phys. Rev. B*, 85:134446.

[Hahn et al., 2014] Hahn, C., Naletov, V., de Loubens, G., Klein, O., d'Allivy Kelly, O., Anane, A., Bernard, R., Jacqet, E., Bortolotti, P., Cros, V., Prieto, J. L., and Muñoz, M. (2014). Measurement of the intrinsic damping constant in individual nanodisks of YIG and YIG/Pt. *ArXiv[cond-mat.mtrl.sci] e-prints*.

[Haney et al., 2007] Haney, P. M., Waldron, D., Duine, R. A., Núñez, A. S., Guo, H., and MacDonald, A. H. (2007). Ab initio giant magnetoresistance and current-induced torques in Cr/Au/Cr multilayers. *Phys. Rev. B*, 75:174428.

[Haug and Jauho, 2008] Haug, H. and Jauho, A. (2008). *Quantum Kinetics in Transport and Optics of Semiconductors*. Springer, second rev edition.

[Huai et al., 2004] Huai, Y., Albert, F., Nguyen, P., Pakala, M., and Valet, T. (2004). Observation of spin-transfer switching in deep submicron-sized and low-resistance magnetic tunnel junctions. *Applied Physics Letters*, 84(16):3118–3120.

[Ikeda et al., 2008] Ikeda, S., Hayakawa, J., Ashizawa, Y., Lee, Y. M., Miura, K., Hasegawa, H., Tsunoda, M., Matsukura, F., and Ohno, H. (2008). Tunnel magnetoresistance of 604% at 300k by suppression of ta diffusion in CoFeB/MgO/CoFeB pseudo-spin-valves annealed at high temperature. *Applied Physics Letters*, 93(8):082508.

[Ikeda et al., 2007] Ikeda, S., Hayakawa, J., Lee, Y. M., Matsukura, F., Ohno, Y., Hanyu, T., and Ohno, H. (2007). Magnetic tunnel junctions for spintronic memories and beyond. *Electron Devices, IEEE Transactions on*, 54(5):991–1002.

[Inaba et al., 1997] Inaba, N., Uesaka, Y., Nakamura, A., Futamoto, M., Sugita, Y., and Narishige, S. (1997). Damping constants of Co-Cr-Ta and Co-Cr-Pt thin films. *Magnetics, IEEE Transactions on*, 33(5):2989–2991.

[Inomata et al., 2008] Inomata, K., Ikeda, N., Tezuka, N., Goto, R., Sugimoto, S., M., W., and E., J. (2008). Highly spin-polarized materials and devices for spintronics. *Sci. Technol. Adv. Mater*, 9:127202.

[Inomata et al., 2002] Inomata, K., Nozaki, T., Tezuka, N., and Sugimoto, S. (2002). Magnetic switching field and giant magnetoresistance effect of multilayers with synthetic antiferromagnet free layers. *Applied Physics Letters*, 81(2):310–312.

[Julliere, 1975] Julliere, M. (1975). Tunneling between ferromagnetic films. *Physics Letters A*, 54(3):225–226.

[Kaiser and Parkin, 2006] Kaiser, C. and Parkin, S. S. P. (2006). High negative tunneling magnetoresistance in magnetic tunnel junctions with a ferrimagnetic cofeâgd electrode and a CoFe interface layer. *Applied Physics Letters*, 88(11).

[Kalitsov et al., 2009] Kalitsov, A., Chshiev, M., Theodonis, I., Kioussis, N., and Butler, W. H. (2009). Spin-transfer torque in magnetic tunnel junctions. *Phys. Rev. B*, 79:174416.

[Kalitsov et al., 2006] Kalitsov, A., Theodonis, I., Kioussis, N., Chshiev, M., Butler, W. H., and Vedyayev, A. (2006). Spin-polarized current-induced torque in magnetic tunnel junctions. *Journal of Applied Physics*, 99(8):08G501.

[Kasuya, 1956] Kasuya, T. (1956). A theory of metallic ferro- and antiferromagnetism on zener's model. *Progress of Theoretical Physics*, 16(1):45–57.

[Klaer et al., 2011] Klaer, P., Jenkins, C. A., Alijani, V., Winterlik, J., Balke, B., Felser, C., and Elmers, H. J. (2011). Disentangling the Mn moments on different sublattices in the half-metallic ferrimagnet $Mn_{3-x}Co_xGa$. *Applied Physics Letters*, 98(21):212510.

[Kollar et al., 2005] Kollar, M., Eckstein, M., Byczuk, K., Blumer, N., van Dongen, P., Radke de Cuba, M. H., Metzner, W., Tanaskovic, D., Dobrosavljevic, V., Kotliar, G., and Vollhardt, D. (2005). Green functions for nearest- and next-nearest-neighbor hopping on the Bethe lattice. *arXiv:cond-mat/0504637v2*.

[Kubota et al., 2008] Kubota, H., Fukushima, A., Yakushiji, K., Nagahama, T., Yuasa, S., Ando, K., Maehara, H., Nagamine, Y., Tsunekawa, K., Djayaprawira, D. D., Watanabe, N., and Suzuki, Y. (2008). Quantitative measurement of voltage dependence of spin-transfer torque in MgO-based magnetic tunnel junctions. *Nature Physics*, 4:37–41.

[Lakshmanan, 2011] Lakshmanan, M. (2011). The fascinating world of Landau-Lifshitz-Gilbert equation: An overview. *Phil. Trans. R. Soc.*, 369(1939):1280 – 1300.

[Lifshitz and Pitaievskii, 1981] Lifshitz, E. M. and Pitaievskii, L. P. (1981). *Physical Kinetics, Course of Theoretical Physics*, volume 10. Pergamon, Oxford, Oxford.

[Logan et al., 2012] Logan, J. M., Kim, H. C., Rosenmann, D., Cai, Z., Divan, R., Shpyrko, O. G., and Isaacs, E. D. (2012). Antiferromagnetic domain wall engineering in chromium films. *Applied Physics Letters*, 100(19):192405.

[Lombard et al., 2010] Lombard, L., Gapihan, E., Sousa, R. C., Dahmane, Y., Conraux, Y., Portemont, C., Ducruet, C., Papusoi, C., Prejbeanu, I. L., Noziéres, J. P., Dieny, B., and Schuhl, A. (2010). IrMn and FeMn blocking temperature dependence on heating pulse width. *Journal of Applied Physics*, 107(9):09D728.

[MacDonald and Tsoi, 2011] MacDonald, A. H. and Tsoi, M. (2011). Antiferromagnetic metal spintronics. *Phil. Trans. R. Soc.*, 369(1948):3098–3114.

[Manchon et al., 2008a] Manchon, A., Ryzhanova, N., Vedyayev, A., Chschiev, M., and Dieny, B. (2008a). Description of current-driven torques in magnetic tunnel junctions. *Journal of Physics: Condensed Matter*, 20(14):145208.

[Manchon et al., 2008b] Manchon, A., Ryzhanova, N., Vedyayev, A., and Dieny, B. (2008b). Spin-dependent diffraction at ferromagnetic/spin spiral interface. *Journal of Applied Physics*, 103(7):07A721.

[Martí et al., 2014] Martí, X., Fina, I., Contrera, C., Liu, J., Wadley, P., He, Q., Paull, R. J., Clarkson, J. D., Kudrnovsky, J., Turek, I., Kunes, J., Yi, D., Chu, J. H., Nelson, C. T., You, L., Arenholz, E., Salahuddin, S., Fontcuberta, J., Jungwirth, T., and Ramesh, R. (2014). Room-temperature antiferromagnetic memory resistor. *Nat. Mat.*, 13:367–374.

[Martí et al., 2012] Martí, X., Park, B. G., Wunderlich, J., Reichlová, H., Kurosaki, Y., Yamada, M., Yamamoto, H., Nishide, A., Hayakawa, J., Takahashi, H., and Jungwirth, T. (2012). Electrical measurement of antiferromagnetic moments in exchange-coupled IrMn/NiFe stacks. *Phys. Rev. Lett.*, 108:017201.

[Mathon and Umerski, 2001] Mathon, J. and Umerski, A. (2001). Theory of tunneling magnetoresistance of an epitaxial Fe/MgO/Fe(001) junction. *Phys. Rev. B*, 63:220403.

[Mendes et al., 2014] Mendes, J. B. S., Cunha, R. O., Alves Santos, O., Ribeiro, P. R. T., Machado, F. L. A., Rodríguez-Suárez, R. L., Azevedo, A., and Rezende, S. M. (2014). Large inverse spin hall effect in the antiferromagnetic metal $Ir_{20}Mn_{80}$. *Phys. Rev. B*, 89:140406.

[Merodio et al., 2014a] Merodio, P., Ghosh, A., Lemonias, C., Gautier, E., Ebels, U., Chshiev, M., Béa, H., Baltz, V., and Bailey, W. E. (2014a). Penetration depth and absorption mechanisms of spin currents in $Ir_{20}Mn_{80}$ and $Fe_{50}Mn_{50}$ polycrystalline films by ferromagnetic resonance and spin pumping. *Applied Physics Letters*, 104(3):032406.

[Merodio et al., 2014b] Merodio, P., Kalitsov, A., Béa, H., Baltz, V., and Chshiev, M. (2014b). Spin-dependent transport in antiferromagnetic tunnel junctions. *Applied Physics Letters*, 105(12):122403.

[Merodio et al., 2014c] Merodio, P., Kalitsov, A., Béa, H., Baltz, V., and Chshiev, M. (2014c). Spin-modulated torque waves in ferrimagnetic tunnel junctions. *Phys. Rev. B*, 90:224422.

[Mizukami et al., 2001] Mizukami, S., Ando, Y., and Miyazaki, T. (2001). The study on ferromagnetic resonance linewidth for NM/80NiFe/NM (NM=Cu, Ta, Pd and Pt) films. *Jap. J. Appl. Phys.*, 40(580).

[Moodera et al., 1995] Moodera, J. S., Kinder, L. R., Wong, T. M., and Meservey, R. (1995). Large magnetoresistance at room temperature in ferromagnetic thin film tunnel junctions. *Phys. Rev. Lett.*, 74:3273–3276.

[Myers et al., 1999] Myers, E. B., Ralph, D. C., Katine, J. A., Louie, R., and Buhrman, R. A. (1999). Current-induced switching of domains in magnetic multilayer devices. *Science*, 285(867).

[Nogués and Schuller, 1999] Nogués, J. and Schuller, I. K. (1999). Exchange bias. *Journal of Magnetism and Magnetic Materials*, 192(203):203–232.

[Núñez et al., 2006] Núñez, A. S., Duine, R. A., Haney, P., and MacDonald, A. H. (2006). Theory of spin torques and giant magnetoresistance in antiferromagnetic metals. *Phys. Rev. B*, 73:214426.

[Odashima et al., 2013] Odashima, M. M., Marmodoro, A., Buczek, P., Ernst, A., and Sandratskii, L. (2013). Chirality-dependent magnon lifetime in a compensated half-metallic ferrimagnet. *Phys. Rev. B*, 87:174420.

[Park et al., 2011] Park, B. G., Wunderlich, J., Martí, X., Holý, V., Kurosaki, Y., Yamada, M., Yamamoto, H., Nishide, A., Hayakawa, J., Takahashi, H., Shick, A. B., and Jungwirth, T. (2011). A spin-valve-like magnetoresistance of an antiferromagnet-based tunnel junction. *Nat. Mat.*, 10:347–351.

[Park et al., 2000] Park, W., Baxter, D. V., Steenwyk, S., Moraru, I., Pratt, W. P., and Bass, J. (2000). Measurement of resistance and spin-memory loss (spin relaxation) at interfaces using sputtered current perpendicular-to-plane exchange-biased spin valves. *Phys. Rev. B*, 62:1178–1185.

[Petti et al., 2013] Petti, D., Albisetti, E., Reichlová, H., Gazquez, J., Varela, M., Molina-Ruiz, M., Lopeandía, A. F., Olejník, K., Novák, V., Fina, I., Dkhil, B., Hayakawa, J., Marti, X., Wunderlich, J., Jungwirth, T., and Bertacco, R. (2013). Storing magnetic information in IrMn/MgO/Ta tunnel junctions via field-cooling. *Applied Physics Letters*, 102(19):192404.

[Prejbeanu et al., 2013] Prejbeanu, I. L., Bandiera, S., Alvarez-Hérault, J., Sousa, R. C., Dieny, B., and J-P Nozières, J.-P. (2013). Thermally assisted MRAMs: ultimate scalability and logic functionalities. *Journal of Physics D: Applied Physics*, 46(7):074002.

[Ralph and Stiles, 2008] Ralph, D. and Stiles, M. (2008). Spin transfer torques. *Journal of Magnetism and Magnetic Materials*, 320(7):1190–1216.

[Rammer and Smith, 1986] Rammer, J. and Smith, H. (1986). Quantum field-theoretical methods in transport theory of metals. *Rev. Mod. Phys.*, 58:323–359.

[Rezende et al., 2013] Rezende, S. M., Rodríguez-Suárez, R. L., and Azevedo, A. (2013). Magnetic relaxation due to spin pumping in thick ferromagnetic films in contact with normal metals. *Phys. Rev. B*, 88:014404.

[Roermund, 2010] Roermund, R. V. (2010). *Theoretical Study of non-equilibrium transport in Kondo quantum dots*. PhD thesis, Université de Grenoble.

[Ruderman and Kittel, 1954] Ruderman, M. A. and Kittel, C. (1954). Indirect exchange coupling of nuclear magnetic moments by conduction electrons. *Phys. Rev.*, 96:99–102.

[Saidaoui et al., 2014] Saidaoui, H. B. M., Manchon, A., and Waintal, X. (2014). Spin transfer torque in antiferromagnetic spin valves: From clean to disordered regimes. *Phys. Rev. B*, 89:174430.

[Sankey et al., 2006] Sankey, J. C., Braganca, P. M., Garcia, A. G. F., Krivorotov, I. N., Buhrman, R. A., and Ralph, D. C. (2006). Spin-transfer-driven ferromagnetic resonance of individual nanomagnets. *Phys. Rev. Lett.*, 96:227601.

[Sankey et al., 2008] Sankey, J. C., Cui, Y. T., Sun, J. Z., Slonczewski, J. C., Buhrman, R. A., and Ralph, D. C. (2008). Measurement of the spin-transfer-torque vector in magnetic tunnel junctions. *Nature Physics*, 4:67–71.

[Scholl et al., 2004] Scholl, A., Liberati, M., Arenholz, E., Ohldag, H., and Stöhr, J. (2004). Creation of an antiferromagnetic exchange spring. *Phys. Rev. Lett.*, 92:247201.

[Serrano-Guisan et al., 2011] Serrano-Guisan, S., Skowronski, W., Wrona, J., Liebing, N., Czapkiewicz, M., Stobiecki, T., Reiss, G., and Schumacher, H. W. (2011). Inductive determination of the optimum tunnel barrier thickness in magnetic tunneling junction stacks for spin torque memory applications. *Journal of Applied Physics*, 110(2):023906.

[Sinova and Zutic, 2012] Sinova, J. and Zutic, I. (2012). New moves of the spintronics tango. *Nat. Mat.*, 11:368–371.

[Slonczewski, 1995] Slonczewski, J. C. (1995). Current-driven excitation of magnetic multilayers. *J. Magn. Magn. Mater.*, 159:L1–L7.

[Slonczewski, 2005] Slonczewski, J. C. (2005). Currents, torques, and polarization factors in magnetic tunnel junctions. *Phys. Rev. B*, 71:024411.

[Smith et al., 2008] Smith, N., Maat, S., Carey, M. J., and Childress, J. R. (2008). Coresonant enhancement of spin-torque critical currents in spin valves with a synthetic-ferrimagnet free layer. *Phys. Rev. Lett.*, 101:247205.

[Sousa et al., 2002] Sousa, R. C., Zhang, Z., and Freitas, P. P. (2002). Synthetic ferrimagnet free layer tunnel junction for magnetic random access memories. *Journal of Applied Physics*, 91(10):7700–7702.

[Srinivasan et al., 2008] Srinivasan, K., Piramanayagam, S. N., and Sbiaa, R. (2008). Antiferromagnetic iridium manganese based intermediate layers for perpendicular magnetic recording media. *Applied Physics Letters*, 93(7).

[Stamenova et al., 2005] Stamenova, M., Sanvito, S., and Todorov, T. N. (2005). Current-driven magnetic rearrangements in spin-polarized point contacts. *Phys. Rev. B*, 72:134407.

[Stearns, 1977] Stearns, M. B. (1977). Simple explanation of tunneling spin-polarization of fe, co, ni and its alloys. *Journal of Magnetism and Magnetic Materials*, 5(2):167–171.

[Stefanucci and Leeuwen, 2013] Stefanucci, G. and Leeuwen, R. (2013). *Nonequilibrium Many-Body Theory of Quantum Systems*. Cambridge University Press, Cambridge, first edition.

[Stiles and Zangwill, 2002] Stiles, M. D. and Zangwill, A. (2002). Anatomy of spin-transfer torque. *Phys. Rev. B*, 66:014407.

[Swaving and Duine, 2011] Swaving, A. C. and Duine, R. A. (2011). Current induced torques in continuous antiferromagnetic textures. *Phys. Rev. B*, 83:054428.

[Takano et al., 1997] Takano, K., Kodama, R. H., Berkowitz, A. E., Cao, W., and Thomas, G. (1997). Interfacial uncompensated antiferromagnetic spins: Role in unidirectional anisotropy in polycrystalline $Ni_{81}Fe_{19}$/CoO bilayers. *Phys. Rev. Lett.*, 79:1130–1133.

[Tezuka et al., 2003a] Tezuka, N., Koike, N., Inomata, K., and Sugimoto, S. (2003a). Magnetization reversal and domain structure of antiferromagnetically coupled submicron elements. *Journal of Applied Physics*, 93(10):7441–7443.

[Tezuka et al., 2003b] Tezuka, N., Koike, N., Inomata, K., and Sugimoto, S. (2003b). Single domain observation for synthetic antiferromagnetically coupled bits with low aspect ratios. *Applied Physics Letters*, 82(4):604–606.

[Theodonis et al., 2006] Theodonis, I., Kioussis, N., Kalitsov, A., Chshiev, M., and Butler, W. H. (2006). Anomalous bias dependence of spin torque in magnetic tunnel junctions. *Phys. Rev. Lett.*, 97:237205.

[Tsoi et al., 1998] Tsoi, M., Jansen, A. G. M., Bass, J., Chiang, W.-C., Seck, M., Tsoi, V., and Wyder, P. (1998). Excitation of a magnetic multilayer by an electric current. *Phys. Rev. Lett.*, 80:4281–4284.

[Tsymbal et al., 2003] Tsymbal, E. Y., Mryasov, O. N., and LeClair, P. R. (2003). Spin-dependent tunnelling in magnetic tunnel junctions. *Journal of Physics: Condensed Matter*, 15(4):R109.

[Tulapurkar et al., 2005] Tulapurkar, A., Suzuki, Y., Fukushima, A., Kubota, H., Maehara, H., Tsunekawa, K., Djayaprawira, D., Watanabe, N., and Yuasa, S. (2005). Spin-torque diode effect in magnetic tunnel junctions. *Nature*, 438:339–342.

[Urazhdin and Anthony, 2007] Urazhdin, S. and Anthony, N. (2007). Effect of polarized current on the magnetic state of an antiferromagnet. *Phys. Rev. Lett.*, 99:046602.

[van Leuken and de Groot, 1995] van Leuken, H. and de Groot, R. A. (1995). Half-metallic antiferromagnets. *Phys. Rev. Lett.*, 74:1171–1173.

[Wang et al., 2014] Wang, H., Du, C., Chris Hammel, P., and Yang, F. (2014). Spin current and inverse spin hall effect in ferromagnetic metals probed by $Y_3Fe_5O_{12}$-based spin pumping. *Applied Physics Letters*, 104(20):202405.

[Wang et al., 2009] Wang, L., Wang, S. G., Rizwan, S., Qin, Q. H., and Han, X. F. (2009). Magnetoresistance effect in antiferromagnet/nonmagnet/antiferromagnet multilayers. *Applied Physics Letters*, 95(15):152512.

[Wang et al., 2008] Wang, S., Xu, Y., and Xia, K. (2008). First-principles study of spin-transfer torques in layered systems with noncollinear magnetization. *Phys. Rev. B*, 77:184430.

[Wei et al., 2007] Wei, Z., Sharma, A., Nunez, A. S., Haney, P. M., Duine, R. A., Bass, J., MacDonald, A. H., and Tsoi, M. (2007). Changing exchange bias in spin valves with an electric current. *Phys. Rev. Lett.*, 98:116603.

[Wieser et al., 2011] Wieser, R., Vedmedenko, E. Y., and Wiesendanger, R. (2011). Indirect control of antiferromagnetic domain walls with spin current. *Phys. Rev. Lett.*, 106:067204.

[Wolf et al., 2001] Wolf, S. A., Awschalom, D. D., Buhrman, R. A., Daughton, J. M., von Molna, S., Roukes, M. L., Chtchelkanova, A. Y., and Treger, D. M. (2001). Spintronics: A spin-based electronics vision for the future. *Science*, 159(4):1488–1495.

[Xu et al., 2008] Xu, Y., Wang, S., and Xia, K. (2008). Spin-transfer torques in antiferromagnetic metals from first principles. *Phys. Rev. Lett.*, 100:226602.

[Yosida, 1957] Yosida, K. (1957). Magnetic properties of Cu-Mn alloys. *Phys. Rev.*, 106:893–898.

[You et al., 2011] You, C.-Y., Yoon, J., Park, S.-Y., Yuasa, S., and Jung, M.-H. (2011). Magnetic noise spectra and spin transfer torque of a magnetic tunnel junction with an exchange biased synthetic ferrimagnetic reference layer. *Current Applied Physics*, 11(2, Supplement):e92–e94. International Symposium on Next Generation Terabit Memory Technology CAP/ 2010 {ISNGTMT} Supplement.

[Zhang and Willis, 2001] Zhang, R. and Willis, R. F. (2001). Thickness-dependent curie temperatures of ultrathin magnetic films: Effect of the range of spin-spin interactions. *Phys. Rev. Lett.*, 86:2665–2668.

[Zhang and Li, 2004] Zhang, S. and Li, Z. (2004). Roles of nonequilibrium conduction electrons on the magnetization dynamics of ferromagnets. *Phys. Rev. Lett.*, 93:127204.

Appendix A

Calculation of the nonequilibrium Keldysh function

The Dyson or Quantum Kinetic equation for the nonequilibrium 2×2 Keldysh function matrix reads:

$$\hat{F}_{pq} = \hat{f}_{pq} + \hat{g}_{pq1}\Sigma_{q_1q_2}\hat{F}_{q_2q} + \hat{f}_{pq_1}\Sigma_{q_1q_2}\hat{G}^a_{q_2q} \tag{A.1}$$

where the self-energy Σ_{pq} is defined as [Caroli et al., 1971]:

$$\Sigma_{pq} = T(\delta_{p\alpha}\delta_{aq} + \delta_{pa}\delta_{\alpha q}) + T'(\delta_{pb}\delta_{\alpha' q} + \delta_{p\alpha'}\delta_{bq}) \tag{A.2}$$

T is the hopping parameter across the left barrier interface and the non-equilibrium Green function matrices for the uncoupled left and right leads at local equilibrium are:

$$\hat{f}_{\lambda\mu} = (1 - 2f_L)(\hat{g}^r_{\lambda\mu} - \hat{g}^a_{\lambda\mu}) \tag{A.3}$$

$$\hat{f}_{\lambda'\mu'} = (1 - 2f_R)(\hat{g}^r_{\lambda'\mu'} - \hat{g}^a_{\lambda'\mu'}) \tag{A.4}$$

where f_L and f_R are the Fermi-Dirac distribution functions in the isolated left and right leads. In particular, at the left and right interfaces, we have:

$$\hat{f}_{\alpha\alpha} = (1 - 2f_L)(\hat{g}^r_{\alpha\alpha} - \hat{g}^a_{\alpha\alpha}) \tag{A.5}$$

$$\hat{f}_{\alpha'\alpha'} = (1 - 2f_R)(\hat{g}^r_{\alpha'\alpha'} - \hat{g}^a_{\alpha'\alpha'}) \tag{A.6}$$

Using the definition (A.2) in Eq. (A.1) gives:

$$\hat{F}_{pq} = \hat{f}_{pq} + \hat{g}_{p\alpha} T \hat{F}_{aq} + \hat{g}_{pa} T \hat{F}_{\alpha q} + \hat{g}_{pb} T' \hat{F}_{\alpha' q} + \hat{g}_{p\alpha'} T' \hat{F}_{bq} + \hat{f}_{p\alpha} T \hat{G}^a_{aq} + \hat{f}_{pa} T \hat{G}^a_{\alpha q} + \hat{f}_{pb} T' \hat{G}^a_{\alpha' q} + \hat{f}_{p\alpha'} T' \hat{G}^a_{bq}$$

As explained above, we are interested in evaluating the observables at the right lead, so that the three Keldysh functions $\hat{F}_{b\alpha'}$, $\hat{F}_{\alpha' b}$ and $\hat{F}_{\lambda',\mu'}$ are needed. These Keldysh functions are coupled via the Quantum Kinetic Equation. For instance, the Quantum Kinetic Equation for $\hat{F}_{b\alpha'}$ involves three more coupled equations:

$$\hat{F}_{b\alpha'} = \hat{g}_{ba} T \hat{F}_{\alpha\alpha'} + \hat{g}_{bb} T' \hat{F}_{\alpha'\alpha'} + \hat{f}_{ba} T \hat{G}^a_{\alpha\alpha'} + \hat{f}_{bb} T' \hat{G}^a_{\alpha'\alpha'}$$

$$\hat{F}_{\alpha\alpha'} = \hat{g}_{\alpha\alpha} T \hat{F}_{a\alpha'} + \hat{f}_{\alpha\alpha} T \hat{G}^a_{a\alpha'}$$

$$\hat{F}_{\alpha'\alpha'} = \hat{f}_{\alpha'\alpha'} + \hat{g}_{\alpha'\alpha'} T' \hat{F}_{b\alpha'} + \hat{f}_{\alpha'\alpha'} T \hat{G}^a_{b\alpha'}$$

$$\hat{F}_{a\alpha'} = \hat{g}_{aa} T \hat{F}_{\alpha\alpha'} + \hat{g}_{ab} T' \hat{F}_{\alpha'\alpha'} + \hat{f}_{aa} T \hat{G}^a_{\alpha\alpha'} + \hat{f}_{ab} T' \hat{G}^a_{\alpha'\alpha'}$$

As previously discussed by Caroli et al [Caroli et al., 1971] we assume that in the range of energy of interest, the density of states of the uncoupled barrier is strictly zero. The tunnelling process of electrons occurs in the gap of the insulator. The density of states is related to the imaginary part of the retarded Green function. In particular, the local density of states at the atomic site i reads: $LDOS(E) = -\frac{1}{\pi} Im[g^r_{i,i}(E)]$. This means that the retarded Green functions inside the barrier are real (the vanishing of the imaginary part applies also to the retarded Green function correlating different atomic sites). In addition, as will be seen below, the retarded Green functions for a given spin are symmetric in real space: $g^r_{i,j} = g^r_{j,i}$. The following relations are thus valid inside the barrier:

$$g^r_{i,j} = g^r_{j,i} = (g^a_{i,j})^* = g^a_{i,j} = g^r_{j,i} = g^r_{i,j} \longrightarrow g^r_{i,j} = g^a_{i,j}$$

Therefore, inside the insulator, $f_{i,j} = 0$, so that:

$$\hat{f}_{ba} = \hat{f}_{bb} = \hat{f}_{ba} = \hat{f}_{ab} = 0$$

The Quantum Kinetic equations for the interfacial Keldysh function $\hat{F}_{b\alpha'}$ are then simplified to give the following system of coupled equations:

1.

$$\hat{F}_{b\alpha'} = \hat{g}_{ba} T \hat{F}_{\alpha\alpha'} + \hat{g}_{bb} T' \hat{F}_{\alpha'\alpha'}$$

2.
$$\hat{F}_{\alpha\alpha'} = \hat{g}_{\alpha\alpha} T \hat{F}_{a\alpha'} + \hat{f}_{\alpha\alpha} T \hat{G}^a_{a\alpha'}$$

3.
$$\hat{F}_{\alpha'\alpha'} = \hat{f}_{\alpha'\alpha'} + \hat{g}_{\alpha'\alpha'} T' \hat{F}_{b\alpha'} + \hat{f}_{\alpha'\alpha'} T \hat{G}^a_{b\alpha'}$$

4.
$$\hat{F}_{a\alpha'} = \hat{g}_{aa} T \hat{F}_{\alpha\alpha'} + \hat{g}_{ab} T' \hat{F}_{\alpha'\alpha'}$$

Injecting 2. and 3. into 1. and 4. gives:

$$(\hat{I} - \hat{g}_{bb}\hat{\Sigma}_{bb})\hat{F}_{b\alpha'} = \hat{g}_{ba}\hat{\Sigma}_{aa}\hat{F}_{a\alpha'} + \hat{g}_{ba} T \hat{f}_{\alpha\alpha} T \hat{G}^a_{a\alpha'} + \hat{g}_{bb} T' \hat{f}_{\alpha'\alpha'} + \hat{g}_{bb} T' \hat{f}_{\alpha'\alpha'} T' \hat{G}^a_{b\alpha'}$$

$$(\hat{I} - \hat{g}_{aa}\hat{\Sigma}_{aa})\hat{F}_{a\alpha'} = \hat{g}_{aa} T \hat{f}_{\alpha\alpha} T \hat{G}^a_{a\alpha'} + \hat{g}_{ab} T' \hat{f}_{\alpha'\alpha'} + \hat{g}_{ab}\hat{\Sigma}_{bb}\hat{F}_{b'\alpha'} + \hat{g}_{ab} T' \hat{f}_{\alpha'\alpha'} T' \hat{G}^a_{b\alpha'}$$

where

$$\hat{\Sigma}_{bb} = T' \hat{g}_{\alpha'\alpha'} T'$$

$$\hat{\Sigma}_{aa} = T \hat{g}_{\alpha\alpha} T$$

Setting

$$\hat{A} = (\hat{I} - \hat{g}_{aa}\hat{\Sigma}_{aa})^{-1}$$

$$\hat{B} = (\hat{I} - \hat{g}_{bb}\hat{\Sigma}_{bb})^{-1}$$

we have, after combining both equations:

$$\begin{aligned}(\hat{I} - \hat{B}\hat{g}_{ba}\hat{\Sigma}_{aa}\hat{A}\hat{g}_{ab}\hat{\Sigma}_{bb})\hat{F}_{b\alpha'} = \hat{B}[&\hat{g}_{ba}\hat{\Sigma}_{aa}\hat{A}(\hat{g}_{aa} T \hat{f}_{\alpha\alpha} T \hat{G}^a_{a\alpha'} + \hat{g}_{ab} T' \hat{f}_{\alpha'\alpha'} + \hat{g}_{ab} T' \hat{f}_{\alpha'\alpha'} T' \hat{G}^a_{b\alpha'}) \\ &+ \hat{g}_{ba} T \hat{f}_{\alpha\alpha} T \hat{G}^a_{a\alpha'} + \hat{g}_{bb} T' \hat{f}_{\alpha'\alpha'} + \hat{g}_{bb} T' \hat{f}_{\alpha'\alpha'} T' \hat{G}^a_{b\alpha'}]\end{aligned}$$

If we call

$$\hat{D} = (\hat{I} - \hat{B}\hat{g}_{ba}\hat{\Sigma}_{aa}\hat{A}\hat{g}_{ab}\hat{\Sigma}_{bb})^{-1}$$

$$\hat{F}_{b\alpha'} = \hat{F}^L_{b\alpha'} + \hat{F}^R_{b\alpha'}$$

where $\hat{F}^L_{b\alpha'}$ and $\hat{F}^R_{b\alpha'}$ make reference to the uncoupled surface Keldysh function at the left and right leads respectively:

$$\begin{aligned}\hat{F}^L_{b\alpha'} &= T^2\hat{D}\hat{B}\hat{g}_{ba}(\hat{\Sigma}_{aa}\hat{A}\hat{g}_{aa}\hat{f}_{\alpha\alpha}\hat{G}^a_{a\alpha'} + \hat{f}_{\alpha\alpha}\hat{G}^a_{a\alpha'}) \\ &= T^2\hat{D}\hat{B}\hat{g}_{ba}(\hat{I} + \hat{\Sigma}_{aa}\hat{A}\hat{g}_{aa})\hat{f}_{\alpha\alpha}\hat{G}^a_{a\alpha'}\end{aligned}$$

$$\begin{aligned}\hat{F}^R_{b\alpha'} &= \hat{D}\hat{B}\hat{g}_{ba}\hat{\Sigma}_{aa}\hat{A}\hat{g}_{ab}T'\hat{f}_{\alpha'\alpha'}(\hat{I} + T'\hat{G}^a_{b\alpha'}) + \hat{D}\hat{B}\hat{g}_{bb}T'\hat{f}_{\alpha'\alpha'}(\hat{I} + T'\hat{G}^a_{b\alpha'}) \\ &= \hat{D}\hat{B}(\hat{g}_{ba}\hat{\Sigma}_{aa}\hat{A}\hat{g}_{ab} + \hat{g}_{bb})T'\hat{f}_{\alpha'\alpha'}(\hat{I} + T'\hat{G}^a_{b\alpha'})\end{aligned}$$

An equivalent system of equations for $\hat{F}_{\alpha' b}$ can be established:

1. $$\hat{F}_{\alpha' b} = \hat{g}_{\alpha'\alpha'}T'\hat{F}_{bb} + \hat{f}_{\alpha'\alpha'}T'\hat{G}^a_{bb}$$

2. $$\hat{F}_{bb} = \hat{g}_{ba}T\hat{F}_{\alpha b} + \hat{g}_{bb}T'\hat{F}_{\alpha' b}$$

3. $$\hat{F}_{\alpha b} = \hat{g}_{\alpha\alpha}T\hat{F}_{ab} + \hat{f}_{\alpha\alpha}T\hat{G}^a_{ab}$$

4. $$\hat{F}_{ab} = \hat{g}_{aa}T\hat{F}_{\alpha b} + \hat{g}_{ab}T'\hat{F}_{\alpha' b}$$

Combining 1.-2. and 4.-3., we have:

$$(\hat{I} - \hat{\Sigma}_{bb}\hat{g}_{bb})\hat{F}_{\alpha' b} = \hat{g}_{\alpha'\alpha'}T'\hat{g}_{ba}T\hat{F}_{\alpha b} + \hat{f}_{\alpha'\alpha'}T'\hat{G}^a_{bb}$$

$$(\hat{I} - \hat{\Sigma}_{aa}\hat{g}_{aa})\hat{F}_{\alpha b} = \hat{g}_{\alpha\alpha}T\hat{g}_{ab}T'\hat{F}_{\alpha' b} + \hat{f}_{\alpha\alpha}T\hat{G}^a_{ab}$$

Setting

$$\hat{N} = (\hat{I} - \hat{\Sigma}_{bb}\hat{g}_{bb})^{-1}$$

$$\hat{M} = (\hat{I} - \hat{\Sigma}_{aa}\hat{g}_{aa})^{-1}$$

and combining both equations:

$$(\hat{I} - \hat{N}\hat{\Sigma}_{bb}\hat{g}_{ba}\hat{M}\hat{\Sigma}_{aa}\hat{g}_{ab})\hat{F}_{\alpha' b} = T^2T'\hat{N}\hat{g}_{\alpha'\alpha'}\hat{g}_{ba}\hat{M}\hat{f}_{\alpha\alpha}\hat{G}^a_{ab} + T'\hat{N}\hat{f}_{\alpha'\alpha'}\hat{G}^a_{bb}$$

Setting

$$(\hat{I} - \hat{N}\hat{\Sigma}_{bb}\hat{g}_{ba}\hat{M}\hat{\Sigma}_{aa}\hat{g}_{ab})^{-1} = \hat{L}$$

we have:

$$\hat{F}_{\alpha' b} = \hat{F}^L_{\alpha' b} + \hat{F}^R_{\alpha' b}$$

$$\hat{F}^L_{\alpha' b} = T^2 T' \hat{L}\hat{N}\hat{g}_{\alpha'\alpha'}\hat{g}_{ba}\hat{M}\hat{f}_{\alpha\alpha}\hat{G}^a_{ab}$$

$$\hat{F}^R_{\alpha' b} = T'\hat{L}\hat{N}\hat{f}_{\alpha'\alpha'}\hat{G}^a_{bb}$$

We shall use $T' = T$ for simplicity, so that:

$$\hat{F}^L_{\alpha' b} = T\hat{L}\hat{N}\hat{\Sigma}_{bb}\hat{g}_{ba}\hat{M}\hat{f}_{\alpha\alpha}\hat{G}^a_{ab}$$

$$\hat{F}^R_{\alpha' b} = T\hat{L}\hat{N}\hat{f}_{\alpha'\alpha'}\hat{G}^a_{bb}$$

In the same way:

$$\hat{F}_{\lambda'\mu'} = \hat{F}^L_{\lambda'\mu'} + \hat{F}^R_{\lambda'\mu'}$$

$$\hat{F}^L_{\lambda'\mu'} = \hat{g}_{\lambda'\alpha'} T \hat{Den}^{-1} \hat{g}_{ba} T(\hat{I} + \hat{\Sigma}_{aa}\hat{A}\hat{g}_{aa})\hat{f}_{\alpha\alpha} T \hat{G}^a_{ab} T \hat{g}^a_{\alpha'\mu'}$$

$$\hat{F}^R_{\lambda'\mu'} = \hat{f}_{\lambda'\mu'} + \hat{f}_{\lambda'\alpha'} T \hat{G}^a_{bb} T \hat{g}^a_{\alpha'\mu'} + \hat{g}_{\lambda'\alpha'} T \hat{Den}^{-1} (\hat{g}_{bb} + \hat{g}_{ba}\hat{\Sigma}_{aa}\hat{A}\hat{g}_{ab}) T (\hat{f}_{\alpha'\mu'} + \hat{f}_{\alpha'\alpha'} T \hat{G}^a_{bb} T \hat{g}^a_{\alpha'\mu'})$$

where

$$\hat{Den} = \hat{I} - \hat{g}_{bb}\hat{\Sigma}_{bb} - \hat{g}_{ba}\hat{\Sigma}_{aa}\hat{A}\hat{g}_{ab}\hat{\Sigma}_{bb}$$

Appendix B

Calculation of the retarded Green function for a 1-D ferrimagnetic chain

B.1 Calculation of the Retarded Green function for a one dimensional ferrimagnet

A 1-D FI chain of localized moments seen by one itinerant spin is characterized in a TB model by two on-site energies ϵ_1 and ϵ_2 (alternating from one site to the next one) and a hopping parameter t. This 1-D chain corresponds to a lattice without closed loops that can be mapped into a Bethe lattice or Cayley which is completely characterized by its number of nearest neighbours $Z = 2$ or its connectivity $K = Z - 1$ [Economou, 2006]. Splitting the 1-D TB Hamiltonian into an unperturbed site-diagonal part plus an off-diagonal perturbation and using renormalized perturbation expansion [Economou, 2006] allows to perform the calculation of the the system's resolvent $\hat{g}_{\lambda',\mu'}(z)$, where z is a complex variable. This resolvent is a more general definition of the Green function in the complex plane, from which the retarded Green function can be defined as follows:

$$\hat{g}^r_{\lambda'.\mu'}(E) = \lim_{s \to 0^+} \hat{g}_{\lambda',\mu'}(z = E + is)$$

where E stands for the energy variable belonging to the real axis of the complex plane.

The first step to obtain the retarded Green function for a given spin in the Bethe lattice is the calculation of the diagonal elements or locators of this function in the two types of site of the lattice. As seen below, the off diagonal elements or two site correlation functions can be expressed in terms of these locators. Let's start with the expression (5.57) of [Economou, 2006] for the locator or resolvent on a site l / $\epsilon_l = \epsilon_1$ owning to a Bethe lattice with Z nearest neighbours and a connectivity $K = Z - 1$:

$$g(l,l,z) = \frac{2K(z-\epsilon_2)}{(K-1)(z-\epsilon_1)(z-\epsilon_2) + (K+1)\sqrt{(z-\epsilon_1)(z-\epsilon_2)[(z-\epsilon_1)(z-\epsilon_2) - 4Kt^2]}} \tag{B.1}$$

In order to calculate the retarded Green function from the resolvent Eq. (B.1), it must be taken into account that the local density of states on a site l is proportional to the retarded Green function:

$$LDOS(l,E) = -\frac{1}{\pi} Im[g^r(l,l,E)]$$

For E owning to the energy spectrum of the system, the $LDOS$ is $\neq 0$, so that the imaginary part of the retarded Green function $Im[g^r(l,l,E)]$ is therefore $\neq 0$ as well. On the real axis, ($z = E \in \mathbb{R}$), the only way to fulfil this condition is to have a square root of a negative real quantity in Eq. (B.1). Allowed states will be confined in those regions of energy where

$$(E-\epsilon_1)(E-\epsilon_2)[(E-\epsilon_1)(E-\epsilon_2) - 4Kt^2] < 0 \tag{B.2}$$

Let's study the sign of (B.2) to find these energy bands:

1. $(E-\epsilon_1) > 0 \longrightarrow E > \epsilon_1$
2. $(E-\epsilon_2) > 0 \longrightarrow E > \epsilon_2$
3. $(E-\epsilon_1)(E-\epsilon_2) - 4Kt^2 = E^2 - (\epsilon_1+\epsilon_2)E + (\epsilon_1\epsilon_2 - 4Kt^2)$

Expression 3. is a concave parabola whose discriminant is

$$\Delta = (\epsilon_1+\epsilon_2)^2 - 4(\epsilon_1\epsilon_2 - 4Kt^2) = (\epsilon_1-\epsilon_2)^2 + 16Kt^2 \longrightarrow \Delta > 0$$

The two real roots of this second degree equation are given by:

$$E_1 = \frac{(\epsilon_1+\epsilon_2) + \sqrt{\Delta}}{2} \quad \text{and} \quad E_2 = \frac{(\epsilon_1+\epsilon_2) - \sqrt{\Delta}}{2}$$

and the vertical axis of the parabola is given by the mean value of ϵ_1 and ϵ_2: $E_c = (\epsilon_1+\epsilon_2)/2$.
According to the relative position of ϵ_1, ϵ_2, E_1 and E_2, we have three different cases (recall that $\epsilon_1 > \epsilon_2$):

a) $\epsilon_2 < E_2 < E_1 < \epsilon_1$
b) $\epsilon_2 = E_2 < E_1 = \epsilon_1$
c) $E_2 < \epsilon_2 < \epsilon_1 < E_1$

Conditions a) and b) imply that $4Kt^2 < 0$, so that the only possibility is $E_2 < \epsilon_2 < \epsilon_1 < E_1$. In this particular configuration, the product of the three factors at the left

hand side of equation (B.2) is negative only in two intervals, so that the spectrum of the extended states splits into two sub bands, the lower one extending from $E_2 = \frac{(\epsilon_1+\epsilon_2)}{2} - \sqrt{(\epsilon_1-\epsilon_2)^2/4+4Kt^2}$ to ϵ_2 and the upper one extending from ϵ_1 to $E_1 = \frac{(\epsilon_1+\epsilon_2)}{2} + \sqrt{(\epsilon_1-\epsilon_2)^2/4+4Kt^2}$. Both sub bands have the same bandwidth $B = \frac{(\epsilon_2-\epsilon_1)}{2} + \sqrt{(\epsilon_2-\epsilon_1)^2/4+4Kt^2}$, and they are symmetric with respect to the vertical axis of the parabola: $(\epsilon_1+\epsilon_2)/2 = (E_1+E_2)/2 = E_c$.
In these sub bands, we have:

$$R = (E-\epsilon_1)(E-\epsilon_2)[(E-\epsilon_1)(E-\epsilon_2) - 4Kt^2] < 0$$

so that the denominator of Eq.(B.1) exhibit two purely imaginary square roots: $\sqrt{R} = \pm i\sqrt{-R}$. The resolvent on the real axis (depending on the real variable E) then becomes:

$$g(l,l,E) = \frac{2K(E-\epsilon_2)}{(K-1)(E-\epsilon_1)(E-\epsilon_2) \pm i(K+1)\sqrt{(E-\epsilon_1)(E-\epsilon_2)[4Kt^2-(E-\epsilon_1)(E-\epsilon_2)]}} \tag{B.3}$$

According to the condition $0 \leq DOS(l,E) = -\frac{1}{\pi} Im[g^r(l,l,E)]$, determining the retarded Green function on the allowed energy spectrum $g^r(l,l,E)$ consists in choosing the sign $\pm i$ in such a way that $Im[g^r(l,l,E)] < 0$. As seen above, outside the allowed energy spectrum $R > 0$ and the imaginary part $Im[g^r(l,l,E)]$ vanishes.

Forbidden states: $E < E_2$, $\epsilon_2 < E < \epsilon_1$ and $E > E_1$

The square root in the denominator corresponds to the product [Kollar et al., 2005]

$$\sqrt{(E-\epsilon_1)(E-\epsilon_2)} \cdot \sqrt{(E-\epsilon_1)(E-\epsilon_2) - 4Kt^2}$$

where the square roots are given by their principal branches.

$\underline{E < E_2}$

In this region, $(E-\epsilon_1)(E-\epsilon_2) > 0$ and $(E-\epsilon_1)(E-\epsilon_2) - 4Kt^2 > 0$, so we take the positive square roots:

$$g_{f1}^{r/a}(l,l,E) = \frac{2K(E-\epsilon_2)}{(K-1)(E-\epsilon_1)(E-\epsilon_2) + (K+1)\sqrt{(E-\epsilon_1)(E-\epsilon_2)[(E-\epsilon_1)(E-\epsilon_2) - 4Kt^2]}} \tag{B.4}$$

$\underline{\epsilon_2 < E < \epsilon_1}$

In this region, both $(E-\epsilon_1)(E-\epsilon_2) < 0$ and $(E-\epsilon_1)(E-\epsilon_2) - 4Kt^2 < 0$, so the two

square roots are purely imaginary and we take

$$\sqrt{(E-\epsilon_1)(E-\epsilon_2)}\cdot\sqrt{(E-\epsilon_1)(E-\epsilon_2)-4Kt^2} = i\sqrt{-(E-\epsilon_1)(E-\epsilon_2)}\cdot i\sqrt{4Kt^2-(E-\epsilon_1)(E-\epsilon_2)}$$
$$= -\sqrt{(E-\epsilon_1)(E-\epsilon_2)[(E-\epsilon_1)(E-\epsilon_2)-4Kt^2]}$$

$$g^{r/a}_{f2}(l,l,E) = \frac{2K(E-\epsilon_2)}{(K-1)(E-\epsilon_1)(E-\epsilon_2)-(K+1)\sqrt{(E-\epsilon_1)(E-\epsilon_2)[(E-\epsilon_1)(E-\epsilon_2)-4Kt^2]}} \tag{B.5}$$

$E > E_1$

In this region, $(E-\epsilon_1)(E-\epsilon_2) > 0$ and $(E-\epsilon_1)(E-\epsilon_2)-4Kt^2 > 0$, so we take the positive square roots as well:

$$g^{r/a}_{f3}(l,l,E) = \frac{2K(E-\epsilon_2)}{(K-1)(E-\epsilon_1)(E-\epsilon_2)+(K+1)\sqrt{(E-\epsilon_1)(E-\epsilon_2)[(E-\epsilon_1)(E-\epsilon_2)-4Kt^2]}} \tag{B.6}$$

In the three cases, the locator has no imaginary part: $g(l,l,z)$ is analytic so that $g^r(l,l,E)$ and $g^a(l,l,E)$ coincide.

Inside the two sub band regions $E_2 < E < \epsilon_2$ and $\epsilon_1 < E < E_1$:

In order to identify the real and imaginary parts of $g(l,l,E)$ in the two sub bands, the denominator in the r.h.s. of Eq. (B.3) must be multiplied by its complex conjugate:

$$g(l,l,E) = \frac{2K(E-\epsilon_2)}{(K-1)(E-\epsilon_1)(E-\epsilon_2)\pm i(K+1)\sqrt{(E-\epsilon_1)(E-\epsilon_2)[4Kt^2-(E-\epsilon_1)(E-\epsilon_2)]}}$$
$$= \frac{2K(E-\epsilon_2)}{A\pm iB} = \frac{2K(E-\epsilon_2)(A\mp iB)}{A^2+B^2}$$

where $A = (K-1)(E-\epsilon_1)(E-\epsilon_2)$ and $B = (K+1)\sqrt{(E-\epsilon_1)(E-\epsilon_2)[4Kt^2-(E-\epsilon_1)(E-\epsilon_2)]} > 0$, by definition. The imaginary part then reads:

$$Im[g(l,l,E)] = \frac{\mp 2K(E-\epsilon_2)B}{A^2+B^2}$$

The sign of $Im[g(l,l,E)]$ is determined by the sign of $E-\epsilon_2$

Lower band: $E_2 < E < \epsilon_2$

Here $(E-\epsilon_2) < 0 \longrightarrow$ we take the **negative** square root:

$$g^r_{lb}(l,l,E) = \frac{2K(E-\epsilon_2)}{(K-1)(E-\epsilon_1)(E-\epsilon_2) - i(K+1)\sqrt{(E-\epsilon_1)(E-\epsilon_2)[4Kt^2-(E-\epsilon_1)(E-\epsilon_2)]}} \tag{B.7}$$

Upper band: $\epsilon_1 < E < E_1$

Here $(E-\epsilon_2) > 0 \longrightarrow$ we take the **positive** square root:

$$g^r_{ub}(l,l,E) = \frac{2K(E-\epsilon_2)}{(K-1)(E-\epsilon_1)(E-\epsilon_2) + i(K+1)\sqrt{(E-\epsilon_1)(E-\epsilon_2)[4Kt^2-(E-\epsilon_1)(E-\epsilon_2)]}} \tag{B.8}$$

One could also have chosen the sign of the square root by imposing $Im[g(l,l,z) < 0]$ in the bands and use Kramers-Kronig relations:

$$Re[g(E)] = -\frac{1}{\pi} P \int_{-\infty}^{+\infty} \frac{Im[g(E')]}{E-E'} dE' \tag{B.9}$$

$$Im[g(E)] = \frac{1}{\pi} P \int_{-\infty}^{+\infty} \frac{Re[g(E')]}{E-E'} dE' \tag{B.10}$$

where P denotes the principal value of the integral.

CONCLUSION

The retarded Green function at site l (locator) is a function of the energy E, and takes different expressions depending on which interval of E it is evaluated on:

$$g^r(l,l,E) = \begin{cases} g^r_{f1}(l,l,E) & \text{if } E < E_2 \\ g^r_{f2}(l,l,E) & \text{if } \epsilon_2 < E < \epsilon_1 \\ g^r_{f3}(l,l,E) & \text{if } E_1 < E \\ g^r_{lb}(l,l,E) & \text{if } E_2 < E < \epsilon_2 \\ g^r_{ub}(l,l,E) & \text{if } \epsilon_1 < E < E_1 \end{cases}$$

If the locator $g(l,l,z)$ is evaluated on a site l / $\epsilon_l = \epsilon_2$, the numerator in Eq. (B.1) becomes $2K(z-\epsilon_1)$, but the choice of the square root sign remains valid:

Lower band: $(E_2 < E < \epsilon_2)$ implies $(E-\epsilon_1) < 0$ and $(E-\epsilon_2) < 0$.
Upper band: $(\epsilon_1 < E < E_1)$ implies $(E-\epsilon_1) > 0$ and $(E-\epsilon_2) > 0$.

From now on, we shall deal with a 1D FI chain, which is a Cayley tree with two nearest neighbours: $K = 1$.

B.1.1 One-site correlation functions (locators)

Forbidden states: $E < E_2$)

- $\epsilon_l = \epsilon_1$

$$g_f^r(l_1, l_1, E) = \frac{(E - \epsilon_2)}{\sqrt{(E - \epsilon_1)(E - \epsilon_2)[(E - \epsilon_1)(E - \epsilon_2) - 4t^2]}} \tag{B.11}$$

- $\epsilon_l = \epsilon_2$

$$g_f^r(l_2, l_2, E) = \frac{(E - \epsilon_1)}{\sqrt{(E - \epsilon_1)(E - \epsilon_2)[(E - \epsilon_1)(E - \epsilon_2) - 4t^2]}} \tag{B.12}$$

Forbidden states: $\epsilon_2 < E < \epsilon_1$

$$g_f^r(l_1, l_1, E) = -\frac{(E - \epsilon_2)}{\sqrt{(E - \epsilon_1)(E - \epsilon_2)[(E - \epsilon_1)(E - \epsilon_2) - 4t^2]}} \tag{B.13}$$

$$g_f^r(l_2, l_2, E) = -\frac{(E - \epsilon_1)}{\sqrt{(E - \epsilon_1)(E - \epsilon_2)[(E - \epsilon_1)(E - \epsilon_2) - 4t^2]}} \tag{B.14}$$

Forbidden states: $E > E_1$

$$g_f^r(l_1, l_1, E) = \frac{(E - \epsilon_2)}{\sqrt{(E - \epsilon_1)(E - \epsilon_2)[(E - \epsilon_1)(E - \epsilon_2) - 4t^2]}} \tag{B.15}$$

$$g_f^r(l_2, l_2, E) = \frac{(E - \epsilon_1)}{\sqrt{(E - \epsilon_1)(E - \epsilon_2)[(E - \epsilon_1)(E - \epsilon_2) - 4t^2]}} \tag{B.16}$$

Lower band:($E_2 < E < \epsilon_2$)

$$g_{lb}^r(l_1, l_1, E) = \frac{i(E - \epsilon_2)}{\sqrt{(E - \epsilon_1)(E - \epsilon_2)[4t^2 - (E - \epsilon_1)(E - \epsilon_2)]}} \tag{B.17}$$

$$g_{lb}^r(l_2, l_2, E) = \frac{i(E - \epsilon_1)}{\sqrt{(E - \epsilon_1)(E - \epsilon_2)[4t^2 - (E - \epsilon_1)(E - \epsilon_2)]}} \tag{B.18}$$

Upper band: $(\epsilon_1 < E < E_1)$

$$g^r_{ub}(l_1, l_1, E) = \frac{-i(E-\epsilon_2)}{\sqrt{(E-\epsilon_1)(E-\epsilon_2)[4t^2-(E-\epsilon_1)(E-\epsilon_2)]}} \tag{B.19}$$

$$g^r_{ub}(l_2, l_2, E) = \frac{-i(E-\epsilon_1)}{\sqrt{(E-\epsilon_1)(E-\epsilon_2)[4t^2-(E-\epsilon_1)(E-\epsilon_2)]}} \tag{B.20}$$

B.1.2 Two-site correlation functions

As mentioned above, the two site correlation functions can be expressed in terms of the already calculated locators using the expressions (5.59a) and (5.59b) and the intermediate functions (5.60) and (5.61) of [Economou, 2006]. The mathematical expression for these correlation functions not only changes depending on the energy region through the locators, but also depending on the type of sites they correlate.

The intermediate functions read:

$$g(l+1, l+1[l], E) = \frac{2}{E-\epsilon_{l+1}+[g(l+1,l+1,E)]^{-1}}$$

$$g(l, l[l+1], E) = \frac{2}{E-\epsilon_{l}+[g(l,l,E)]^{-1}}$$

Forbidden states: $(E < E_2) \cup (\epsilon_2 < E < \epsilon_1) \cup (E > E_1)$

- $\epsilon_l = \epsilon_1, \quad |m-l|$ even: first site ϵ_1, second site ϵ_1

$$\begin{aligned} g^r(l,m,E) &= g^r(l,l,E)t^{|m-l|}[g(l+1,l+1[l],E)]^{|m-l|/2}[g(l,l[l+1],E)]^{|m-l|/2} \\ &= g^r(l,l,E)t^{|m-l|}\left(\frac{2}{E-\epsilon_{l+1}+[g(l+1,l+1,E)]^{-1}}\right)^{|m-l|/2}\left(\frac{2}{E-\epsilon_{l}+[g(l,l,E)]^{-1}}\right)^{|m-l|/2} \end{aligned}$$

$$\begin{aligned} g_f(l_1, m_1, E) = g_f(l_1, l_1, E)t^{|m_1-l_1|}&\left(\frac{2}{E-\epsilon_2+[g_f(l_2,l_2,E)]^{-1}}\right)^{|m_1-l_1|/2} \\ \cdot&\left(\frac{2}{E-\epsilon_1+[g_f(l_1,l_1,E)]^{-1}}\right)^{|m_1-l_1|/2} \end{aligned} \tag{B.21}$$

- $\epsilon_l = \epsilon_1, \quad |m-l|$ odd: first site ϵ_1, second site ϵ_2

$$g_f(l_1,m_2,E) = g_f(l_1,l_1,E)t^{|m_2-l_1|}\left(\frac{2}{E-\epsilon_2+[g_f(l_2,l_2,E)]^{-1}}\right)^{\frac{|m_2-l_1|+1}{2}} \cdot\left(\frac{2}{E-\epsilon_1+[g_f(l_1,l_1,E)]^{-1}}\right)^{\frac{|m_2-l_1|-1}{2}} \tag{B.22}$$

- $\epsilon_l = \epsilon_2, \quad |m-l|$ even: first site ϵ_2, second site ϵ_2

$$g^r(l,m,E) = g^r(l,l,E)t^{|m-l|}\left(\frac{2}{E-\epsilon_{l+1}+[g(l+1,l+1,E)]^{-1}}\right)^{|m-l|/2}\left(\frac{2}{E-\epsilon_l+[g(l,l,E)]^{-1}}\right)^{|m-l|/2}$$

$$g_f(l_2,m_2,E) = g_f(l_2,l_2,E)t^{|m_2-l_2|}\left(\frac{2}{E-\epsilon_1+[g_f(l_1,l_1,E)]^{-1}}\right)^{|m_2-l_2|/2} \cdot\left(\frac{2}{E-\epsilon_2+[g_f(l_2,l_2,E)]^{-1}}\right)^{|m_2-l_2|/2} \tag{B.23}$$

- $\epsilon_l = \epsilon_2, \quad |m-l|$ odd: first site ϵ_2, second site ϵ_1

$$g_f(l_2,m_1,E) = g_f(l_2,l_2,E)t^{|m_1-l_2|}\left(\frac{2}{E-\epsilon_1+[g_f(l_1,l_1,E)]^{-1}}\right)^{\frac{|m_1-l_2|+1}{2}} \cdot\left(\frac{2}{E-\epsilon_2+[g_f(l_2,l_2,E)]^{-1}}\right)^{\frac{|m_1-l_2|-1}{2}} \tag{B.24}$$

Lower band: $(E_2 < E < \epsilon_2)$

The correlation functions in the lower band are extracted from the expressions above, replacing the on-site correlation functions (locators) $g_f(l_i,l_i,E)$ by $g_{lb}(l_i,l_i,E)$.

Upper band:$(\epsilon_1 < E < E_1)$

The correlation functions in the upper band are also extracted from the expressions above, replacing in this case the on-site correlation functions (locators) $g_f(l_i,l_i,E)$ by $g_{ub}(l_i,l_i,E)$.

Note that all the Green functions correlating sites l and m depend only on the absolute value $|l-m|$, and they are therefore symetric in real space for this TB Hamiltonian.

Appendix C

Effect of a spin polarized current on an antiferromagnet: nanofabrication

C.1 Introduction

One of the initial objectives of this thesis was also to experimentally investigate the effect of a spin-polarized current on an AF in a F_a/NM/F_p/AF exchange-biased spin valve, following the experiments shown in Ref [Wei et al., 2007]. These experiments showed partial evidence of STT acting on the AF due to high density currents spin polarized in the exchange-biased F_p in contact with the AF. The second F_a was merely used as an analyser to probe the magnetization direction of the F_p layer (namely the switching field at which its magnetization reverses orientation) through GMR detection. The exchange-biased spin valves consisted of two CoFe layers of 10 (analyser) and 3 nm (polariser) separated by a nonmagnetic (NM) Cu-spacer of 10 nm used to get a vanishing exchange coupling between both F layers. The complete polycrystalline spin valve was: CoFe(10 nm)/Cu(10 nm)/CoFe(3 nm)/FeMn(8 nm). Fig. C.1 illustrates the qualitative explanation of the STT effects on the AF.

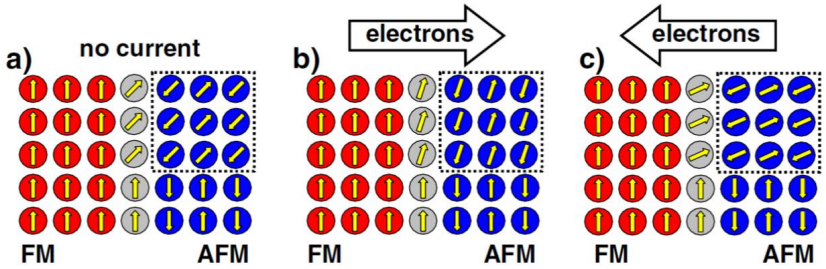

Figure C.1 – Schematic representation of the STT on the AF in the F_p/AF interface [Wei et al., 2007]. Gray magnetic moments indicate uncompensated spins at the AF surface.

The transmitted (reflected) polarized current from the F exerts a torque on the AF spins that tends to rotate the AF order parameter to a direction parallel (perpendicular) to

the F magnetization. Since the AF uncompensated spins at the interface are exchanged-coupled to the bulk AF, torques acting on the bulk will vary their orientation. In addition, the exchange bias field increases (decreases) when the component of the uncompensated spins along the exchange-bias direction is altered to increase (decrease) due to STT. These changes in the exchange bias are then monitored through the switching field of the F_p by GMR detection for different current densities to evidence the effects of STT on the AF. The point contact used to generate a high density electrical current and the typical variations of the electrical resistance reported in [Wei et al., 2007] are illustrated in Fig. C.2. Although the reversal of the free F_a seems to be little affected by the applied current, the average exchange-bias field of F_p is significantly altered, which is ascribed to AF-STT.

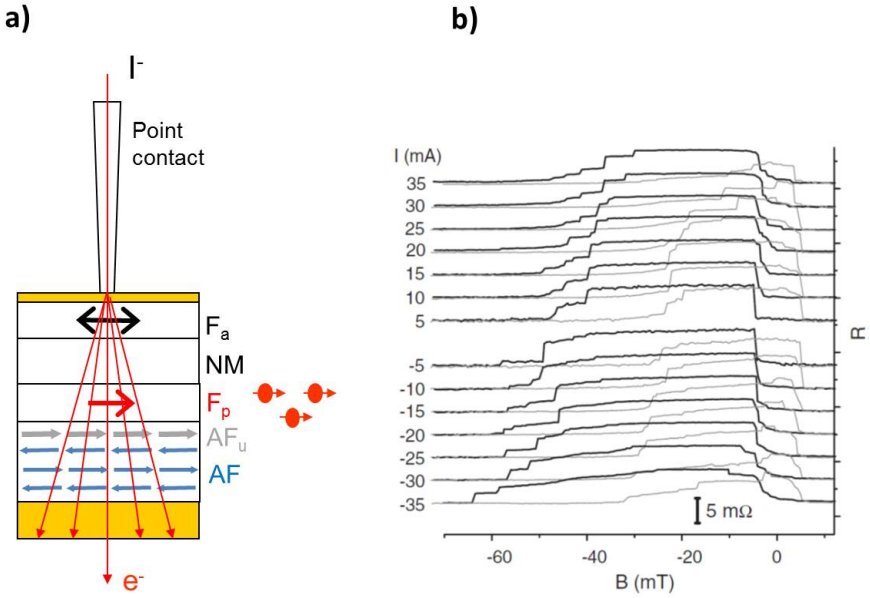

Figure C.2 – **a)** Schematic illustration of the point contact experimental measurement. Spins are polarized in F_p and exert a torque on the AF. The F_a layer probes the F_p reversal. **b)** Magnetoresistance measurements at different current densities. The action of the spin-polarized current on the AF leads to variations of the F_p reversal field for different amplitudes of the bias current due to changes of the exchange bias, proportional to the hysteresis loop shift [Wei et al., 2007].

Joule heating was ruled out as responsible for these effects since not symmetric variations of the exchange bias were observed for positive and negative current polarities. Mutual STT between F_a and F_p was also discarded due to the invariant reversal field of F_a, even for different F thicknesses.

These experimental attempts to show AF-STT only obtained qualitative results due to the uncontrolled current path inherent to the point contact technique, which makes difficult to know precisely the injected current density values. One possible solution is the use of patterned arrays of spin valve nanopillars with controlled geometries to better control the injected electric current density. In an attempt to obtain quantitative results

following the experiments described above, I carried out the nanofabrication of these spin valve arrays. The nanofabrication process I used is the object of the next section.

C.2 Process

Around 1000 elliptical and circular nanopillars of different sizes were patterned from a full sheet 2 inch wafers. Resulting from a collaboration with the Universities of Texas and Michigan, $Si/SiO_2/(Ta(5)/Cu(10))\times5/Ta(5)/Cu(5)/CoFe(10)/Cu(10)/CoFe(3)/FeMn(8)/$ $/Au(5)$ (nm) stacks were provided by the authors of [Wei et al., 2007] in order to avoid differences due the deposition process. Two additional 5 and 170 nm layers of Al and Ta respectively were later deposited at SPINTEC.

I carried out the fabrication of the spin valve nanostructures at the Grenoble PTA (plateforme technologique amont) clean room. The different nanofabrication steps are described by the following text, figures and captions. The process that I used was developed earlier at SPINTEC by Ricardo Sousa, Laurent Vila and Marie-Thérèse Delaye.

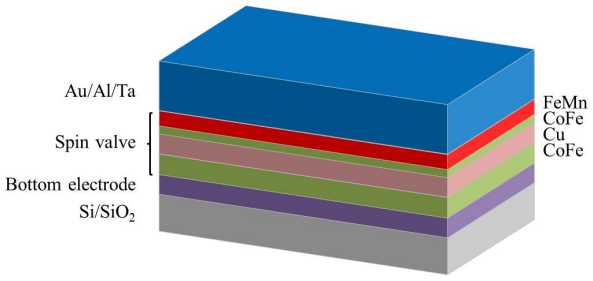

Figure C.3 – First step: annealing of the stack for 30 minutes at 250°C under in plane magnetic field in a 10^{-6} mbar vacuum chamber.

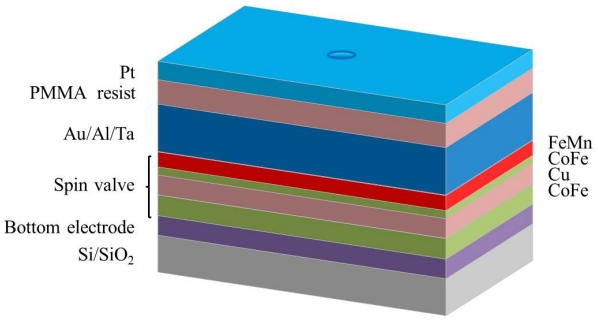

Figure C.4 – Second step: spin coating of the sample with PMMA resist. Electron-beam lithography to custom the nanopillars' shapes: ellipses and circles of diameter ranging from 50 to 1000 nm. Third step: resist development and electron-beam evaporation of 20 nm of Pt to protect the nanopillars from following etching.

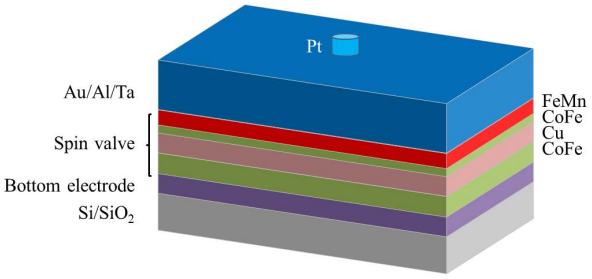

Figure C.5 – Fourth step: resist lift-off to leave only the Pt layer on the ellipses and circles covering the stack.

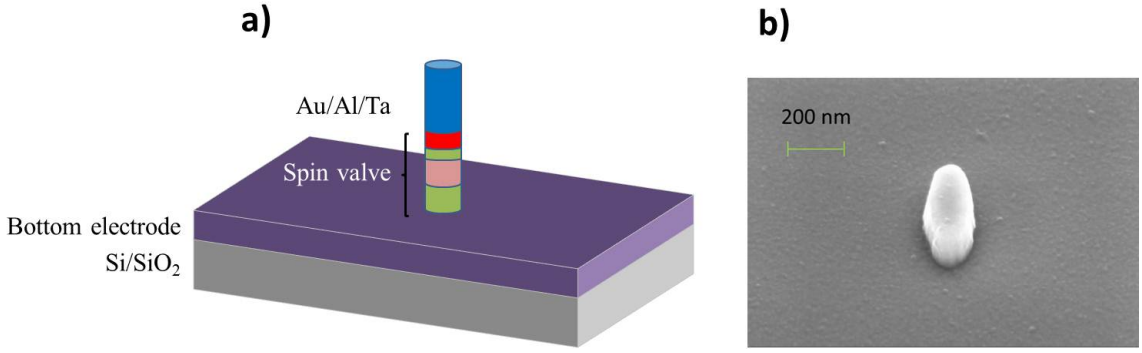

Figure C.6 – Fifth step: **a)** Reactive-ion etching (RIE) of the 150 nm of Ta. The Pt protects the nanopillars from etching. The end of the etching process is checked by laser monitoring. Subsequent ion beam etching (IBE) down to the bottom electrode is performed to remove the rest of the layers. Secondary ion mass spectrometry is used to know when to stop etching. **b)** Scanning electron microscope (SEM) image of the bare nanopillar (around 150 nm wide).

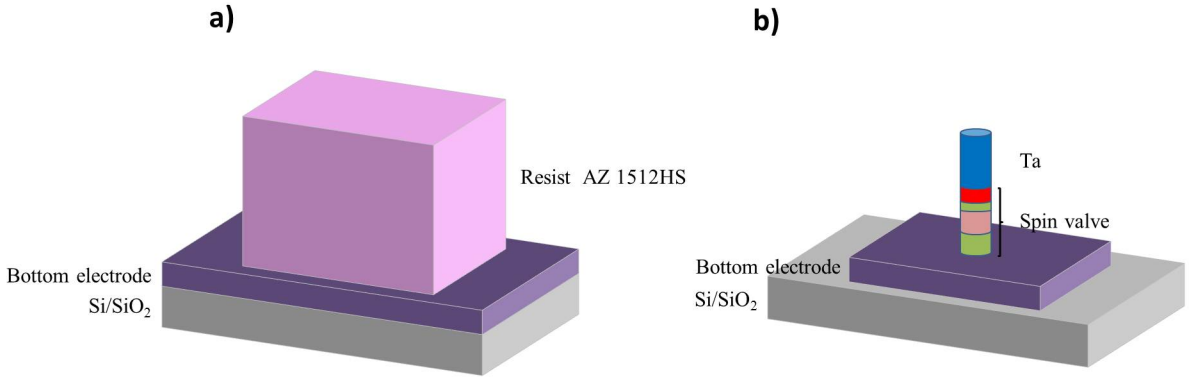

Figure C.7 – **a)** Sixth step: spin coating of the sample with AZ 1512HS resist, ultra violet lithography and resist development to pattern the bottom electrode. **b)** Seventh step. IBE of the bottom electrode. Resist lift off by RIE using a O_2 plasma to remove the resist burnt during the IBE, acetone and ultra sounds.

The thickness of the bottom electrode is checked by a Dektak profilometer. The shapes of the bottom electrode and nanopilars are also checked using an optical microscope and the SEM, respectively.

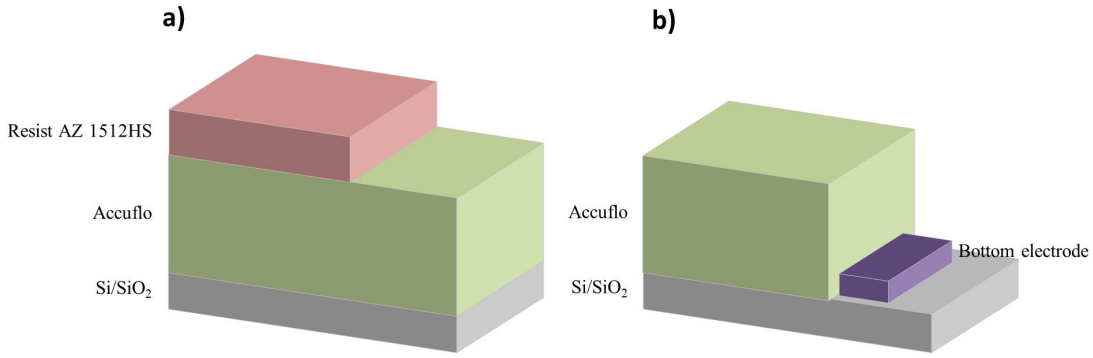

Figure C.8 – **a)** Eighth step: spin coating of the sample with Accuflo polymer to insulate the bottom and top electrodes. Spin coating with AZ 1512HS resist, ultra violet lithography and resist development to custom the insulating zone near the nanopillar. **b)** Ninth step. RIE of the insulator. The end of the etching process is checked by laser monitoring.

The thickness of he Accuflo insulator is checked using the Dektak profilometer; the Accuflo etching rate can be then deduced from the etching time and the Dektak measurements.

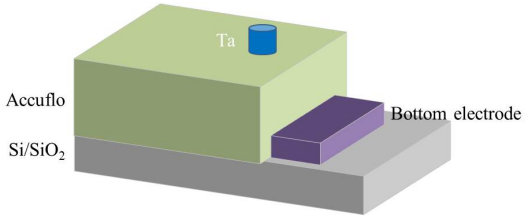

Figure C.9 – Tenth step: RIE to thin down the Accuflo to 90-100 nm and open the nanopillars for the top electrode to come.

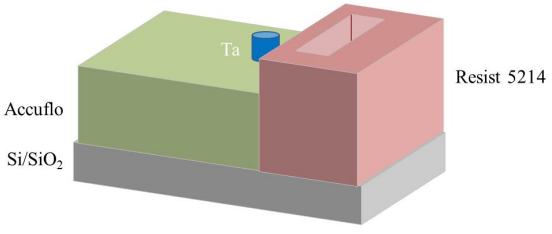

Figure C.10 – Eleventh step: spin coating of the sample with AZ 5214 resist. Ultra-violet lithography and development to custom the shape of the top electrode.

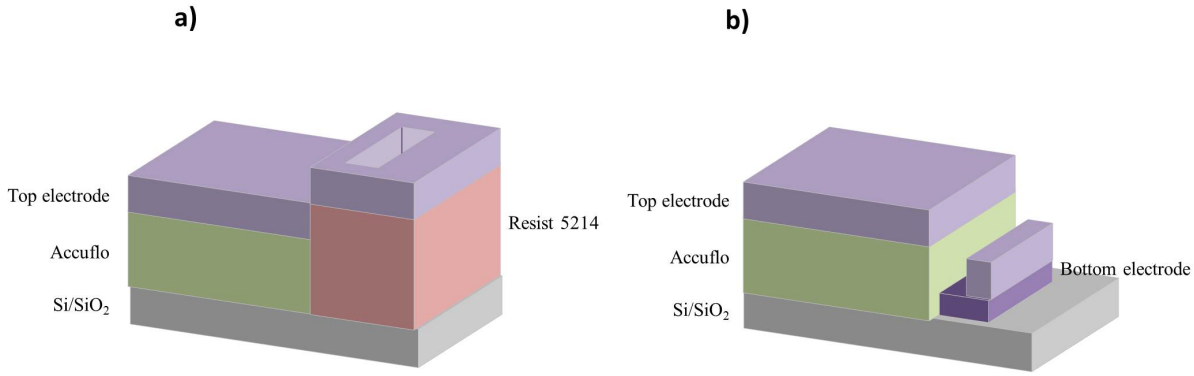

Figure C.11 – **a)** Twelfth step: electron-beam evaporation of the top electrode: Cr(10)/Al(200)/Ti(5)/Au(100). **b)** Thirteenth step. Resist lift-off.

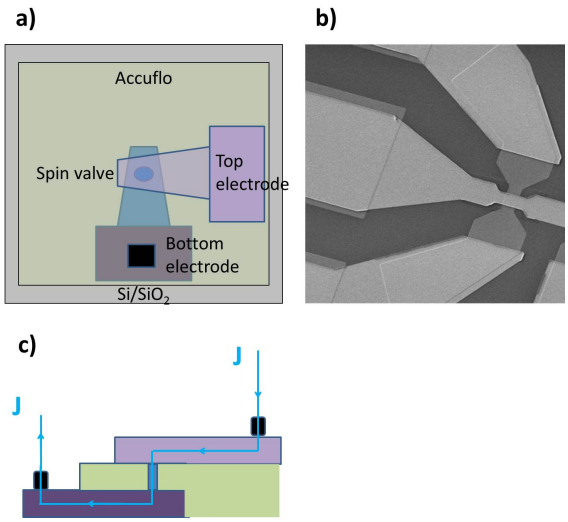

Figure C.12 – **a)** Schematic top view of the magnetic nanostructure. **b)** SEM image of the patterned nanostructure showing the top and bottom contacts. **c)** Schematic illustration of the current flow through the nanostructure. The nanopillar is encapsulated in the Accuflo insulator and contacted by the electrodes.

C.3 Magnetotransport measurements of the patterned nanopillars

The R vs H response of every nanopillar on the wafer was measured by an automated electrical mapper. The nanopillars showing a good GMR signal can be studied applying different current polarities and amplitudes to follow the pinned F_p layer switching field behaviour. A typical R vs H curve is shown in Fig. C.13. Unfortunately, less than 5 percent of the nanopillars gave exploitable R vs H signals resulting in poor statistics.

In addition, very large dispersions were obtained in the R vs H vs j mappings (see Fig. C.14) for the few working pillars, i.e., different dependences on the current density of the F_p switching field were observed for (in principle) comparable nanopillars. The dispersions observed are likely process related and more work is needed to stabilize a

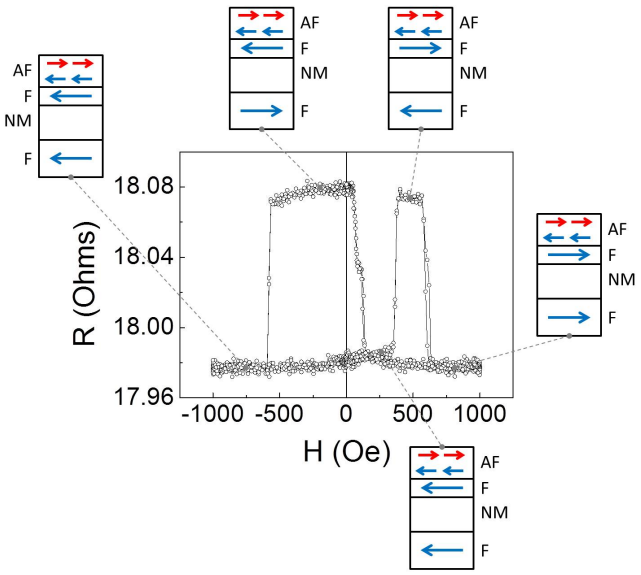

Figure C.13 – R vs H response for a selected nanopillar showing a good GMR signal.

nanofabrication procedure for such spin valve structures.

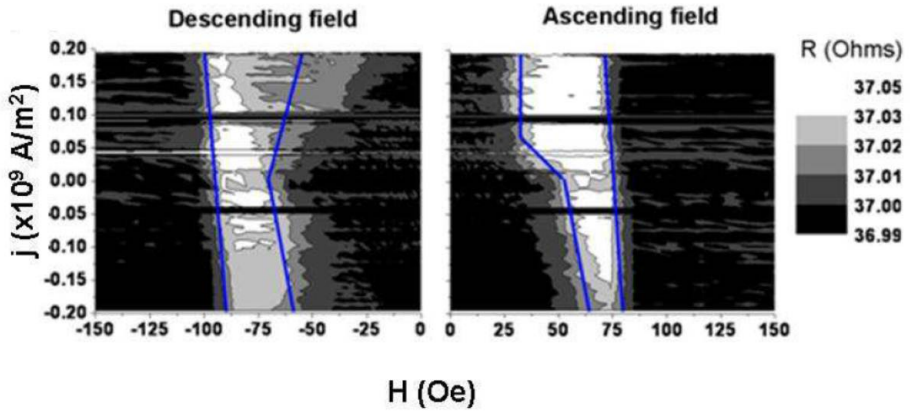

Figure C.14 – Mapping of R vs H loops for increasing and decreasing current densities showing variations of the exchange bias. These loops were measured by Nicolas Mante during his Master thesis. Blue lines highlight the dependence of the F_p switching field on the electrical current density.

One possible solution could be using perpendicular anisotropy stacks, which would probably result in less sensitivity to the edge to edge related dispersions. An additional advantage of stacks with perpendicular anisotropy is that the F/AF configuration can be read using extraordinary Hall effect (EHE) (see Fig. C.15). The analyser F_a is no longer necessary, which avoids mutual F_a-F_p STT and makes the results easier to interpret.

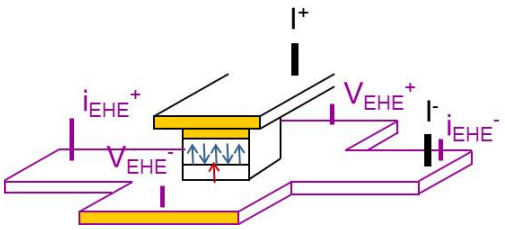

Figure C.15 – Schematic illustration of a nanostructure with perpendicular anisotropy, controlled geometry and EHE reading.

Abstract

Spin transfer torque (STT) and tunnelling magnetoresistance (TMR) in magnetic tunnel junctions with ferromagnetic (F) leads are two essential underlying phenomena of modern spintronics. We present here a theoretical study of STT in antiferromagnet (AF) based tunnel junctions, where two AF metal electrodes are separated by a thin nonmagnetic insulating barrier. In particular, the behaviour of STT and TMR in epitaxial AF-based tunnel junctions is investigated using tight binding calculations in the framework of the Keldysh formalism. The spatial distribution of the STT out-of-plane component is found to be staggered, similar to the in-plane component. This behaviour is specific to the use of a tunnel barrier and significantly differs from the out-of-plane torques reported in previous works using a metallic spacer. Additionally, we show that unlike conventional ferromagnetic-based tunnel junctions, the TMR can increase with applied bias and reach values comparable to typical magnetoresistances found for usual spin valves.

Next, the analysis carried out for AFs is extended to ferrimagnets (FI), for which AFs constitute simpler limiting cases. The additional magnetic complexity inherent to FI materials yields to a richer physics concerning the STT spatial behaviour in FI based tunnel junctions. Electronic structure parameters such as band widths and exchange splittings of the FI are shown to have a strong influence on STT. In particular, the STT spatial distribution within the leads exhibits a striking spin-modulated wave-like behaviour resulting from the interplay between the exchange splittings of the two FI sublattices. This wave-like behaviour can also be tuned via the applied voltage across the junction. Furthermore, the fundamental intrinsic parameter for quantifying STT characteristic lengths in FI metals is identified. This fundamental parameter can be considered as an effective exchange field in FIs, similar to the homogeneous exchange field in the F case.

Finally, the STT characteristic lengths in AF materials are investigated experimentally. Here, room temperature critical depths and absorption mechanisms of spin currents in $Ir_{20}Mn_{80}$ and $Fe_{50}Mn_{50}$ are determined by F-resonance and spin pumping. In particular, room temperature critical depths are observed to be originated from different absorption mechanisms: dephasing for $Ir_{20}Mn_{80}$ and spin flipping for $Fe_{50}Mn_{50}$.

Résumé

En électronique de spin, le couple de transfert de spin (STT) et la magnétorésistance tunnel (TMR) dans les jonctions tunnel magnétiques à électrodes ferromagnétiques (F) sont deux phénomènes physiques essentiels. Dans cette thèse, nous présentons une étude théorique du STT dans des jonctions tunnel antiferromagnétiques (AF), où deux électrodes non plus F mais AF sont séparées par une barrière isolante non-magnétique. Plus concrètement, les comportements du STT et de la TMR sont étudiés dans des jonctions tunnel AF cristallines, et ce, à l'aide de calculs de liaisons fortes dans le cadre du formalisme de Keldysh. Nous avons observé une distribution spatiale uniforme et de signe alternatif de la composante perpendiculaire du STT, ce qui est similaire au comportement de la composante parallèle. Ces variations spatiales de la composante perpendiculaire sont cependant spécifiques à l'utilisation d'une barrière tunnel et contrastent avec les effets observés par le passé pour le cas de couches séparatrices métalliques. De plus, contrairement aux jonctions tunnel F conventionnelles, nous avons montré que la TMR peut augmenter avec la tension appliquée et atteindre des valeurs du même ordre de grandeur que pour des vannes de spin usuelles : tout-métallique et à électrodes F.

L'analyse effectuée pour des AF est ensuite étendue aux matériaux ferrimagnétiques (FI), pour lesquels les AF constituent, somme toute, des cas limites. La complexité magnétique additionnelle inhérente aux FI se traduit par un comportement spatial du STT beaucoup plus riche dans les jonctions tunnel FI. Nous observons notamment que les paramètres électroniques tels que les largeurs et les décalages de bandes ont une très forte influence sur le STT. Plus particulièrement, la différence entre les couplages d'échange inter-spin locaux des deux sous-réseaux du FI donne lieu à une distribution spatiale du STT ondulatoire qui est modulée par la densité locale de spin. Il est possible d'ajuster cet effet en jouant sur la tension appliquée aux bornes de la jonction tunnel FI. Nous trouvons de plus que la différence entre les couplages d'échange inter-spin locaux constitue un paramètre fondamental pour la quantification des longueurs caractéristiques du STT dans les FIs. Ce paramètre peut être considéré comme un champ d'échange effectif, par similitude avec le cas usuel des Fs qui présentent un champ d'échange homogène.

Pour finir, nous avons sondé expérimentalement les longueurs caractéristiques du STT dans des AFs polycristallins. Pour de l'$Ir_{20}Mn_{80}$ et du $Fe_{50}Mn_{50}$, nous avons déterminé les longueurs de pénétration de spin et les mécanismes d'absorption de courants de spin à température ambiante en utilisant la résonance F et le pompage de spin. Plus précisément, nous avons associé les profondeurs de pénétration critiques à deux mécanismes d'absorption distincts: du déphasage pour l'$Ir_{20}Mn_{80}$ et du retournement de spin pour le $Fe_{50}Mn_{50}$.